

# Non-Hermitian physics in deformed optical microdisk cavities: Asymmetric backscattering and $Q$ -spoiling

**Dissertation**

zur Erlangung des akademischen Grades

**doctor rerum naturalium**

**(Dr. rer. nat.)**

genehmigt durch die Fakultät für Naturwissenschaften  
der Otto-von-Guericke-Universität Magdeburg

von Dipl.-Phys. Julius Kullig  
geb. am 03.12.1989 in Dresden

Gutachter: Prof. Dr. rer. nat. habil. Jan Wiersig  
Prof. Dr. rer. nat. habil. Henning Schomerus

eingereicht am: 21.06.2017

verteidigt am: 23.10.2017



## Abstract

Optical microdisk cavities can confine light for very long times in a small volume due to total internal reflection. This ability makes them interesting for many applications. However, in wave mechanics microdisk cavities belong to a non-Hermitian Hamiltonian of a weakly open system and not to an Hermitian Hamiltonian of a closed system. Consequently, they show pronounced aspects of non-Hermitian physics. One prominent phenomenon of this nature is the asymmetric backscattering which occurs when the cavity's boundary is deformed in a way that all mirror-reflection symmetries are destroyed. Such a fully asymmetric cavity exhibits generically an imbalance between clockwise (CW) and counter-clockwise (CCW) traveling waves inside the cavity. This imbalance also manifests in the optical modes: They appear in nearly degenerate pairs, they are highly pairwise non-orthogonal, and both modes of such a pair have the same preferred sense of rotation what is quantified by a finite chirality.

In the first part of this thesis the asymmetric backscattering is studied in the ray dynamics. To this end the Frobenius-Perron operator which describes the time evolution of classical intensity distributions in phase space is constructed for microdisk cavities. The eigenstates of the Frobenius-Perron operator reveal the interesting non-Hermitian properties of the optical modes like non-orthogonality and chirality. A nice agreement to the wave mechanics is observed for cavities with strong deformed boundaries in terms of an averaged Husimi function of long-lived modes with relatively small wavelength.

Furthermore in this thesis a perturbation theory for fully asymmetric microdisk cavities is derived. For this purpose a slightly deformed circular cavity is considered such that the modes can be expanded perturbatively in solutions of the circular cavity. By properly accounting the degeneracy of CW and CCW propagating waves in the circular cavity this perturbation theory is able to capture also the interesting non-Hermitian effects in asymmetric deformed cavities like a finite chirality of the mode pairs. Additionally, the established perturbation theory for slightly deformed symmetric cavities with a mirror-reflection symmetry is extended to the next higher order in this thesis.

Another manifestation of the non-Hermitian physics in optical microdisk cavities is the long but finite lifetime of the whispering-gallery modes which is commonly expressed in a large  $Q$ -factor. In deformed cavities the  $Q$ -factor is usually spoiled. In this thesis it is revealed that the  $Q$ -spoiling in slightly deformed microdisk cavities is a consequence of resonance-assisted tunneling due to nonlinear resonance chains in the phase space. A nice agreement between the derived predictions of the  $Q$ -spoiling and full numerical wave simulations is observed.



# Contents

<b>1</b>	<b>Introduction</b>	<b>1</b>
<b>2</b>	<b>Ray dynamics</b>	<b>5</b>
2.1	Poincaré section for ray dynamics . . . . .	5
2.2	Billiard dynamics in deformed cavities . . . . .	7
2.2.1	Integrable and chaotic billiard dynamics . . . . .	7
2.2.2	Symmetries . . . . .	14
2.3	From billiards to microdisk cavities . . . . .	15
2.3.1	Partial leakage and true-time dynamics . . . . .	16
2.3.2	Far-field emission and invariant sets in phase space . . . . .	18
<b>3</b>	<b>Wave dynamics</b>	<b>21</b>
3.1	From Maxwell's equations to a scalar mode equation . . . . .	21
3.2	The circular microdisk . . . . .	25
3.3	Deformed microdisk cavities . . . . .	27
3.3.1	Symmetric deformations . . . . .	28
3.3.2	Asymmetric deformations and asymmetric backscattering . . . . .	30
3.4	Ray-wave correspondence . . . . .	35
3.4.1	The boundary Husimi representation . . . . .	35
3.4.2	Comparing ray and wave dynamics . . . . .	36
<b>4</b>	<b>Asymmetric backscattering in ray dynamics</b>	<b>41</b>
4.1	Asymmetric backscattering of uniform intensity distributions . . . . .	41
4.2	Frobenius-Perron operator for optical microdisk cavities . . . . .	45
4.2.1	Construction of the Frobenius-Perron operator . . . . .	46
4.2.2	Eigenstates and eigenvalues in the presence of asymmetric backscattering	49
4.2.3	Application . . . . .	55
4.3	1D model for asymmetric backscattering . . . . .	66
4.4	Chapter summary . . . . .	71
<b>5</b>	<b>Perturbation theory for slightly deformed symmetric microdisk cavities</b>	<b>73</b>
5.1	General setup for the symmetric perturbation theory . . . . .	74

5.2	Review on first- and second-order perturbation theory . . . . .	77
5.3	Extension to third-order perturbation theory . . . . .	79
5.4	Applications – Improvements from the third order? . . . . .	84
5.5	Chapter summary . . . . .	87
<b>6</b>	<b>Perturbation theory for slightly deformed asymmetric microdisk cavities</b>	<b>91</b>
6.1	General setup . . . . .	91
6.2	First-order perturbation theory . . . . .	93
6.3	Second-order perturbation theory . . . . .	94
6.4	Applications . . . . .	97
6.5	Chapter summary . . . . .	109
<b>7</b>	<b>Resonance-assisted tunneling for slightly deformed microdisk cavities</b>	<b>111</b>
7.1	Outline and basic ideas for the RAT predictions in microdisk cavities . . . . .	111
7.2	The pendulum Hamiltonian – Phase-space approximation of a resonance chain	114
7.3	$Q$ -spoiling and mode prediction from the phase-space approximation . . . . .	118
7.4	Outlook: $kR$ splitting of even and odd parity modes . . . . .	130
7.5	Chapter summary . . . . .	136
<b>8</b>	<b>Summary and conclusion</b>	<b>137</b>
<b>A</b>	<b>Appendix</b>	<b>139</b>
A.1	Calculation of billiard dynamics . . . . .	139
A.2	Asymmetric backscattering in the angular momentum . . . . .	141
A.2.1	The Fourier-truncated spiral: An example system for asymmetric backscattering . . . . .	141
A.2.2	The curve $L_z(q, p) = 0$ in phase space . . . . .	142
A.2.3	Backscattering concerning $L_z(q, p) = 0$ . . . . .	143
A.2.4	Shifting the angular momentum center . . . . .	147
A.3	Derivatives of the function $\tilde{D}_m^l(x)$ . . . . .	149
A.4	Derivatives for the asymmetric perturbation theory . . . . .	152
A.5	Improving the perturbation theory using scaling . . . . .	155
A.6	Illustration of the BEM error for the splitting $\Delta x$ . . . . .	158
	<b>Bibliography</b>	<b>161</b>

# 1 Introduction

Optical microcavities are small dielectric devices which are of particular interest in physics for many reasons. On the one hand they promise lots of practical applications due to their ability to store the energy of light for very long times in a small volume [Vahala, 2003]. For example they can be used as detecting devices such as label-free sensors for small particles like viruses or molecules [Armani et al., 2007, Vollmer et al., 2008, Vollmer and Arnold, 2008]; or as small sensors for rotating motion using the Sagnac effect [Post, 1967, Sunada and Harayama, 2006, Sunada and Harayama, 2007]. A large class of applications is based on the fact that deformed microcavities can exhibit directional light emission [Levi et al., 1993, Nöckel and Stone, 1997, Gmachl et al., 1998, Wiersig and Hentschel, 2008, Shinohara et al., 2009, Wang et al., 2010, Schermer et al., 2015]. Therefore they can be used, e.g., as microlaser with a very low threshold [Wiersig et al., 2009, Park et al., 2004] or as single photon emitters [Michler et al., 2000, Pelton et al., 2002]. Recently, an application as a narrow-band and speckle-free light source has been considered for imaging [Hokr et al., 2016] as well. Further applications of microcavities, e.g., as optical frequency filters [Lohmeyer, 2002, Ilchenko and Matsko, 2006] or frequency comp generators for telecommunication technology, astronomy or microwave photonics have been discussed [Kippenberg et al., 2011].

On the other hand microcavities are of particular interest also in theoretical physics. For example they allow to study the correspondence of ray and wave dynamics in a regime where the size of the cavity is almost comparable the wavelength. For this reason deformed microcavities are of interest in the field of quantum chaos [Stöckmann, 2000, Haake, 2010] where one studies the signatures in the quantum (or wave) dynamics of systems whose classical (or ray) dynamics is chaotic [Stone, 2001, Türeci et al., 2005]. Furthermore, microcavities are ideal model systems for non-Hermitian physics [Cao and Wiersig, 2015, Lee et al., 2009, Zhu et al., 2010, Brandstetter et al., 2014, Peng et al., 2014b, Peng et al., 2016]. Since they store the energy of light for very long but finite times they are described by a non-Hermitian Hamiltonian of an open system instead of an Hermitian Hamiltonian of a closed system. Generic non-Hermitian systems exhibit so-called exceptional points (EPs) where, depending on multiple system parameters, the eigenvalues and simultaneously the wave functions coalesce [Kato, 1966, Heiss, 2000, Heiss and Harney, 2001, Berry, 2004]. In microcavities EPs can be generated e.g. by boundary deformations [Lee et al., 2009, Lee et al., 2008b], external scatterers [Peng et al., 2016] or balanced regions of amplification and absorption [El-Ganainy et al., 2007a, Guo

et al., 2009a, Ruter et al., 2010]. Cavities which operate at such an EP are proposed to have improved sensitivity against perturbations which is advantageous, e.g., for sensing devices [Wiersig, 2016, Wiersig, 2014b].

So far microcavities have been fabricated in various shapes. As three-dimensional objects the most prominent realizations are e.g. microspheres [Collot et al., 1993, Garrett et al., 1961, Göttinger et al., 2006], microtoroids [Ilchenko et al., 2001, Armani et al., 2003], microjets [Yang et al., 2006, Lee et al., 2002], micropillars [Albert et al., 2010, Böckler et al., 2008], or microrings [Zhang et al., 1995]. However, another large class of realizations which are often studied experimentally, theoretically, and numerically are microdisk cavities [McCall et al., 1992, Levi et al., 1993, Harayama and Shinohara, 2011]. They can be treated within the effective refractive index approximation as quasi-two-dimensional objects in the  $x$ - $y$  plane. For these microdisk cavities a lot of shapes have been considered and realized experimentally for their own desired purposes; e.g. the Limaçon [Wiersig and Hentschel, 2008, Song et al., 2009, Shinohara et al., 2009, Yan et al., 2009, Yi et al., 2009], the annular cavity [Hentschel and Richter, 2002, Hackenbroich and Nöckel, 1997, Bäcker et al., 2009], the spiral [Chern et al., 2003, Luo and Poon, 2007, Lee et al., 2008a, Hentschel and Kwon, 2009], or the quadrupole [Tureci et al., 2002, Nöckel et al., 1996] just to mention a few representative examples.

Such quasi-two-dimensional optical microdisk cavities are the scope of this thesis. The aim here is to get a deeper understanding of the dynamics and the mode properties in microdisk cavities by using perturbation theory and methods from quantum chaos. In particular three main topics are discussed in this thesis as follows.

As the first topic of the thesis the so-called asymmetric backscattering [Wiersig, 2014a] is issued. This phenomenon occurs if a microcavity is deformed or perturbed in a way such that all mirror-reflection symmetries of the system are destroyed. Accordingly, an imbalance between clockwise and counter-clockwise propagating waves inside the cavity arises. As a consequence of this imbalance these fully asymmetric cavities exhibit nearly degenerate pairs of non-orthogonal modes where both modes have the same preferred sense of rotation [Wiersig et al., 2008, Wiersig et al., 2011, Wiersig et al., 2008, Wiersig, 2011] (for experiments see Refs. [Peng et al., 2016, Redding et al., 2012, Ryu et al., 2017]). In other words, the modes inside the cavity are no longer standing waves but (partially) traveling waves which is quantified by a finite chirality of the modes. Asymmetric backscattering is wave mechanically well explained by an effective non-Hermitian  $2 \times 2$  Hamiltonian describing the dynamics of such a mode pair. In this thesis it is shown that not only such a two-mode Hamiltonian but also proper eigenstates can be constructed within the ray dynamics. To do so, the Frobenius–Perron operator [Altmann et al., 2013] (FPO) for microcavities is introduced. This operator describes the classical dynamics of intensities in a Poincaré section of the phase space. The eigenstates of the FPO can be seen as classical analogues to long-lived optical modes. In particular they also appear in nearly degenerate pairs where both eigenstates are non-orthogonal and have the same preferred sense



of rotation. Numerically a good agreement of the FPO eigenstates with an average of long-lived modes with relatively small wavelength (or large dimensionless wave number  $kR$ ) is observed.

The second topic in this thesis is the perturbation theory for slightly-deformed microdisk cavities. This perturbation theory was originally developed by Dubertrand *et al.* [Dubertrand et al., 2008] for TM polarization and symmetric deformations, i.e. cavities whose deformed boundary still has a mirror-reflection symmetry. By this restriction one avoids a coupling between degenerate modes of the circular cavity because the modes of the deformed cavity still fall into two orthogonal classes of even and odd parity with respect to the mirror-reflection symmetry line. In the past years this perturbation theory has been shown to give reliable predictions in many cases e.g. for the Limaçon [Kraft and Wiersig, 2014] or cavities with local boundary deformations [Wiersig, 2012] (and also for the case of TE polarization [Ge et al., 2013]). In this thesis the perturbation theory (for TM polarization) is reviewed and extended to one higher (third) order. However, the remaining restriction to symmetric cavities prevents to capture the interesting non-Hermitian phenomena in cavities with asymmetric deformed boundaries such as copropagating and non-orthogonal mode pairs. Therefore, the perturbation theory is also generalized here such that it includes the coupling between degenerate circular modes. Consequently, this generalized perturbation theory is now applicable to fully asymmetric boundary deformations without any mirror-reflection symmetry. Furthermore, the derived formulas verify analytically the existence of nearly degenerate pairs of non-orthogonal modes with same preferred sense of rotation in cavities without mirror-reflection symmetry. In the regime of large wavelength (i.e. small dimensionless wave number  $kR$ ) the perturbation theory is in very good agreement with full numerical solutions. Furthermore such a perturbation theory for fully asymmetric cavities provides a solid base for further analytical investigations on e.g. the problem of boundary roughness [Wiersig and Kullig, 2017], optimization procedures to achieve arbitrary desired far-fields [Kraft and Wiersig, 2016] or search procedures for EPs in slightly deformed cavities.

The third topic which is discussed in this thesis deals with the question how optical modes in slightly deformed cavities are influenced by classical resonance chains in the phase space. Such resonance chains consist of an alternating sequence of stable and unstable periodic orbits which naturally develop due to the Poincaré-Birkhoff theorem if an integrable system is slightly perturbed [Poincaré, 1912, Birkhoff, 1913]. In the case of microdisk cavities this perturbation can be seen again as a slight boundary deformation of the circular cavity. The signatures of such resonance chains in the corresponding quantum mechanical systems have been discussed so far intensively at kicked Hamiltonian systems: Here a resonance chain enhances the tunneling process between the separated regions in phase space which is therefore called resonance-assisted tunneling (RAT) [Brodier et al., 2002, Keshavamurthy and Schlagheck, 2011]. RAT has been so far also verified by experiments on microwave billiards [Gehler et al., 2015] and recently in optical microdisk cavities as well [Kwak et al., 2015]. In this thesis the methods describing

RAT in quantum mechanics were adapted to the case of microcavities. Consequently, the RAT mechanism can explain the enhanced decay rates of modes in a slightly deformed cavity. Therefore, RAT in microdisk cavities leads to the so-called  $Q$ -spoiling [Nöckel et al., 1994, Yu et al., 2015]. Furthermore, the RAT mechanism allows to predict the mode pattern inside the cavity and the emission profile of the mode. As an outlook at the end of the thesis it is demonstrated that RAT not only explains the formation of single modes but also the slight differences between modes of even and odd parity in deformed cavity with a mirror reflection-symmetry. In particular this thesis is organized as follows. In Sec. 2 the ray dynamics in a microdisk cavity is introduced. Afterwards in Sec. 3 it is explained how Maxwell's equations reduce to a scalar mode equation for disk-like cavities. Furthermore, some general properties of optical modes in the circular and the deformed cavity are discussed in this section. In the following Sec. 4 the first topic of this thesis, i.e. the asymmetric backscattering in ray dynamics, is targeted. In Sec. 5 then the perturbation theory for slightly deformed symmetric cavities is reviewed. Here, also an extension of the perturbation theory to an higher order (third order) is presented. In Sec. 6 the perturbation theory is extended to the case of fully asymmetric boundary deformations which is the second main topic of this thesis. The third main topic, the resonance-assisted tunneling in microdisk cavities, is discussed in Sec. 7. Finally, in Sec. 8, a summary of the thesis is provided.

## 2 Ray dynamics

In this chapter the ray dynamics of quasi-two-dimensional (2D) microcavities with homogeneous refractive index is discussed. In this model light propagates on straight lines until it is partially reflected at the cavity's boundary. The pure geometrical dynamics of the reflections, i.e. the billiard dynamics, is usually expressed in a Poincaré surface of section along the cavity's boundary (in the following Poincaré section for short). The so-called Birkhoff coordinates of this Poincaré section are introduced in Sec. 2.1. Afterwards, in Sec. 2.2, it is discussed how a deformation of the cavity's boundary effect this billiard dynamics and leads to a transition from integrable to chaotic dynamics. Additionally to the billiard dynamics also the intensity of the light ray and the traveling time are dynamical variables which are discussed in Sec. 2.3. Furthermore, a review is given in this section how the ray model can be used to predict the far-field emission pattern of a microdisk cavity.

### 2.1 Poincaré section for ray dynamics

The billiard dynamics in a microdisk cavity takes place in the 2D  $x$ - $y$  plane. Therefore the phase space for this dynamics consists of two position and two momentum variables; i.e. it is four-dimensional (4D). However, this full 4D phase space contains “trivial” information. Therefore, (i) scaling and (ii) a section along the boundary is commonly used to project the dynamics onto a 2D Poincaré section of the 4D phase space which still contains all relevant information about the dynamics. To first employ the scaling it is used that the light propagation inside the cavity is equivalent to the motion of a classical particle whose billiard dynamics is described by the (dimensionless) Hamiltonian

$$\mathcal{H}(\vec{q}, \vec{p}) = \begin{cases} \frac{\vec{p}^2}{2} & \text{inside the cavity} \\ \infty & \text{outside} \end{cases} \quad (2.1)$$

where  $\vec{q}$  and  $\vec{p}$  are position and momentum in the  $x$ - $y$ -plane. This Hamiltonian has the scaling property

$$\mathcal{H}(\vec{q}, \lambda \vec{p}) = \lambda^2 \mathcal{H}(\vec{q}, \vec{p}) \quad (2.2)$$

which implies that whenever  $[\vec{q}(t), \vec{p}(t)]$  solve Hamiltonian equations of motion

$$\dot{\vec{q}} = \frac{\partial \mathcal{H}(\vec{q}, \vec{p})}{\partial \vec{p}}, \quad \dot{\vec{p}} = -\frac{\partial \mathcal{H}(\vec{q}, \vec{p})}{\partial \vec{q}} \quad (2.3)$$

on the energy shell  $E = \mathcal{H}(\vec{q}, \vec{p})$  then  $[\vec{q}_\lambda(t), \vec{p}_\lambda(t)] = [\vec{q}(\lambda t), \lambda \vec{p}(\lambda t)]$  is the solution of Eq. (2.3) with energy  $\lambda^2 E$  as

$$\dot{\vec{q}}_\lambda = \lambda \dot{\vec{q}} = \lambda^2 \frac{\partial \mathcal{H}}{\partial(\lambda \vec{p})}(\vec{q}, \vec{p}) = \frac{\partial \mathcal{H}}{\partial(\lambda \vec{p})}(\vec{q}, \lambda \vec{p}) = \frac{\partial \mathcal{H}}{\partial \vec{p}_\lambda}(\vec{q}_\lambda, \vec{p}_\lambda) \quad (2.4)$$

$$\dot{\vec{p}}_\lambda = \lambda^2 \dot{\vec{p}} = -\lambda^2 \frac{\partial \mathcal{H}}{\partial \vec{q}}(\vec{q}, \vec{p}) = -\frac{\partial \mathcal{H}}{\partial \vec{q}}(\vec{q}, \lambda \vec{p}) = -\frac{\partial \mathcal{H}}{\partial \vec{q}_\lambda}(\vec{q}_\lambda, \vec{p}_\lambda). \quad (2.5)$$

Note that the dot denotes a derivative with respect to  $t$ . In other words, the geometrical billiard dynamics in a microdisk cavity is invariant under changing the ray's momentum. Throughout the rest of this thesis the scaling property is exploited by fixing  $\vec{p}^2 = 1$ ; i.e. by considering rays with dimensionless energy  $E = 1/2$ . This leads to dynamics on a three-dimensional (3D) energy shell in the full 4D phase space.

Next, the fact is exploited that the ray dynamics between the boundary reflections is “trivial” in the sense that  $\vec{p}$  is constant. Therefore, it is convenient to describe the ray dynamics in a 2D Poincaré section of the 3D energy shell. The most commonly used section for billiard systems is given by so-called Birkhoff coordinates  $(q, p)$ . Here, the position  $q$  along the cavity's boundary is tracked at the reflections. Accordingly, the conjugate momentum  $p$  is the projection of the full momentum vector  $\vec{p}$  of the reflected ray onto the tangent of the boundary at  $q$ . As shown in Fig. 2.1(a) this momentum  $p = \sin \chi$  is given by the angle of incidence/reflection  $\chi$ . The sign of the angle  $\chi$  can be used to identify clockwise (−) and counter-clockwise (+) propagation inside the cavity.

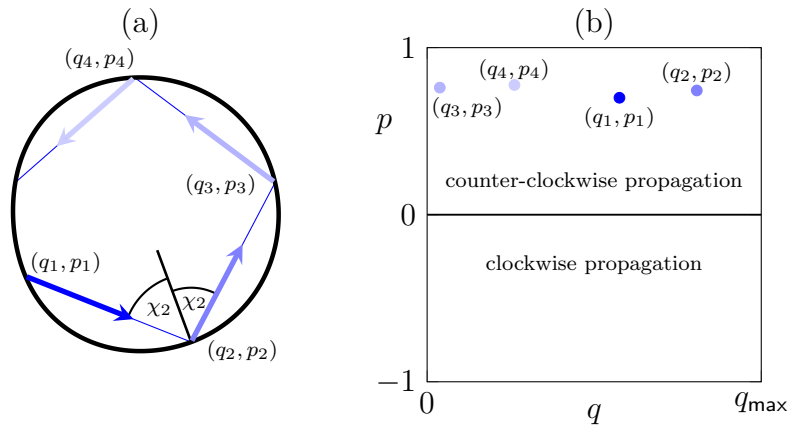


**Figure 2.1:** (a) Blue arrows illustrate a ray propagating in a Limaçon shaped cavity, see Eq. (2.15). (b) The four reflection positions  $q_i$  and momenta  $p_i = \sin \chi_i$  are shown in the Poincaré section of the phase space as blue dots.

Consequently, the time-continuous billiard dynamics in a 4D phase space is effectively described by a discrete mapping

$$(q_{n+1}, p_{n+1}) = \mathcal{M}(q_n, p_n) \quad (2.6)$$

in a 2D Poincaré section of the phase space. In the following this 2D Poincaré section of the phase space is always considered and for convenience simply called “phase space”. Note that billiard dynamics implies that the inverse mapping  $(q_{n-1}, p_{n-1}) = \mathcal{M}^{-1}(q_n, p_n)$  is given by

$$(q_{n-1}, -p_{n-1}) = \mathcal{M}(q_n, -p_n) \quad (2.7)$$

which follows from time-reversal symmetry. And further note that the mapping  $\mathcal{M}$  can only be written explicitly for simple boundary shapes. Generic cavity shapes require a numerical evaluation of  $\mathcal{M}$ .

An often considered case are cavities whose boundary is given in polar coordinates by a (may implicit defined) continuous function  $r(\phi)$ . Therefore it is mentioned that sometimes not the arc length

$$q(\phi) = \int_0^\phi \sqrt{r'^2(x) + r^2(x)} dx \quad (2.8)$$

and  $p$  but also the angle  $\phi$  and the  $z$ -component of the angular momentum  $L_z = (\vec{r} \times \vec{p})_z$  of the ray can be used as proper coordinates for a Poincaré section. However, the tuple  $(\phi, p)$  leads a non-area preserving Poincaré mapping. Note that even in convex cavities the coordinate transformation  $(\phi, L_z) \mapsto (q, p)$  does not need to be bijective; i.e. for some deformations one finds two pairs  $(q, p_1)$  and  $(q, p_2)$  leading to the same  $(\phi, L_z)$ .

## 2.2 Billiard dynamics in deformed cavities

In the previous section an efficient description of the billiard dynamics was explained. The purpose of this section is now to investigate the billiard dynamics depending on the cavity’s boundary shape. In Sec. 2.2.1 it is explained how chaotic dynamics develops by perturbing the boundary of an integrable cavity. Afterwards, in Sec. 2.2.2, the properties of the billiard dynamics in cavities with commonly used symmetries are remarked.

### 2.2.1 Integrable and chaotic billiard dynamics

The billiard dynamics in a 2D microdisk cavity is integrable if there exists two constants of motion. One is always the (dimensionless) energy which is here fixed to  $E = 1/2$ , see Sec. 2.1. Another constant of motion can be extracted in some cases from the particular shape of the

microdisk cavity. Then, in a cavity with integrable dynamics the time evolution of an initial condition at most fills a 2D tori in the 4D phase space and a 1D tori, i.e. a curve, in the 2D Poincaré section of the phase space. If one iterates two nearby initial conditions their distance slowly (sub-exponentially) increases with time.

On the other hand a strongly deformed cavity exhibits regions in phase space where the dynamics depends sensitively on the initial condition, i.e. the distance between two nearby initial conditions exponentially increases with time. This type of dynamics is called chaotic. A chaotic orbit fills a whole area in phase space. For a microdisk cavity with chaotic dynamics one cannot find a second constant of motion.

In the following the transition from integrable to chaotic dynamics due to a boundary deformation which acts as a generic perturbation to the integrable dynamics is discussed. Therefore, first, the integrable dynamics of the circular cavity is reviewed and afterward gradually increasing deformations are considered.

### Integrable dynamics in a circular cavity

The circular cavity is one of the simplest systems and shows integrable billiard dynamics. The reflections at the boundary change the momentum  $\vec{p}$  parallel to  $\vec{r}$ . Therefore, the second conserved quantity is the angular momentum  $L_z = (\vec{r} \times \vec{p})_z$  of a ray. Consequently, also the Birkhoff coordinate  $p = \sin \chi$  remains constant. The billiard dynamics of the circular cavity is given in phase space explicitly by the mapping

$$q_{n+1} = q_n + 2R \arccos(p_n) \quad \text{mod } 2\pi R \quad (2.9a)$$

$$p_{n+1} = p_n \quad (2.9b)$$

where  $R$  is the radius of the circle.

This mapping can be compared to the continuous time evolution

$$\theta(t) = \theta(0) + \omega(J)t \quad (2.10a)$$

$$J(t) = J(0). \quad (2.10b)$$

of a general integrable Hamiltonian system  $H(\theta, J)$  with action-angle variables  $(J, \theta)$  where  $J$  is the constant of motion [Lichtenberg and Lieberman, 1992]. Then

$$\omega(p) = 2R \arccos(p) \quad (2.11)$$

can be deduced as the frequency of orbits in the phase-space map of the circular cavity [see Fig. 2.3]. Strictly speaking this conclusion is only valid for  $p \geq 0$ . For  $p < 0$  the frequency is negative as  $\omega(-|p|) = -\omega(|p|)$  since the real space dynamics is rotating in the clockwise direction and not in the mathematically positive counter-clockwise direction. For the following

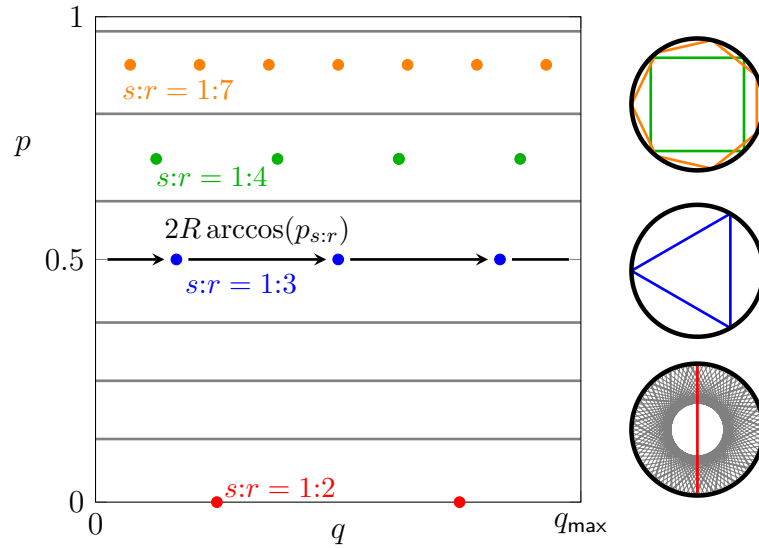


**Figure 2.2:** The billiard dynamics in a circular cavity is shown in phase space. Colored dots mark some (marginally stable) periodic orbits while gray lines illustrate non-periodic orbits filling a whole line in phase space. Corresponding real space trajectories are shown in the right panel.

discussion in this section it is sufficient to consider only the upper half of the phase space with positive frequency  $\omega(p)$ .

In the following, it is useful to distinguish between periodic and non-periodic orbits. Periodic orbits  $(q_n^*, p_n^*)$  with periodicity  $r$  need to fulfill

$$\begin{pmatrix} q_{n+r}^* \\ p_{n+r}^* \end{pmatrix} = \begin{pmatrix} q_n^* \\ p_n^* \end{pmatrix} \quad (2.12)$$

and therefore

$$r\omega(p_n^*) = r\omega_{r:s} = 2\pi sR \quad (2.13)$$

where both  $s$  and  $r$  are integer. This condition means that a periodic orbit/ray needs  $r$  reflections to encircle the origin  $s$  times. By inserting Eq. (2.13) into Eq. (2.11) it follows that in phase space the  $r:s$  periodic orbit is located at the momentum

$$p_{r:s} = \cos\left(\pi\frac{s}{r}\right). \quad (2.14)$$

Therefore this line of constant momentum contains a whole family of  $r:s$  periodic orbits, who are all separated in the sense that one single initial condition cannot discover the whole line of constant momentum. This is fundamentally different for a non-periodic orbit whose momentum is given by Eq. (2.14) with an irrational ratio  $s/r$ . Iterating a single initial condition fills a line  $p = \text{const}$  densely. In a more general framework of dynamical system the fraction

$s/r$  is also called winding number [Lichtenberg and Lieberman, 1992].

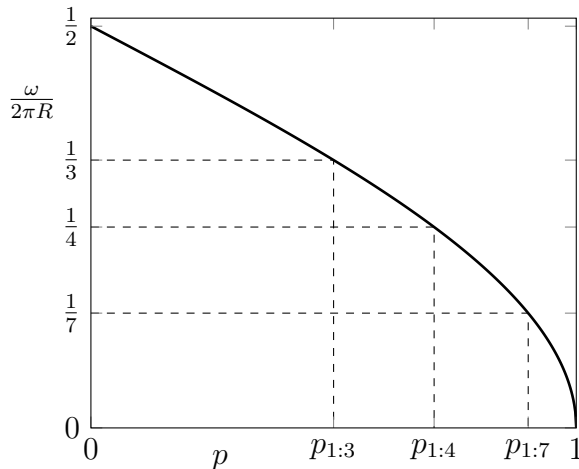


**Figure 2.3:** A black solid curve shows the frequency of orbits in the circular cavity as a function of the momentum  $p = \sin \chi$ , see Eq. (2.11). Dashed lines mark the momentum and frequencies of the periodic orbits shown in Fig. 2.2.

### Generic boundary deformations and transition to chaotic dynamics

A generic boundary deformation acts as a perturbation to the billiard dynamics of the circular cavity. Depending on the perturbation strength the dynamics shows therefore a transition from integrable to near-integrable, to mixed, and finally, to chaotic dynamics. Two well-known theorems describe how such a perturbation influences the dynamics of an integrable system: (i) the Poincaré-Birkhoff theorem [Poincaré, 1912, Birkhoff, 1913] for the resonant (periodic) tori and (ii) the Kolmogorov-Arnold-Moser (KAM) theorem [Kolmogorov, 1954, Arnol'd, 1963, Moser, 1962] for almost-all tori sufficiently away from the resonant tori.

In the following both theorems are discussed in more detail. For an illustration the deformation of the Limaçon cavity is considered. However, the explained mechanisms are quite general for all generic deformations. The boundary of the Limaçon is defined in polar coordinates by

$$\frac{r(\phi)}{R} = 1 + \epsilon \cos(\phi). \quad (2.15)$$

The parameter  $\epsilon$  indicates the perturbation strength. In Fig. 2.4 the boundary of the Limaçon is shown for different values of  $\epsilon$ .

Starting from the circle ( $\epsilon = 0$ ) and increasing  $\epsilon$  slightly the KAM theorem points out that almost all tori of the circular cavity whose winding numbers are sufficiently irrational will remain. But they are slightly deformed. This is illustrated by the gray curves in Fig. 2.5 for the Limaçon with  $\epsilon = 0.15$ .

On the other hand the Poincaré-Birkhoff theorem points out that a tori whose unperturbed



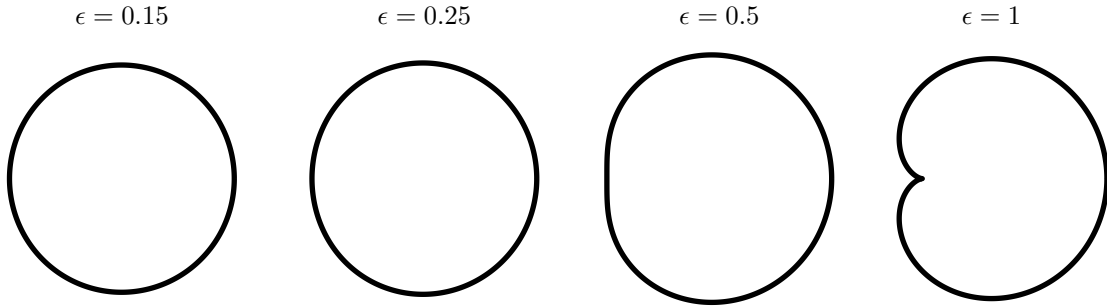


**Figure 2.4:** The boundary of the Limaçon, Eq. (2.15), is shown as black curve for different deformation parameters  $\epsilon$ . Note that the size of the cavity is scaled individually for each  $\epsilon$ .

frequencies  $\omega_{r:s} = 2\pi s/r$  has small integer values  $s$  and  $r$  splits up into an alternating sequence of  $r$  stable and  $r$  unstable periodic orbits, see Fig. 2.5 around  $p = 0.5$ : The unstable periodic orbits are connected by the separatrix (red curve) which encloses the remaining regular dynamics around the stable periodic orbits (blue curves) and separates them from the remaining KAM tori (gray curves). This structure is a so-called resonance chain. The regular dynamics around the stable (and unstable) periodic orbit  $(q^*, p^*)$  can be approximated with the linearized  $r$ -fold mapping

$$\begin{pmatrix} q_{n+r} \\ p_{n+r} \end{pmatrix} = \underline{J}^r \begin{pmatrix} q_n - q^* \\ p_n - p^* \end{pmatrix} + \begin{pmatrix} q^* \\ p^* \end{pmatrix} \quad (2.16)$$

where

$$\underline{J}^r = \left( \begin{array}{cc} \frac{\partial q_{n+r}}{\partial q_n} & \frac{\partial q_{n+r}}{\partial p_n} \\ \frac{\partial p_{n+r}}{\partial q_n} & \frac{\partial p_{n+r}}{\partial p_n} \end{array} \right) \Bigg|_{(q,p)=(q^*,p^*)} \quad (2.17)$$

is the monodromy matrix. The trace  $\text{Tr } \underline{J}^r$  indicates whether the periodic orbit is stable ( $|\text{Tr } \underline{J}^r| < 2$ ), or unstable ( $|\text{Tr } \underline{J}^r| > 2$ ), or marginal ( $|\text{Tr } \underline{J}^r| = 2$ ) [Lichtenberg and Lieberman, 1992]. Furthermore, from the area preservation it follows for all points in phase space  $|\det \underline{J}^1| = 1$ . As an example the linearized dynamics around a stable period-3 orbit in the Limaçon is shown in the magnification in Fig. 2.5 as green dashed curves.

The periodic orbit with the smallest integers  $s:r$  is typically the bouncing ball orbit  $r:s = 2:1$  which travels along the cavity's diameter. The resonance chain of the bouncing ball orbit is therefore typically formed even for very small perturbation strengths  $\epsilon$ . Resonance chains with higher integers  $r:s$  cover typically smaller areas in phase space.

Around the separatrix a thin region of chaotic dynamics exists. This so-called chaotic layer increases with increasing perturbation strength, e.g. in the Limaçon with increasing  $\epsilon$ . Simultaneously, resonance chains of higher orders develop from the remaining regular tori and

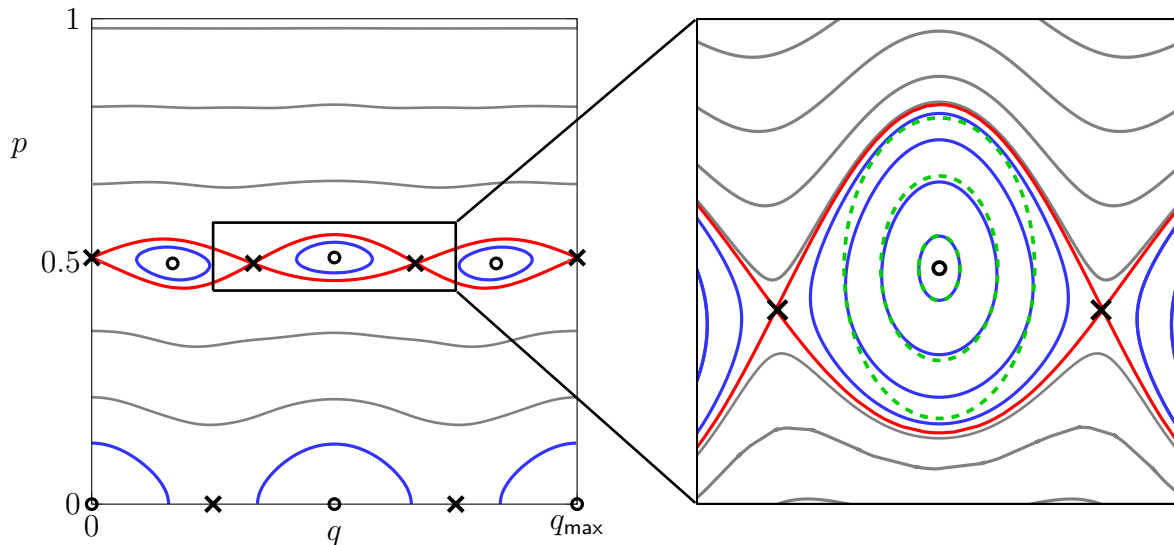


**Figure 2.5:** The figure shows the phase space dynamics in the Limaçon with  $\epsilon = 0.15$ . Some of the remaining KAM tori are shown as gray curves. The separatrix of the  $r:s = 3:1$  resonance chain is shown as red curve. The regular dynamics around stable fixed points (black empty circle) is illustrated by blue curves; some unstable periodic orbits are marked by black crosses. In the magnification on the orbits of the linearized mapping around the central periodic orbit  $(q^*, p^*) \approx (q_{\max}/2, 0.50805)$  are shown as green dashed curves.

increase their area in phase space and overlap with other resonance chains [Chirikov, 1960]. This mechanism leads to a generic mixed system where regions of regular and chaotic dynamics coexist in the phase space. For an illustration of such a system see Fig. 2.6. Here a phase space portrait of the Limaçon with  $\epsilon = 0.25$  is shown. At this deformation strength still islands of regular dynamics exist around the stable periodic orbits. Furthermore, there are regular tori for high momentum  $p$ . The existence of these remaining unbroken tori is a feature of the billiard dynamics. It is explained by the Lazutkin theorem [Lazutkin, 1973] which states that in convex cavities still a set of caustics with a non-zero measure exists. Since these caustics are smooth and closed curves inside the cavity each formed by the envelope of a single orbit it follows that also the orbit itself needs to be on a smooth closed curve in phase space; i.e. on an invariant whispering-gallery-like curve. On the other hand if the cavity is deformed to a non-convex shape, i.e. if there exists at least one point of vanishing curvature along the boundary, then it follows from Mather's theorem [Mather, 1982] that no remaining convex caustic and therefore no whispering-gallery-like curve in phase space exists. However, at these deformations may still regular islands around periodic orbits are embedded in the chaotic region.

Note that the chaotic region is not homogeneous in the sense that transport is limited by partial barriers which are for instance formed from destroyed KAM tori [Meiss, 1992]. Furthermore, chaotic orbits can be trapped at the hierarchical structures formed by partial barriers around regular islands [MacKay et al., 1984, Mackay et al., 1984].

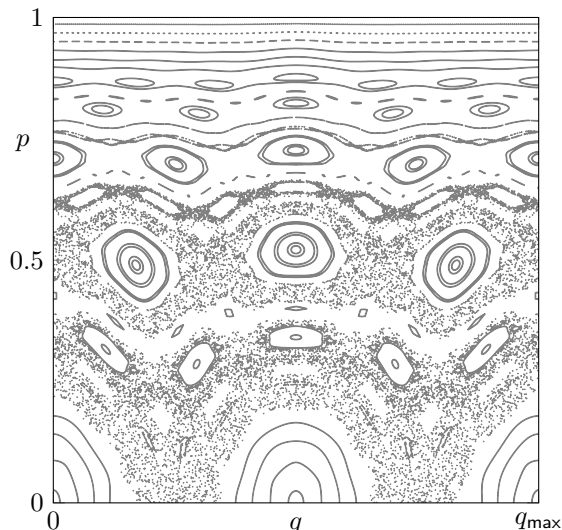


**Figure 2.6:** Orbits of the Limaçon cavity with  $\epsilon = 0.25$  are shown as gray dots/curves.

By further increasing the perturbation strength  $\epsilon$  the regular structures gradually vanish. In the Limaçon at  $\epsilon = 0.5$  macroscopically the phase space looks chaotic [see Figs. 2.4 and 2.7(a)], but small islands still exist at small scales. Full chaotic (ergodic) dynamics is rigorously proven only for a few examples, e.g., the Cardioid (the Limaçon with  $\epsilon = 1$ ) [see Figs. 2.4 and 2.7(b)] or the Sinai billiard [Markarian, 1993].

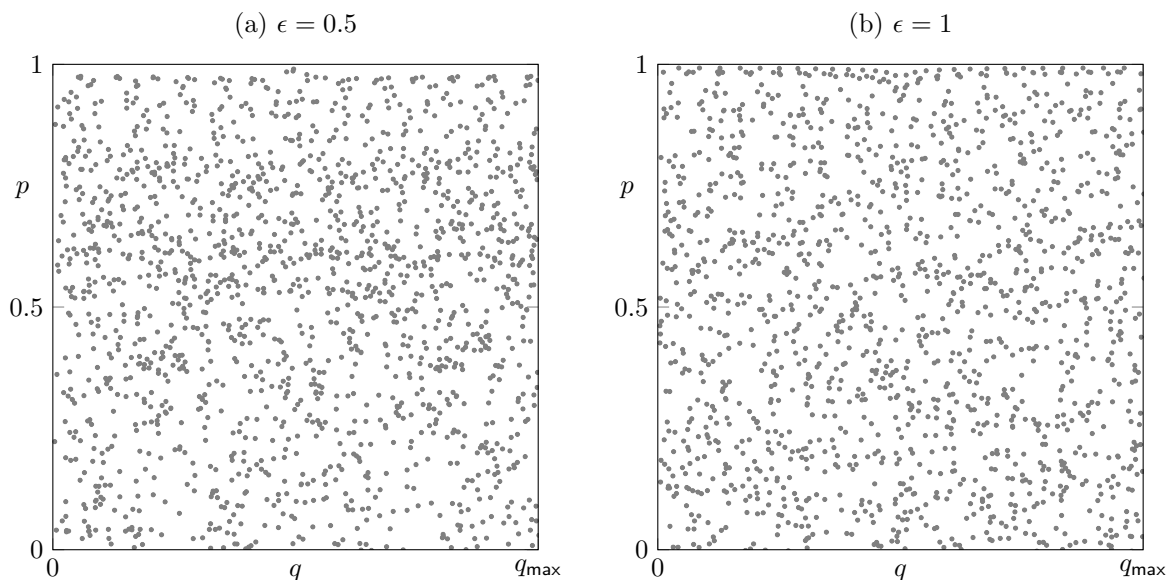


**Figure 2.7:** The figure shows the phase space dynamics (gray dots) of a single initial condition in the Limaçon with (a)  $\epsilon = 0.5$  and (b)  $\epsilon = 1$  (Cardioid).

### Special boundary deformations

Except for the generic deformations of the circular cavity which lead to a smooth transition from integrable to chaotic dynamics there exists special deformations which do not follow the above mentioned mechanism. A first example is given by deforming a circle to an ellipse given by

$$\frac{r(\phi)}{R} = \frac{b}{\sqrt{1 - e^2 \cos^2(\phi)}} \quad (2.18)$$

with scaling parameter  $b$  and eccentricity  $e < 1$ . By increasing the eccentricity the deformation to the circle gets stronger. However, for arbitrary strong deformations the orbits of the billiard dynamics still follow 1D tori in phase space; i.e. the dynamics is integrable. The reason is that in the ellipse a second conserved quantity in addition to the energy of the ray exists. This conserved quantity is the product of the two angular momenta with respect to the two foci [Nöckel, 1997].

Similarly, the deformation of a square to a rectangle does not generate chaotic dynamics even for strong elongations because  $p_x^2$  and  $p_y^2$  are two independent constants of motion resulting in integrable dynamics.

On the other hand even arbitrary small deformations can exhibit chaotic dynamics if they, e.g., exhibit points of infinite curvature such as edges. One example of such a deformation is the spiral cavity which is defined by

$$\frac{r(\phi)}{R} = 1 - \frac{\epsilon}{2\pi} \phi \quad (2.19)$$

where for every  $\epsilon > 0$  chaotic dynamics is generated. Another example of this type is the deformation of the circle to a stadium [Bunimovich, 1979].

### 2.2.2 Symmetries

In cavities where the boundary shape exhibits a symmetry also the phase space dynamics needs to reflect this symmetry. Therefore a reduced phase space is appropriate to describe the dynamics of the whole system. In this section a remark on typical symmetries and their effect on the billiard dynamics is given.

#### Mirror-reflection symmetry to the $x$ -axis

If there exists a mirror-reflection symmetry in the cavity's boundary it is assumed that the coordinate system is tilted such that the symmetry line coincides with the  $x$ -axis. Accordingly, the radius satisfies  $r(\phi) = r(-\phi)$  as, e.g., in the Limaçon, the ellipse, and the circular cavity. Then the dynamics in the lower half ( $p < 0$ ) and the upper half ( $p > 0$ ) of the phase space is

equivalent. Via the relation

$$(q_n, p_n) \mapsto (q_{n+1}, p_{n+1}) \iff (q_{\max} - q_n, -p_n) \mapsto (q_{\max} - q_{n+1}, -p_{n+1}) \quad (2.20)$$

the symmetry connected partner orbit can be constructed. Note that both might be the same. If a mirror-reflection symmetry is present the phase space can be restricted to the upper half without loss of generality as e.g. in Figs. 2.5, 2.6, 2.7.

### Mirror-reflection symmetry to the $x$ -axis and the $y$ -axis

Some systems as e.g. the ellipse exhibit a second mirror-reflection symmetry which is perpendicular to the first one. Then additionally to Eq. (2.20) the following relation

$$\begin{aligned} & (q_n, p_n) \mapsto (q_{n+1}, p_{n+1}) \\ \iff & \left( \frac{q_{\max}}{2} - q_n \pmod{q_{\max}}, -p_n \right) \mapsto \left( \frac{q_{\max}}{2} - q_{n+1} \pmod{q_{\max}}, -p_{n+1} \right) \end{aligned} \quad (2.21)$$

is valid for the symmetry connected orbits. Therefore, the phase space can be partitioned into four parts separated at  $q_{\max}/4$ ,  $q_{\max}/2$ , and  $3q_{\max}/4$ . And additionally, the lower and upper half of the phase space are equivalent.

### $N$ -fold rotational symmetry

Some systems show a general  $N$ -fold rotational symmetry, e.g., if  $r(\phi) = r(\phi + 2\pi j/N)$  with integer  $j = 0 \dots N$ . Then all orbits are  $N$ -fold rotational symmetry related via

$$\begin{aligned} & (q_n, p_n) \mapsto (q_{n+1}, p_{n+1}) \\ \iff & \left( q_n + \frac{j}{N} q_{\max} \pmod{q_{\max}}, p_n \right) \mapsto \left( q_{n+1} + \frac{j}{N} q_{\max} \pmod{q_{\max}}, p_{n+1} \right). \end{aligned} \quad (2.22)$$

Note that a boundary curve could have such a  $N$ -fold rotational symmetry but no mirror-reflection symmetry. However, the existence of a mirror-reflection symmetry implies the existence of at least a 2-fold rotational symmetry. An example for such a cavity shape with a  $N$ -fold rotational symmetry and a mirror reflection symmetry is the microflower  $r(\phi)/R = 1 + \epsilon \cos(N\phi)$  [Boriskina et al., 2006]. However, a circular saw shaped cavity has an  $N$ -fold rotational symmetry but no mirror-reflection symmetry. In this case the phase space is again segmentized in  $N$  parts separated by  $j q_{\max}/N$  but the dynamics in the lower and upper half is not equivalent in the sense of Eq. (2.20).

## 2.3 From billiards to microdisk cavities

So far the billiard dynamics which describes the geometrical propagation of rays inside the cavity was discussed. However, in a microcavity rays are not always totally reflected. If

they hit the boundary with a small angle of incidence they are just partially reflected. The other part of the intensity radiates out of the cavity. Thus not only the reflection direction but also the reflected intensity is a quantity which changes dynamically. In Sec. 2.3.1 this partial leakage is introduced to the phase space dynamics. Since radiation out of the cavity is included to the ray model one is able to construct the resulting far-field emission pattern of the microcavity which is discussed in Sec. 2.3.2.

### 2.3.1 Partial leakage and true-time dynamics

If a ray with intensity  $I$  hits an interface where the refractive index changes from  $n_1$  to  $n_2$  it is partially reflected and partially transmitted depending on the angle of incidence  $\alpha$ , see Fig. 2.8(a). The amount of reflected intensity  $RI$  and transmitted intensity  $(1 - R)I$  can be described with the reflection coefficient  $R$ . In case of large  $|\sin \alpha| > n_2/n_1$  total internal reflection implies  $R = 1$ . Whereas for small  $|\sin \alpha| < n_2/n_1$  the reflection coefficient  $R$  is described by the Fresnel formulas [Jackson, 1998]. In the often considered cases of transverse magnetic (TM) or transverse electric (TE) polarization [for details of TE/TM polarization see Sec. 3.1] the Fresnel formulas reduce to

$$R = \left( \frac{\sin(\alpha - \beta)}{\sin(\alpha + \beta)} \right)^2 \quad \text{for TM polarization} \quad (2.23a)$$

$$R = \left( \frac{\tan(\alpha - \beta)}{\tan(\alpha + \beta)} \right)^2 \quad \text{for TE polarization.} \quad (2.23b)$$

Here, the angle of incidence  $\alpha$  and emission  $\beta$ , see Fig. 2.8(a), are connected via Snell's law

$$n_1 \sin \alpha = n_2 \sin \beta. \quad (2.24)$$

In Fig. 2.8(b) the reflection coefficient for TM/TE polarization is plotted versus the phase space variable  $p = \sin \alpha$  (of a planar interface). Note that in case of TE polarization at the so-called Brewster angle  $p = n_1/\sqrt{n_1^2 + n_2^2}$  all incoming intensity is transmitted because  $R = 0$ . As a consequence of the finite reflectivity a leaky region is introduced in the phase space of a microcavity, see Fig. 2.8(c).

Since the intensity of a ray can only be reduced by boundary reflections it is also important how often a ray is reflected within a certain time interval: For example a ray traveling through a short diameter of the cavity needs less time but the same number of reflections than a ray traveling through the long diameter to lose a certain amount of intensity. This mismatch between number of phase space iterations and the actual flight time of the ray can be incorporated in a so called true-time mapping. Here the flight time  $t_n$  is also a dynamical variable which increases by an increment  $\Delta t$  and is recorded at the reflection points  $(q_n, p_n)$ . Therefore, in order to properly incorporate the openness of the microcavity into the phase space

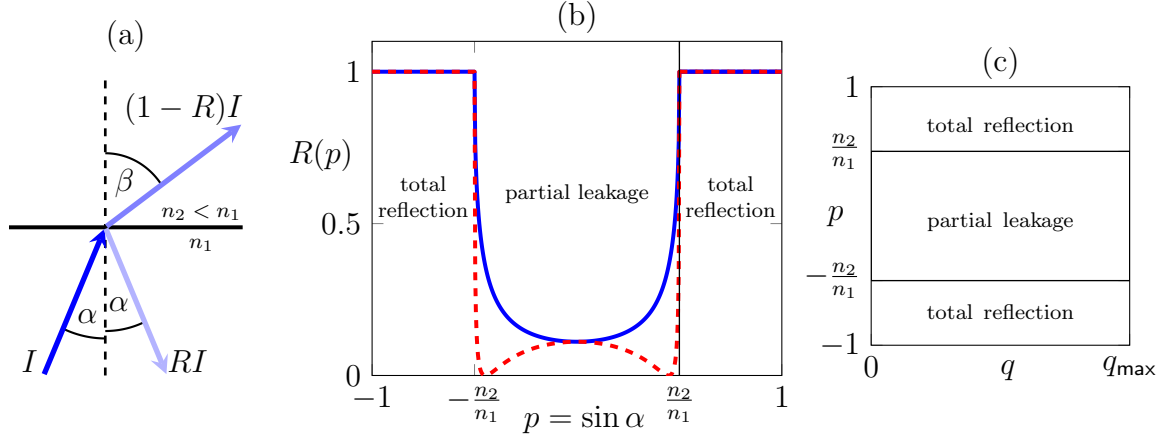


**Figure 2.8:** (a) Illustration of partial reflection and transmission of a ray (blue arrows) at a dielectric interface where the refractive index changes from  $n_1$  to  $n_2 < n_1$ . (b) The reflection coefficient  $R$  for TM (blue curve) and TE (red curve) is plotted versus the phase space momentum  $p = \sin \alpha$ , see Eq. (2.23). For the illustration the ratio  $n_2/n_1 = 1/2$  is chosen. (c) The leaky region according to (b) is shown in the phase space of an arbitrary shaped cavity.

mapping (2.6) the tuple  $(q_n, p_n, I_n, t_n)$  needs to be iterated as [Altmann et al., 2013]

$$(q_n, p_n) \mapsto (q_{n+1}, p_{n+1}) = \mathcal{M}(q_n, p_n) \quad (2.25a)$$

$$I_n \mapsto I_{n+1} = R(p_{n+1})I_n \quad (2.25b)$$

$$t_n \mapsto t_{n+1} = t_n + \Delta t(q_n, p_n). \quad (2.25c)$$

This mapping is illustrated in Fig. 2.9 for the Limaçon with  $\epsilon = 0.5$ .

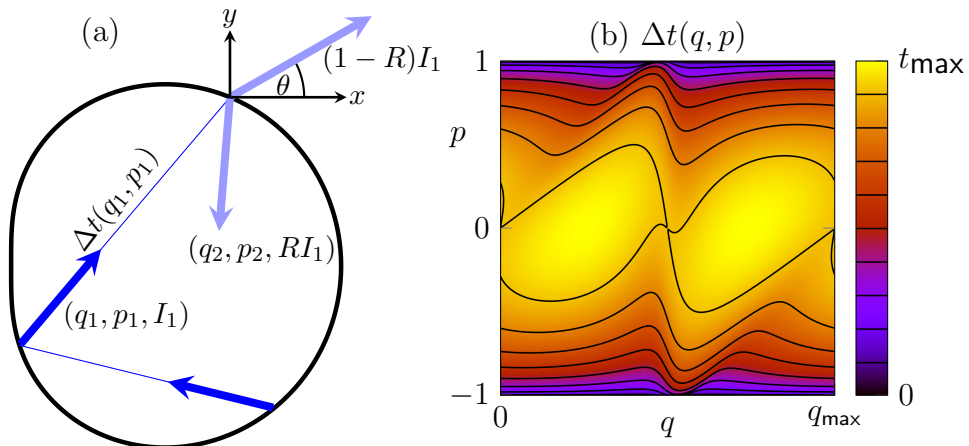


**Figure 2.9:** (a) The ray dynamics in the open Limaçon with  $\epsilon = 0.5$  is illustrated by blue arrows. (b) The length (or normalized flight time)  $\Delta t(q, p)$  of a ray until the next boundary collision is shown.

With the mapping (2.25) the ray model for a microcavity is defined. In the next section the

ray model is used to calculate the far-field emission pattern of a deformed microdisk cavity.

### 2.3.2 Far-field emission and invariant sets in phase space

A property which is important for applications and experiments is the emission pattern of a microdisk cavity. Especially, the emission pattern concerning the light trapped inside the cavity for a long time is of interest. In this section the ray model is applied to predict the emission pattern of this long-trapped light. For weakly deformed cavities regular dynamics is present where rays are trapped forever due to total internal reflection and therefore do not radiate out of the cavity. Hence, the ray model should be applied to predominantly chaotic cavities where the classical transport into the leaky region in phase space determines the far-field emission. For this purpose, first, the invariant sets in phase space of chaotic cavities are introduced. Second, the emission pattern is obtained from these invariant sets (precisely from the unstable manifold).

In a first step it is assumed that the leaky region in phase space is completely open and all intensity entering this region radiates out of the cavity. Then it is naturally to define the set  $\Gamma_{\text{saddle}}$  that contains all phase space points which never in the future nor in the past enter the leaky region [Altmann et al., 2013, Ott, 1993], see Fig. 2.10(b). This set  $\Gamma_{\text{saddle}}$  is called chaotic saddle. However, if one is interested in the emission through the leaky region not the chaotic saddle but its unstable manifold  $\Gamma_{\text{unstable}}$  is important; i.e. the points in phase space that converge to  $\Gamma_{\text{saddle}}$  under backward iteration, see Fig. 2.10(a). For completeness it is mentioned that a third invariant set is the stable manifold  $\Gamma_{\text{stable}}$  of the chaotic saddle which consists of the points in phase space that converge to  $\Gamma_{\text{saddle}}$  under forward iteration. Therefore, the saddle can be written as  $\Gamma_{\text{saddle}} = \Gamma_{\text{stable}} \cap \Gamma_{\text{unstable}}$ .

However, the leaky region of a microcavity is not completely open but only partially open. Therefore also the invariant sets need to be modified by tracking the intensity of the ray according to the Fresnel reflection coefficient, see Fig. 2.10(c) (see Refs. [Wiersig and Hentschel, 2008, Altmann, 2009] and especially Appendix C of Ref. [Altmann et al., 2013] for details on the computation of the intensity weighted invariant sets). This intensity weighted unstable manifold can be used to predict the far-field intensity emission pattern  $|F(\phi)|^2$  which is shown in Fig. 2.10 for the Limaçon, also compare with Ref. [Wiersig and Hentschel, 2008]. Note that because of the mirror-reflection symmetry in the Limaçon the far-field angle is restricted to the interval  $\phi \in [0, \pi]$ .



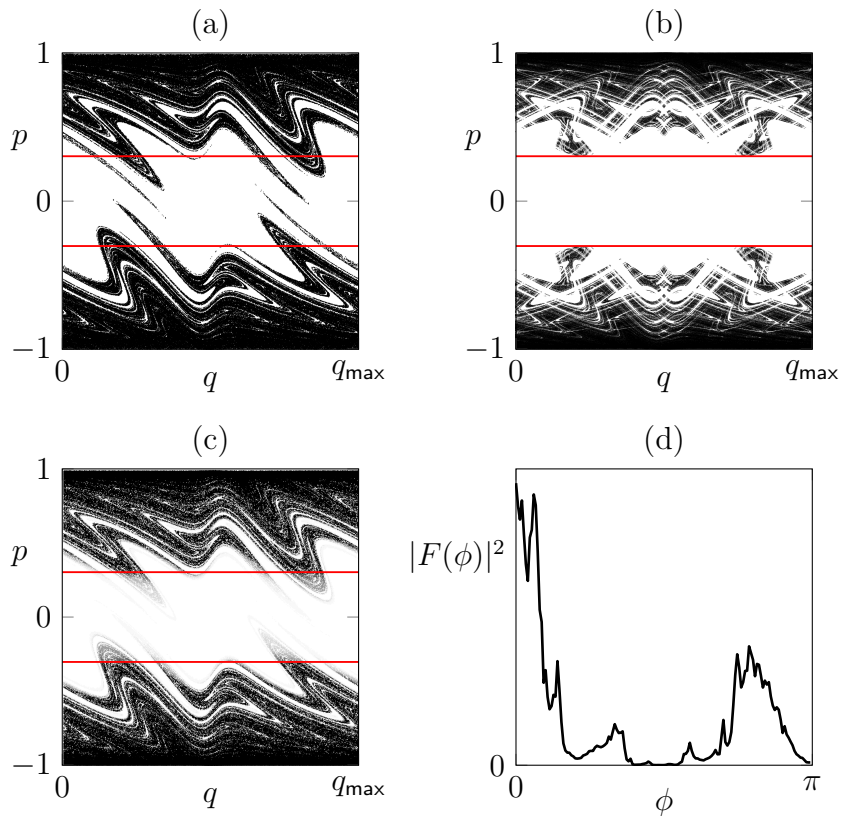


**Figure 2.10:** (a) Unstable manifold and (b) chaotic saddle for the fully open (no reflectivity in leaky region) Limaçon at  $\epsilon = 0.43$  and  $n = 3.3$ . (c) Unstable manifold for the Limaçon cavity with finite reflectivity (TM polarization) [see Eq. (2.23a)] inside the leaky region. (d) The resulting far-field emission pattern  $|F(\phi)|^2$  for the Limaçon is shown (compare to Ref. [Wiersig and Hentschel, 2008]).



# 3 Wave dynamics

In this section the wave dynamics of the electric and magnetic field in a dielectric microcavity is discussed. Therefore, one searches for solutions of Maxwell's equations with a harmonic dependence in time, the so-called optical modes. In case of a thin disk-like cavity these modes are determined by a scalar mode equation with proper boundary conditions which is derived in Sec. 3.1. Since the mode equation is solvable analytically only for a few systems with rotational symmetry the circular cavity with homogeneous refractive index is investigated in Sec. 3.2. However, the more general case of deformed cavities is treated in Sec. 3.3.

## 3.1 From Maxwell's equations to a scalar mode equation

The foundation of classical electrodynamics are Maxwell's equations. In a medium these are inhomogeneous coupled partial differential equations for the electric displacement field  $\vec{D}$ , the magnetic field  $\vec{H}$ , the electric field  $\vec{E}$ , and the magnetic flux density  $\vec{B}$  which are influenced by free charges  $\rho_f$  and free currents  $\vec{j}_f$  as

$$\vec{\nabla} \cdot \vec{D} = \rho_f \quad (3.1a)$$

$$\vec{\nabla} \cdot \vec{B} = 0 \quad (3.1b)$$

$$\vec{\nabla} \times \vec{E} = -\partial_t \vec{B} \quad (3.1c)$$

$$\vec{\nabla} \times \vec{H} = \vec{j}_f + \partial_t \vec{D}. \quad (3.1d)$$

In a general case the relation between  $\vec{D}$  and  $\vec{E}$  ( $\vec{B}$  and  $\vec{H}$ ) depend on the atomic bound charges and currents. Only for a linear and isotropic medium which is considered here it yields

$$\vec{D} = \epsilon_0 \epsilon_r \vec{E} \quad (3.2a)$$

$$\vec{B} = \mu_0 \mu_r \vec{H} \quad (3.2b)$$

where  $(\epsilon_r)$   $\epsilon_0$  is the (relative) permittivity and  $(\mu_r)$   $\mu_0$  is the (relative) permeability. They are related to the refractive index  $\tilde{n} = \sqrt{\epsilon_r \mu_r}$ <sup>1</sup> and the vacuum speed of light  $c = 1/\sqrt{\epsilon_0 \mu_0}$ .

Furthermore, at a dielectric interface where the refractive index changes discontinuously the

---

<sup>1</sup>The symbol  $\tilde{n}$  is used here for the refractive index of the material to distinguish it from the effective refractive index denoted by  $n$  which will be introduced later on in this section.

electromagnetic fields need to fulfill boundary conditions. If the two regions with different refractive indexes are divided into inside (index<sub>in</sub>) and outside (index<sub>out</sub>) and  $\vec{\nu}$  is the local normal vector at the interface then

$$\vec{\nu} \cdot \left( n_{\text{in}}^2 \vec{E}_{\text{in}} - n_{\text{out}}^2 \vec{E}_{\text{out}} \right) = 0 \quad (3.3a)$$

$$\vec{\nu} \cdot \left( \vec{H}_{\text{in}} - \vec{H}_{\text{out}} \right) = 0 \quad (3.3b)$$

$$\vec{\nu} \times \left( \vec{E}_{\text{in}} - \vec{E}_{\text{out}} \right) = 0 \quad (3.3c)$$

$$\vec{\nu} \times \left( \vec{H}_{\text{in}} - \vec{H}_{\text{out}} \right) = 0 \quad (3.3d)$$

needs to be fulfilled [Jackson, 1998].

### Derivation of the mode equations

In the following, the mode equation is derived for a setup where the shape and the dielectric properties of the cavity are given by the refractive index profile  $\tilde{n} = \tilde{n}(\vec{r})$  which is piece-wise constant and discontinuous at the cavity's boundary. Furthermore it is assumed that no external currents and charges are present, i.e.  $\vec{j}_f = 0$  and  $\rho_f = 0$ . In this situation Maxwell's equations can be rewritten for  $\vec{E}$  and  $\vec{H}$  by first calculating the curl of Eqs. (3.1c) and Eqs. (3.1d). On the one hand this yields

$$\vec{\nabla} \times \vec{\nabla} \times \vec{E} = \vec{\nabla}(\vec{\nabla} \cdot \vec{E}) - \vec{\nabla}^2 \vec{E} = -\vec{\nabla}^2 \vec{E} \quad (3.4a)$$

$$\vec{\nabla} \times \vec{\nabla} \times \vec{H} = \vec{\nabla}(\vec{\nabla} \cdot \vec{B})/(\mu_r \mu_0) - \vec{\nabla}^2 \vec{H} = -\vec{\nabla}^2 \vec{H} \quad (3.4b)$$

with piece-wise constant  $\mu_r$ . But on the other hand it gives

$$\vec{\nabla} \times \vec{\nabla} \times \vec{E} = \vec{\nabla} \times \left( -\partial_t \vec{B} \right) = -\mu_r \mu_0 \partial_t (\vec{\nabla} \times \vec{H}) = -\mu_r \mu_0 \partial_t^2 \vec{D} = -\frac{\tilde{n}^2}{c^2} \partial_t^2 \vec{E} \quad (3.5a)$$

$$\vec{\nabla} \times \vec{\nabla} \times \vec{H} = \vec{\nabla} \times \left( \partial_t \vec{D} \right) = \epsilon_r \epsilon_0 \partial_t (\vec{\nabla} \times \vec{E}) = -\epsilon_r \epsilon_0 \partial_t^2 \vec{B} = -\frac{\tilde{n}^2}{c^2} \partial_t^2 \vec{H} \quad (3.5b)$$

with piece-wise constant  $\mu_r$  and  $\epsilon_r$ . Therefore, Eqs. (3.4a)-(3.5b) can be compactly written as the wave equation

$$\vec{\nabla}^2 \vec{\Psi}(\vec{r}, t) - \frac{\tilde{n}^2(\vec{r})}{c^2} \partial_t^2 \vec{\Psi}(\vec{r}, t) = 0 \quad (3.6)$$

for  $\vec{\Psi} \in \{\vec{E}, \vec{H}\}$ . A separation of variables leads to  $\vec{\Psi}(\vec{r}, t) = \vec{\Psi}(\vec{r}) \exp(-i\omega t)$  where  $\omega \in \mathbb{C}$  is the complex frequency of  $\vec{\Psi}(\vec{r})$ . The complex frequency is often expressed as the dimensionless complex wave number  $kR = R\omega/c$  where  $R$  is a typical scale of the system size ( $R$  has the unit of a length). While the real part of  $kR$  is related to the usual wavelength as  $\text{Re } kR = 2\pi R/\lambda$  the imaginary part of  $kR$  determines the temporal decay or amplification of the mode  $\vec{\Psi}(\vec{r})$ . For a passive cavity which radiates to the free space  $\text{Im } kR < 0$ . To quantify the lifetime of a

mode in the cavity the quality- or  $Q$ -factor

$$Q = -\frac{\operatorname{Re} kR}{2\operatorname{Im} kR} \quad (3.7)$$

is introduced. Therefore, high- $Q$  modes oscillate a longer time in the cavity than the lossy low- $Q$  modes. The spatial distribution, the actual mode  $\vec{\Psi}(\vec{r})$ , is determined by the mode equation

$$\vec{\nabla}^2 \vec{\Psi} + \tilde{n}^2 k^2 \vec{\Psi} = 0 \quad (3.8)$$

in its vectorial form. This equation needs to be solved numerically for arbitrary shaped 3D cavities where no further symmetries could be employed as e.g. deformed microspheres/microtoroids or compounds of different 3D dielectric structures.

If however a translation invariance in  $z$ -direction is assumed, i.e. that the cavity is an infinite cylindrical object defined by  $\tilde{n}(\vec{r}) = \tilde{n}(x, y)$ , then the mode equation can be simplified further for the  $z$ -component  $\Psi_z$  of  $\vec{\Psi}$ . A separation of variables leads to  $\Psi_z = \psi(x, y) \exp(-ik_z z)$  with separation constant  $k_z$  describing the plane wave propagation in  $z$ -direction. For the mode profile  $\psi(x, y)$  the scalar mode equation

$$\Delta_{xy} \psi + n^2 k^2 \psi = 0 \quad (3.9)$$

follows from the separation ansatz. Here,  $\Delta_{xy} = \partial_x^2 + \partial_y^2$  is the 2D Laplace operator and  $n = \tilde{n} \sqrt{1 - k_z^2 / (\tilde{n}k)^2}$  is the effective refractive index. Note that the scalar mode equation (3.9) is sufficient to determine all components of the full vector field  $\vec{\Psi}$  in a cylindrical geometry because the components of the vector field in the  $x$ - $y$  plane,  $\vec{\Psi}_{xy}$ , can be computed from the  $z$ -component  $\Psi_z$  as follows: First, one evaluates

$$\vec{\nabla} \times \vec{\Psi} = \left( \vec{\nabla}_{xy} + \partial_z \vec{e}_z \right) \times \left( \vec{\Psi}_{xy} + \Psi_z \vec{e}_z \right) \quad (3.10a)$$

$$= \left( \vec{\nabla}_{xy} \Psi_z \times \vec{e}_z \right) + \left( \vec{\nabla}_{xy} \times \vec{\Psi}_{xy} \right) + \left( \vec{e}_z \times \partial_z \vec{\Psi}_{xy} \right) \quad (3.10b)$$

$$= \left( ik_z \vec{\Psi}_{xy} + \vec{\nabla}_{xy} \Psi_z \right) \times \vec{e}_z + \left( \vec{\nabla} \times \vec{\Psi} \right)_z \vec{e}_z. \quad (3.10c)$$

The both summands in the last equation are orthogonal vectors where the first one is in  $x$ - $y$  plane. Hence, Maxwell's equations for the curl (3.1c)-(3.1d) and the time harmonic dependence of the modes can be used to obtain

$$-i\omega \epsilon_r \epsilon_0 \vec{E}_{xy} = \left( ik_z \vec{H}_{xy} + \vec{\nabla}_{xy} H_z \right) \times \vec{e}_z \quad (3.11a)$$

$$i\omega \mu_r \mu_0 \vec{H}_{xy} = \left( ik_z \vec{E}_{xy} + \vec{\nabla}_{xy} E_z \right) \times \vec{e}_z \quad (3.11b)$$

as system of equations for the fields  $\vec{E}_{xy}$  and  $\vec{H}_{xy}$  in the  $x$ - $y$  plane. By inserting both equations

into each other it yields

$$\vec{E}_{xy} = \frac{i}{n^2} \left( k_z \vec{\nabla}_{xy} E_z - k \vec{e}_z \times \vec{\nabla}_{xy} H_z \right) \quad (3.12a)$$

$$\vec{H}_{xy} = \frac{i}{n^2} \left( k_z \vec{\nabla}_{xy} H_z + k n^2 \vec{e}_z \times \vec{\nabla}_{xy} E_z \right). \quad (3.12b)$$

Here it is mentioned that one can distinguish two ideal polarizations

$$\begin{aligned} \vec{E} = \vec{E}_z \text{ i.e. } \vec{H} = \vec{H}_{xy} & \quad \text{transverse magnetic (TM) polarization} \\ \vec{H} = \vec{H}_z \text{ i.e. } \vec{E} = \vec{E}_{xy} & \quad \text{transverse electric (TE) polarization} \end{aligned} \quad (3.13)$$

where Eqs. (3.12a) and (3.12b) decouple.

The reduction from the vectorial mode equation (3.8) to the scalar mode equation (3.9) is strictly speaking only valid for a cylindrical geometry and not for a disk-like geometry. Nevertheless, one can argue that in a microdisk the light propagation in  $z$ -direction is very slow, i.e.  $k_z \sim 0$ , and therefore the finite cylinder size is not “seen” by the field. Hence, the scalar mode equation (3.9) can predict modes also in a microdisk cavity well within the effective refractive index approximation [Smotrova et al., 2005]. Note that a cylindrical symmetry is almost achieved in microjet cavities [Yang et al., 2006, Lee et al., 2002]. Recently, also the effects of the finite height of the microdisk cavity on the optical modes and their emission profile have been studied at the Limaçon [Kreismann et al., 2017].

### Boundary conditions for the scalar mode equation

In the following the boundary conditions (3.3a)-(3.3d) for the electromagnetic fields at a dielectric interface are adapted to the case of a cylindrical (or disk-like) geometry. Especially for the ideal polarizations TM and TE the boundary conditions can be simplified significantly: First, TM polarization is examined. Here, from Eq. (3.12b) with  $H_z = 0$  it follows

$$\vec{H}_{\text{in}} - \vec{H}_{\text{out}} = \vec{H}_{xy,\text{in}} - \vec{H}_{xy,\text{out}} = ik \left[ \vec{e}_z \times \vec{\nabla}_{xy} (E_{z,\text{in}} - E_{z,\text{out}}) \right]. \quad (3.14)$$

Since in a cylindrical geometry the normal vector  $\vec{\nu}$  lies in the  $x$ - $y$  plane such that  $\vec{\nu} \times (\vec{e}_z \times \vec{\nabla}_{xy}) = \vec{e}_z \cdot (\vec{\nu} \cdot \vec{\nabla}_{xy}) = \vec{e}_z \partial_{\vec{\nu}}$  the boundary condition (3.3d) can be simplified with Eq. (3.14) to

$$\partial_{\vec{\nu}} E_{z,\text{in}} = \partial_{\vec{\nu}} E_{z,\text{out}}. \quad (3.15a)$$

Furthermore from Eq. (3.3c) it follows directly

$$E_{z,\text{in}} = E_{z,\text{out}}. \quad (3.15b)$$

Both Eqs. (3.15a) and (3.15b) are the boundary conditions for the scalar mode equation (3.9) at a dielectric interface for TM polarized fields.

Similarly, in the case of TE polarization where  $E_z = 0$ , Eq. (3.12a) is used to obtain

$$\vec{E}_{\text{in}} - \vec{E}_{\text{out}} = \vec{E}_{xy,\text{in}} - \vec{E}_{xy,\text{out}} = -ik \left[ \vec{e}_z \times \vec{\nabla}_{xy} \left( \frac{H_z}{n_{\text{in}}^2} - \frac{H_z}{n_{\text{out}}^2} \right) \right]. \quad (3.16)$$

With Eq. (3.3d) and  $\vec{\nu} \times (\vec{e}_z \times \vec{\nabla}_{xy}) = \vec{e}_z \partial_{\vec{\nu}}$  this leads to the boundary condition for the mode equation at a dielectric interface for TE polarized fields:

$$H_{z,\text{in}} = H_{z,\text{out}} \quad (3.17a)$$

$$\frac{\partial_{\vec{\nu}} H_{z,\text{in}}}{n_{\text{in}}^2} = \frac{\partial_{\vec{\nu}} H_{z,\text{out}}}{n_{\text{out}}^2}. \quad (3.17b)$$

It is mentioned again that these are ideal polarizations. In experiments maybe slight mixtures of both polarizations are observed.

### The outgoing wave condition

Additionally to the boundary conditions at a dielectric interfaces also the conditions of the fields far away from the microdisk are crucial. The intensity of optical modes is assumed radiate out of the cavity. It should not come from infinity and enter into the cavity. Therefore, in the 2D case general scattering theory implies that the Sommerfeld outgoing wave condition needs to be fulfilled, i.e. that the wave function  $\psi$  behaves asymptotically as

$$\psi(r, \phi) \sim h(\phi; k) \frac{e^{ikr}}{\sqrt{r}} \quad (3.18)$$

for large  $r$ . Note that in the 3D case the  $\sqrt{r}$  is replaced by  $r$ .

The combination of boundary conditions and outgoing wave condition make the mode equation solvable only for discrete values of the complex wave number  $k^2$  where due to radiation the imaginary part of  $k$  needs to be negative.

## 3.2 The circular microdisk

A very special case of a cylindrical or disk-like geometry is the circular cavity. Here, it is possible to employ the continuous rotational symmetry in  $x$ - $y$ -plane additionally such that the scalar mode equation (3.9) can be simplified further. This allows one to obtain an analytical solution of Maxwell's equations. Therefore, the circular cavity is an ideal system to classify optical modes by mode numbers which can be defined rigorously in the circular cavity but

---

<sup>2</sup>The discrete values of the complex wave number  $k$  can be seen as the discrete energy spectra of bounded states in quantum mechanics.

are also often used for slightly deformed microdisk cavities. Furthermore, the circular cavity serves as a starting point to treat deformed cavities perturbatively as it will be discussed in Sec. 5 and Sec. 6. In this section the determination of the modes in a circular microdisk cavity and their properties are discussed.

In case of a continuous rotational symmetry the (effective) refractive index  $n(x, y) = n(r)$  is assumed to be a piecewise constant function of the radius  $r$  and independent of the angle  $\phi$ . Therefore, the ansatz  $\psi(r, \phi) = \Psi(r) \exp(im\phi)$  can be used to separate the variables  $r$  and  $\phi$  in the scalar mode equation (3.9). The  $2\pi$ -periodicity of  $\psi$  implies  $m \in \mathbb{Z}$ . For the radial dependence a Bessel-like ODE of  $m$ -th order<sup>3</sup>

$$r^2 \partial_r^2 \Psi + r \partial_r \Psi + [n^2 k^2 r^2 - m^2] \Psi = 0 \quad (3.19)$$

is obtained. Formally this equation is solved independently by both  $J_m(nkr)$  and  $H_m(nkr)$  being  $m$ -th order Bessel- and Hankel-functions of the first kind. Note that also Neumann-functions solve the Bessel ODE but are adverse solutions for a basis here. Since on the one hand for large  $r \gg R$  the Bessel-functions  $J_m$  do not fulfill the outgoing wave condition (3.18), and on the other hand the Hankel function  $H_m$  diverge for  $r \rightarrow 0$ , it is natural to expand

$$\psi_{m,l}(r, \phi) \equiv \psi(r, \phi) = \begin{cases} \frac{J_m(nkr)}{J_m(nkR)} e^{im\phi} & \text{for } r < R \\ \frac{H_m(kr)}{H_m(kR)} e^{im\phi} & \text{for } r > R \end{cases} \quad (3.20)$$

as the solution of the circular cavity. Here and in the following it is assumed that  $n = n_{\text{in}}$  and  $n_{\text{out}} = 1$ . In case of pure TM [or TE] polarization  $\psi(r, \phi)$  needs to fulfill the boundary conditions (3.15a)-(3.15b) [or (3.17a)-(3.17b)] which results in the conditional equation for the quantized (dimensionless) wave number  $x = kR$  as

$$S_m(x) := \frac{n}{\zeta} \frac{J'_m(nx)}{J_m(nx)} - \frac{H'_m(x)}{H_m(x)} \stackrel{!}{=} 0 \quad (3.21)$$

where  $\zeta = 1$  ( $\zeta = n^2$ ) for TM (TE) polarization. The solutions of Eq. (3.21) are shown in Fig. 3.1 for TM polarization. For fixed  $m \in \mathbb{Z}$  the roots of  $S_m(x)$  are counted with an index  $l \in \mathbb{N}_+$  which has already been used as label in Eq. (3.20). The integers  $m, l$  specifying the mode, i.e.  $\psi_{m,l}(r, \phi)$  and  $x_{m,l}$ . Therefore they are called mode numbers. For fixed  $l$  the mode with higher  $m$  has the higher  $Q$ -factor and the smaller wavelength.

From the symmetry relations  $J_{-m}(x) = (-1)^m J_m(x)$  for Bessel functions (and similar for Hankel functions) it follows that solutions of Eq. (3.21) for  $|m| > 0$  are double degenerate with eigenfunctions  $\psi_{|m|,l}$  and  $\psi_{-|m|,l}$ . Therefore, it is valid to superimpose the optical modes from

<sup>3</sup>The ordinary Bessel differential equation of  $m$ -th order is obtained by substituting  $x = nkr$ . Note that the refractive index  $n$  and therefore  $x$  are different inside ( $n = n_{\text{in}}$ ) and outside ( $n = n_{\text{out}}$ ) the cavity.



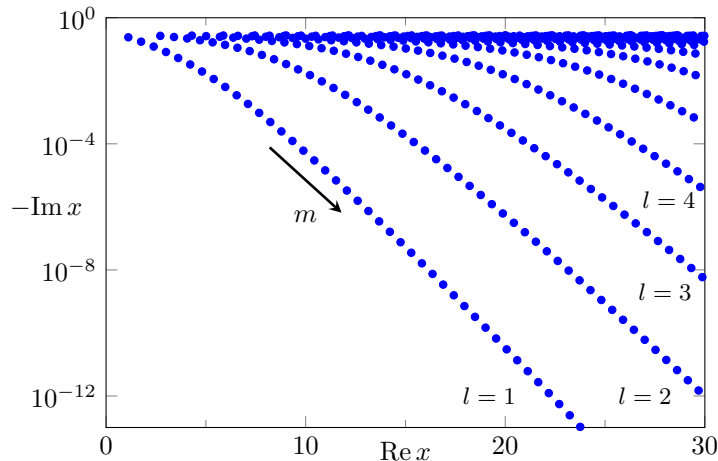


**Figure 3.1:** The roots  $x = kR$  of  $S_m(x)$  [Eq. (3.21)] are shown in complex plane as blue dots for the refractive index  $n = 2$  and TM polarization. For an interpretation of the mode numbers  $m, l$  see Fig. 3.2.

Eq. (3.20) as

$$\psi_{+,|m|,l} = \frac{1}{2} (\psi_{|m|,l} + \psi_{-|m|,l}) \sim \cos(|m|\phi) \quad (3.22a)$$

$$\psi_{-,|m|,l} = \frac{1}{2i} (\psi_{|m|,l} - \psi_{-|m|,l}) \sim \sin(|m|\phi) \quad (3.22b)$$

such that a positive (+) and negative (−) parity with respect to the  $x$ -axis is obtained. In Fig. 3.2 the square modulus of  $\psi_{+,|m|,l}$  is shown for several mode numbers. Here, an interpretation of the mode numbers  $m, l$  is possible:  $m$  determines the number of nodes in azimuthal direction to be  $2m$  and  $l$  is the number of extrema of  $|\psi|^2$  in radial direction.


The mode number  $m$  can also be seen as angular momentum (quantum) number since the mode defined by Eq. (3.20) is an eigenstate of the angular momentum operator  $\hat{L}_z = -i\partial_\phi$  with  $\hat{L}_z\psi_{m,l}(r, \phi) = m\psi_{m,l}(r, \phi)$ . In this sense modes with positive  $m$  are counter-clockwise traveling waves and modes with negative  $m$  are clockwise traveling waves.

It is mentioned again that the above discussion is valid for circular cavities with homogeneous refractive index. For example spherical cavities where  $n(r)$  is not stepwise constant can be treated in a perturbation theory of arbitrary high order, see Ref. [Lee et al., 1998].

### 3.3 Deformed microdisk cavities

The treatment of deformed cavities is essential since boundary deformations allow to design the cavity for a desired purpose, e.g. as unidirectional light emitters. Therefore, in this section a closer look to the modes in deformed cavities is taken. First, in Sec. 3.3.1 the ideal case of symmetric deformations is examined, i.e. deformations which preserve at least one mirror-reflection symmetry. However, in a real experiment the deformations are in general

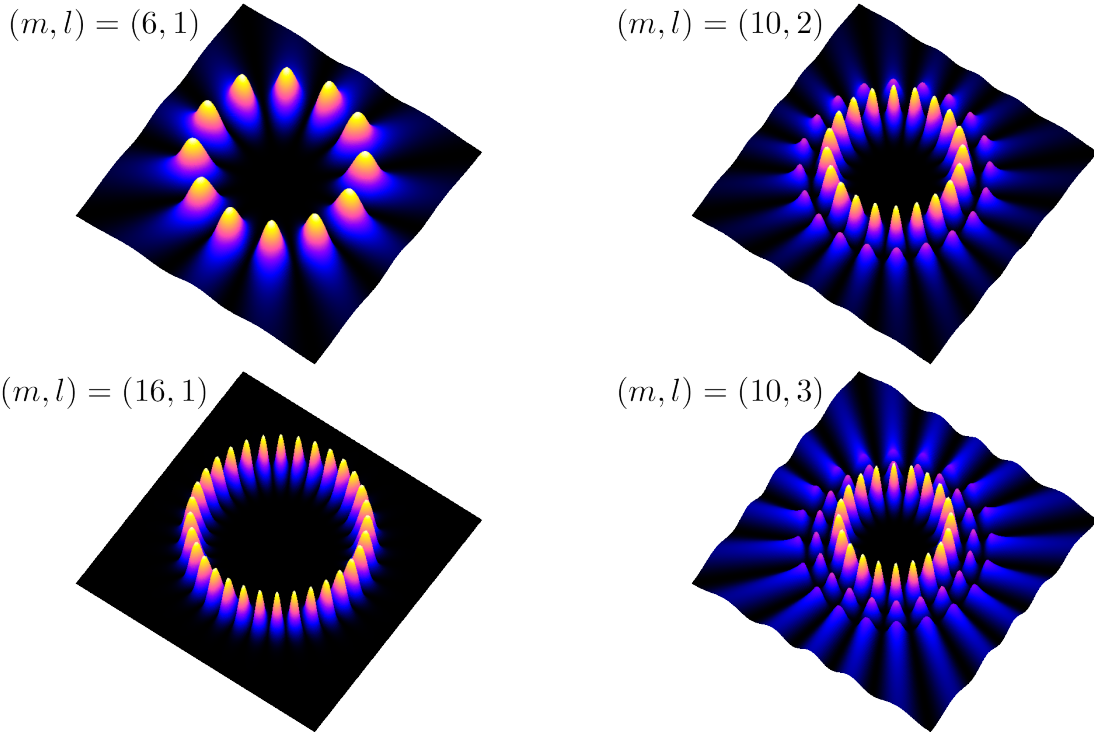


**Figure 3.2:** The figure shows the square modulus of  $\psi_{+,m,l}$  for modes in the circular cavity for different combinations of mode numbers  $m, l$ . The color scale ranges from black to white (  ).

asymmetric either intended or unintended due to fabrication tolerances. Therefore, the case of fully asymmetric deformations is discussed in Sec. 3.3.2.

### 3.3.1 Symmetric deformations

Deformed cavities whose boundary still has a mirror-reflection symmetry (for simplicity the  $x$ -axis) are treated in this section. For the wave function the symmetry implies  $|\psi(r, \phi)| = |\psi(r, -\phi)|$  so that the modes fall into two orthogonal classes: the ones with positive and the ones with negative parity. As long as the cavity is not extremely deformed the modes can be expanded into a series<sup>4</sup>

$$\psi_+(r, \phi) = \begin{cases} \sum_{m \geq 0} \alpha_{+,m} \frac{J_m(nkr)}{J_m(nkR)} \cos(m\phi) & \text{for } r < R \\ \sum_{m \geq 0} \beta_{+,m} \frac{H_m(kr)}{H_m(kR)} \cos(m\phi) & \text{for } r > R \end{cases} \quad (3.23)$$

<sup>4</sup>This so-called Rayleigh hypothesis states that the expansion of a mode into waves of a circular cavity is possible for deformed microcavities. The scope of the Rayleigh hypothesis is still an open research field, see e.g. [van den Berg and Fokkema, 1979, Yeo and Selvaraju, 1993, Watanabe et al., 2004, Wauer and Rother, 2009]. Violations to the Rayleigh hypothesis could occur for deformations where rays leaving the cavity do not radiate to the far-field but reenter again into the cavity.

with  $k \equiv k_+$  for the modes with positive parity and

$$\psi_-(r, \phi) = \begin{cases} \sum_{m \geq 0} \alpha_{-,m} \frac{J_m(nkr)}{J_m(nkR)} \sin(m\phi) & \text{for } r < R \\ \sum_{m \geq 0} \beta_{-,m} \frac{H_m(kr)}{H_m(kR)} \sin(m\phi) & \text{for } r > R \end{cases} \quad (3.24)$$

with  $k \equiv k_-$  for the modes with negative parity. Furthermore, there might be whispering-gallery-like modes in the deformed cavity which have one dominant contribution for  $a_{\pm, m}$ . For these modes  $m, l$  can still be used as mode numbers whereas they are not as rigorously defined as in the circle. The modes associated to  $x_+ = k_+ R$  and  $x_- = k_- R$ , which are degenerate in the circular cavity, show a small complex frequency splitting

$$\Delta x = x_+ - x_- \quad (3.25)$$

in the deformed cavity. Typically, this splitting increases with increasing deformation strength. A large splitting  $\Delta x$  is of experimental relevance [Leymann et al., 2013, Kwak et al., 2015, Kim et al., 2015] and advantageous for, e.g., polarization control [Daraei et al., 2006]. Note that similar to Eqs. (3.23) and (3.24) it is also valid to expand the wave function into a basis of traveling waves, i.e. in linear combinations of  $\exp(im\phi)$ . In such a case the mirror-reflection symmetry enforces the expansion coefficients to fulfill  $|\alpha_{-m}| = |\alpha_m|$ .

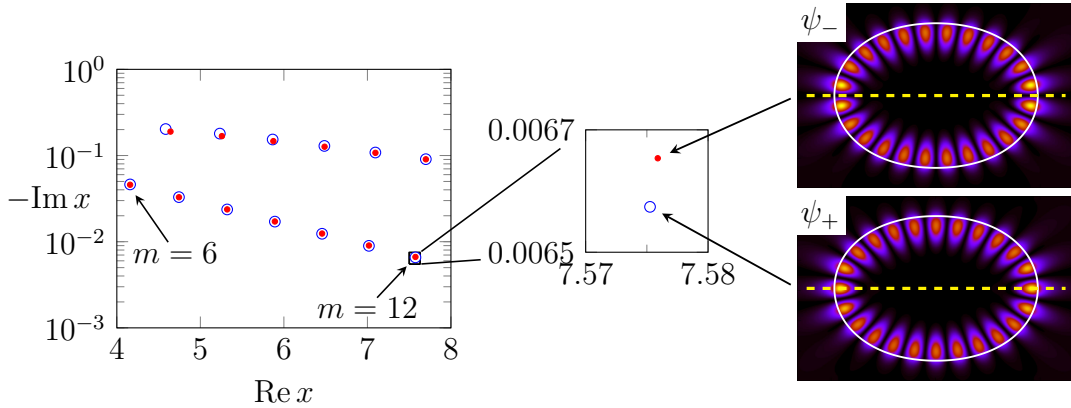


**Figure 3.3:** The complex wave numbers  $x = kR$  are shown in complex plane for even (blue open circles) and odd (red dots) parity modes with  $l = 1, 2$  in the quadrupole cavity with  $(\epsilon, n) = (0.1, 2)$ . For the mode numbers  $(m, l) = (12, 1)$  the complex plane is magnified and the corresponding intensity mode pattern are shown. A mirror-reflection symmetry line is shown as yellow dashed line.

Next, the dynamics of the modes associated to  $x_+$  and  $x_-$  is expressed in an effective two-mode model where the effective Hamiltonian takes the matrix form

$$H = \begin{pmatrix} \Omega & A \\ B & \Omega \end{pmatrix} \quad (3.26)$$

in the basis of CCW and CW propagating waves [Wiersig et al., 2008, Wiersig et al., 2011, Wiersig, 2011, Wiersig, 2014a] (for billiards see also Ref. [Hackenbroich et al., 1998]). Therefore, the off-diagonal element  $A$  ( $B$ ) describes the coupling of a pure CCW (CW) waves to pure CW (CCW) waves conveyed by the boundary deformation, and  $\Omega$  refers to the intensity being not backscattered. Here, mirror-reflection symmetry implies  $A = B$ . The eigenvalues of this symmetric matrix are

$$\lambda_{\pm} = \Omega \pm A \quad (3.27)$$

and the eigenstates are

$$\psi_+ = \frac{1}{\sqrt{2}} \begin{pmatrix} 1 \\ 1 \end{pmatrix} \quad \psi_- = \frac{1}{\sqrt{2}} \begin{pmatrix} 1 \\ -1 \end{pmatrix}. \quad (3.28)$$

Here,  $\psi_+$  ( $\psi_-$ ) reflect the eigenstates regarding positive (negative) parity of the mode pair. The splitting in the eigenvalues  $\Delta x \equiv \lambda_+ - \lambda_- = 2A$  depends on the coupling strength  $A = B$  of CW and CCW waves; i.e. on the backscattering.

Note that the Hamiltonian (3.26) represents the dynamics of even and odd parity modes. However, a formally similar Hamiltonian can be used to describe the interaction between two levels  $l$ . Such an interaction leads to an avoided resonance crossing and occurs, e.g., if one varies a system parameter [Carmon et al., 2008, Wiersig, 2006, Unterhinninghofen et al., 2008, Yi et al., 2011, Wiersig and Hentschel, 2006].

If weak boundary deformations are considered the actual modes and their complex wave number can be determined by a perturbation theory for TM polarization [Duberland et al., 2008] which is reviewed in Secs. 5.1-5.2 (for TE polarization see Ref. [Ge et al., 2013]). For stronger boundary deformations the mode equation needs to be solved numerically e.g. with boundary element method (BEM) [Wiersig, 2003], boundary integral method [Boriskina et al., 2004], finite-difference-time-domain (FDTD) calculations [Inan and Marshall, 2011, Oskooi et al., 2010], wave-matching [Nöckel and Stone, 1996, Hentschel and Richter, 2002] or numerical scattering matrix approaches [Türeci et al., 2005]. In this thesis all full numerical results are obtained using the boundary element method <sup>5 6</sup>.

### 3.3.2 Asymmetric deformations and asymmetric backscattering

In this section microdisk cavities are discussed that do not exhibit any mirror-reflection symmetry. Such fully asymmetric cavities can be constructed by deforming a circular cavity e.g. to a spiral [Chern et al., 2003]. An alternative way to construct asymmetric cavities is to place

<sup>5</sup>Note that the boundary element method has the advantage that it does not assume the Rayleigh hypothesis. Therefore, the BEM gives accurate results also for, e.g., non-convex cavities.

<sup>6</sup>The cpp code of the boundary element method [Wiersig, 2003] which is used in this thesis was provided by Prof. J. Wiersig.

external scatterers such as nanoparticles [Wiersig, 2011], waveguides [Redding et al., 2012] or microfiber tips [Mazzei et al., 2007] along the cavity's boundary. The latter procedure can be used experimentally to easily control the asymmetry parameter, e.g. the position of the microfiber tips, in order to drive the system in an exceptional point [Peng et al., 2016]. In microjet cavities an asymmetric shape can be induced by using a noncircular orifice [Yang et al., 2006].

In asymmetric cavities the modes are no longer separated into even and odd parity classes but still, as long as the deformation is not too large, one observes mode pairs as illustrated in Fig. 3.4. However, these modes do not form standing waves any longer but partially traveling waves; i.e. the modes exhibit a finite chirality  $\alpha_{\text{ch}}$ . From the angular momentum decomposition of the mode

$$\psi(r, \phi) = \begin{cases} \sum_{m \in \mathbb{Z}} \alpha_m \frac{J_m(nkr)}{J_m(nkR)} e^{im\phi} & \text{for } r < R \\ \sum_{m \in \mathbb{Z}} \beta_m \frac{H_m(kr)}{H_m(kR)} e^{im\phi} & \text{for } r > R \end{cases} \quad (3.29)$$

this chirality can be computed as

$$\alpha_{\text{ch}} = \frac{\sum_{m < 0} |\alpha_m|^2 - \sum_{m > 0} |\alpha_m|^2}{\sum_{m < 0} |\alpha_m|^2 + \sum_{m > 0} |\alpha_m|^2} \quad (3.30)$$

which is  $-1$  for pure CCW propagation, zero for standing waves and  $1$  for pure CW propagation. Note that often, e.g. in Refs. [Wiersig, 2011, Wiersig et al., 2011, Wiersig, 2014a], an alternative definition

$$\tilde{\alpha}_{\text{ch}} = 1 - \frac{\min \left( \sum_{m < 0} |\alpha_m|^2, \sum_{m > 0} |\alpha_m|^2 \right)}{\max \left( \sum_{m < 0} |\alpha_m|^2, \sum_{m > 0} |\alpha_m|^2 \right)} \quad (3.31)$$

is used which is zero for standing waves and converge to one for any direction of propagation. As show in the intensity pattern in Fig. 3.4 the modes do not have defined node lines, i.e. they form ring-like structures which indicates them as (partially) traveling waves.

### Two mode model for asymmetric backscattering

As long as the optical modes still come in nearly degenerate pairs it is valid to use a two-mode model to describe the dynamics of such a pair. The effective two-mode Hamiltonian (3.26)

$$H = \begin{pmatrix} \Omega & A \\ B & \Omega \end{pmatrix}. \quad (3.32)$$

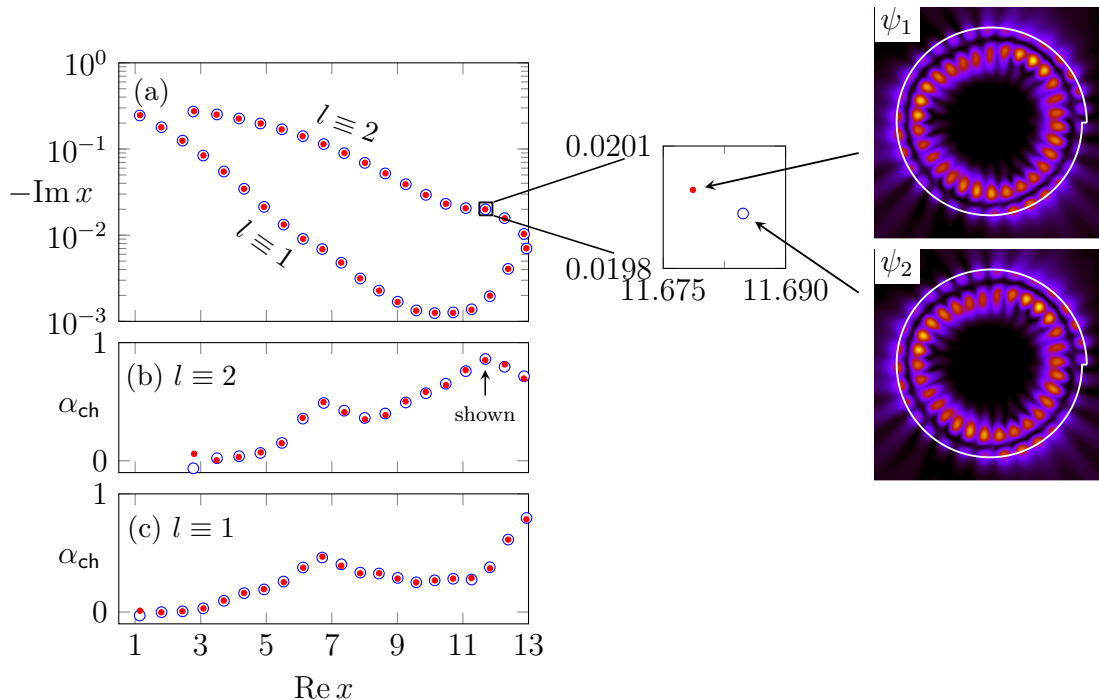


**Figure 3.4:** (a) The complex wave numbers of optical modes in the spiral cavity with  $(\epsilon, n) = (0.05, 2.0)$  are shown in complex plane for mode pairs  $l \leq 2$ . (b) and (c) shown the numerically determined chirality  $\alpha_{\text{ch}}$ , see Eq. (3.30), for  $l = 1$  and  $l = 2$  respectively. The magnification show a highly copropagating mode pair around  $\text{Re } x \approx 11.68$ . The intensity pattern of the modes is shown in right panels with a white curve illustrating the cavity's boundary.

is repeated here for convenience. In contrast to the symmetric case (3.26), here, for fully asymmetric cavities, the matrix  $H$  is not symmetric and, because of the openness of the system, it is also not Hermitian; consequently  $|A| \neq |B|$ . This phenomenon is called asymmetric backscattering, see Refs. [Wiersig et al., 2008, Wiersig et al., 2011, Wiersig, 2011, Wiersig, 2014a]. As a result of the asymmetric backscattering the eigenvalues

$$\lambda_{\pm} = \Omega \pm \sqrt{AB} \quad (3.33)$$

and unnormalized eigenvectors

$$\psi_{\pm} = \begin{pmatrix} \sqrt{A} \\ \pm \sqrt{B} \end{pmatrix} \quad (3.34)$$

differ from the symmetric case. From the eigenvectors of two-mode model the three main aspects of asymmetric backscattering in microdisk cavities are obvious: (i) Since  $|A| < |B|$  ( $|A| > |B|$ ) the modes are partially traveling waves in (C)CW direction. (ii) Both modes are copropagating with the same preferred sense of rotation as  $\alpha_{\text{ch},+} = \alpha_{\text{ch},-} = (|A| - |B|)/(|A| + |B|)$  [compare to Eq. (3.30)]. (iii) The mode pair is non-orthogonal with  $\psi_{+}^* \cdot \psi_{-} = |A| -$

$|B| \neq 0$ . These three aspects have been verified by full numerical simulations [Wiersig et al., 2011, Wiersig, 2011] and experiments [Peng et al., 2016, Redding et al., 2012]. In Sec. 6 these properties of modes in asymmetric cavities will be verified also within a perturbative approach to slightly deformed microcavities.

Moreover, the eigenvectors (3.34) nicely reflect the properties of the expansion coefficients  $\alpha_m$  of the optical modes [Wiersig et al., 2008, Wiersig et al., 2011], see Fig. 3.5 for the angular momentum distribution of the mode pair shown in Fig. 3.4. The pattern  $|a_m|^2$  of the expansion coefficients are almost identical for both modes. Since,  $\sum_{m>0} |a_m|^2 > \sum_{m<0} |a_m|^2$  it yields  $A > B$  which identifies both modes as copropagating in CCW direction. Furthermore the expansion coefficients  $a_m$  of the second mode (blue circles) have the opposite signs than the  $a_m$  of the first mode (red dots) for negative  $m$  which can also be explained by the eigenvectors (3.34). Additionally, the  $\alpha_m$  of the two modes can be superimposed to reconstruct purely CW/CCW propagating states, see Fig. 3.5(d). Accordingly, this can be done with the eigenvectors (3.34) to reconstruct the basis of the two-mode Hamiltonian (3.32) as

$$\frac{\psi_+ + \psi_-}{2\sqrt{A}} = \begin{pmatrix} 1 \\ 0 \end{pmatrix} \quad \text{pure CCW propagating} \quad (3.35a)$$

$$\frac{\psi_+ - \psi_-}{2\sqrt{B}} = \begin{pmatrix} 0 \\ 1 \end{pmatrix} \quad \text{pure CW propagating.} \quad (3.35b)$$

Note that these superpositions are not eigenstates of the system due to a small splitting in  $kR$ ,  $\lambda$  respectively.

### Exceptional points

An interesting aspect of the mode dynamics in asymmetric microcavities are so-called exceptional points (EPs) in parameter space [Kato, 1966, Heiss, 2000, Heiss and Harney, 2001, Berry, 2004, Heiss, 2012]. They are straightforwardly explained by the two-mode model: Considering a deformation where the backscattering in only one direction vanishes, e.g.  $B = 0$  in the Hamiltonian (3.32) but the backscattering in the other direction is still finite with  $A \neq 0$ . Then, from Eq. (3.33) it follows directly that the eigenvalues  $\lambda$  are degenerate. However, in contrast to an ordinary (diaboloic) degeneracy, at an EP also the eigenvectors coalesce and become collinear, i.e.  $\psi_+ = \psi_-$  in Eq. (3.34). Therefore, if the microcavity is tuned into an EP the mode pair vanishes and is replaced by a single degenerate mode with one complex wave number  $x = kR$ . Note that this mode is a purely traveling wave, e.g. in CCW direction if  $B = 0$ . Experimentally and numerically it is hard to tune the system exactly into an EP. Therefore, also the properties of the system close to an EP are important and provide interesting physics. From Eq. (3.33) it follows that the eigenvalues  $\lambda$ , i.e. the complex wave numbers  $kR$ , show a characteristic square root topology close to the EP as illustrated in Fig. 3.6. Therefore, a way to identify an EP numerically and experimentally is to encircling it in parameter space: After

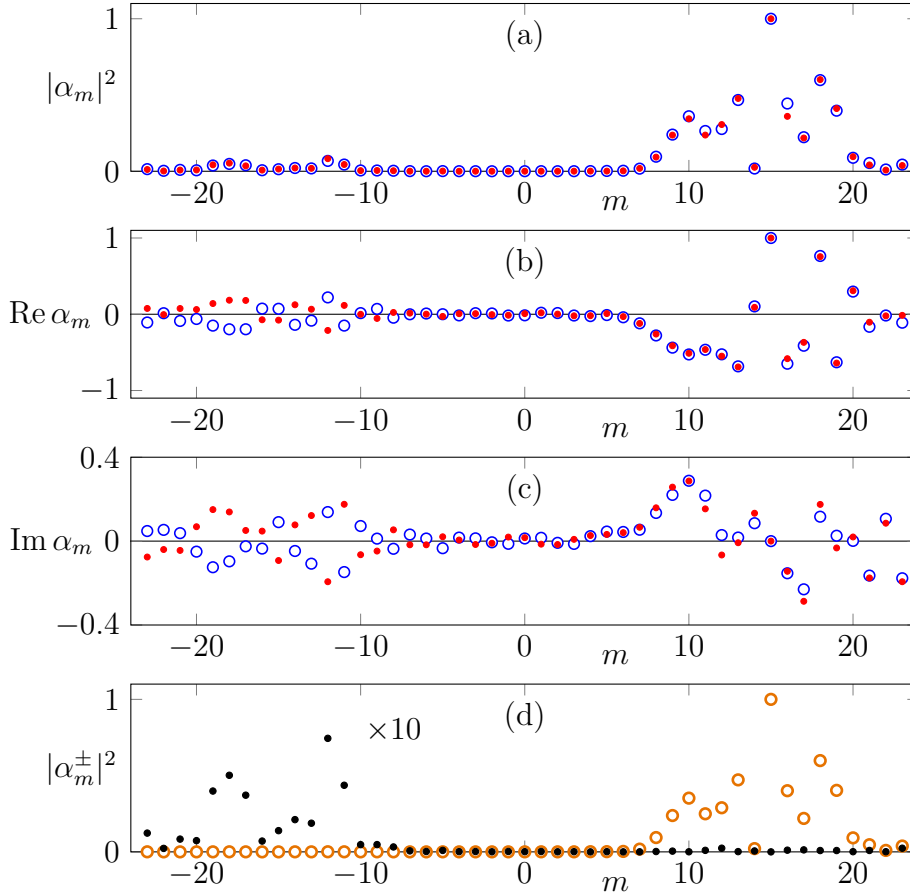


**Figure 3.5:** For the two modes shown in Fig. 3.4 the circular-mode expansion coefficients  $\alpha_m$  from Eq. (3.29) are shown in (a-c). In (d) the superpositions (orange open circles)  $\alpha_m^+ = (\alpha_m^{(1)} + \alpha_m^{(2)})/2$  and (black dots)  $\alpha_m^- = (\alpha_m^{(1)} - \alpha_m^{(2)})/2$  representing purely CW/CCW propagating states are shown. The coefficients  $\alpha_m^-$  are enlarged by a factor 10.

one encircling the eigenvalues have exchanged; i.e. one need two encircling of the EP to restore the eigenvalue. However to reestablish the wave function one needs actually four encirclings because of a sign flip after the first two encirclings. These properties of the EP have been first measured in microwave experiments [Dembowski et al., 2001, Dembowski et al., 2004] and later in single optical microcavities [Lee et al., 2008b, Lee et al., 2009, Zhu et al., 2010]. Furthermore, EPs are important in  $\mathcal{PT}$ -symmetric systems [Bender and Boettcher, 1998] such as coupled optical structures with amplification and absorption [El-Ganainy et al., 2007b, Guo et al., 2009b, Rüter et al., 2010, Hodaei et al., 2014, Peng et al., 2014a]. EPs in microcavities also have promising applications, e.g. for improved sensitivity of nanoparticle sensors [Wiersig, 2014b], mechanical motion sensors [Liu et al., 2016], optical gyroscopes [Sarma et al., 2015], and for the construction of optical waveguides with special transport properties [Schomerus and Wiersig, 2014].



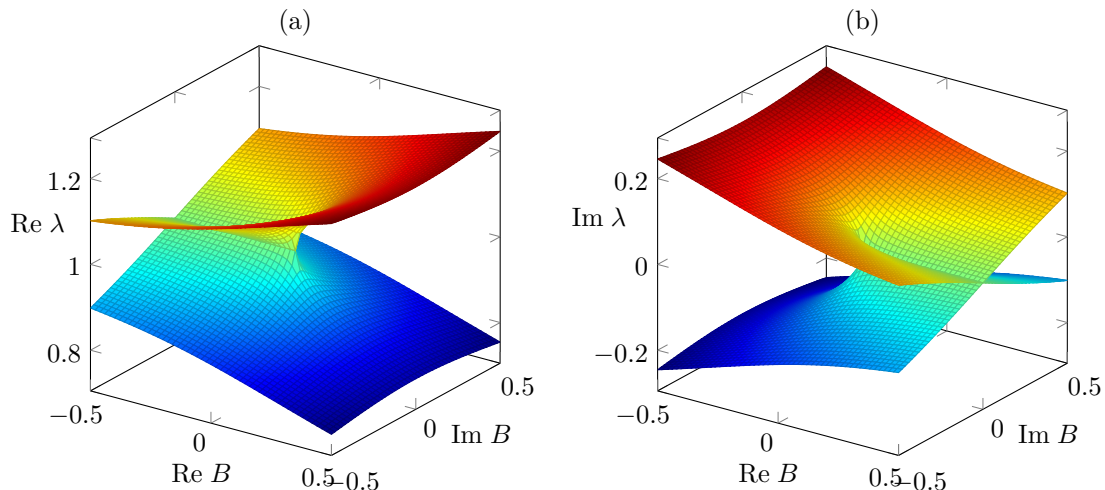


**Figure 3.6:** The (a) real and (b) imaginary part of the eigenvalues  $\lambda$  of the two-mode Hamiltonian (3.26) are shown as surface plot for parameters  $\Omega = 1$ ,  $A = 0.1$  and varying complex  $B$ . For  $B = 0$  an exceptional point is observed.

## 3.4 Ray-wave correspondence

So far two ways to describe a microcavity are explained: The ray model in chapter 2 and the wave model in the current chapter. In this section the two approaches are now compared. Therefore, in Sec. 3.4.1 the boundary Husimi function [Hentschel et al., 2003] is reviewed which projects the wave function  $\psi$  (and its normal derivative) at the cavity's boundary into the phase space; to be precise into the section of the phase space taken along the cavity's interface. In Sec. 3.4.2 some fundamental aspects of the ray and wave comparison are discussed.

### 3.4.1 The boundary Husimi representation

The ray dynamics is effectively expressed in phase space where regions of regular and chaotic dynamics are clearly separated. However, the wave function  $\psi(\vec{r})$  as solution of the mode equation (3.9) acts in real space. In quantum mechanics therefore a Husimi function [Husimi, 1940] is used to project the wave function into the full phase space. Similarly, in case of optical microcavities the boundary Husimi function [Hentschel et al., 2003]<sup>7</sup> is used to project  $\psi(\vec{r})$  into the phase space spanned by the Birkhoff coordinates  $(q, p)$  which were introduced in Sec. 2.1. Consistently with the ray dynamics, the Husimi function can be constructed from the component of  $\psi$  approaching the boundary (inc) or emerging (em) from the boundary. Hence, the overlap of the wave function  $\psi$  and its normal derivative  $\partial_\nu \psi$  with a minimal uncertainty wave packet  $\zeta(\tilde{q}, q, p)$  at  $(q, p)$  [and folding parameter  $\tilde{q}$ ] is used to define the boundary Husimi

<sup>7</sup>See also Ref. [Crespi et al., 1993] for the Husimi function in closed billiards.

function as

$$H_0^{\text{inc(em)}}(q, p) = \frac{n\text{Re } k}{2\pi} \left| \mathcal{F}h_\psi(q, p) + (-) \frac{i}{\mathcal{F}k} h_{\partial\psi}(q, p) \right|^2 \quad (3.36)$$

with  $\mathcal{F} = \sqrt{n\sqrt{1-p^2}}$  and the functions

$$h_\psi(q, p) = \int_0^{q_{\text{max}}} \psi(\tilde{q}) \zeta(\tilde{q}, q, p) d\tilde{q} \quad (3.37a)$$

$$h_{\partial\psi}(q, p) = \int_0^{q_{\text{max}}} \partial_\nu \psi(\tilde{q}) \zeta(\tilde{q}, q, p) d\tilde{q} \quad (3.37b)$$

$$\zeta(\tilde{q}, q, p) = (\sigma\pi)^{-1/4} \sum_{l=-\infty}^{\infty} \exp \left[ -\frac{(\tilde{q} - q + lq_{\text{max}})^2}{2\sigma} - inkp(\tilde{q} + lq_{\text{max}}) \right]. \quad (3.37c)$$

Here, the parameter  $\sigma/R^2 = \sqrt{2}/(n\text{Re } kR)$  fixes the extension of the minimal-uncertainty wave packet  $\zeta(\tilde{q}, q, p)$ . Note that in Ref. [Hentschel et al., 2003] in a similar manner also an external Husimi function  $H_1^{\text{inc(em)}}(q, p)$  is defined that evaluates the components of  $\psi$  and  $\partial_\nu \psi$  being outside of the cavity which is advantageous, e.g., for the comparison with scattering experiments. In this thesis the emerging Husimi function  $H_0^{\text{em}}(q, p)$  inside the cavity is used to be consistent with the ray dynamics explained in chapter 2.

### 3.4.2 Comparing ray and wave dynamics

In the following, aspects of classical dynamics and their wave mechanical (or quantum mechanical) manifestations in phase space are discussed. Therefore, it is practical to define an effective Planck constant

$$\hbar = \frac{1}{n\text{Re } kR}. \quad (3.38)$$

for a particular optical mode which determines the resolution in phase space.

#### Regular dynamics

The circular cavity is an integrable system whose ray dynamics follow straight lines of constant momentum in phase space, see Sec. 2.2.1. Therefore, also the optical modes follow these integrable lines since the momentum  $p$  is a conserved quantity. The momentum where the optical mode localizes is predicted via [Nöckel, 1997]

$$p = \hbar m = \frac{m}{n\text{Re } kR}, \quad (3.39)$$

see Fig. 3.7. The profile of the Husimi function in  $p$  is in a good agreement with a Gaussian. Since the mode shown in Fig. 3.7 is a standing wave (with a positive parity) the Husimi function

has same contributions on upper and lower half of phase space; i.e. same contributions of CW and CCW parts.

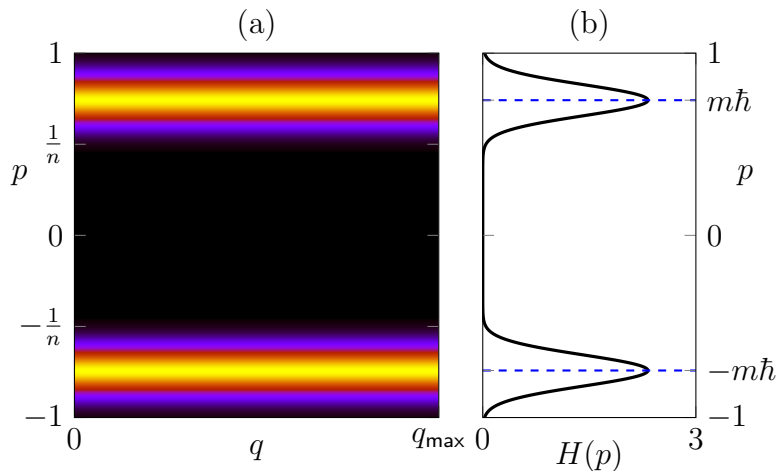


**Figure 3.7:** In (a) the Husimi function of the (positive parity) mode  $(m, l) = (8, 1)$ , see Eq. (3.22a), in a circular cavity with  $n = 2$  is shown from low intensity (black) to high intensity (yellow). In (b) the momentum distribution of the Husimi function is shown as black curve. Blue dashed lines indicate the localization at  $p$  given by Eq. (3.39).

If the microcavity is slightly deformed such that families of KAM curves in phase space exist (see Sec. 2.2) then also the wave function in general follows the KAM curves with quantizing actions [Gutzwiller, 1991]. Although the deformation is slightly stronger such that KAM curves are already destroyed then there exists so called adiabatic curves [Robnik and Berry, 1985, Nöckel, 1997]

$$p_{\text{adi}}(q) = \sqrt{1 - \left(\frac{\kappa(q)}{K}\right)^{2/3}} \quad (3.40)$$

which roughly describe the ray dynamics for short times. Here,  $\kappa(q)$  is the curvature of the cavity at  $q$  and  $K$  is an integration constant. Whispering-gallery-like optical modes follow these adiabatic curves [Nöckel and Stone, 1997, Nöckel et al., 1996].

### Localization along periodic orbits

If the cavity is moderately deformed regular islands around stable periodic orbits establish due to the Poincaré-Birkhoff theorem. A wave mechanical signature of the regular islands is the localization of modes in these regions. By properly adjusting the refractive index this localization on the regular island can be used to create directional emission from the cavity [Gmachl et al., 1998].

If all islands of a periodic orbit are outside the leaky region the lifetime of the concerning rays is infinite. However, an optical mode localizing on such a regular island clearly has a finite

lifetime. The origin is the so-called dynamical tunneling [Davis and Heller, 1981] which couples classically separated regions in phase space. Therefore the mode radiates out of the cavity in a two step process: First, the intensity leaves the regular island via dynamical tunneling and, second, the chaotic dynamics around the island lead to an intensity transport into the leaky region where it radiates out of the cavity [Shinohara et al., 2010, Shinohara et al., 2011]. Since the transport in the chaotic component of the phase space is rather fast such a process is called chaos-assisted tunneling.

However, optical modes not only localize at the regular region around stable fixed points but also along unstable fixed points without regular dynamics around. This phenomenon is called scarring [Heller, 1984, Rex et al., 2002, Lee et al., 2002, Gmachl et al., 2002].

Interestingly, even in microcavities where no periodic orbit is present in classical ray dynamics optical modes can localize along simple geometric structures. This has been observed e.g. in the spiral cavity by Lee *et al.* [Lee et al., 2008a, Lee et al., 2004] and experimentally verified by Kim *et al.* [Kim et al., 2009]. Such modes are called quasiscarred modes.

### Partial barriers

If the microcavity is strongly deformed the phase space becomes predominantly chaotic, see Sec. 2.2. However the transport in the chaotic region is usually not homogeneous. Partial barriers which are formed e.g. from broken KAM tori (so-called cantori) can reduce the transport, e.g., in the momentum  $p$ . The effects of such a partial barrier on the wave dynamics strongly depend on the ratio  $\Delta A/\hbar$  of the wavelength, i.e.  $\hbar$  from Eq. (3.38), and the area  $\Delta A$  transported through the partial barrier via the turnstile mechanism [Mackay et al., 1984, Michler et al., 2012]: If the wavelength is small enough the wave can penetrate the partial barrier otherwise the partial barrier acts similar as an invariant curve. Consequently, it is possible that long-lived whispering-gallery-like modes are formed in a predominantly chaotic cavity [Shim et al., 2011]: Here, a partial barrier with small turnstile flux along a high momentum  $p$  prevent the mode from spreading into the leaky region. For the similar effect in quantum maps see also Ref. [Körber et al., 2015].

### Unstable manifold

In a microcavity with chaotic ray dynamics the emission pattern of very long trapped rays is predicted via an intensity-weighted unstable manifold as explained in Sec. 2.3.2. In Ref. [Wiersig and Hentschel, 2008] it has been shown that also long-lived optical modes localize on the unstable manifold and therefore exhibit a similar far-field pattern. This knowledge can be used to design cavities with unidirectional light emission by designing the boundary shape to result in a “proper” unstable manifold, see Ref. [Schermer et al., 2015].

### Resonance chains in phase space

Classical resonance chains in phase space which develop naturally due to Poincaré-Birkhoff theorem have an impact on optical modes: If the order of the resonance chain is  $(r:s)$ , i.e. the resonance chain has  $r$  islands in phase space (see Sec. 2.2.1), then circular modes whose mode number difference  $(\Delta m, \Delta l)$  is a multiple of  $(r:s)$  are coupled [Brodier et al., 2002, Kwak et al., 2015]. This situation is illustrated in Fig. 3.8. Here, the mode of the deformed cavity at  $kR = 105.79408 - 0.00291i$  is dominantly the circular mode  $(m, l) = (115, 4)$  localizing below the resonance chain but has also noticeable contributions from the circular mode  $(m, l) = (133, 1)$  localizing above the resonance chain. The mode number difference  $(\Delta m, \Delta l) = (18, 3)$  coincides with three times the order of the resonance chain  $(r:s) = (6:1)$ . Remarkable in the situation of Fig. 3.8 is that a low- $Q$  mode  $(m, l) = (115, 4)$  gets contributions from a high- $Q$  mode  $(m, l) = (133, 1)$  which leads to the interesting fact that the  $Q$ -factor of the deformed cavity  $Q_{\text{deformed}} = 18155$  is larger than the  $Q$ -factor of the corresponding circular mode  $Q_{\text{circle},(115,4)} = 16838$ .

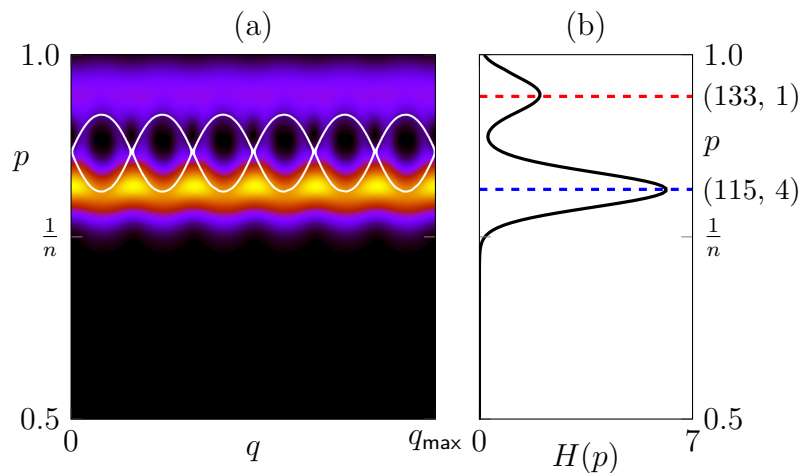


**Figure 3.8:** In (a) the Husimi function of an optical mode with  $kR = 105.79408 - 0.00291i$  is shown from low intensity (black) to high intensity (yellow). The cavity shape is given by  $r(\phi)/R = 1 + 0.003 \cos 6\phi$  and the cavity has a refractive index  $n = 4/3$ . The resonance chain of the billiard dynamics is shown as white curve. In (b) the momentum distributions of the Husimi function is shown as black curve. Red and blue dashed lines indicate the momenta of the modes  $(m, l) = (133, 1)$  and  $(m, l) = (115, 4)$  in a circular cavity respectively, see Eq. (3.39).

However, a generic whispering-gallery mode with radial mode number  $l = 1$  can only couple to modes with lower  $Q$ -factors via a classical resonance chain. Therefore one observes in general a  $Q$ -spoiling of high- $Q$  modes due to the resonance-assisted tunneling. This  $Q$ -spoiling mechanism is discussed in detail in Sec. 7.

### Extended ray dynamics

Whenever, ray and wave dynamics are compared one should keep in mind that a very good agreement is only expected in the so-called semiclassical limit  $\text{Re } kR \rightarrow \infty$  ( $\lambda/R \rightarrow 0$ ). However, for a finite wavelength  $\lambda$  slight deviations are observable. One prominent effect is the Goos-Hänchen shift [Goos and Hänchen, 1947]: In ray dynamics the reflection takes place at a single point where the ray hits the dielectric interface. At this point the ray is instantly reflected. However, in the wave picture a reflected beam is slightly shifted away from the position of an incoming beam. This shift can be explained such that the beam is not directly reflected at the interface but penetrates the material by roughly a wavelength and is there reflected at an effective boundary [Hentschel and Schomerus, 2002].

A second important effect for the dynamics in the cavity is the Fresnel filtering [Tureci et al., 2002] (or to be precise the angular Goos-Hänchen shift [Merano et al., 2009, Götze et al., 2013]): In ordinary ray dynamics the angle of incidence is always equal to the angle of reflection. However, in wave mechanics the angle at which a beam is reflected can be slightly different from the angle of incidence. The origin here is that a beam actually exhibits a distribution of incident angles some of which are only partially reflected. Therefore, the mean reflection angle of the reflected beam is shifted. In this sense the Fresnel filtering is naturally explained in ray dynamics if one iterates not a single ray but an intensity weighted distribution of rays. However, if a single ray with finite wavelength is considered then the phase space dynamics is effected by both the Goos-Hänchen shift and the Fresnel filtering [Schomerus and Hentschel, 2006]. The incorporations of these wave effects in the ray dynamics can lead to non-Hamiltonian (non-area-preserving) phase-space dynamics [Altmann et al., 2008]. Models for the wave corrections to the ray dynamics exist for planar [Artmann, 1948, Lai et al., 1986, Unterhinninghofen and Wiersig, 2010] and curved [Stockschröder et al., 2014] interfaces. Note that the extended ray dynamics also shift periodic orbits in phase space at which modes can localize [Unterhinninghofen and Wiersig, 2010]. Moreover, incorporating extended ray dynamics can create new periodic orbits which are not present in ordinary ray dynamics. Therefore extended ray dynamics explains the occurrence of quasiscarred modes.

# 4 Asymmetric backscattering in ray dynamics

Asymmetric optical cavities, i.e. cavities whose boundary does not have any mirror-reflection symmetry, exhibit asymmetric backscattering between clockwise and counter-clockwise propagating waves. As described in Sec. 3.3.2 asymmetric backscattering therefore leads wave mechanically to non-orthogonal and copropagating mode pairs with a finite chirality. Wave mechanically this is straightforwardly explained within an effective non-Hermitian two-mode Hamiltonian. However, the ray dynamical correspondence of asymmetric backscattering is not fully understood. So far, in Ref. [Lee et al., 2008a] it was demonstrated at a spiral cavity that the classical survival probability has main contributions in one half of the phase space which can be interpreted as a finite chirality. Furthermore, in Ref. [Wiersig et al., 2011] it was shown for a smooth asymmetric cavity that the intensity transported from the lower to the upper half of the phase space is different than vice versa when rays are tracked over time. So far still missing points are (i) the existence of classical pairs of intensity distributions, (ii) their copropagating nature, and (iii) their non-orthogonality. In this chapter the points (i)-(iii) are explained by introducing the Frobenius-Perron operator (FPO)  $\mathcal{F}$  for microcavities. This operator  $\mathcal{F}$  defines the time evolution of intensity distributions in phase space such that the eigenstates of this operator refer to classical intensity distributions with the expected properties (i)-(iii).

First, in Sec. 4.1 the time evolution and backscattering of uniform intensity distributions is discussed. Afterwards, in Sec. 4.2, the FPO  $\mathcal{F}$  for microcavities is introduced and the eigenstates and eigenvalues are discussed. At the end of the chapter, in Sec. 4.3, an analytically solvable toy-model for the FPO  $\mathcal{F}$  in one dimension is presented.

## 4.1 Asymmetric backscattering of uniform intensity distributions

In this section the backscattering process between clockwise (CW) and counter-clockwise (CCW) components of the phase space is discussed from the ray dynamics using uniformly

distributed intensities. The target is to set up an effective  $2 \times 2$  matrix

$$H = \begin{pmatrix} \Omega_1 & A \\ B & \Omega_2 \end{pmatrix} \quad (4.1)$$

from the ray dynamics which qualitatively reflects the properties of the two-mode Hamiltonian (3.32). To illustrate the derivation of the matrix elements the generalized Fourier-truncated spiral is used here. This cavity has a smooth boundary which violates mirror-reflection symmetry for an asymmetry parameter  $\delta > 0$ . Details of the definition and illustrations are provided in the Appendix A.2.1.

The essential point in the derivation of the matrix elements is the definition of CW and CCW regions in phase space since they represent the basis for the matrix (4.1). First, the intuitive identification that the lower [upper] part of the phase space correspond to CW [CCW] propagation is used.<sup>1</sup> As illustrated in Fig. 4.1(a)-(b) a single iteration of the billiard map  $\mathcal{M}$  leads to an area exchange between CW and CCW regions. Since the mapping  $\mathcal{M}$  is area preserving the area transferred from CW to CCW is the same as the area transferred from CCW to CW. However, microcavities are open systems such that the intensity in the cavity is reduced due to a finite reflectivity. Therefore, as illustrated in Fig. 4.1(c)-(f), the effective intensity transport from CW to CCW and from CCW to CW is different. This amount of transported intensity (normalized to the overall started intensity) is the matrix element  $A$  [ $B$ ] as illustrated by the yellow [green] shaded areas in Fig. 4.1(d) [(e)]. Similarly, the amount of intensity remaining in the CW [CCW] component of the phase space is measured by  $\Omega_2$  [ $\Omega_1$ ]. Since the billiard mapping is only known numerically the matrix elements are computed by tracing a large set of initial conditions ( $\approx 10^7 \dots 10^9$ ) in phase space.

This procedure of numerically determining the matrix elements is done for increasing asymmetry parameter  $\delta$  in the generalized Fourier-truncated spiral. The results are summarized in Tab. 4.1. As expected the normalized overlap  $S = (A - B)/(A + B)$  of the eigenstates, see Sec. 3.3.2, and therefore also the chirality of the eigenstates of the two-mode Hamiltonian increases with increasing  $\delta$ . However, in the ray dynamics the diagonal matrix elements  $\Omega_1$  and  $\Omega_2$  are different which is a violation of the two-mode Hamiltonian for asymmetric backscattering in Sec. 3.3.2. Since the order of the difference in  $\Omega_1$  and  $\Omega_2$  is the same as the difference between  $A$  and  $B$  it can not be seen as a small correction.

The origin of the inconsistency between the matrix (4.1) from ray dynamics and the two-mode Hamiltonian (3.32) is the definition of CW and CCW regions in phase space: In the wave picture CW and CCW propagation is measured via the terms proportional to  $a_m \exp(im\phi)$ , i.e. via the angular momentum with respect to the origin. Therefore, to be consistent with the wave mechanics, also in the ray dynamics CW and CCW propagation need to be defined with respect to the curve  $L_z(s, p) = 0$  of vanishing angular momentum, see yellow curve in

<sup>1</sup>This identification is often used in literature, e.g., in Refs. [Wiersig et al., 2011, Lee et al., 2008a].



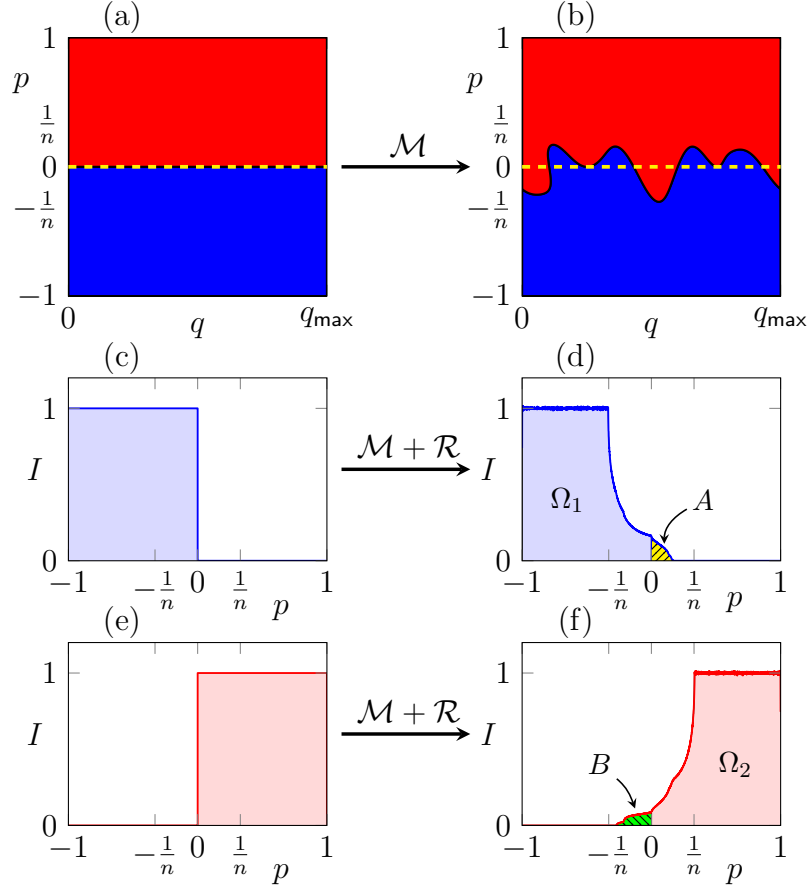


**Figure 4.1:** (a) and (b) shows the billiard mapping of initially CW (blue) and CCW (red) regions in the phase space of the Fourier-truncated spiral, see Eq. (A.14), with  $(\epsilon, \delta, N_p, n) = (0.07, 1, 4, 3.0)$ . A yellow dashed line indicate  $p = 0$  which separates CW and CCW propagation. In (c), (d) [(e), (f)] the intensity iteration of initially CW [CCW] regions is shown as a histogram over momentum  $p$ . Therefore the area below the curves in (d) and (f) corresponds to the matrix elements in Eq. (4.1) as labeled in the plots.

Fig. 4.2(a). This curve  $L_z = 0$  is clearly different from the line  $p = 0$  which is traditionally used in the ray picture to distinguish CW and CCW regions. As shown in Appendix A.2.2 the curve of vanishing angular momentum can be calculated analytically for cavities that are defined via a continuous function  $r(\phi)$ . Furthermore, it is shown that the image of the curve  $L_z = 0$  is its mirror-reflection at  $p = 0$  [see Fig. 4.2(b)]. Therefore the phase space area which is shuffled via one map iteration from CW to CCW region is again the same as the one shuffled from CCW to CW (regarding  $L_z = 0$ ), but the effective intensity transport is different. From the shuffled intensity the matrix elements [see Fig. 4.2(c)] can be again determined numerically. The results for increasing asymmetry parameter  $\delta$  are listed in Tab. 4.2. Except for statistical fluctuations from the finite sample size of computed trajectories which are of the order  $10^{-5}$  the diagonal matrix elements  $\Omega_1$  and  $\Omega_2$  are the same and the normalized overlap  $S$  of the eigenstates increases with increasing asymmetry parameter  $\delta$ . Moreover, in Appendix A.2.3 analytical expressions for the matrix elements are derived [under the assumption that the

$\delta$	$\Omega_1$	$\Omega_2$	$A$	$B$	$ S $
0.0	0.76871	0.76871	0.01563	0.01563	$< 10^{-4}$
0.2	0.76890	0.76855	0.01544	0.01578	0.01089
0.4	0.76908	0.76844	0.01525	0.01590	0.02087
0.6	0.76926	0.76840	0.01508	0.01594	0.02772
0.8	0.76942	0.76844	0.01492	0.01589	0.03148
1.0	0.76958	0.76860	0.01475	0.01573	0.03215

**Table 4.1:** Numerically determined matrix elements of the  $2 \times 2$  Hamiltonian (4.1) and resulting asymmetry in the backscattering  $S = (A - B)/(A + B)$  for the Fourier-truncated spiral with  $(\epsilon, \delta, N_p, n) = (0.07, 1, 4, 3.0)$ . The definition of CW and CCW propagation is regarding the line  $p = 0$ .

reflectivity (2.23a) has a Taylor expansion and the refractive index is not too small].

However, the definition of CW and CCW regions using the angular momentum also has a general disadvantage: It depends on the choice of the origin whereas the backscattering with respect to  $p = 0$  is origin independent. In Appendix A.2.4 further comments on the backscattering with a shifted origin are provided. In this Appendix it is also shown that the main advantage  $\Omega_1 = \Omega_2$  holds under the origin shift. However, the asymmetry in the backscattering  $S$  changes.

Here, it is mentioned again that the above discussion deals with initially uniform intensity distributions and therefore captures overall properties of the open billiard. However, in wave dynamics optical modes are never uniformly distributed but show large fluctuations and/or localization in phase space. Therefore, it is not assumed that this ray picture provides quantitative comparable results. Nevertheless, some qualitative results regarding the two-mode Hamiltonian could be obtained, e.g. the fact that it has the same diagonal terms  $\Omega_1 = \Omega_2$  and different off-diagonals  $|A| \neq |B|$ . Furthermore, these aspects could be shown almost analytically (see Appendix A.2.3). In order to obtain results for asymmetric backscattering from ray dynamics which are also quantitatively comparable to wave dynamics and go beyond the

$\delta$	$\Omega_1$	$\Omega_2$	$A$	$B$	$ S $
0.0	0.76610	0.76610	0.01823	0.01823	$< 10^{-4}$
0.2	0.76607	0.76606	0.01796	0.01859	0.01730
0.4	0.76598	0.76598	0.01776	0.01895	0.03241
0.6	0.76592	0.76590	0.01763	0.01923	0.04354
0.8	0.76590	0.76587	0.01753	0.01937	0.04975
1.0	0.76592	0.76590	0.01749	0.01937	0.05084

**Table 4.2:** The numerically determined matrix elements of the  $2 \times 2$  Hamiltonian (4.1) and the resulting asymmetry in the backscattering  $S = (A - B)/(A + B)$  for the Fourier-truncated spiral with  $(\epsilon, \delta, N_p, n) = (0.07, 1, 4, 3.0)$  are shown. The definition of CW and CCW propagation is regarding the curve  $L_z = 0$ .

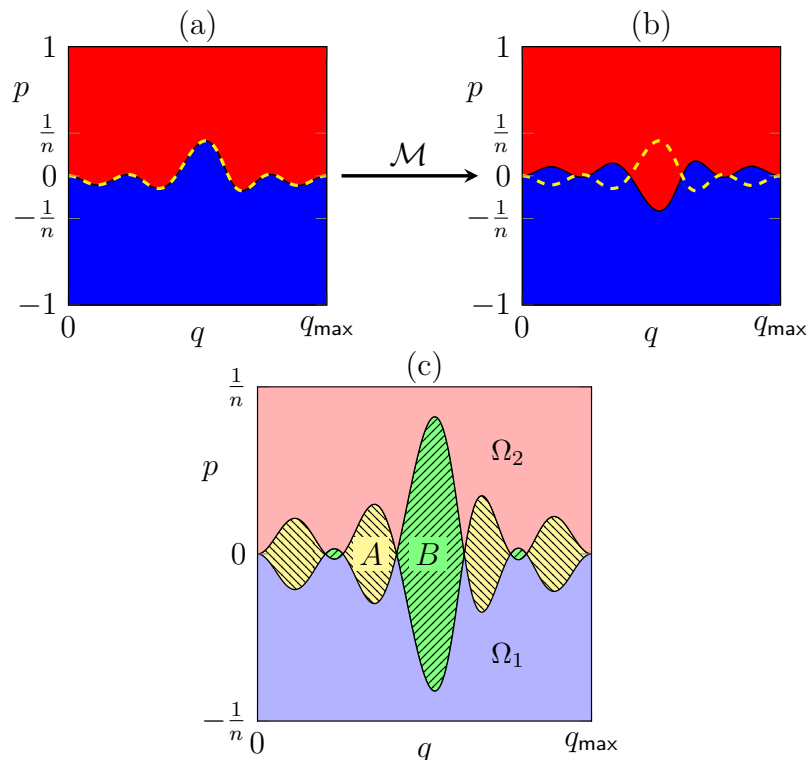


**Figure 4.2:** (a) Initially CW (blue) and CCW (red) regions are shown in the phase space of the Fourier-truncated spiral with  $(\epsilon, \delta, N_p, n) = (0.07, 1, 4, 3.0)$ . (b) The image of these regions after one billiard map iteration is shown. In both pictures a yellow dashed curve represents the curve of vanishing angular momentum  $L_z(q, p) = 0$ . In (c) an integration of the intensity in the shaded region defines the matrix elements in Eq. (4.1) as labeled.

simple two-region approximation in phase space the next section provides a more elaborated approach using the Frobenius-Perron operator.

## 4.2 Frobenius-Perron operator for optical microdisk cavities

In this section asymmetric backscattering is investigated in the ray dynamics with the so-called Frobenius-Perron operator (FPO) which time-evolves intensity distributions in phase space. The FPO has previously been used for Hamiltonian maps [Beck and Schögl, 1993, Weber et al., 2001, Weber et al., 2000, Frahm and Shepelyansky, 2010], dissipative maps [Ermann and Shepelyansky, 2010, Frahm and Shepelyansky, 2013, Carlo et al., 2015], and leaking chaotic billiard [Altmann et al., 2013]. In this section the FPO is adapted to the case of predominantly chaotic microdisk cavities. First, in Sec. 4.2.1, the construction of the FPO for microcavities is explained. Afterwards, in Sec. 4.2.2, it is shown that the long-lived eigenstates of the FPO have interesting properties similar to optical modes: They are pairwise non-orthogonal where

both eigenstates have the same preferred sense of rotation. Therefore the FPO eigenstates are the classical counterparts of optical modes and explain asymmetric backscattering from a ray dynamical point of view. In Sec. 4.2.3 further properties of the FPO eigenstates are discussed and demonstrated at example systems.

### 4.2.1 Construction of the Frobenius-Perron operator

The Frobenius-Perron operator (FPO) maps an initial intensity distribution  $\rho(q, p)$  in phase space to its time-evolved counterpart  $\tilde{\rho}$  as

$$\rho \mapsto \tilde{\rho} = \mathcal{F}\rho. \quad (4.2)$$

This mapping is point-wise defined in closed systems as [Beck and Schögl, 1993]

$$\tilde{\rho}(\tilde{q}, \tilde{p}) = \sum_{(q,p) \in \mathcal{M}^{-1}(\tilde{q}, \tilde{p})} \frac{\rho(q, p)}{|J(q, p)|} \quad (4.3)$$

where the Jacobian determinant  $|\det J(q, p)| = 1$  for the Hamiltonian dynamics. However, microcavities are open systems that lose intensity through the leaky region in phase space. Therefore this definition of the FPO needs to be adapted. Additionally, it needs to be taken into account that the time increment  $\Delta t$  from one reflection to the next is not uniform but depends on the phase space variables  $(q, p)$ . Therefore, in Ref. [Altmann et al., 2013] the FPO for leaking billiards is defined point-wise as

$$\tilde{\rho}(\tilde{q}, \tilde{p}) = \sum_{(q,p) \in \mathcal{M}^{-1}(\tilde{q}, \tilde{p})} e^{\kappa \Delta t(q,p)} R(\tilde{p}) \rho(q, p). \quad (4.4)$$

Here,  $\kappa$  is a classical escape rate that determines the overall loss of the cavity and  $R$  is the reflectivity (2.23). Note that the sum in Eq. (4.4) contains only one term for the ray dynamics in convex cavities. More terms could occur if e.g. non-Hamiltonian extended ray dynamics or rays which leave and reenter the cavity again are considered.

Since the FPO has to describe the whole (may chaotic) ray dynamics inside the cavity it is clear from the point-wise definition (4.4) of the FPO that this is an operator of infinite dimension. In order to make the FPO numerically accessible such that its eigenstates can be computed a finite approximation of the FPO needs to be constructed. In Ref. [Weber et al., 2001] a matrix for the FPO  $\mathcal{F}_{ij}$  is constructed using a set of basis functions<sup>2</sup>  $\rho_j(q, p)$  in phase space. Then

---

<sup>2</sup>In Ref. [Weber et al., 2001] spherical harmonics are used as basis functions  $\rho$  in phase space.

the matrix form of  $\mathcal{F}$  is defined by

$$\mathcal{F}_{ij} = \int_{-1}^1 \int_0^{q_{\max}} \rho_i^*(q, p) \mathcal{F} \rho_j(q, p) dq dp \quad (4.5a)$$

$$= \int_{-1}^1 \int_0^{q_{\max}} \rho_i^*(q, p) R(p) \exp[\kappa \Delta t (\mathcal{M}^{-1}(q, p))] \rho_j(\mathcal{M}^{-1}(q, p)) dq dp. \quad (4.5b)$$

This matrix  $\mathcal{F}_{ij}$  maps the coefficients  $a_j$  of an arbitrary intensity distribution  $\rho = \sum_j a_j \rho_j$  to the coefficients  $\tilde{a}_i$  of the time-evolved intensity  $\tilde{\rho} = \sum_j \tilde{a}_i \rho_j$ . In order to obtain a finite matrix for  $\mathcal{F}$  one needs a truncation, i.e. a finite set of basis functions needs to be considered. Therefore a proper choice of the basis functions  $\rho_j$  is crucial. Since the cavities considered in this chapter are predominantly chaotic it is not practical to use basis functions each supporting the whole phase space. A rather better choice for  $\rho_j$  are the characteristic function of small cells in phase space. In Fig. 4.3 such a phase space discretization is shown. In Refs. [Frahm and Shepelyansky, 2010, Ermann and Shepelyansky, 2010, Frahm and Shepelyansky, 2013] such a discretization of the phase space has been used for maps to get a simple algorithm for a finite matrix approximation of the FPO. This procedure is also known as (slightly modified) Ulam's method [Ulam, 1960]. Instead of performing the integrals in Eqs. (4.5) here the intensity transport between the cells is measured. In the following the construction of the FPO matrix for microcavities using Ulam's method is explained in detail: First, the phase space is divided equally into  $N_{\text{grid}} \times N_{\text{grid}}$  cells labeled with an index as shown in Fig. 4.3. In each cell  $j$  random initial conditions  $(q_\tau, p_\tau)$  with intensity  $I_\tau = 1$  are chosen. They are iterated once via the billiard map to points  $(\tilde{q}_\tau, \tilde{p}_\tau)$ . Thus, the intensity of the iterated points is  $\tilde{I}_\tau = R(\tilde{p}_\tau)$ . From the points that are iterated from cell  $j$  to cell  $i$  the scattered intensity  $I(j \rightarrow i)$  is calculated as

$$I(j \rightarrow i) = \frac{1}{N_\tau} \sum_{\substack{(q_\tau, p_\tau) \text{ in cell } j \\ (\tilde{q}_\tau, \tilde{p}_\tau) \text{ in cell } i}} R(\tilde{p}_\tau) \quad (4.6)$$

where  $N_\tau$  is the number of trajectories started in cell  $j$ . This procedure is sketched in Fig. 4.3.

Next, the true-time aspect of the billiard dynamics needs to be incorporated in the FPO approximation. Therefore, the scattered intensity  $I(j \rightarrow i)$  is weighted with a factor according to the length (or flight time) of the orbit. The weighting factor consistent with (4.4) is

$$T_{ij} = \frac{e^{\kappa \Delta t_{ij}}}{\langle e^{\kappa \Delta t} \rangle}. \quad (4.7)$$

Here,  $\Delta t_{ij}$  is the average time for one iteration from cell  $j$  to cell  $i$  and  $\langle e^{\kappa \Delta t} \rangle$  is the average value of the terms  $e^{\kappa \Delta t_{ij}}$  that enter to the matrix  $T_{ij}$ . In Eq. (4.7) the escape rate  $\kappa$  enters. In Ref. [Altmann et al., 2013] accurate schemes to compute this quantity are given. However, in the examples shown in this thesis it is sufficient to use a simple estimate of the escape rate

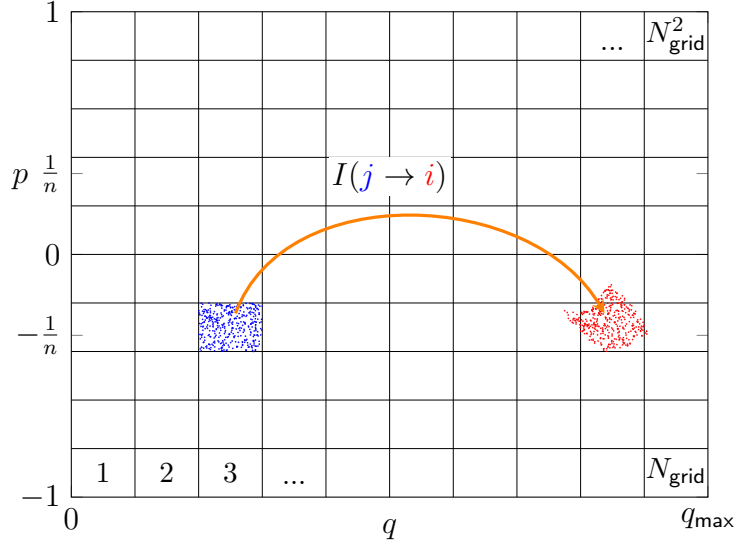


**Figure 4.3:** An illustration of the phase space discretization and the construction of the FPO approximation is shown. Black squares are the cells labeled by an index  $i = 1 \dots N_{\text{grid}}^2$ . The intensity transport from cell  $j$  to cell  $i$  is measured by iterating random initial condition in  $j$  (blue dots). Red dots are the iterated initial conditions.

which is given by

$$\kappa = -\frac{\ln(1 - \mu)}{\langle \Delta t \rangle}. \quad (4.8)$$

Here,  $\mu = 1/n - \int_0^{1/n} R(p) dp$  is the measure of the leak and  $\langle \Delta t \rangle$  is the average time between boundary collisions [Altmann et al., 2013].

Finally, the finite approximation of the FPO for microcavities is given by

$$\mathcal{F}_{ij} = T_{ij} I(j \rightarrow i). \quad (4.9)$$

For typical calculations  $N_{\text{grid}} = 100$  up to  $N_{\text{grid}} = 2000$  is chosen and  $N_{\text{grid}}^2 N_{\tau} \approx 10^{10} \dots 10^{11}$  trajectories are iterated in phase space to get a statistically satisfying result.

The final FPO matrix is of dimension  $N_{\text{grid}}^2 \times N_{\text{grid}}^2$ , i.e. it has typically up to  $\sim 10^{13}$  elements ( $10^{13} \cdot 64\text{bit} = 80\text{TB}$  memory). However, a single cell in phase space is typically coupled to just a few other cells via the billiard dynamics. Therefore, the FPO matrix is very sparse such that it can be stored easily at the computer ( $\sim 800\text{MB}$  memory for  $N_{\text{grid}} = 2000$ ).

For an illustration how the FPO acts on an intensity distribution in phase space see Fig. 4.4. Here, the iteration of an initially Gaussian distribution is shown in the phase space of the Fourier-truncated spiral. By applying  $\mathcal{F}$  the intensity is shifted and elongated according to the billiard dynamics and loses intensity through the leaky region in phase space.

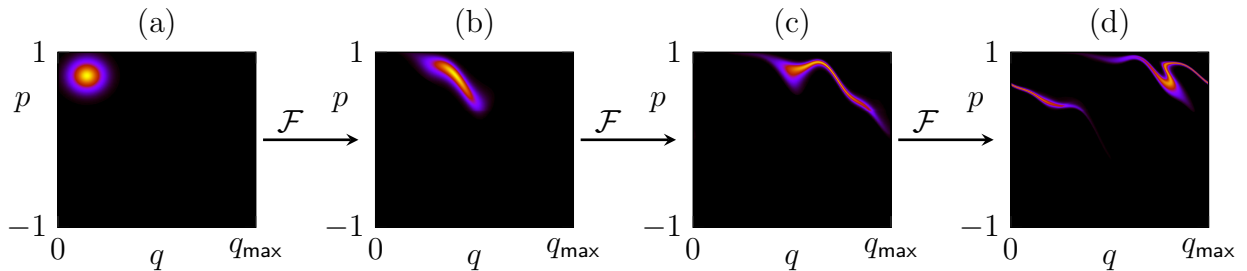


**Figure 4.4:** (a) A Gaussian intensity distribution centered at  $(q, p) = (0.15, 0.73)$  in the phase space of the Fourier-truncated spiral with  $(\epsilon, N_p, \delta, n) = (0.07, 4, 1, 3.0)$  is shown. The 1-3 fold iterations are shown in (b-d) respectively. The FPO is approximated using  $N_{\text{grid}} = 2000$  cells in phase space. Note that in each plot the color map (from black to yellow) is scaled to maximum of the intensity.

## 4.2.2 Eigenstates and eigenvalues in the presence of asymmetric backscattering

Since the FPO time-evolves classical intensity distributions in phase space, the eigenstates of the FPO represent stationary intensity pattern. Because of the openness, i.e. the leaky region in phase space, the norm of such an intensity pattern is reduced each time the FPO is applied. Therefore the eigenvalues of the FPO need to be inside the unite circle in the complex plane. The only exception is the intensity pattern supporting the chaotic saddle. Since the chaotic saddle does not enter the leaky region neither in forward nor in backward iteration its overall intensity stays constant. The chaotic saddle is typically a fractal set such that the corresponding eigenstate vanishes if a finite approximation of the FPO is considered. However, non-fractal eigenstates of the FPO are accessible with the finite approximation derived in the previous section. Typically, one is interested in the long-lived eigenstates whose eigenvalues have large absolute modulus. Therefore the numerical diagonalization of the large sparse FPO matrix  $\mathcal{F}_{ij}$  can be done with a suitable algorithm, e.g. Arnoldi method [Stewart, 2001], to get not all but a few relevant eigenvalues  $\lambda_i$  and eigenvectors  $\rho_i$  with the desired large modulus eigenvalue.

### Eigenvalues

In the following the Fourier-truncated spiral with  $(\epsilon, N_p, \delta, n) = (0.07, 4, 1, 3.0)$ , see Appendix A.2.1, is used to illustrate the results for a typical asymmetric and chaotic cavity. The numerically computed eigenvalues are shown in Fig. 4.5.

As expected all eigenvalues are inside the unit circle. The eigenvalues with largest modulus are close to one and they are on the real axis.

Mathematically only one eigenvalue with the largest modulus determines the long-time dynamics of a general dynamical system. But here the physical interpretation is different. Two eigen-

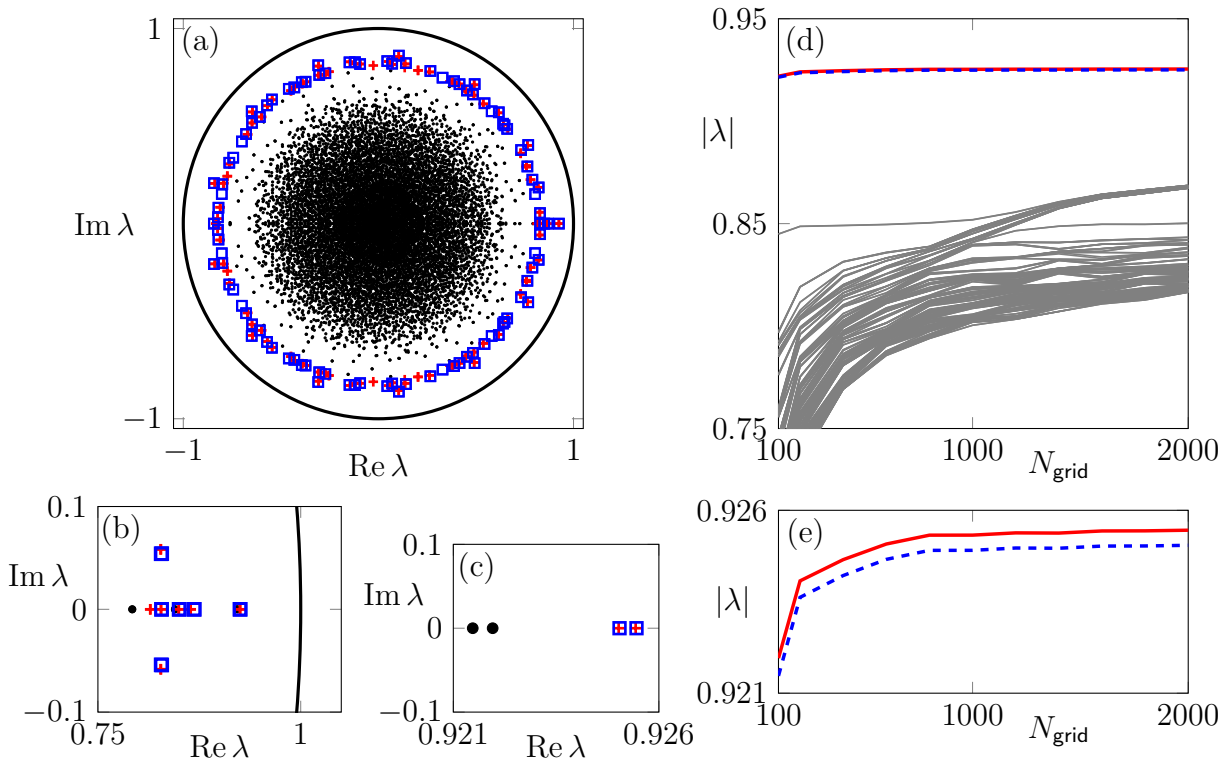


**Figure 4.5:** (a-c) The FPO eigenvalues  $\lambda$  for the Fourier-truncated spiral with  $(\epsilon, N_p, \delta, n) = (0.07, 4, 1, 3.0)$  and for different discretizations (black dots)  $N_{\text{grid}} = 100$ , (red crosses)  $N_{\text{grid}} = 1600$ , and (blue squares)  $N_{\text{grid}} = 2000$  are shown in the complex plane. For  $N_{\text{grid}} = 1600$  and  $N_{\text{grid}} = 2000$  only the 200 largest modulus eigenvalues are shown. The unit circle is drawn as black curve in (a-b). The convergence of the largest modulus (d) 200 and (e) 2 eigenvalues with  $N_{\text{grid}}$  is shown. The largest eigenvalue is illustrated as red solid curve, the second largest as blue dashed curve, and the others as gray solid curves.

values with large modulus are nearly degenerate and clearly separated from the next pair of eigenvalues, see Fig. 4.5(d). Consequently even in the long-time dynamics both largest modulus eigenvalues have to be taken into account. The importance of the second eigenvalue (and corresponding eigenstate) can be illustrated with the fraction  $(\lambda_2/\lambda_1)^m = (0.925043/0.925456)^m \approx 0.999554^m$  for  $N_{\text{grid}} = 2000$ . To neglect the second eigenstate in the dynamics, this fraction needs to be much smaller than one which is true for  $m \rightarrow \infty$ . But up to  $m = 1000$  iterations this fraction is still about 64%. During this time (or iterations) the measure of eigenstate  $\rho_1$  is reduced by  $\lambda_1^{1000} \approx 10^{-34}$ . So the cavity would lose more or less all of its intensity until one can neglect the second eigenstate. Note that also other eigenvalues come in pairs: For example for  $|\lambda| > 0.82$  the distance from an eigenvalue to the next-next neighbor is at least  $\sim 30$  times larger than the distance to the next neighbor.

The convergence of the eigenvalues with the phase space discretization  $N_{\text{grid}}$  is shown in Fig. 4.5(d-e). The eigenvalue pair with largest modulus converges rapidly such that already for small values of  $N_{\text{grid}}$  reliable results can be obtained. The convergence of the lower modulus eigenvalues seems in general slower such that even for  $N_{\text{grid}} = 2000$  not all eigenvalues shown



in Fig. 4.5(d) are converged.

### Eigenstates

Next, the corresponding long-lived eigenstates of the largest modulus eigenvalue pair are discussed. They are shown in Fig. 4.6(a-b). As expected from the Frobenius-Perron theorem [Perron, 1907, Frobenius, 1912] the first eigenstate is completely real and positive. Here, also the second eigenstate is completely real but changes the sign between upper and lower half of the phase space. Both eigenstates support the same sets namely the unstable manifold.

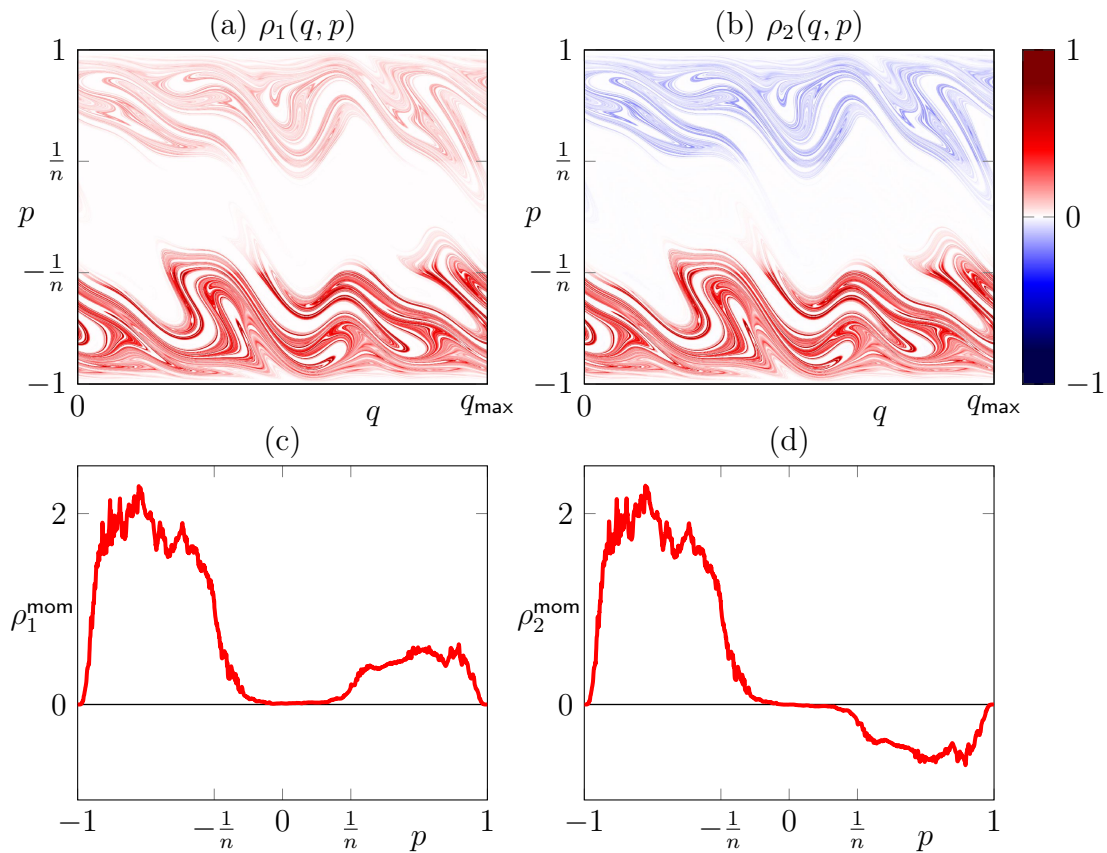


**Figure 4.6:** (a) The first and (b) the second eigenstate of the Fourier-truncated spiral with  $(\epsilon, N_p, \delta, n) = (0.07, 4, 1, 3.0)$  are shown in phase space. (c) and (d) show the momentum representation of the eigenstates, see Eq. (4.10). The discretization of the phase space is  $N_{\text{grid}} = 2000$ .

As a signature of the asymmetry in the system the overall intensity in the upper half of the phase space is smaller than in the lower half for both eigenstates. Therefore CW propagation is featured by the system. To see this in a cleaner way the momentum distributions of the eigenstates defined via

$$\rho^{\text{mom}}(p) = \frac{1}{\mathcal{N}} \int_0^{q_{\text{max}}} \rho(q, p) dq \quad (4.10)$$

are shown in Fig. 4.6(c-d). Since both eigenstates have more weight on the lower half of the phase space they are not orthogonal rather their scalar product

$$\langle \rho_1, \rho_2 \rangle = \frac{1}{2q_{\max}} \int_{-1}^1 \int_0^{q_{\max}} \rho_1^*(q, p), \rho_2(q, p) dq dp \quad (4.11)$$

is  $\langle \rho_1, \rho_2 \rangle = 0.872248$  (for normalized eigenstates with  $\langle \rho_i, \rho_i \rangle = 1$ ). Therefore, the eigenstates are highly copropagating. The propagation of the eigenstates can also be quantified by the (ray dynamical) chirality

$$\tilde{\alpha}_{\text{ch}} = 1 - \frac{\min \left( \int_{-1}^0 |\rho^{\text{mom}}|^2 dp, \int_0^{-1} |\rho^{\text{mom}}|^2 dp \right)}{\max \left( \int_{-1}^0 |\rho^{\text{mom}}|^2 dp, \int_0^{-1} |\rho^{\text{mom}}|^2 dp \right)} \quad (4.12)$$

of the momentum distributions [compare to the wave dynamical definition of the chirality in Eq. (3.31)]. For  $\rho_1$  one obtains  $\tilde{\alpha}_{\text{ch}} = 0.932096$  and for  $\rho_2$   $\tilde{\alpha}_{\text{ch}} = 0.931519$ . In Ref. [Wiersig et al., 2011] it was shown that the chirality  $\tilde{\alpha}_{\text{ch}}$  of each single mode is related to the overlap/scalar product  $S$  of the mode pair via  $\tilde{\alpha}_{\text{ch}} = 2S/(1 + S)$ . Here, this relation is also valid for ray dynamics since  $S = |\langle \rho_1, \rho_2 \rangle|$  leads to  $\tilde{\alpha}_{\text{ch}} = 0.931766$  which is in good agreement to the chirality of each eigenstate.

Note that the eigenstates are pairwise highly non-orthogonal since e.g. the overlap  $\langle \rho_1, \rho_3 \rangle = 0.142122$  with the third eigenstate at  $\lambda_3 = 0.868647$  is much smaller than the overlap of the first pair.

## Two-mode approximation from the FPO

In the following the  $2 \times 2$  model for the phase-space dynamics of (C)CW regions is reconstructed from the full FPO. As discussed in Sec. 4.1 proper basis states representing pure (C)CW propagation in phase space are crucial for the construction of such a  $2 \times 2$  model from the ray dynamics. In the wave dynamics a proper basis of purely propagating states can be obtained from linear combinations of the modes with nearly degenerate complex frequencies [see Fig. 3.5(d)]. Now, with the nearly degenerate eigenstates  $\rho_{1/2}$  from the FPO the same ansatz is suitable for the ray dynamics: Therefore, the linear combinations

$$\rho_{\text{CCW}} = \frac{\rho_1 - \rho_2}{\mathcal{N}_{\text{CCW}}}, \quad \rho_{\text{CW}} = \frac{\rho_1 + \rho_2}{\mathcal{N}_{\text{CW}}} \quad (4.13)$$

represent proper CCW and CW basis states for the  $2 \times 2$  model. The normalization factors are given by

$$N_{\text{CCW}} = \sqrt{2[1 - \text{Re} \langle \rho_1, \rho_2 \rangle]}, \quad N_{\text{CW}} = \sqrt{2[1 + \text{Re} \langle \rho_1, \rho_2 \rangle]}. \quad (4.14)$$

The linear combinations and their momentum distributions are shown in Fig. 4.7. Indeed they represent (C)CW propagating states because they are dominantly localized either on the lower or the upper half of the phase space. Note that both linear combinations are not eigenstates of the FPO. Therefore, they are not invariant under time evolution such that the  $2 \times 2$  matrix

$$H = \begin{pmatrix} \langle \rho_{CCW}, \mathcal{F} \rho_{CCW} \rangle & \langle \rho_{CCW}, \mathcal{F} \rho_{CW} \rangle \\ \langle \rho_{CW}, \mathcal{F} \rho_{CCW} \rangle & \langle \rho_{CW}, \mathcal{F} \rho_{CW} \rangle \end{pmatrix} \quad (4.15)$$

has finite off-diagonal elements which describe the backscattering between CW and CCW regions. Due to the definition of  $\rho_{(C)CW}$  the diagonal elements in the  $2 \times 2$  matrix are the same. Using the scalar product for real  $\rho_1$  and  $\rho_2$  one can explicitly obtain the matrix elements of (4.15) in connection with the two-mode Hamiltonian (3.32) as

$$\Omega = \frac{\lambda_1 + \lambda_2}{2} \quad (4.16a)$$

$$A = \frac{\lambda_1 - \lambda_2}{2} \sqrt{\frac{1 - \langle \rho_1, \rho_2 \rangle}{1 + \langle \rho_1, \rho_2 \rangle}} \quad (4.16b)$$

$$B = \frac{\lambda_1 - \lambda_2}{2} \sqrt{\frac{1 + \langle \rho_1, \rho_2 \rangle}{1 - \langle \rho_1, \rho_2 \rangle}}. \quad (4.16c)$$

Therefore, the backscattering  $S$  in the  $2 \times 2$  Hamiltonian is

$$S = \left| \frac{A - B}{A + B} \right| = |\langle \rho_1, \rho_2 \rangle| \quad (4.17)$$

with normalized  $\rho_{1/2}$ .

The only difference to the effective Hamiltonian of the wave dynamics (3.32) is that in the matrix (4.15) the elements  $\Omega, A, B$  are real. For the Fourier-truncated spiral the matrix elements  $(\Omega, A, B) \approx (0.925249, 5.4 \cdot 10^{-5}, 7.9 \cdot 10^{-4})$  are obtained where  $B > A$  indicates that CW propagation is preferred as shown in the eigenstates. The openness is again reflected in  $\Omega + A < 1$  and  $\Omega + B < 1$ .

### Comparison to wave dynamics

Qualitatively the two largest modulus eigenstates of the FPO nicely reflect the properties of optical modes including the properties of the effective two-mode Hamiltonian. Next, the intensity pattern of the FPO eigenstates is compared to the wave dynamics. To avoid the fluctuations of a single mode the comparison is done to an average of several modes  $\Psi_{kR}$  which are in a small interval  $\text{Re } kR \in [70, 72]$ . Since the FPO eigenstates represent long-lived intensity pattern also long-lived modes should be taken into account for the comparison, i.e. modes whose  $Q$ -factor is larger than a threshold  $Q_c$ . From these modes the averaged Husimi

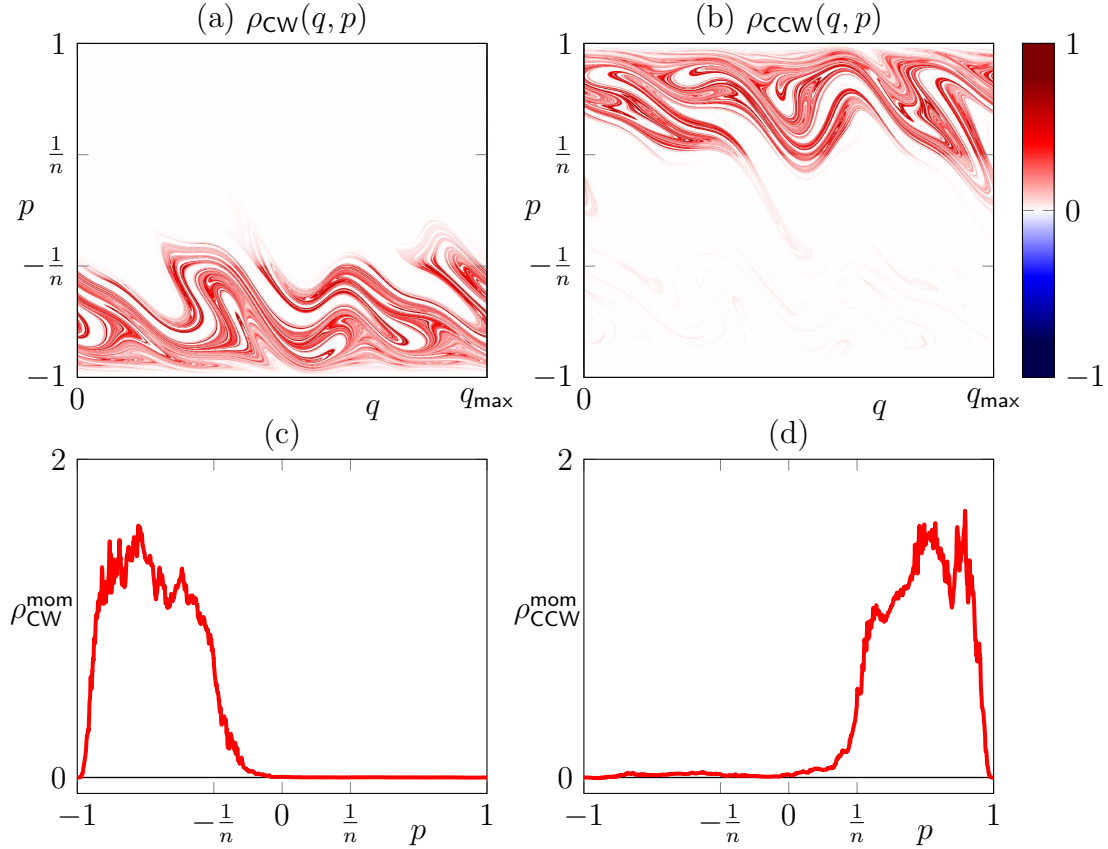


**Figure 4.7:** (a-b) The linear combinations of the FPO eigenstates (see Fig. 4.6) according to Eq. (4.13) are shown in phase space. The momentum distribution of the linear combinations are shown in (c-d) as red curves.

function

$$\bar{H}(q, p) = \frac{1}{\mathcal{N}} \sum_{\substack{kR \\ Q > Q_c}} H_0^{(\text{em})}(q, p; kR) \quad (4.18)$$

can be constructed. A rough approximation of a reasonable threshold  $Q_c$  can be obtained by comparing the wave mechanical intensity time evolution  $\|\Psi(\langle \Delta t \rangle)\|^2 = \exp[2\text{Im } kR \langle \Delta t \rangle] \|\Psi(0)\|^2$  with the FPO time evolution  $\|\mathcal{F}\rho_1\| = \lambda_1 \|\rho_1\|$  of the eigenstate  $\rho_1$ . Since  $\text{Re } kR$  is fixed to a small range this leads to  $Q_c \approx \langle \Delta t \rangle \text{Re } kR / \ln \lambda_1 \approx 1450$ . The resulting averaged Husimi function is shown in Fig. 4.8(a). The corresponding momentum distribution [similar to Eq. (4.10)] of the averaged Husimi is compared to the one of the eigenstate  $\rho_1$  in Fig. 4.8(c). The visual good agreement is also confirmed numerically by the chirality  $\tilde{\alpha}_{\text{ch}} = 0.945874$  for the averaged Husimi (compare to  $\tilde{\alpha}_{\text{ch}} = 0.932096$  for  $\rho_1$ ). As shown in Fig. 4.8(b,d) the choice of  $Q_c$  is not too restrictive since also for a slightly higher  $Q_c = 2000$  a very good agreement is observed. Here, the chirality of the averaged Husimi is  $\tilde{\alpha}_{\text{ch}} = 0.9523108$ .

Finally, a short conclusion of this section is given: In this section it was shown that the

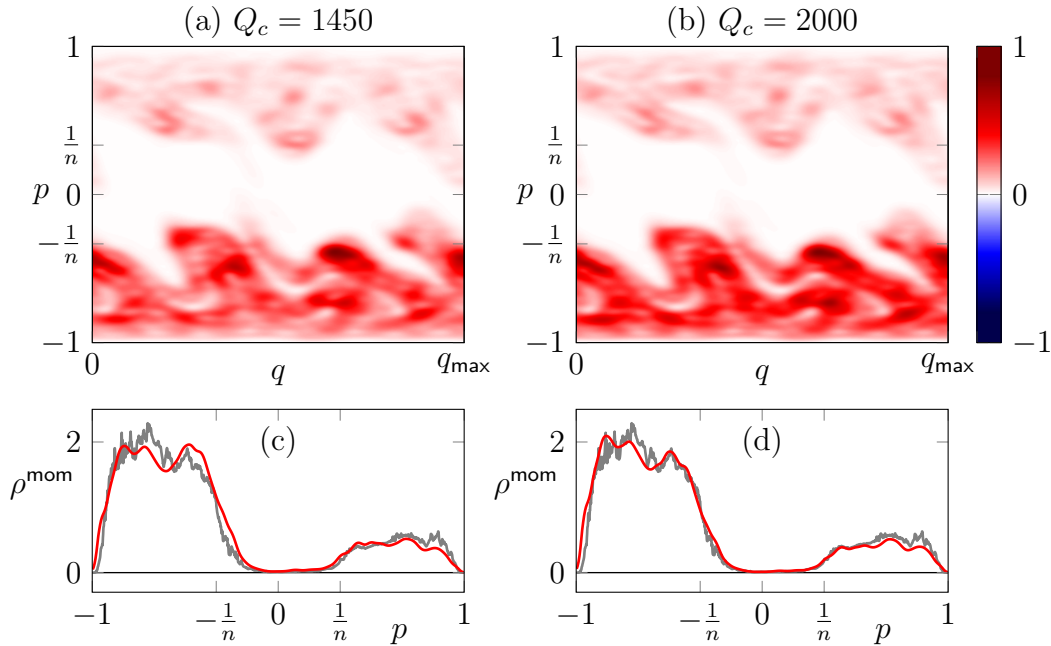


**Figure 4.8:** The averaged Husimi function, Eq. (4.18), for modes with  $\text{Re } kR \in [70, 72]$  and (a)  $Q_c = 1450$ , (b)  $Q_c = 2000$  is shown. In (c) and (d) the momentum distributions of the (red curve) averaged Husimi and the (gray curve) FPO eigenstate  $\rho_1$  are compared.

eigenstate of the FPO for microcavity are valuable to describe asymmetric backscattering in ray dynamics. The basic requirements are that the ray dynamics is dominantly chaotic and that the backscattering regarding  $p = 0$  is visible in the ray dynamics.<sup>3</sup> Then the eigenvalues of the FPO are pairwise nearly degenerate such that two largest modulus eigenvalues have to be taken into account for the long-time dynamics. The corresponding eigenstates are real and show the signatures of the asymmetric backscattering: They have the same preferred sense of rotation and they are nonorthogonal. Because of these properties it is possible to construct an effective two-mode model from the ray dynamics including a proper definition of CW and CCW states which is consistent with the wave dynamics. An overall good agreement between ray and wave calculations is given by an averaged Husimi function. In this section the results for the Fourier-truncated spiral were presented.

In the next section further aspects of the FPO and its eigenstates are discussed including variation of parameters and also counter-examples where asymmetric backscattering cannot be captured by the ray dynamics.

### 4.2.3 Application

In the last section the properties of the FPO eigenstates regarding asymmetric backscattering were the main issue. In this section now further applications of the FPO for microdisk cavities

<sup>3</sup>A counter-example is the billiard of constant width which is discussed below in Sec. 4.2.3. Note also the comment in Appendix A.2.3 for the backscattering regarding  $L_z = 0$ .

are discussed.

### Symmetric deformations

The construction of the FPO matrix is also possible for symmetrically deformed cavities; i.e. cavities that exhibit at least one mirror-reflection symmetry (for simplicity the  $x$ -axis). Here, the symmetry in the billiard mapping, see Sec. 2.2.2, can be incorporated in the construction of the FPO matrix: Whenever a random initial condition is iterated from cell  $j$  to  $i$  also the symmetry related orbit from cell  $i' = N_{\text{grid}}^2 + 1 - i$  to  $j' = N_{\text{grid}}^2 + 1 - j$  is taken into account ( $i, j = 1, \dots, N_{\text{grid}}^2$ ). Finally, the FPO matrix has a sparse block structure

$$\mathcal{F} = \begin{pmatrix} \mathbf{CCW} & \mathbf{A} \\ \mathbf{B} & \mathbf{CW} \end{pmatrix} \quad (4.19)$$

where the elements are related via

$$\mathcal{F}[j, i] = \mathcal{F}[N_{\text{grid}}^2 + 1 - j, N_{\text{grid}}^2 + 1 - i] \equiv \mathcal{F}[-i, -j]. \quad (4.20)$$

Such a matrix is called centrosymmetric matrix. For even  $N_{\text{grid}}^2$  it yields  $\mathbf{CW} = \mathbf{JCCWJ}$  and  $\mathbf{A} = \mathbf{JBJ}$  with  $\mathbf{J} = (\delta_{i, N_{\text{grid}}^2 + 1 - j})_{i,j}$  having unity elements in the counter-diagonal only. Since the sub-matrices  $\mathbf{A}$  and  $\mathbf{B}$  have nonzero elements a backscattering between CW and CCW regions in phase space is observed. However, due to the relation (4.20) the backscattering is symmetric and therefore also the eigenstates of the FPO are symmetric with  $|\rho(q, p)| = |\rho(q_{\text{max}} - q, -p)|$ .

### Far-field emission from the eigenstates

In Sec. 2.3.2 it was shown that each point  $(q, p)$  in phase space with intensity  $I$  represent an emerging ray from the cavity's boundary that can contribute to the far-field intensity pattern  $|F(\phi)|^2$  via the transmitted intensity  $[1 - R(\tilde{p})]I$  at  $(\tilde{s}, \tilde{p})$ , see Fig. 2.9(a). Since the eigenstates of the FPO represent such an intensity distribution in phase space it is possible to construct the far-field intensity pattern from the FPO eigenstates. To this end each cell  $i$  in phase space is presented by its midpoint  $(q_i, p_i)$  and the intensity  $\rho_1(q_i, p_i)$  of the eigenstate with largest modulus eigenvalue. Summation over the contributions from each cells in phase space results in the far-field pattern shown in Fig. 4.9 for the Fourier-truncated spiral.

### Regular islands in a mixed phase space

Although, for the construction of the FPO matrix it was assumed that the ray dynamics inside the cavity is almost chaotic it is an interesting question what results can be obtained for a mixed phase space. As an example here the Limaçon with  $\epsilon = 0.3$  is treated where three

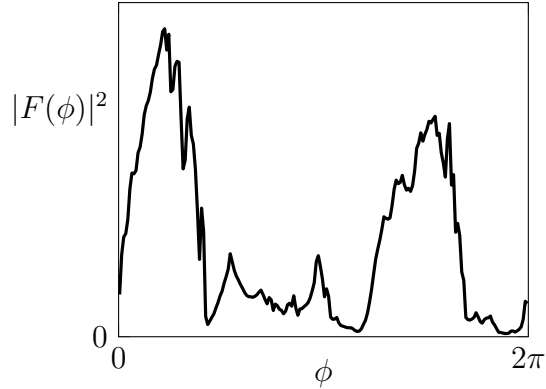


**Figure 4.9:** The (normalized) far-field emission pattern of FPO eigenstate  $\rho_1$  [see Fig. 4.6(a)] for the Fourier-truncated spiral with  $(\epsilon, N_p, \delta, n) = (0.07, 4, 1, 3.0)$  is shown.

large islands are observable in the phase space around  $p = 0.5$ . For  $n = 3.0$  these regular islands have no overlap with the leaky region such that rays are trapped infinitely long in the island without losing any intensity. Therefore the long-lived eigenstates of the FPO localize at these regular island as shown in Fig. 4.10(b-c). However, the eigenvalue of the corresponding eigenstate do not reflect any proper intensity decay in sense that  $|\lambda| > 1$  is obtained, see Fig. 4.10(a). The origin for this is the rescaling of the intensity transport with time weighting factor  $T_{ij}$ , see Eq. (4.7): For quite long periodic orbits with large  $\Delta t_{ij}$  the matrix  $T_{ij}$  effectively leads to an artificial amplification of the transport  $I(i \rightarrow j)$ . However, the largest modulus eigenvalues are still on the real axis and occur in pairs. Also the order of the eigenvalue pairs is reasonable: The first eigenstate from the largest modulus eigenvalue pair [Fig. 4.10(b)] shows a simple localization on the island while the eigenstate of the second-largest pair [Fig. 4.10(c)] and of the third-largest pair [Fig. 4.10(d)] correspond to “excited states” of the island. Note that these excited eigenstates also change their sign inside the island. The localization of FPO eigenstates on regular phase-space structures was also observed in Ref. [Weber et al., 2000, Weber et al., 2001] for Hamiltonian maps with a mixed phase space.

It is mentioned here that in Ref. [Frahm and Shepelyansky, 2010] a slight modification to the Ulam’s method for the FPO was introduced which is valuable if one is interested only in the chaotic component of a mixed system: Instead of iterating many random initial conditions to get the intensity transport from cell  $i$  to  $j$  one follows one single chaotic trajectory for a long time to compute  $I(i \rightarrow j)$ . This single trajectory does not penetrate the regular regions which are therefore omitted in the FPO matrix.

### Connection to extended ray dynamics

So far the FPO is based on ordinary ray dynamics which does not depend on  $kR$ . Next, it is discussed how extended ray dynamics effect the eigenstates and eigenvalues of the FPO for a

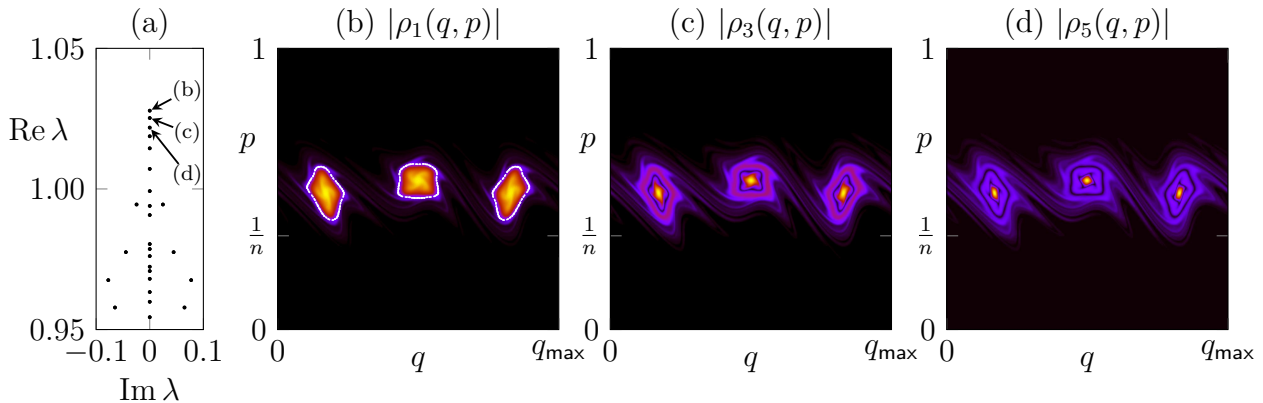


**Figure 4.10:** (a) The eigenvalues of the FPO ( $N_{\text{grid}} = 600$ ) for a Limaçon with  $(\epsilon, n) = (0.3, 3.0)$  are shown in complex plane. (b-d) The modulus of the eigenstates to the eigenvalues labeled in (a) are shown in phase space. They localize at the period three regular islands which is illustrated by the (white dots) orbit shown in (b).

finite  $kR$ .<sup>4</sup> First, the Goos-Hänchen (GH) shift  $\Delta q_{\text{GH}}$  [see Sec. 3.4.2] is applied on top of the billiard dynamics. Here, the numerical model for the GH shift from Ref. [Unterhinninghofen and Wiersig, 2010] is used which results in  $\Delta q_{\text{GH}}$  shown in Fig. 4.11(a) for  $n = 3.0$ . The long-lived eigenstate  $\rho_1(q, p)$  of the Fourier-truncated spiral with incorporated GH shift are shown in Fig. 4.11(c-d). The intensity pattern look similar to the one obtained from ordinary ray dynamics. However, the detailed phase space structures are blurred for smaller  $kR$ . Nevertheless, the momentum distribution of the eigenstates shown in Fig. 4.11(b) are almost identical for all values of  $kR$ . Therefore also the asymmetry in the backscattering, i.e. the overlap  $S = |\langle \rho_1, \rho_2 \rangle|$  and the eigenvalues  $\lambda_{1/2}$  do not change much with  $kR$ , see Tab. 4.3: For small  $kR$  just a slightly smaller asymmetry is noticeable.

$kR$ for GH	$\lambda_1$	$\lambda_2$	$S$
5	0.934473	0.934308	0.849765
10	0.926056	0.925811	0.864740
20	0.925717	0.925360	0.871597
30	0.925732	0.925357	0.887056
40	0.925717	0.925339	0.883398

**Table 4.3:** Eigenvalues  $\lambda_{1/2}$  and overlap  $S = |\langle \rho_1, \rho_2 \rangle|$  for the FPO eigenstates for the Fourier-truncated spiral with  $(\epsilon, N_p, n, N_{\text{grid}}) = (0.07, 4, 3.0, 1600)$  and additional GH shift.

In Ref. [Hentschel and Schomerus, 2002] it is shown that a curved interface effectively changes the reflection law to become smooth and  $kR$  depended as shown in Fig. 4.11(e). However, this modified reflection law also does not perturb the FPO eigenstates strongly as shown in the phase space pattern in Fig. 4.11(f) and in the momentum distribution [dashed curve in

<sup>4</sup>Note that the  $kR$  dependent corrections to the billiard dynamics vanish for  $kR \rightarrow \infty$ .



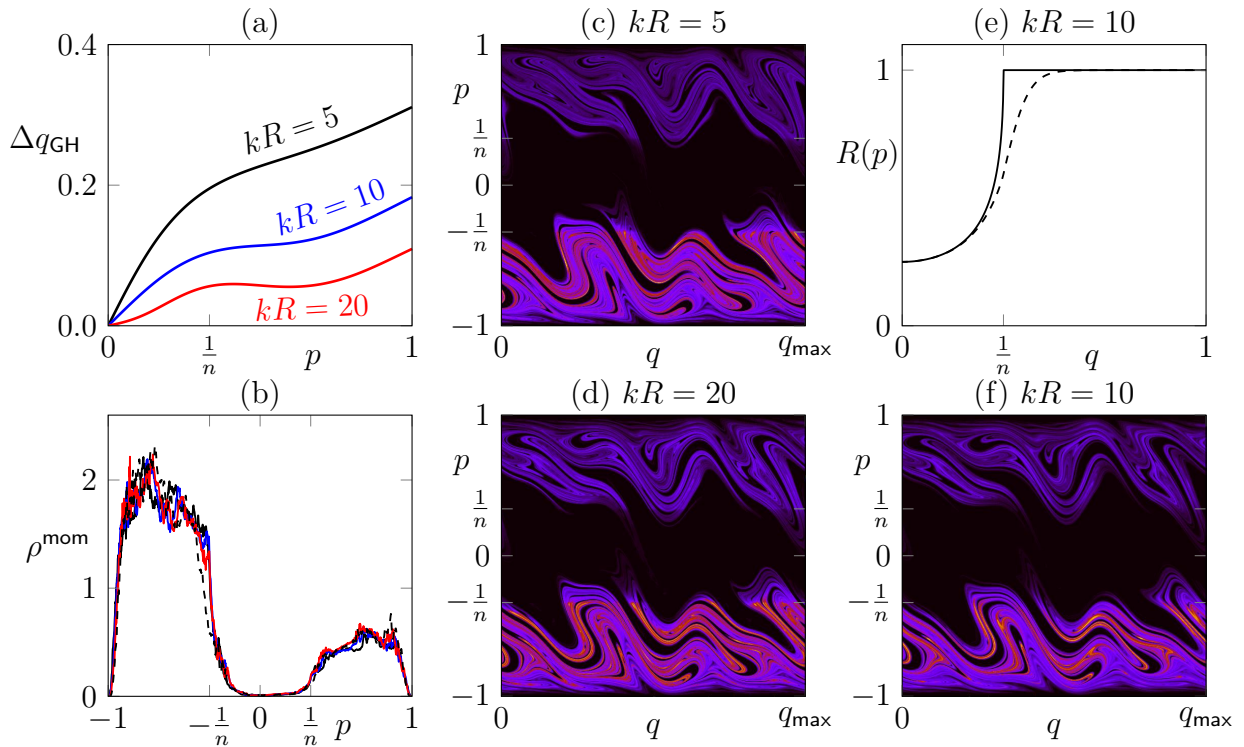


**Figure 4.11:** (a) The GH shift obtained numerically from the method presented in Ref. [Unterhinninghofen and Wiersig, 2010] for different values of  $kR$  and  $n = 3$ . In (b) the momentum distributions of the FPO eigenstate with largest modulus eigenvalue for the Fourier-truncated spiral with  $(\epsilon, N_p, n, N_{\text{grid}}) = (0.07, 4, 3.0, 1600)$  are shown: Solid curves represent the eigenstates with implemented GH shift [color according to (a)] and the black dashed curve is obtained from the implementation of the modified reflection law for curved interfaces. The phase space representation of the long-lived FPO eigenstate is shown for (c) a GH shift according  $kR = 5$ , (d) a GH shift according  $kR = 20$ , and (f) the modified reflection law for  $kR = 10$ . (e) Comparison of the (dashed curve) modified reflection law [Hentschel and Schomerus, 2002] with the (solid curve) Fresnel reflection law for TM polarization.

Fig. 4.11(b)].<sup>5</sup> Therefore it is expected that also more elaborated models for  $\Delta q_{\text{GH}}$  as in Ref. [Stockschlader et al., 2014] which properly account for the curved interface of the cavity do not change the eigenstates of the FPO drastically.

Note again that the eigenstates of the FPO are intensity distributions and also the FPO itself iterates intensity distributions. Therefore, the Fresnel filtering, which has its origin in the time evolution of intensity distributions (see Sec. 3.4), is already captured by the FPO. Moreover, in Ref. [Unterhinninghofen, 2011] it is shown that the incorporation of the Fresnel filtering into the dynamics of a single ray does not change the unstable manifold much. Therefore, additional effects of Fresnel filtering can be omitted here.

However, an interesting consequence of the GH shift was discussed in Ref. [Unterhinninghofen and Wiersig, 2010]: The GH shift  $\Delta q_{\text{GH}}$  effectively also shifts a periodic orbit in  $p$  which is

<sup>5</sup>The modified reflection coefficient is usually smaller than the one from the Fresnel law therefore the eigenvalue of the long-lived FPO eigenstate pair is slightly reduced to  $\lambda \approx 0.902$ .

called periodic orbit shift (POS,  $\Delta p_{\text{POS}}$ ). To illustrate this effect of the POS in the FPO eigenstates it is practical to use a system where the eigenstates localize at the regular region around a periodic orbit, e.g. the Limaçon at  $\epsilon = 0.3$  which was discussed above [see Fig. 4.10(b)]. As shown in Fig. 4.12 the GH shift indeed shifts the localization of the eigenstate in  $q$  but also in  $p$  what is exactly the POS. Furthermore, the eigenstates show a strong leakage to the chaotic part of the phase space e.g. for  $kR = 10$  where the corrections to the ordinary ray dynamics are strong. This is in good agreement to the fact that the GH shift breaks some tori of the regular island resulting in a larger chaotic component of the phase space.

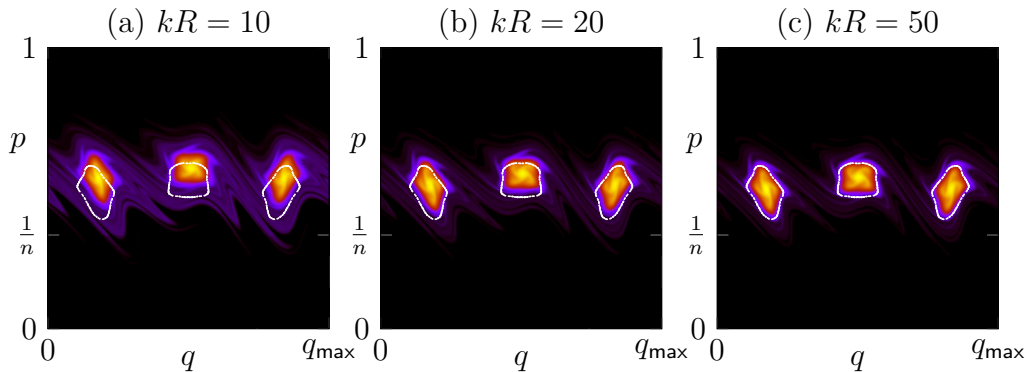


**Figure 4.12:** The eigenstates of the largest modulus eigenvalue of the FPO for the Limaçon with  $(\epsilon, n, N_{\text{grid}}) = (0.3, 3.0, 600)$  are shown for different  $kR$  depended GH shifts. The regular island from ordinary ray dynamics is shown in white.

However, for increasing  $kR \rightarrow \infty$  the effects of the GH shift and the POS vanish again such that already for  $kR = 50$  the localization at the island obtained from ordinary ray dynamics is almost restored, see Fig. 4.12(c). Consequently, the GH shift and the POS do not effect the comparison to the ray dynamics illustrated by the averaged Husimi function in Sec. 4.2.2 [Fig. 4.8] which was obtained for  $kR \approx 70$ .

### Asymmetry parameter of the Fourier-truncated spiral

In Sec. 4.1 it was shown that with increasing asymmetry parameter  $\delta$  the asymmetry in the backscattering of uniform intensity distributions also increases. However, the eigenstates of the FPO represent special long-lived intensity distributions such that the backscattering with increasing  $\delta$  is slightly different. In Fig. 4.13 the effects from a variation of  $\delta$  to the FPO eigenstates are presented. For  $\delta = 0$  the cavity is symmetric. Therefore also the eigenstates of the FPO are symmetric with vanishing  $S = |\langle \rho_1, \rho_2 \rangle|$ , see cyan curve/dot in Fig. 4.13(a/c). With slightly increasing  $\delta$  also the FPO eigenstates show the expected increasing asymmetry. At  $\delta \approx 0.3$  a smaller interruption occurs which is may due to very small regular structures in phase space. However, around the golden mean  $\delta = (\sqrt{5}-1)/2 \approx 0.618$  the asymmetry reaches a maximum (orange curve/dot) and surprisingly decreases afterwards. The eigenvalues of the

long-lived eigenstates, see Fig. 4.13(b), decrease with increasing parameter  $\delta$  (except a small fluctuation at  $\delta = 0.8$ ), i.e. also the long-lived states become more lossy with increasing  $\delta$ .

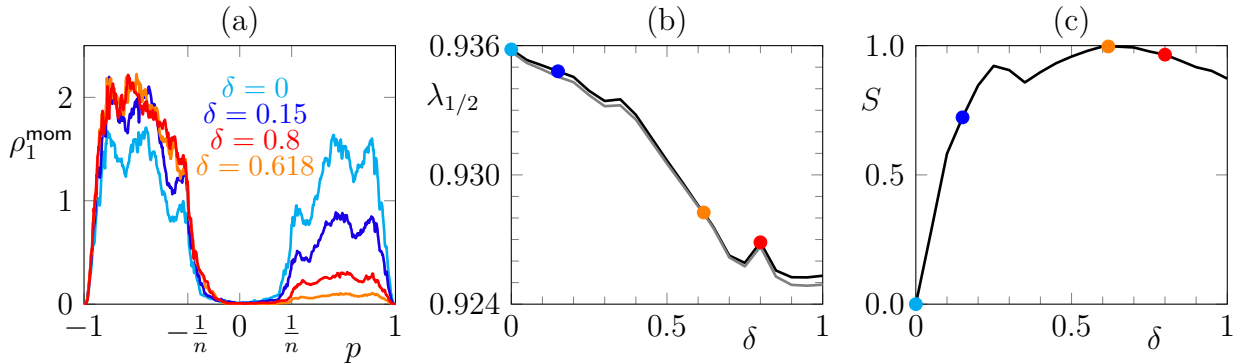


**Figure 4.13:** Variation of the asymmetry parameter  $\delta$  in the Fourier-truncated spiral, see Eq. (A.14). In (a) the momentum distribution of the eigenstate with largest modulus eigenvalue is shown for different values of  $\delta$ . In (b) the largest (black curve) and second largest (gray curve) eigenvalue is plotted versus  $\delta$ . The overlap  $S = |\langle \rho_1, \rho_2 \rangle|$  of the first and the second eigenstate is shown in (c). In (b-c) colored dots represent the states shown in (a). Other parameters are fixed to  $(\epsilon, n, N_p, N_{\text{grid}}) = (0.07, 3.0, 4, 1000)$ .

### The refractive index and TE polarization

In the next step the properties of the leaky region are changed. Therefore, first, the refractive index  $n$  is varied. As demonstration example serves again the Fourier-truncated spiral with  $(\epsilon, N_p, \delta) = (0.07, 4, 1)$  where the both eigenstates of the FPO with largest modulus are shown in Fig. 4.14 for a varying refractive index  $n$ . Obviously with increasing  $n$  the leaky region becomes smaller such that the eigenstates spread over a larger fraction of the phase space. Furthermore, with increasing refractive index the asymmetry in the eigenstates, i.e. the asymmetric backscattering, is getting weaker. In the concrete example the fraction of intensity in the upper half of the phase space rises in comparison to the intensity in the lower half. Note that when the leaky region gets smaller the unstable manifold from the upper half of the phase space meanders into the lower half of the phase space (and vice versa). This can be seen well e.g. in Fig. 4.14(h) where the eigenstate  $\rho_2$  has also some negative (blue) tails in the lower phase space half. Therefore, for these high refractive indexes it is again controversial if the line  $p = 0$  is a proper ray dynamical criterion to separate CW and CCW propagation or if the linear combinations of  $\rho_1$  and  $\rho_2$ , see Eqs. (4.13), are a rather better choice, especially if one compares the eigenstates to optical modes.

Note that since the leaky region is getting smaller also the largest modulus eigenvalue of the FPO increases from  $\lambda_1 \approx 0.9407$  for  $n = 3.5$  to  $\lambda_1 \approx 0.9637$  for  $n = 5$ .

It is mentioned that also results for smaller refractive indexes are obtained (not shown). However, for  $n \lesssim 2.5$  the coupling of the upper and the lower half of the phase space is very weak

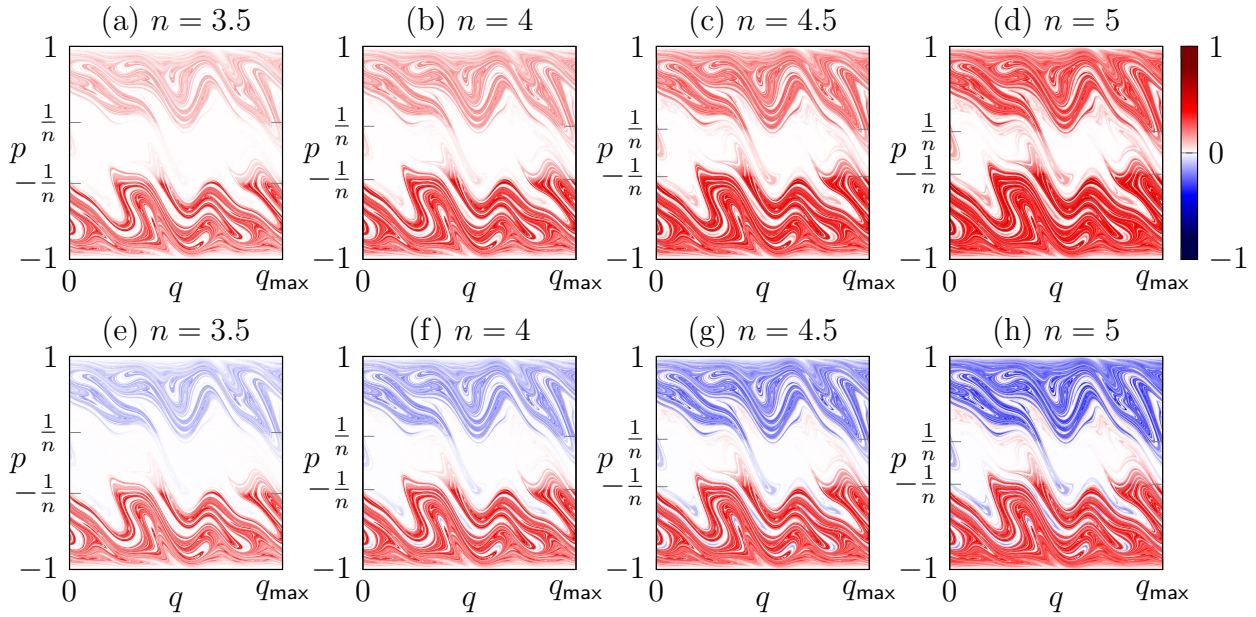


**Figure 4.14:** The eigenstate of the FPO with (a-d) largest and (e-h) second-largest eigenvalue modulus are shown in the phase space of the Fourier-truncated spiral with  $(\epsilon, \delta, N_p, N_{\text{grid}}) = (0.07, 1, 4, 1600)$  and varying refractive index  $n$ .

due to a small reflectivity in the large leaky region. Therefore the numerical diagonalization of the sparse FPO matrix is getting more and more elaborated and one needs to iterate a larger number of trajectories to obtain accurate matrix elements.

Additionally, also the FPO eigenstates for TE polarization have been analyzed. In principle they look quite similar to the ones for TM polarization. In particular they also come in pairs with finite chirality and copropagation in CW direction (for the Fourier-truncated spiral), see Fig. 4.15 for the momentum distribution of  $\rho_{1/2}$ . However, the following differences are remarkable: (i) Since the reflectivity in the leaky region for TE polarization is smaller than for TM polarization, also the weight of the eigenstate inside the leaky region is much smaller. (ii) For TE polarization the reflectivity  $R(p)$  is zero at Brewster's angle  $p = \pm 1/\sqrt{n^2 + 1}$ . The eigenstates of the FPO also show this characteristic root as indicated by the arrows in Fig. 4.15. (iii) The overlap  $S = |\langle \rho_1, \rho_2 \rangle| = 0.9526$  is slightly larger than for TM polarization.

### Billiard of constant width

Next, an example of an asymmetric cavity is discussed where the FPO eigenstates cannot describe the asymmetric backscattering: The billiard of constant width [Gutkin, 2007]. This cavity is parametrized with  $\alpha \in [0, 2\pi)$  in the  $x$ - $y$  plane via the complex variable

$$z(\alpha) = x(\alpha) + iy(\alpha) = z(0) - i \sum_{n \in \mathbb{Z}} \frac{a_n}{n+1} (e^{i(n+1)\alpha} - 1). \quad (4.21)$$

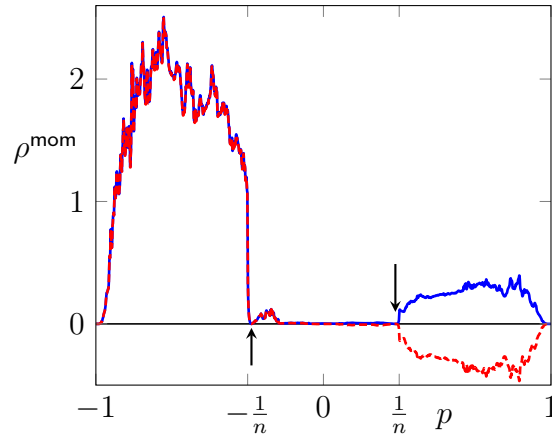


**Figure 4.15:** Momentum distribution of the eigenstates with (blue solid curve) largest and (red dashed curve) second largest modulus eigenvalue in case of TE polarization. The system is the Fourier-truncated spiral with  $(\epsilon, \delta, n, N_{\text{grid}}) = (0.07, 1, 3.0, 1600)$ . The arrows at  $p = \pm 1/\sqrt{n^2 + 1}$  mark Brewster's angle.

In Ref. [Wiersig et al., 2011] it has been shown that for  $[z(0), a_0, a_3, a_5] = R[1/4 - i, 1, i/8, (i + 1)/4]$ , and  $a_{-n} = a_n^*$ , and vanishing  $a_n$  for  $n \notin \{0, \pm 3, \pm 5\}$  the cavity violates any mirror-reflection symmetry [see Fig. 4.16(a)] and exhibits asymmetric backscattering in wave dynamics. However, in the ray dynamics backscattering regarding the line  $p = 0$  is not possible since this line is an invariant curve in phase space which cannot be crossed by a ray orbit. Since there is no coupling of CW and CCW propagation (regarding  $p = 0$ ) in ray dynamics the finite FPO matrix has the block structure

$$\mathcal{F} = \begin{pmatrix} \mathbf{CCW} & 0 \\ 0 & \mathbf{CW} \end{pmatrix} \quad (4.22)$$

where, due to the asymmetry of the boundary, the sub-matrix  $\mathbf{CCW}$  is not related to the sub-matrix  $\mathbf{CW}$ . Therefore the eigenstate intensity pattern, see Fig. 4.16(c-d), is different in the upper and lower half of the phase space. Note that the eigenvalues obtained numerically for  $N_{\text{grid}} = 1200$  are  $\lambda_1 = 0.863792$  and  $\lambda_2 = 0.863788$  such that the difference  $\lambda_1 - \lambda_2$  is of the order  $10^{-6}$ . Since the matrix elements are calculated from a finite set of initial conditions and also the diagonalization is done only approximately (with the Arnoldi method), it is likely that this small splitting is just a numerical artifact and that the actual eigenvalues of the infinite FPO are degenerate. Hence, no effective two-mode Hamiltonian for the asymmetric backscattering [see Eq. (4.15)] can be obtained from the FPO eigenstates in this case.

### Artificial asymmetry in symmetric cavities

In this section it is discussed that also symmetric cavities can exhibit asymmetric backscattering if they are perturbed locally such that the mirror-reflection symmetry is destroyed. In

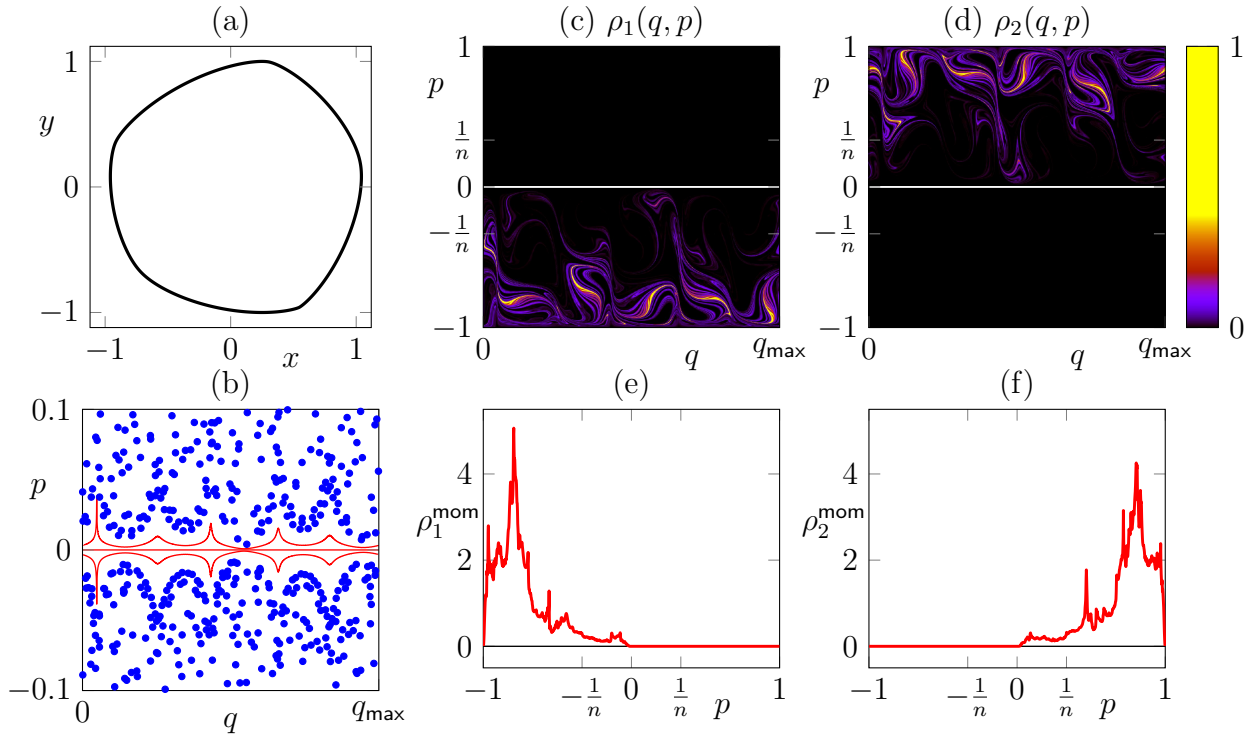


**Figure 4.16:** (a) A black curve illustrates the boundary of the constant width billiard, see Eq. (4.21) with parameters as in the text. (b) The phase space dynamics near  $p = 0$  with (red) regular curves and (blue) chaotic orbits is shown in phase space. (c-d) The first and second eigenstate of the FPO are shown in phase space for  $(N_{\text{grid}}, n) = (1200, 3.0)$ . A white line indicates  $p = 0$ . (e-f) The momentum distribution of the eigenstates, see Eq. (4.10), is shown as red curve.

an recent experiment [Redding et al., 2012] such local asymmetric perturbation was realized by placing a waveguide close to a symmetric Limaçon cavity. Depending on the position of the waveguide along the cavity’s boundary the output is either dominated by CW or by CCW traveling waves.

Since the ray dynamics does not “see” the waveguide outside the cavity one needs to model such external perturbations effectively. Here this is done by an artificial local change of the reflection coefficient as illustrated in Fig. 4.17(a). The purpose of this part is not to model the coupling to a waveguide exactly but to show that such a small perturbation in general lead to asymmetric backscattering in the ray dynamics. Therefore the reflectivity of the red phase space region in Fig. 4.17(a) is simply set to zero. Hence, the symmetry in the ray dynamics of the Limaçon is broken and the eigenstates of the FPO matrix show the signatures of asymmetric backscattering as illustrated in Fig. 4.17: In (b) it is shown that the long-lived FPO eigenstate pair indeed has a finite overlap; i.e. a finite chirality [as also seen in the intensity pattern (d-f)] depending on the position  $q_{\text{PT}}$  of the perturbation along the cavity’s interface. Furthermore, the splitting  $\Delta\lambda$  of the largest modulus eigenvalue pair is small whenever  $|S|$  is large, i.e. whenever the eigenstates  $\rho_{1/2}$  become copropagating. Note that symmetry arguments

can be exploited to restrict  $q_{\text{PT}} \in [0, q_{\text{max}}/2]$ .

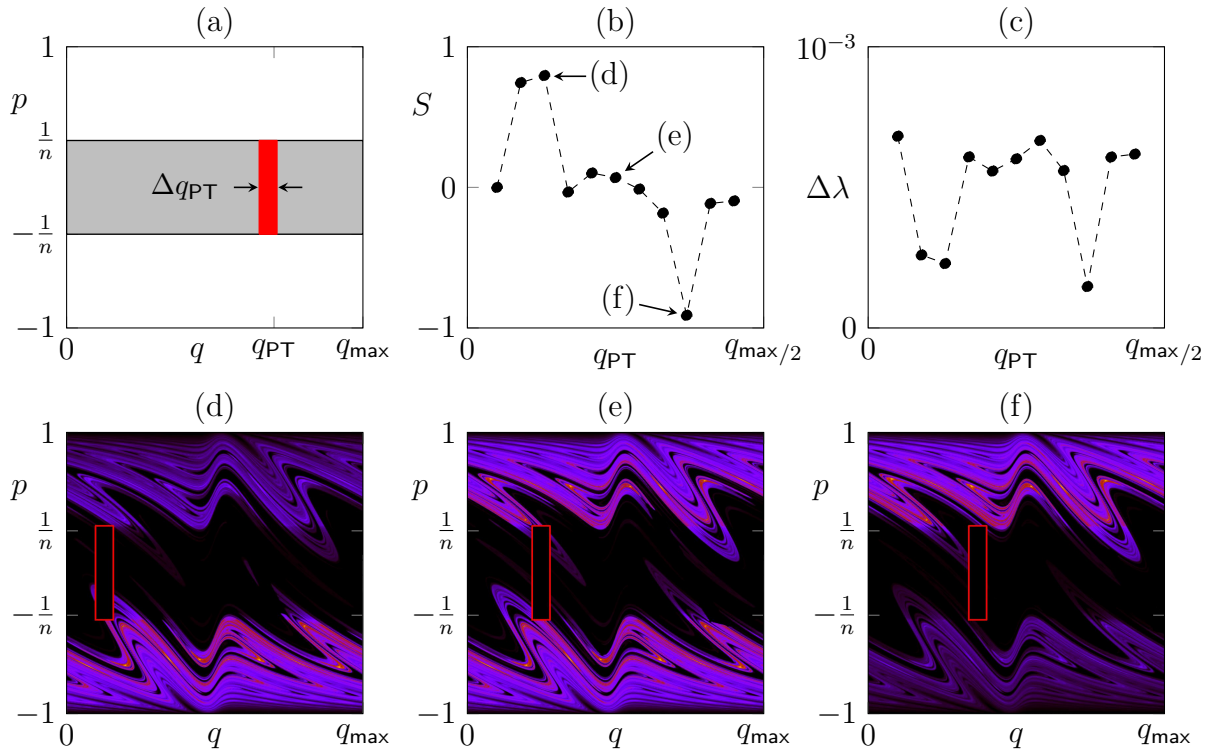


**Figure 4.17:** In (a) the artificial asymmetric perturbation of the Limaçon is illustrated in phase space: The reflectivity in the gray leaky region is given by the reflection law (2.23a) and in the red region the reflectivity is set to zero. (b) The normalized overlap  $S = \langle \rho_1, \rho_2 \rangle$  of the long-lived FPO eigenstate pair is shown by black dots. (c) The splitting  $\Delta\lambda = \lambda_1 - \lambda_2$  of the largest modulus eigenvalue pair is plotted. (d-e) The phase space pattern of the eigenstate with largest modulus is shown for different  $q_{\text{PT}}$ . The red frame illustrates the region where the reflection law is modified. The parameters are fixed to  $(\epsilon, n, N_{\text{grid}}, \Delta q_{\text{PT}}) = (0.5, 3.0, 600, 0.06 q_{\text{max}})$ .

However for a comparison to experimental data a more elaborated modeling of the external perturbation (e.g. the waveguide) is necessary which may change the dependency  $S(q_{\text{PT}})$  shown in the figure.

### The spiral cavity

Another well known example for an asymmetric cavity is the spiral, see Eq. 2.19. Here, Lee *et al.* [Lee et al., 2008a, Lee et al., 2004] have shown that the classical ray-survival probability is larger in one half of the phase space than in the other. This can be interpreted such that the spiral exhibits a finite chirality in the ray dynamics. This finite chirality is also reflected in the eigenstates of the FPO which are shown in Fig. 4.18 for a spiral with  $(\epsilon, n) = (0.04, 3.3)$ . Here, almost all intensity of the first and the second eigenstate is located in the upper half of the phase space. In the momentum distributions of the eigenstates  $\rho_{1/2}$  [see Fig. 4.18(c-d)] it can be seen that a small fraction of the intensity is also in the lower half of the phase space and that

the second eigenstate shows the characteristic change of the sign. However, in the spiral the asymmetry in the backscattering is extremely large such that the numerical approximation of the FPO and the numerical diagonalization of the corresponding sparse matrix is problematic: The difference between largest  $\lambda_1 = 0.902020$  and second-largest  $\lambda_2 = 0.901993$  eigenvalue is quite small such that it may cannot be captured exactly by approximative diagonalization algorithms for sparse matrices. Consequently, also the numerically determined eigenstates suffer from this inaccuracy which manifests e.g. in different weights between  $\rho_1$  and  $\rho_2$  in the lower half of the phase space [see magnifications in Fig. 4.18(c-d)]. Except for these numerical problems the overall shape of the eigenstates is in good agreement with the survival probability shown in Ref. [Lee et al., 2008a].

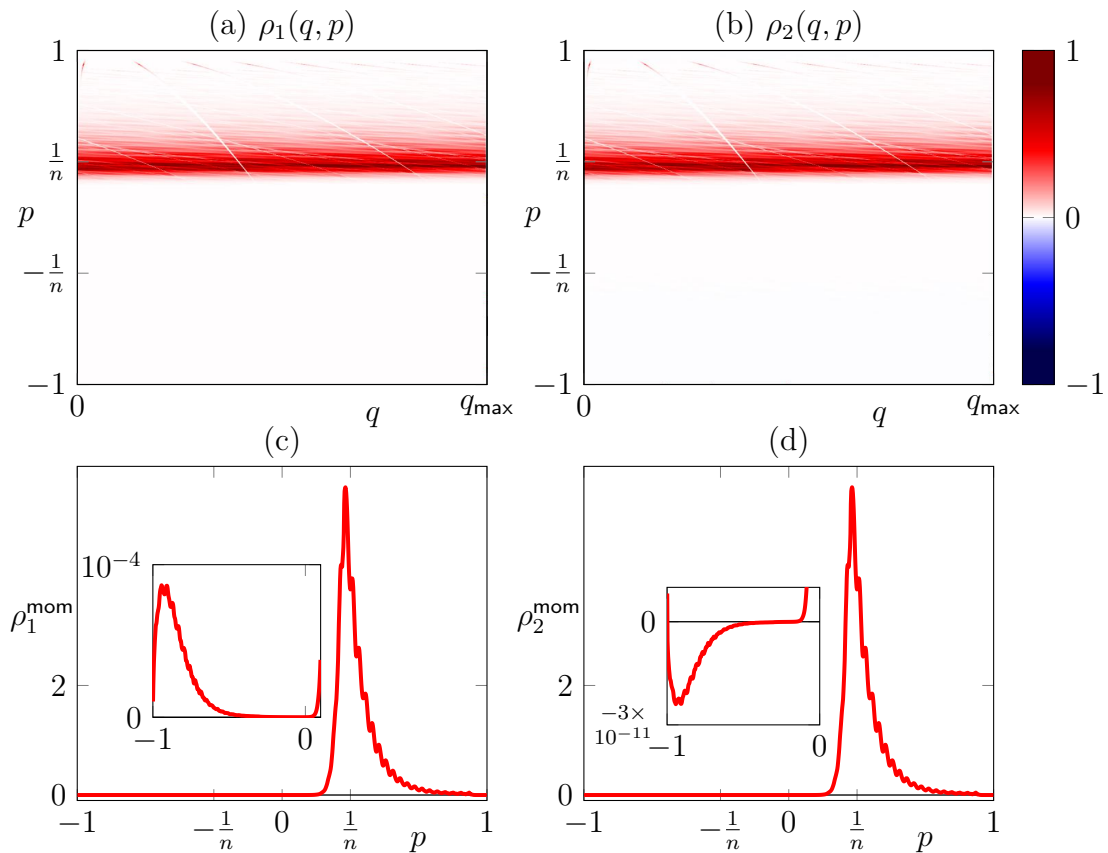


**Figure 4.18:** The eigenstate of the FPO matrix with (a) the largest and (b) the second-largest eigenvalue modulus are shown in phase space. The corresponding momentum representations are shown in (c) and (d) as red curve.

### 4.3 1D model for asymmetric backscattering

In this section a toy model with asymmetric backscattering in one dimension is constructed. For this toy model the FPO eigenvalue problem can be solved analytically and the eigen-



states show all signatures of asymmetric intensity backscattering including non-orthogonality, chirality, and copropagation.

The dynamics of the toy model take place in the interval  $[-1, 1]$ . It is given in three steps that are illustrated in Fig. 4.19. First, random dynamics take place in each of the two separated intervals  $[-1, 0)$  and  $[0, 1]$  [see Fig. 4.19(a)]. In comparison to microcavities this should symbolize the chaoticity of the billiard dynamics in the lower and the upper part of the phase space. Afterwards the two separated regions are coupled via an exchange of interval  $[-a, 0)$  and  $[0, a]$  with  $0 < a \ll 1$  [see Fig. 4.19(b)], which symbolizes the backscattering between CW and CCW regions in phase space. In a third step the intensity in the interval  $[-a, a]$  is reduced by a function  $R(x)$  [see Fig. 4.19(c)]. In contrast to the reflectivity in a microcavity here it is assumed that the function  $R(x)$  itself is asymmetric in the region of exchange  $[-a, a]$  such that

$$A = \int_{-a}^0 R(x) dx \neq \int_0^a R(x) dx = B. \quad (4.23)$$

Here,  $A$  and  $B$  quantify the intensity which is scattered from  $[-1, 0)$  to  $[0, 1]$  and vice versa. The fraction of intensity which remains in either  $[-1, -a)$  or  $[a, 1]$  is given by

$$\Omega = \int_a^1 R(x) dx = 1 - a. \quad (4.24)$$

Thus, the time evolution of a given intensity  $\rho(x)$  for one time step is given by

$$\mathcal{F}\rho(x) = R(x) \begin{cases} \langle \rho \rangle_1 & \text{for } x \in [-1, -a) \cup [0, a] \\ \langle \rho \rangle_2 & \text{for } x \in [-a, 0) \cup (a, 1] \end{cases} \quad (4.25)$$

where  $\langle \rho \rangle_1$  denote the average of  $\rho$  in the interval  $[-1, 0)$  and  $\langle \rho \rangle_2$  is the average of  $\rho$  in the interval  $[0, 1]$ . These averages are a result from instantaneous mixing random dynamics in the separated intervals.

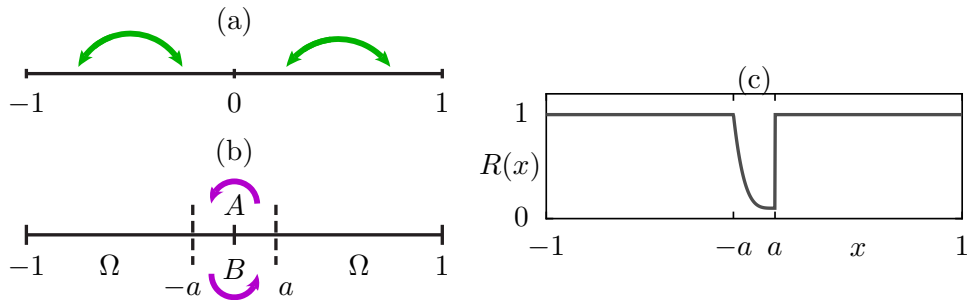


**Figure 4.19:** The three steps of the dynamics in the 1D model are illustrated: (a) green/gray arrows for the random dynamics in the separated intervals, (b) illustration of backscattering via an exchange of intervals and (c) the reflectivity function  $R(x)$  defined by Eq. (4.28).

The eigenvalue problem  $\mathcal{F}\rho = \lambda\rho$  of the FPO is solved in the following with the ansatz

$$\rho(x) = R(x) \begin{cases} C_1 & \text{for } x \in [-1, -a) \cup [0, a] \\ C_2 & \text{for } x \in [-a, 0) \cup (a, 1] \end{cases} \quad (4.26)$$

where  $C_1$  and  $C_2$  are constants to be determined. Applying  $\mathcal{F}$  given by Eq. (4.25) and comparing both sides of the eigenvalue problem it yields

$$\begin{pmatrix} \Omega & A \\ B & \Omega \end{pmatrix} \begin{pmatrix} C_1 \\ C_2 \end{pmatrix} = \lambda \begin{pmatrix} C_1 \\ C_2 \end{pmatrix}. \quad (4.27)$$

This equation is the equivalent to the eigenvalue problem of the two-mode model in Eq. (3.32). Hence, the FPO for the 1D model has two eigenvalues  $\lambda_{1,2} = \Omega \pm \sqrt{AB}$  and two normalized eigenstates  $\rho_{1,2}$  given by Eq. (4.26) with  $(C_1, C_2) = (\sqrt{A}, \pm\sqrt{B})/\sqrt{|A| + |B|}$ .

For an illustration of the dynamics in the 1D toy model in the following  $R(x)$  is specified to

$$R(x) = \begin{cases} 0.9(x-a)^4/(2a)^4 + 0.1 & \text{for } |x| < a \\ 1 & \text{else} \end{cases} \quad (4.28)$$

and  $a = 0.1$  is fixed. Therefore,  $A = 0.044875$ ,  $B = 0.011125$ , and  $\Omega = 0.9$  is obtained which results in  $\lambda_1 \approx 0.922$  and  $\lambda_2 \approx 0.878$ . The eigenstates and the eigenvalues of the FPO are shown in Fig. 4.20. Both eigenstates are localized dominantly in the interval  $[-1, 0)$ . Therefore, they exhibit a finite chirality and they are significantly non-orthogonal with a normalized overlap  $S = (A - B)/(A + B) \approx 0.6$ . Furthermore, the second eigenstate shows the characteristic flip of the sign.

Next, the analytical results are confirmed by the construction and diagonalization of a random matrix as approximation of the FPO. The construction of the  $2N \times 2N$  matrix  $\mathcal{F}_{ij}$  is explained in the following: Suppose the interval  $[-1, 1]$  is sampled with points  $x_i = -1 + i/N$  with  $i = 0, 1, \dots, 2N$  then the finite matrix  $\mathcal{F}_{ij}$  time-evolves an intensity  $\rho_i = \rho(x_i)$  according to the three steps of the dynamics. In particular  $\mathcal{F}_{ij}$  can be written as

$$(\mathcal{F}_{ij}) = \mathbf{R}\mathbf{X}\mathbf{D} \quad (4.29)$$

where  $\mathbf{D}$  is a block matrix for the random dynamics in each of the separated intervals  $[-1, 0)$  and  $[0, 1]$ . Consequently,  $\mathbf{D}$  consists of two  $N \times N$  blocks in the diagonal. The matrix elements of each block are uniformly distributed random numbers, which are normalized afterwards so that the sum over each row in  $\mathbf{D}$  gives unity. The matrix  $\mathbf{X}$  represents the exchange of the interval  $[-a, 0)$  with the interval  $[0, a]$ . Therefore, the matrix  $\mathbf{X}$  consists of ones in the diagonal except for elements  $\mathbf{X}_{ij}$  where  $x_i$  or  $x_j$  are inside  $[-a, a]$ . This sub-matrix has ones in the counterdiagonal. Finally, the matrix  $\mathbf{R}$  determines the partial leakage of the system and has only diagonal elements  $\mathbf{R}_{ii}$  according to the (asymmetric) function  $R(x_i)$ . Because of this matrix  $\mathbf{R}$  the random matrix approximation of the FPO becomes sub-unitary with

eigenvalues inside the unit circle in the complex plane. As shown in Fig. 4.20 the analytical values are in very good agreement to the random matrix approximation of the FPO. All the other eigenvalues of the random matrix are close to zero and represent very short lived states.

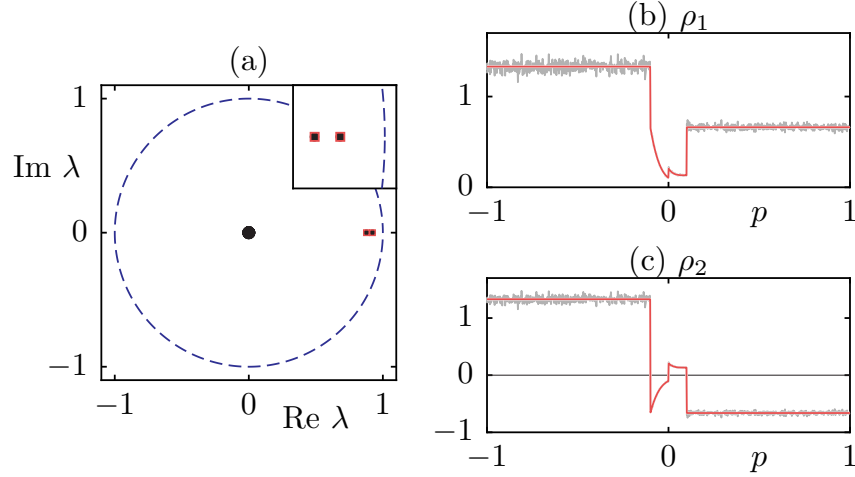


**Figure 4.20:** The analytical eigenvalues of the toy model FPO are shown as red squares in (a). Black dots represent numerically determined eigenvalues of the corresponding  $1000 \times 1000$  random matrix for the FPO. All eigenvalues are inside the unit circle (blue dashed curve). The eigenvalues close to one are magnified in the upper right inset. (b) and (c) show the first and the second eigenstates of the toy model FPO as red curve. The corresponding eigenstates of the random matrix are represented as bright gray curves.

Linear combinations of the long-lived eigenstates according to Eqs. (4.13) lead to states that are dominantly localized either on the left or the right side of the exchange interval as shown in Fig. 4.21(a-b). Therefore, they are identified with CW and CCW propagating states respectively. To confirm the asymmetry of the backscattering the time evolution of  $10^7$  trajectories is traced. Thus, the scattered intensity from  $[-1, 0]$  to  $[0, 1]$  and vice versa can be obtained numerically. As shown in Fig. 4.21(c) more intensity is scattered from CCW to CW region than in the reverse process while the loss of intensity from the initial region is almost equal for both CW and CCW.

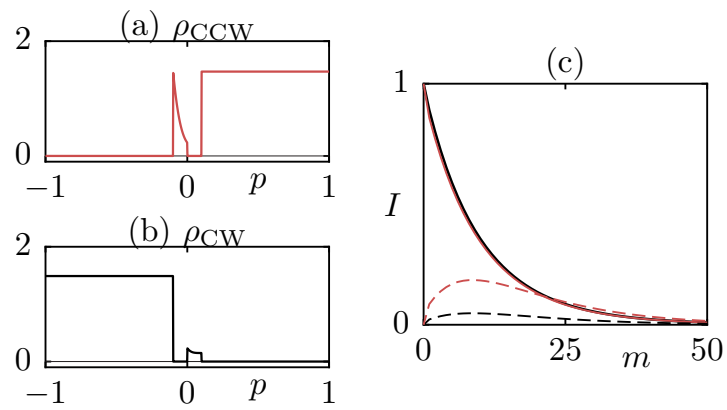


**Figure 4.21:** In (a) and (b) linear combinations of the eigenstates of the toy model are shown. (c) shows the time evolution as  $m = 0, 1, 2, \dots$  iterations of a CW and CCW intensity respectively. A black solid (dashed) line is the component of the initial CW intensity in the CW (CCW) region and a red solid (dashed) curve is the component of the initial CCW intensity in the CCW (CW) region.

---

## 4.4 Chapter summary

In this chapter the wave mechanical phenomenon of asymmetric backscattering is investigated in the ray dynamics. First, it was focused on the backscattering of uniform intensity distributions in order to treat the asymmetric backscattering as a simple exchange of intensities between two regions in phase space which represent CW and CCW propagating motion. Here, a qualitative agreement with the effective two-mode model can be observed when the proper definition of CW and CCW is used namely with respect to  $L_z = 0$  and not with the intuitively line  $p = 0$ .

In the second part of the chapter the more elaborate approach to the asymmetric backscattering in the ray dynamics was introduced based on the FPO. It has been shown that the eigenstates of the FPO with the largest modulus eigenvalue nicely reflect the properties of long-lived optical modes. In particular they are pairwise nearly degenerate, they are pairwise non-orthogonal, and both eigenstates of such a pair have the same preferred sense of rotation. Furthermore, from the FPO eigenstates the two-mode model can be reconstructed in the same manner as in the wave mechanics, namely by superpositions of the eigenstates. A good agreement between ray and wave dynamics is obtained qualitatively within an averaged Husimi function of long-lived modes. However, to see the asymmetric backscattering in the FPO eigenstates the cavity needs to have predominantly chaotic dynamics with a mixing of CW and CCW regions which is fulfilled for generic moderate or strongly deformed cavities.

In the last part of this chapter a 1D toy-model for asymmetric backscattering was introduced where the eigenvalue problem of the FPO is solved analytically. The results from the 1D toy-model illustrate and confirm the properties of the FPO eigenstates in microcavities.

The main results of this chapter are published in Ref. [Kullig and Wiersig, 2016a].



# 5 Perturbation theory for slightly deformed symmetric microdisk cavities

For many applications it is necessary to deform the cavity's boundary such that optical modes show a desired property, e.g. unidirectional light emission. Such a boundary deformation then acts as a perturbation to the ideal circular cavity. Thus, the  $Q$ -factor is typically spoiled what is unwanted in many cases. Consequently, just slight boundary deformations are considered as a compromise with the following advantages: (i) Already slight deformations can have huge intended impact on optical modes and their far-field emission [Kraft and Wiersig, 2016, Ge et al., 2013], e.g. the change from isotropic to unidirectional emission. (ii) The  $Q$ -spoiling is in many cases in an acceptable range. (iii) Slight boundary deformations allow to solve the mode equation, and the boundary conditions, not only numerically but also with an analytical perturbation theory [Duberland et al., 2008, Ge et al., 2013, Wiersig, 2012, Kraft and Wiersig, 2014].

In this chapter the perturbation theory for microcavities with symmetric boundary deformations is discussed. This perturbation theory was originally developed for TM polarization by Duberland *et al.* [Duberland et al., 2008] up to second order. It has been shown that reliable results can be obtained for slight deformations, e.g. in a cut disk [Duberland et al., 2008], the Limaçon [Kraft and Wiersig, 2014], and cavities with local boundary deformations [Wiersig, 2012]. The perturbation theory provides analytical formulas for the near- and the far-field mode pattern, and the complex wave number depending on the cavity's boundary deformation. In Ref. [Kraft and Wiersig, 2016] it has been shown that these formulas can be inverted in order to search for an optimal boundary shape which lead to a desired far-field emission pattern of an optical mode. Furthermore, in Ref. [Ge et al., 2013] the perturbation theory was also derived for the case of TE polarization which is a more elaborate task because of the more complicated boundary conditions at the cavity's interface.

The first aim of this chapter is to review the perturbation theory for symmetric cavities and TM polarization. Therefore, in Sec. 5.1 the key idea and the general framework of the perturbation theory is introduced. So far the perturbation theory has been derived in literature up to second order. This derivation is reviewed in Sec. 5.2.

As a new result of this thesis the third-order corrections to the complex wave number are derived in Sec. 5.3 and they are discussed in Sec. 5.4. A summary of the chapter is provided in Sec. 5.5.

## 5.1 General setup for the symmetric perturbation theory

In this Section the general framework of the perturbation theory for TM polarization is introduced following Ref. [Dubertrand et al., 2008]. It is assumed that a slight deformation of the circular cavity is present which is of the form

$$r(\phi) = R + \lambda f(\phi) \quad (5.1)$$

where  $\lambda$  is the formally small perturbation parameter such that  $|\lambda f(\phi)| \ll 1$ . Here, the deformation is assumed to be symmetric, i.e.  $f(\phi) = f(-\phi)$ . Hence, the optical modes with positive/even (+) or negative/odd (-) parity can be classified. They are labeled in the interior with  $\psi_{\pm,\text{in}}$  and in the exterior with  $\psi_{\pm,\text{out}}$ . The modes need to fulfill the mode equation (3.9) and the boundary conditions for TM polarization (3.15a)-(3.15b) at the cavity's interface. With Eq. (5.1) the boundary conditions can be expanded in a series of the perturbation parameter  $\lambda$  as

$$\begin{aligned} [\psi_{\pm,\text{in}} - \psi_{\pm,\text{out}}](R, \phi) &= -\frac{\lambda}{1!} f(\phi) \partial_r [\psi_{\pm,\text{in}} - \psi_{\pm,\text{out}}](R, \phi) \\ &\quad - \frac{\lambda^2}{2!} f^2(\phi) \partial_r^2 [\psi_{\pm,\text{in}} - \psi_{\pm,\text{out}}](R, \phi) \\ &\quad - \frac{\lambda^3}{3!} f^3(\phi) \partial_r^3 [\psi_{\pm,\text{in}} - \psi_{\pm,\text{out}}](R, \phi) + \mathcal{O}(\lambda^4) \end{aligned} \quad (5.2a)$$

$$\begin{aligned} \partial_r [\psi_{\pm,\text{in}} - \psi_{\pm,\text{out}}](R, \phi) &= -\frac{\lambda}{1!} f(\phi) \partial_r^2 [\psi_{\pm,\text{in}} - \psi_{\pm,\text{out}}](R, \phi) \\ &\quad - \frac{\lambda^2}{2!} f^2(\phi) \partial_r^3 [\psi_{\pm,\text{in}} - \psi_{\pm,\text{out}}](R, \phi) \\ &\quad - \frac{\lambda^3}{3!} f^3(\phi) \partial_r^4 [\psi_{\pm,\text{in}} - \psi_{\pm,\text{out}}](R, \phi) + \mathcal{O}(\lambda^4). \end{aligned} \quad (5.2b)$$

Since the boundary deformation is small the modes can still be identified via two mode numbers  $m > 0$  and  $l > 0$ . In order to solve the mode equation with the corresponding boundary conditions, the mode  $\psi_{\pm}$  is expanded into solutions of the circular cavity as

$$\psi_{\pm,\text{in}}(r, \phi) = \frac{J_m(nkr)}{J_m(nx)} \chi_{\pm,m}(\phi) + \sum_{p \neq m} a_p \frac{J_p(nkr)}{J_p(nx)} \chi_{\pm,p}(\phi) \quad (5.3a)$$

$$\psi_{\pm,\text{out}}(r, \phi) = (1 + b_m) \frac{H_m(kr)}{H_m(x)} \chi_{\pm,m}(\phi) + \sum_{p \neq m} (a_p + b_p) \frac{H_p(kr)}{H_p(x)} \chi_{\pm,p}(\phi) \quad (5.3b)$$

where for the positive parity  $\chi_{+,p}(\phi) = \cos(p\phi)$  and for the negative parity  $\chi_{-,p}(\phi) = \sin(p\phi)$



are the radial dependencies. With this ansatz the mode equation is automatically fulfilled but not the boundary conditions at the cavity's interface. The target of the perturbation theory is now to determine the complex wave number  $x = kR$  and the coefficients  $a_p, b_p$  such that also the boundary conditions Eqs. (5.2a)-(5.2b) are fulfilled in the orders  $\lambda^1, \lambda^2, \dots$  for a given deformation function  $f(\phi)$ . Therefore, the complex wave number and the coefficients need to be expanded in a power series as

$$\begin{aligned} x &= x_0 + x_1\lambda + x_2\lambda^2 + x_3\lambda^3 + \mathcal{O}(\lambda^4) \\ a_p &= a_p^{(1)}\lambda + a_p^{(2)}\lambda^2 + a_p^{(3)}\lambda^3 + \mathcal{O}(\lambda^4) \\ b_p &= b_p^{(2)}\lambda^2 + b_p^{(3)}\lambda^3 + \mathcal{O}(\lambda^4) \end{aligned} \quad (5.4)$$

where here and in the following a superscripted parenthetical number  $^{(i)}$  indicates the  $i$ -th order in the perturbation parameter  $\lambda$ . For convenience the corrections to the wave number  $x$  in different orders of  $\lambda$  are indicated by a subscripted number. Note that by inserting Eq. (5.2b) into Eq. (5.2a) it follows that the terms  $a_p^{(0)}, b_p^{(0)}$ , and  $b_p^{(1)}$  are absent in the expansion scheme.

In the circular cavity the complex wave number of an optical mode  $(m, l)$  is determined as the root of the scattering function  $S_m(x_0)$  [see Eq. (3.21)]. For the derivation of the perturbation theory one needs to expand  $S_p(x)$  also for  $p \neq m$  around  $x_0$  as

$$S_p(x) = S_p(x_0) + \lambda x_1 \partial_x S_p(x_0) + \lambda^2 \left( x_2 \partial_x S_p(x_0) + \frac{1}{2} x_1^2 \partial_x^2 S_p(x_0) \right) + \mathcal{O}(\lambda^3) \quad (5.5)$$

where in particular for  $p = m$  it can be obtained [Duberland et al., 2008]

$$S_m(x_0) = 0 \quad (5.6a)$$

$$\partial_x S_m(x_0) = -(n^2 - 1) \quad (5.6b)$$

$$\partial_x^2 S_m(x_0) = (n^2 - 1) \left( \frac{1}{x_0} + 2 \frac{H'_m}{H_m}(x_0) \right). \quad (5.6c)$$

Furthermore it is necessary for the derivation of the first- and second-order perturbation theory to calculate the terms  $\partial_r^u [\psi_{\pm, \text{in}} - \psi_{\pm, \text{out}}](R, \phi)$  ( $u = 0, 1, 2, 3$ ) explicitly for the ansatz (5.3) as [Duberland et al., 2008]

$$[\psi_{\pm, \text{in}} - \psi_{\pm, \text{out}}] = - \sum_p b_p^{(2)} \chi_{\pm, p}(\phi) + \mathcal{O}(\lambda^3) \quad (5.7a)$$

$$\begin{aligned} \partial_r [\psi_{\pm, \text{in}} - \psi_{\pm, \text{out}}] &= k \left\{ S_m(x) \chi_{\pm, m}(\phi) + \sum_{p \neq m} a_p S_p(x) \chi_{\pm, p}(\phi) \right. \\ &\quad \left. - \sum_p b_p^{(2)} \frac{H'_p}{H_p}(x_0) \chi_{\pm, p}(\phi) \right\} + \mathcal{O}(\lambda^3) \end{aligned} \quad (5.7b)$$

$$\partial_r^2 [\psi_{\pm,\text{in}} - \psi_{\pm,\text{out}}] = -\frac{k}{R} \left\{ [S_m(x) + x(n^2 - 1)] \chi_{\pm,m}(\phi) + \sum_{p \neq m} a_p^{(1)} [S_p(x_0) x_0 (n^2 - 1)] \chi_{\pm,p}(\phi) \right\} + \mathcal{O}(\lambda^2) \quad (5.7c)$$

$$\partial_r^3 [\psi_{\pm,\text{in}} - \psi_{\pm,\text{out}}] = \left\{ k S_m(x_0) \left( \frac{m^2 + 2}{R^2} - k^2 n^2 \right) - k^3 (n^2 - 1) \frac{H'_p}{H_p}(x_0) + k^2 \frac{n^2 - 1}{R} \right\} \chi_{\pm,m}(\phi) + \mathcal{O}(\lambda). \quad (5.7d)$$

Note that whenever one has a product of two quantities  $g, h$  which depend on  $\lambda$ , the  $l$ -th order in  $\lambda$  denoted by  $^{(l)}$  fulfills the product rule

$$[gh]^{(l)} = \sum_{i=0}^l g^{(i)} h^{(l-i)} \quad (5.8)$$

which is used, e.g., in the derivation of the terms above.

The perturbation theory is supposed to give reliable results if the deformation  $|\lambda f(\phi)|$  and the wave number  $x$  is small. In Ref. [Dubertrand et al., 2008] Dubertrand *et al.* derived a criterion for the applicability of the perturbation theory based on the area  $\delta a$  where the refractive index is changed via the boundary deformation. This criterion is given by

$$s_n \frac{\delta a}{8\pi R^2} (\text{Re } x)^2 n^2 \ll 1 \quad (5.9)$$

with

$$s_n = 1 - \frac{2}{\pi} \left( \arcsin \frac{1}{n} + \frac{1}{n} \sqrt{1 - \frac{1}{n^2}} \right). \quad (5.10)$$

In Ref. [Kraft and Wiersig, 2014] it was demonstrated that the criterion (5.9) is not too strict, i.e. the perturbation theory (of second order) predicts  $x$  also well if the left hand side of Eq. (5.9) is close to one. However, quasi-degeneracies in  $\text{Re } x$  between modes of different branches  $l$  can cause additional corrections to the perturbation theory and may spoil the accuracy of the prediction. The treatment of such quasi-degeneracies between two and three modes is also discussed in Ref. [Dubertrand et al., 2008].

Once the coefficients in the scheme (5.4) are evaluated not only the internal mode pattern but also the far-field pattern  $F(\phi)$  is determined as

$$F(\phi) = (1 + b_m) \frac{e^{-i\pi m/2}}{H_m(x)} \chi_{\pm,m}(\phi) + \sum_{p \neq m} (a_p + b_p) \frac{e^{-i\pi p/2}}{H_p(x)} \chi_{\pm,p}(\phi). \quad (5.11)$$

## 5.2 Review on first- and second-order perturbation theory

This section reviews the perturbation theory for symmetric deformed microdisk cavities up to second order following the original derivation by Dubertrand *et al.* [Dubertrand et al., 2008]. The purpose is not to show each step of the calculation explicitly but to illustrate the key ideas of the derivation and to provide the analytical results. For applications and examples of the perturbation theory see Sec. 5.4.

### First-order perturbation theory

In the first-order perturbation theory the boundary conditions Eqs. (5.2a)-(5.2a) are evaluated in order  $\lambda^1$  as

$$[\psi_{\pm,\text{in}} - \psi_{\pm,\text{out}}]^{(1)}(R, \phi) = -f(\phi)\partial_r [\psi_{\pm,\text{in}} - \psi_{\pm,\text{out}}]^{(0)}(R, \phi) \quad (5.12a)$$

$$\partial_r [\psi_{\pm,\text{in}} - \psi_{\pm,\text{out}}]^{(1)}(R, \phi) = -f(\phi)\partial_r^2 [\psi_{\pm,\text{in}} - \psi_{\pm,\text{out}}]^{(0)}(R, \phi). \quad (5.12b)$$

With the ansatz for the wave function (5.3a)-(5.3b) and the expansion of the coefficients according to the scheme (5.4) the first equation is automatically fulfilled [see Eqs. (5.7) for the derivatives]. The latter equation results in the conditional equation

$$-x_1(n^2 - 1)\chi_{\pm,m}(\phi) + \sum_{p \neq m} a_p^{(1)} S_p(x_0) \chi_{\pm,p}(\phi) = \frac{f(\phi)}{R} x_0(n^2 - 1)\chi_{\pm,m}(\phi) \quad (5.13)$$

for  $x_1$  and  $a_p^{(1)}$ . Using the orthogonality of the  $\chi_{\pm,p}(\phi)$  for different  $p$  the first-order results

$$x_1 = -x_0 A_{mm} \quad (5.14)$$

$$\alpha_p^{(1)} = (n^2 - 1) \frac{x_0}{S_p(x_0)} A_{pm}. \quad (5.15)$$

can be extracted. Here,  $A_{pm}$  are the Fourier harmonics of the boundary which are defined as

$$A_{pm} = \frac{\varepsilon_p}{2\pi R} \int_0^{2\pi} \chi_{\pm,p}(\phi) f(\phi) \chi_{\pm,m}(\phi) d\phi \quad (5.16)$$

with  $\varepsilon_p = 2 - \delta_{0,p}$ . Note that the  $A_{pm}$  are dimensionless since the deformation function  $f(\phi)$  has the same dimension as  $R$ .

The first-order results provide corrections in the complex wave number  $x = x_0(1 - \lambda A_{mm})$  and via the  $a_p^{(1)}$  the first-order gives rough predictions for the mode pattern. However, since  $b_p^{(1)} = 0$  and  $A_{mm}$  is real, the first-order results cannot provide corrections to the  $Q$ -factor

because

$$Q(x_0 + \lambda x_1) = -\frac{\operatorname{Re} [x_0(1 - \lambda A_{mm})]}{2\operatorname{Im} [x_0(1 - \lambda A_{mm})]} = -\frac{\operatorname{Re} x_0}{2\operatorname{Im} x_0} = Q(x_0). \quad (5.17)$$

Therefore,  $Q$ -spoiling in deformed cavities is an effect of higher order in the boundary deformation and requires at least second-order perturbation theory.

## Second-order perturbation theory

In order to obtain the results for the second-order corrections of the perturbation theory, Eqs. (5.2a) and (5.2a) are evaluated in order  $\lambda^2$  as

$$\begin{aligned} [\psi_{\pm,\text{in}} - \psi_{\pm,\text{out}}]^{(2)}(R, \phi) &= -f(\phi)\partial_r [\psi_{\pm,\text{in}} - \psi_{\pm,\text{out}}]^{(1)}(R, \phi) \\ &\quad - \frac{f^2(\phi)}{2}\partial_r^2 [\psi_{\pm,\text{in}} - \psi_{\pm,\text{out}}]^{(0)}(R, \phi) \end{aligned} \quad (5.18a)$$

$$\begin{aligned} \partial_r [\psi_{\pm,\text{in}} - \psi_{\pm,\text{out}}]^{(2)}(R, \phi) &= -f(\phi)\partial_r^2 [\psi_{\pm,\text{in}} - \psi_{\pm,\text{out}}]^{(1)}(R, \phi) \\ &\quad - \frac{f^2(\phi)}{2}\partial_r^3 [\psi_{\pm,\text{in}} - \psi_{\pm,\text{out}}]^{(0)}(R, \phi). \end{aligned} \quad (5.18b)$$

By inserting the Eqs. (5.7) into Eq. (5.18a) it follows

$$\sum_p b_p^{(2)} \chi_{\pm,p}(\phi) = \frac{1}{2}(n^2 - 1)x_0^2 \frac{f^2(\phi)}{R^2} \chi_{\pm,m}(\phi) \quad (5.19a)$$

and from Eq. (5.18b) one obtains

$$\begin{aligned} &\left\{ (n^2 - 1) \left[ -x_2 + \frac{1}{2x_0} x_1^2 \left( 1 + 2x_0 \frac{H'_m}{H_m} \right) \right] + b_m^{(2)} \frac{H'_m}{H_m} \right\} \chi_{\pm,m}(\phi) \\ &\quad + \sum_{p \neq m} \left[ x_1 a_p^{(1)} \partial_x S_p + a_p^{(2)} S_p + b_p^{(2)} \frac{H'_m}{H_m} \right] \chi_{\pm,p}(\phi) \\ &= (n^2 - 1) \frac{f(\phi)}{R} \left( x_0 \sum_{p \neq m} a_p^{(1)} \chi_{\pm,p}(\phi) + x_1 \chi_{\pm,m}(\phi) \right) \\ &\quad + (n^2 - 1) x_0 \frac{f^2(\phi)}{2R^2} \left( 1 + x_0 \frac{H'_m}{H_m} \right) \chi_{\pm,m}(\phi). \end{aligned} \quad (5.19b)$$

These are the conditional equations for the second order coefficients  $a_p^{(2)}$ ,  $b_p^{(2)}$ , and  $x_2$ . Using the (dimensionless) second-order Fourier harmonics of the boundary defined by

$$B_{pm} = \frac{\epsilon_p}{2\pi R^2} \int_0^{2\pi} f^2(\phi) \chi_{\pm,p}(\phi) \chi_{\pm,m}(\phi) \, d\phi \quad (5.20)$$

with  $\epsilon_p = 2 - \delta_{0,p}$  one can exploit the orthogonality of the  $\chi_{\pm,p}(\phi)$  in Eq. (5.19a) such that

$$b_p^{(2)} = \frac{1}{2}(n^2 - 1)x_0^2 B_{pm} \quad (5.21)$$

is obtained. Hence, Eq. (5.19b) can now be solved for  $x_2$  and  $a_p^{(2)}$  as

$$\begin{aligned} x_2 &= \frac{1}{2}x_0 (3A_{mm}^2 - B_{mm}) + x_0^2 (A_{mm}^2 - B_{mm}) \frac{H'_m(x_0)}{H_m} \\ &\quad - (n^2 - 1)x_0^2 \sum_{p \neq m} \frac{A_{mp}A_{pm}}{S_p(x_0)} \\ a_p^{(2)} &= (n^2 - 1) \frac{x_0}{S_p(x_0)} \left\{ A_{pm}A_{mm} \left[ \frac{x_0}{S_p(x_0)} \partial_x S_p(x_0) - 1 \right] \right. \\ &\quad \left. + \frac{1}{2}B_{pm} \left[ 1 - x_0 \left( \frac{H'_m(x_0)}{H_m} - \frac{H'_p(x_0)}{H_p} \right) \right] \right. \\ &\quad \left. + x_0(n^2 - 1) \sum_{k \neq m} \frac{A_{pk}A_{km}}{S_k(x_0)} \right\}. \end{aligned} \quad (5.22)$$

Therefore, all coefficients in the expansion scheme (5.4) are computed up to second order in  $\lambda$  which completes the derivation of second-order perturbation theory. Since, the corrections to  $x = kR$  in second order are in general complex the second-order results give also non-trivial predictions for the  $Q$ -factor, i.e.  $Q(x_0 + \lambda x_1 + \lambda^2 x_2) \neq Q(x_0)$ .

Note that in case of local boundary deformations the formulas can be further simplified such that not the matrices  $A_{pm}$  and  $B_{pm}$  but only the first two moments  $\langle f \rangle$  and  $\langle f^2 \rangle$  of the deformation function enter [Wiersig, 2012].

### 5.3 Extension to third-order perturbation theory

As a new result of this thesis, the third-order corrections of the complex wave number  $x$  are derived in this section. By the extension to the third order one in general expects a higher accuracy. Furthermore, since the second-order gives access to the  $Q$ -factor corrections one expects for third-order perturbation theory to capture further interesting effects: In Sec. 5.4 it is e.g. shown that the splitting  $\Delta x = x_+ - x_-$  of even and odd parity modes is predicted more accurate by third-order perturbation theory.

As starting point for the derivation of the third-order corrections the boundary conditions

(5.2a) and (5.2a) are evaluated in order  $\lambda^3$  as

$$\begin{aligned} [\psi_{\pm,\text{in}} - \psi_{\pm,\text{out}}]^{(3)}(R, \phi) &= -f(\phi)\partial_r [\psi_{\pm,\text{in}} - \psi_{\pm,\text{out}}]^{(2)}(R, \phi) \\ &\quad - \frac{f^2(\phi)}{2}\partial_r^2 [\psi_{\pm,\text{in}} - \psi_{\pm,\text{out}}]^{(1)}(R, \phi) \\ &\quad - \frac{f^3(\phi)}{6}\partial_r^3 [\psi_{\pm,\text{in}} - \psi_{\pm,\text{out}}]^{(0)}(R, \phi) \end{aligned} \quad (5.24a)$$

$$\begin{aligned} \partial_r [\psi_{\pm,\text{in}} - \psi_{\pm,\text{out}}]^{(3)}(R, \phi) &= -f(\phi)\partial_r^2 [\psi_{\pm,\text{in}} - \psi_{\pm,\text{out}}]^{(2)}(R, \phi) \\ &\quad - \frac{f^2(\phi)}{2}\partial_r^3 [\psi_{\pm,\text{in}} - \psi_{\pm,\text{out}}]^{(1)}(R, \phi) \\ &\quad - \frac{f^3(\phi)}{6}\partial_r^4 [\psi_{\pm,\text{in}} - \psi_{\pm,\text{out}}]^{(0)}(R, \phi). \end{aligned} \quad (5.24b)$$

Here, in principle one could insert the terms according to expansion in  $\lambda$  given by Eqs. (5.7). But in the following a more convenient way to derive the third-order corrections is chosen. Therefore, first, the function

$$D_m^l(x) = \partial_r^l \left[ \frac{J_m(nkr)}{J_m(nx)} - \frac{H_m(kr)}{H_m(x)} \right] \Big|_{r=R} = \left( \frac{x}{R} \right)^l \left[ n^l \frac{J_m^{[l]}(nx)}{J_m} - \frac{H_m^{[l]}(x)}{H_m} \right] \quad (5.25)$$

is defined where  $^{[l]}$  indicates the  $l$ -th derivative (and not the  $l$ -th order in  $\lambda$ ). Note that  $D_m^l(x)$  does not depend on the specific boundary deformation  $f(\phi)$  but it depends on  $\lambda$  via  $x$ . Therefore, it needs to be expanded as

$$\begin{aligned} D_m^l(x) &= D_m^l + \lambda x_1 \partial_x D_m^l + \lambda^2 \left( x_2 \partial_x D_m^l + \frac{1}{2} x_1^2 \partial_x^2 D_m^l \right) \\ &\quad + \lambda^3 \left( x_3 \partial_x D_m^l + x_1 x_2 \partial_x^2 D_m^l + \frac{1}{6} x_1^3 \partial_x^3 D_m^l \right) + \mathcal{O}(\lambda^4). \end{aligned} \quad (5.26)$$

Here, for convenience, the dependencies on  $x_0$  are not explicitly written, i.e.  $D_m^l = D_m^l(x_0)$ ,  $\partial_x D_m^l = \partial_x D_m^l(x_0)$ , ... is shorten. By using the function  $D_m^l(x)$  the terms  $\partial_r^l [\psi_{\pm,\text{in}} - \psi_{\pm,\text{out}}](R, \phi)$  can be written compactly as

$$\partial_r^l [\psi_{\pm,\text{in}} - \psi_{\pm,\text{out}}](R, \phi) = D_m^l(x) \chi_{\pm,m}(\phi) + \sum_{p \neq m} a_p D_p^l(x) \chi_{\pm,p}(\phi) - \sum_p b_p \left( \frac{x}{R} \right)^l \frac{H_p^{[l]}(x)}{H_p} \chi_{\pm,p}(\phi). \quad (5.27)$$

In order to write down the conditional equations (5.24) explicitly one needs to evaluate Eq. (5.27) for different  $l$  and in different orders of the perturbation parameter  $\lambda$ . The terms needed are listed below [their computation is straight forward by using the product rule (5.8)]

and the expansion (5.26)]

$$[\psi_{\pm,\text{in}} - \psi_{\pm,\text{out}}]^{(3)} = - \sum_p b_p^{(3)} \chi_{\pm,p}(\phi) \quad (5.28a)$$

$$\begin{aligned} \partial_r[\psi_{\pm,\text{in}} - \psi_{\pm,\text{out}}]^{(3)} &= \left( x_3 \partial_x D_m^1 + x_1 x_2 \partial_x^2 D_m^1 + \frac{1}{6} x_1^3 \partial_x^3 D_m^1 \right) \chi_{\pm,m}(\phi) \\ &+ \sum_{p \neq m} \left( a_p^{(3)} D_p^1 + a_p^{(2)} x_1 \partial_x D_p^1 \right. \\ &\quad \left. + a_p^{(1)} \left[ x_2 \partial_x D_p^1 + \frac{1}{2} x_1^2 \partial_x^2 D_p^1 \right] \right) \chi_{\pm,p}(\phi) \\ &- \sum_p \left( b_p^{(3)} \frac{x_0}{R} \frac{H'_p}{H_p} + b_p^{(2)} \left\{ \frac{x}{R} \frac{H'_p}{H_p}(x) \right\}^{(1)} \right) \chi_{\pm,p}(\phi) \end{aligned} \quad (5.28b)$$

$$\begin{aligned} \partial_r[\psi_{\pm,\text{in}} - \psi_{\pm,\text{out}}]^{(2)} &= \left( x_2 \partial_x D_m^1 + \frac{1}{2} x_1^2 \partial_x^2 D_m^1 \right) \chi_{\pm,m}(\phi) \\ &+ \sum_{p \neq m} \left( a_p^{(2)} D_p^1 + a_p^{(1)} x_1 \partial_x D_p^1 \right) \chi_{\pm,p}(\phi) - \sum_p b_p^{(2)} \frac{x_0}{R} \frac{H'_p}{H_p} \chi_{\pm,p}(\phi) \end{aligned} \quad (5.28c)$$

$$\begin{aligned} \partial_r^2[\psi_{\pm,\text{in}} - \psi_{\pm,\text{out}}]^{(2)} &= \left( x_2 \partial_x D_m^2 + \frac{1}{2} x_1^2 \partial_x^2 D_m^2 \right) \chi_{\pm,m}(\phi) \\ &+ \sum_{p \neq m} \left( a_p^{(2)} D_p^2 + a_p^{(1)} x_1 \partial_x D_p^2 \right) \chi_{\pm,p}(\phi) - \sum_p b_p^{(2)} \frac{x_0^2}{R^2} \frac{H''_p}{H_p} \chi_{\pm,p}(\phi) \end{aligned} \quad (5.28d)$$

$$\partial_r^2[\psi_{\pm,\text{in}} - \psi_{\pm,\text{out}}]^{(1)} = x_1 \partial_x D_m^2 \chi_{\pm,m}(\phi) + \sum_{p \neq m} a_p^{(1)} D_p^2 \chi_{\pm,p}(\phi) \quad (5.28e)$$

$$\partial_r^3[\psi_{\pm,\text{in}} - \psi_{\pm,\text{out}}]^{(1)} = x_1 \partial_x D_m^3 \chi_{\pm,m}(\phi) + \sum_{p \neq m} a_p^{(1)} D_p^3 \chi_{\pm,p}(\phi) \quad (5.28f)$$

$$\partial_r^3[\psi_{\pm,\text{in}} - \psi_{\pm,\text{out}}]^{(0)} = D_m^3 \chi_{\pm,m}(\phi) \quad (5.28g)$$

$$\partial_r^4[\psi_{\pm,\text{in}} - \psi_{\pm,\text{out}}]^{(0)} = D_m^4 \chi_{\pm,m}(\phi). \quad (5.28h)$$

For convenience the dependencies  $(R, \phi)$  at the left-hand-side and  $(x_0)$  at the Hankel-functions and at the terms  $\partial_x^u D_p^l$  have been omitted. Inserting these terms into Eqs. (5.24) one obtains

the conditional equations for the third-order perturbation theory in the explicit form

$$\begin{aligned}
-\sum_p b_p^{(3)} \chi_{\pm,p}(\phi) &= \left[ -f(\phi) \left( x_2 \partial_x D_m^1 + \frac{1}{2} x_1^2 \partial_x^2 D_m^1 \right) - \frac{1}{2} f^2(\phi) x_1 \partial_x D_m^2 - \frac{1}{6} f^3(\phi) D_m^3 \right] \chi_{\pm,m}(\phi) \\
&+ \sum_{p \neq m} \left[ -f(\phi) \left( a_p^{(2)} D_p^1 + a_p^{(1)} x_1 \partial_x D_p^1 \right) - \frac{1}{2} f^2(\phi) a_p^{(1)} D_p^2 \right] \chi_{\pm,p}(\phi) \\
&+ \sum_p f(\phi) b_p^{(2)} \frac{x_0}{R} \frac{H'_p}{H_p} \chi_{\pm,p}(\phi) \tag{5.29a}
\end{aligned}$$

$$\begin{aligned}
&\left( x_3 \partial_x D_m^1 + x_1 x_2 \partial_x^2 D_m^1 + \frac{1}{6} x_1^3 \partial_x^3 D_m^1 \right) \chi_{\pm,m}(\phi) \\
&+ \sum_{p \neq m} \left( a_p^{(3)} D_p^1 + a_p^{(2)} x_1 \partial_x D_p^1 + a_p^{(1)} \left[ x_2 \partial_x D_p^1 + \frac{1}{2} x_1^2 \partial_x^2 D_p^1 \right] \right) \chi_{\pm,p}(\phi) \\
&- \sum_p \left( b_p^{(3)} \frac{x_0}{R} \frac{H'_p}{H_p} + b_p^{(2)} \left\{ \frac{x}{R} \frac{H'_p}{H_p}(x) \right\}^{(1)} \right) \chi_{\pm,p}(\phi) \\
&= \left[ -f(\phi) \left( x_2 \partial_x D_m^2 + \frac{1}{2} x_1^2 \partial_x^2 D_m^2 \right) - \frac{1}{2} f^2(\phi) x_1 \partial_x D_m^3 - \frac{1}{6} f^3(\phi) D_m^4 \right] \chi_{\pm,m}(\phi) \\
&+ \sum_{p \neq m} \left[ -f(\phi) \left( a_p^{(2)} D_p^2 + a_p^{(1)} x_1 \partial_x D_p^2 \right) - \frac{1}{2} f^2(\phi) a_p^{(1)} D_p^3 \right] \chi_{\pm,p}(\phi) \\
&+ \sum_p f(\phi) b_p^{(2)} \frac{x_0^2}{R^2} \frac{H''_p}{H_p} \chi_{\pm,p}(\phi). \tag{5.29b}
\end{aligned}$$

These equations can be solved for the third-order corrections  $x_3$ ,  $b_p^{(3)}$ , and  $a_p^{(3)}$ . Using the orthogonality of the  $\chi_{\pm,p}$  for different  $p$  and with the (dimensionless) third-order Fourier harmonics

$$C_{pm} = \frac{\epsilon_p}{2\pi R^3} \int_0^\pi f^3(\phi) \chi_{\pm,m}(\phi) \chi_{\pm,p}(\phi) d\phi \tag{5.30}$$

of the boundary deformation, Eq. (5.29a) can be solved for  $b_m^{(3)}$  as

$$b_p^{(3)} = \left( x_2 \partial_x D_m^1 + \frac{1}{2} x_1^2 \partial_x^2 D_m^1 \right) R A_{mp} + \frac{1}{2} x_1 \partial_x D_m^2 R^2 B_{mp} + \frac{1}{6} D_m^3 R^3 C_{mp} \tag{5.31}$$

$$\begin{aligned}
&+ \sum_{k \neq m} \left[ \left( a_k^{(2)} D_k^1 + a_k^{(1)} x_1 \partial_x D_k^1 \right) R A_{kp} + \frac{1}{2} a_k^{(1)} D_k^2 R^2 B_{kp} \right] - \sum_k b_k^{(2)} x_0 \frac{H'_k}{H_k} A_{pk} \\
&= \left( x_2 \partial_x \tilde{D}_m^1 + \frac{1}{2} x_1^2 \partial_x^2 \tilde{D}_m^1 \right) A_{mp} + \frac{1}{2} x_1 \partial_x \tilde{D}_m^2 B_{mp} + \frac{1}{6} \tilde{D}_m^3 C_{mp} \tag{5.32} \\
&+ \sum_{k \neq m} \left[ \left( a_k^{(2)} \tilde{D}_k^1 + a_k^{(1)} x_1 \partial_x \tilde{D}_k^1 \right) A_{kp} + \frac{1}{2} a_k^{(1)} \tilde{D}_k^2 B_{kp} \right] - \sum_k b_k^{(2)} x_0 \frac{H'_k}{H_k} A_{pk}
\end{aligned}$$



where in the last equation the rescaled function  $\tilde{D}_m^l = R^l D_m^l$  is introduced. Using the orthogonality of  $\chi_{\pm,p}(\phi)$  in Eq. (5.29b) one obtains

$$\begin{aligned}
\left( x_3 \partial_x \tilde{D}_m^1 + x_1 x_2 \partial_x^2 \tilde{D}_m^1 + \frac{1}{6} x_1^3 \partial_x^3 \tilde{D}_m^1 \right) &= b_m^{(3)} x_0 \frac{H'_m}{H_m} + b_m^{(2)} \left\{ x \frac{H'_m}{H_m}(x) \right\}^{(1)} \\
&- \left( x_2 \partial_x \tilde{D}_m^2 + \frac{1}{2} x_1^2 \partial_x^2 \tilde{D}_m^2 \right) A_{mm} \\
&- \frac{1}{2} x_1 \partial_x \tilde{D}_m^3 B_{mm} - \frac{1}{6} \tilde{D}_m^4 C_{mm} + b_m^{(2)} x_0^2 \frac{H''_m}{H_m} A_{mm} \\
&- \sum_{p \neq m} \left[ A_{mp} \left( a_p^{(2)} \tilde{D}_p^2 + a_p^{(1)} x_1 \partial_x \tilde{D}_p^2 \right) \right. \\
&\quad \left. + \frac{1}{2} B_{mp} a_p^{(1)} \tilde{D}_p^3 - A_{mp} b_p^{(2)} x_0^2 \frac{H''_p}{H_p} \right] \quad (5.33)
\end{aligned}$$

which can be solved for the third-order correction in complex wave number as

$$\begin{aligned}
x_3 \partial_x \tilde{D}_m^1 &= -x_1 x_2 \partial_x^2 \tilde{D}_m^1 - \frac{1}{6} x_1^3 \partial_x^3 \tilde{D}_m^1 + b_m^{(3)} x_0 \frac{H'_m}{H_m} + b_m^{(2)} \left\{ x \frac{H'_m}{H_m}(x) \right\}^{(1)} \\
&- \left( x_2 \partial_x \tilde{D}_m^2 + \frac{1}{2} x_1^2 \partial_x^2 \tilde{D}_m^2 \right) A_{mm} \\
&- \frac{1}{2} x_1 \partial_x \tilde{D}_m^3 B_{mm} - \frac{1}{6} \tilde{D}_m^4 C_{mm} + b_m^{(2)} x_0^2 \frac{H''_m}{H_m} A_{mm} \\
&- \sum_{p \neq m} \left[ A_{mp} \left( a_p^{(2)} \tilde{D}_p^2 + a_p^{(1)} x_1 \partial_x \tilde{D}_p^2 \right) + \frac{1}{2} B_{mp} a_p^{(1)} \tilde{D}_p^3 - A_{mp} b_p^{(2)} x_0^2 \frac{H''_p}{H_p} \right] \quad (5.34)
\end{aligned}$$

with  $\partial_x \tilde{D}_m^1 = -(n^2 - 1)x_0$  and

$$\left\{ x \frac{H'_m}{H_m}(x) \right\}^{(1)} = x_0 \left\{ \frac{H'_m}{H_m}(x) \right\}^{(1)} + x_1 \frac{H'_m}{H_m} = x_0 x_1 \left( \frac{H''_m}{H_m} - \frac{H_m'^2}{H_m^2} \right) + x_1 \frac{H'_m}{H_m}. \quad (5.35)$$

For the implementation of these equations the terms  $\partial_x^u \tilde{D}_p^l(x_0)$  need to be evaluated explicitly. This can be done with a computer algebra system; e.g. Maple. The necessary terms are listed for completeness in the Appendix A.3. Also for completeness the terms  $a_p^{(3)}$  are deduced from Eq. (5.29b) as

$$\begin{aligned}
a_p^{(3)} \tilde{D}_p^1 &= -a_p^{(2)} x_1 \partial_x \tilde{D}_p^1 - a_p^{(1)} \left[ x_2 \partial_x \tilde{D}_p^1 + \frac{1}{2} x_1^2 \partial_x^2 \tilde{D}_p^1 \right] + b_p^{(3)} x_0 \frac{H'_p}{H_p} + b_p^{(2)} \left\{ x \frac{H'_p}{H_p}(x) \right\}^{(1)} \\
&- \left( x_2 \partial_x \tilde{D}_m^2 + \frac{1}{2} x_1^2 \partial_x^2 \tilde{D}_m^2 - b_m^{(2)} x_0^2 \frac{H'_m}{H_m} \right) A_{mp} - \frac{1}{2} x_1 \partial_x \tilde{D}_m^3 B_{mp} - \frac{1}{6} \tilde{D}_m^4 C_{mp} \\
&- \sum_{k \neq m} \left[ \left( a_k^{(2)} \tilde{D}_k^2 + a_k^{(1)} x_1 \partial_x \tilde{D}_k^2 - b_k^{(2)} x_0^2 \frac{H'_k}{H_k} \right) A_{kp} + \frac{1}{2} a_k^{(2)} \tilde{D}_k^3 B_{kp} \right] \quad (5.36)
\end{aligned}$$

with  $\tilde{D}_p^1 = x_0 S_p(x_0)$ .

## 5.4 Applications – Improvements from the third order?

In this section the results from the perturbation theory are applied and discussed at some example systems. A main question here is whether the third-order perturbation theory improves the predictions of the complex wave numbers. In order to illustrate the difficulty of this question, first, two trivial deformations are discussed: (i) A uniform deformation  $f(\phi) = -\epsilon R$  which leads to a shrunken circular cavity with reduced radius. (ii) A shift of the circular cavity by  $\epsilon$  along the  $x$ -axis. Here, the radius of the shifted circle is given by

$$\frac{r(\phi)}{R} = -\epsilon \cos(\phi) + \sqrt{1 - \epsilon^2 [1 - \cos^2(\phi)]} \quad (5.37)$$

which implies a deformation function  $f(\phi) = r(\phi) - R$ . The advantage of these two trivial deformations is that the exact value of the complex wave number is known analytically: In case (i) scaling can be used to obtain  $x = x_0/(1 - \epsilon)$  as complex wave number of the deformed cavity. In case (ii) the complex wave number of the “deformed” cavity is again  $x_0$ . Therefore, the error of the predictions from the perturbation theory

$$\text{Err } x = |x_{\text{PT}} - x_{\text{analyt}}| \quad (5.38)$$

can be computed for the first-, second-, and third order. The results for these two cases are shown in Fig. 5.1. For the shrunken circle the error  $\text{Err } x$  scales as expected: The error in the  $i$ -th order is proportional to  $\epsilon^{i+1}$  which definitely leads to an improvement of the predictions by the third order in comparison to the second order.

However, in case of the shifted circle the error scaling is quite different. Here, already the second-order perturbation theory scales with  $\epsilon^4$  and predicts the same values as the third order. Consequently, evaluating the third order does not yield an improvement. Note, that for the shifted circle  $\epsilon$  does not one to one correspond to the perturbation parameter  $\lambda$  since it enters also nonlinear in  $r(\phi)$ . However, also in the case of the shifted circle the parameter  $\epsilon$  sets the strength of the perturbation. Furthermore, the leading order in  $r(\phi)$  is linear in  $\epsilon$ . Hence,  $\epsilon$  and  $\lambda$  can be seen as equivalent parameter for the error scaling.

Further note that one cannot argue that the absence of the term proportional to  $\epsilon^3$  in the  $\epsilon$ -expansion of  $r(\phi)$  [Eq. (5.37)] is responsible for the vanishing third-order correction in  $x$ . Otherwise every deformation linear in  $\epsilon$  would lead to a vanishing  $x_2$ .

The above discussed deformations are trivial in the sense that they do not change the circular shape of the cavity. Therefore, next, more generic boundary deformations are considered which immediately results in the problem that the analytical reference value of  $x$  is not known. Here, the numerical boundary element method (BEM) [Wiersig, 2003] is used to provide a proper reference value of  $x$ . First, a circular cavity with two Gaussian notches symmetrically placed

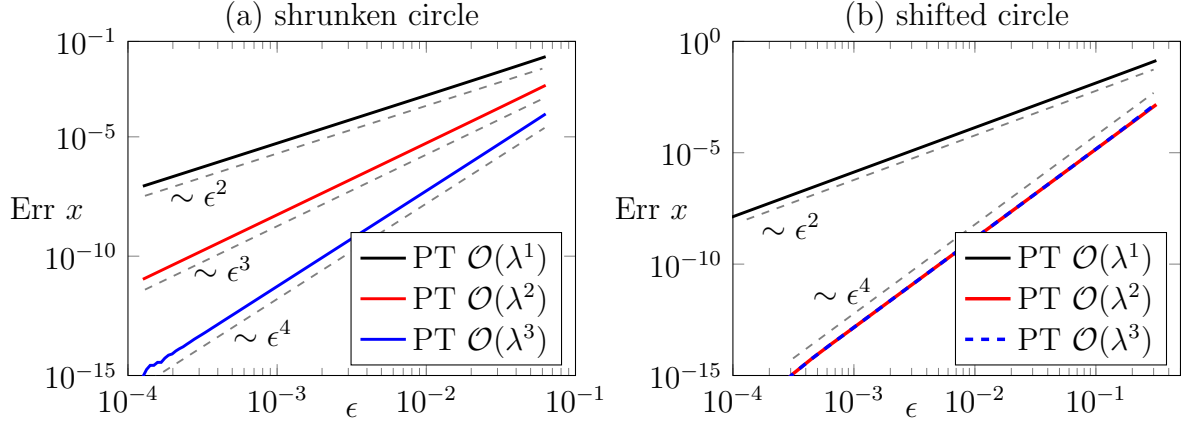


**Figure 5.1:** The error  $\text{Err } x$  of the perturbation theory predictions of (black) first, (red) second and (blue) third order for (a) a uniform deformation [shrunken circle] and (b) a shifted circle are shown for the mode  $(m, l) = (8, 1)$ . The refractive index is  $n = 2.0$ . Gray dashed lines illustrate the scaling with  $\epsilon^2$ ,  $\epsilon^3$ , and  $\epsilon^4$ .

at the  $x$ -axis is studied. The cavity is defined by

$$\frac{r(\phi)}{R} = 1 - \epsilon \sum_{l \in \mathbb{Z}} \exp \left[ -\frac{(\phi - \pi l)^2}{2\sigma^2} \right] \quad (5.39)$$

where  $\sigma$  is the width parameter of the notches. In Fig. 5.2(a) the resulting error scaling of  $x$  for the positive parity mode  $(m, l) = (8, 1)$  is shown for  $n = 2$ . The notch width is set via  $\sigma = 0.2$  what results in a relatively broad notch. The perturbation theory shows the expected error scaling, i.e., the second order scales proportional to  $\epsilon^3$  and the third order scales with  $\epsilon^4$ . Therefore, evaluating the third-order corrections again provide more accurate results. This situation is in good agreement with the example of the shrunken circle in Fig. 5.1(a). However, note that the intrinsic numerical errors of the BEM prevent to observe the error scaling over many magnitudes of  $\epsilon$ . In particular around  $\epsilon \sim 10^{-2}$  the numerical error of the BEM is considerable for the third-order perturbation theory and results in a saturation of the error  $\text{Err } x$ .

The second example for a non-trivial boundary deformation is the flatten quadrupole which is defined by

$$\frac{r(\phi)}{R} = \sqrt{1 + 2\epsilon \cos 2\phi}. \quad (5.40)$$

The reason for exploiting the flatten quadrupole rather than the quadrupole (no square root) is to prevent the vanishing of lots of elements in the matrices  $A_{pm}$ ,  $B_{pm}$ , and  $C_{pm}$  due to the simple cosine deformation. Therefore the flatten quadrupole represents a more generic deformation than the quadrupole. The results of the error scaling in the perturbation theory are shown in Fig. 5.2(b) for the even parity mode  $(m, l) = (8, 1)$ . Here, the scaling is quite

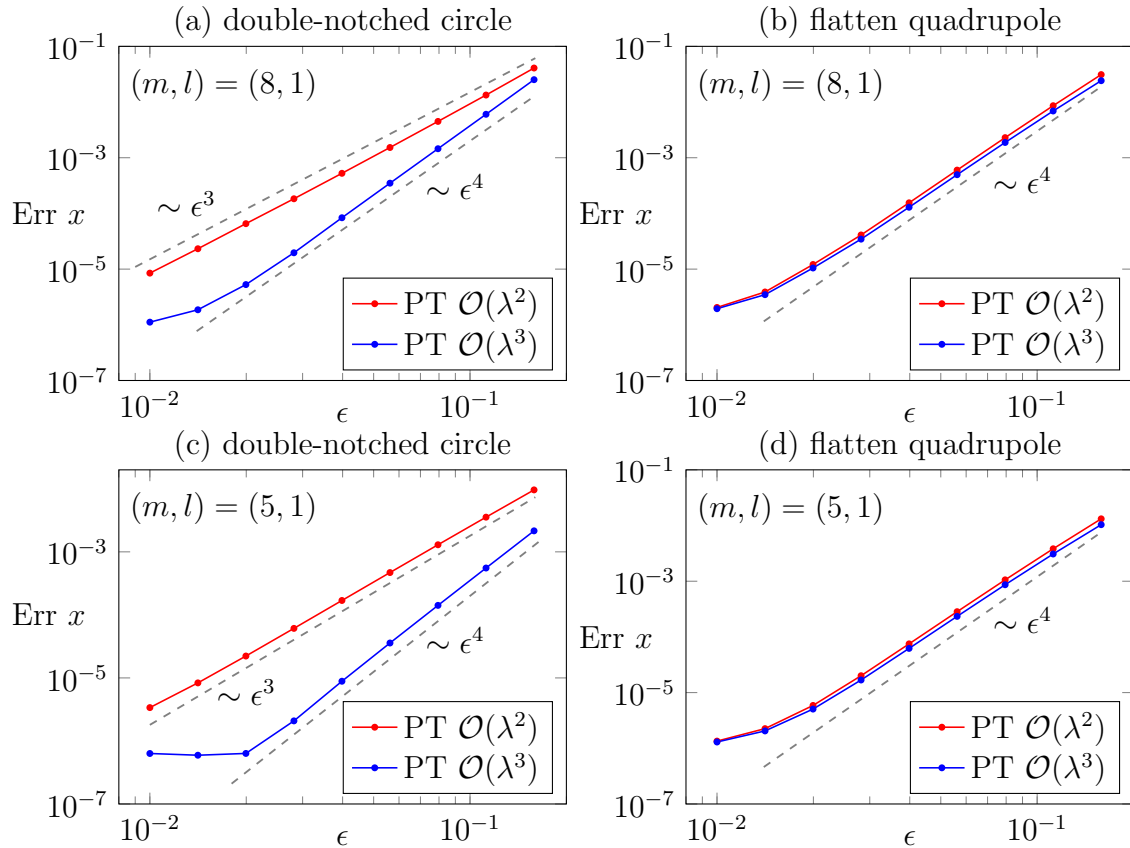


**Figure 5.2:** The error  $\text{Err } x$  of the perturbation theory predictions of (red) second and (blue) third order for (a,c) the double-notched circle and (b,d) the flatten quadrupole are shown for the mode (a,b)  $(m, l) = (8, 1)$  and (c,d)  $(m, l) = (5, 1)$ . The refractive index is  $n = 2.0$ . Gray dashed lines illustrate the scaling with  $\epsilon^3$ , and  $\epsilon^4$ . Reference values of  $x$  are obtained with numerical BEM. Therefore a saturation of  $\text{Err } x$  is observed for very small  $\epsilon$ .

similar to the case of the shifted circle: The error of the perturbation theory of second- and third-order scale similar to  $\epsilon^4$ . Note that the blue curve of the third-order perturbation theory is slightly below the red curve for the second-order perturbation theory. Therefore, also for the flatten quadrupole the third-order predictions are slightly more accurate than the second-order predictions.

In Fig. 5.2(c) and (d) the error scaling for the even parity mode  $(m, l) = (5, 1)$  in the double notched-circle and the flatten quadrupole is shown. Also here the same error scaling as for the mode  $(m, l) = (8, 1)$  is observed. Moreover the same error scaling can be seen also for an refractive index  $n = 1.5$  (not shown) and for the modes with the odd/negative parity (not shown). This suggests that the type of the boundary deformation causes the different scalings of  $\text{Err } x$ .

However, up to now it is not clear which mechanism is responsible for the error scaling. In order to illustrate that the situation is even more delicate as discussed so far, next, the elliptical cavity [see Eq. (2.18)] is studied. In particular the axis ratio  $v$  is varied such that

the parameters  $b = \sqrt{v}$  and eccentricity  $e^2 = (1 - v^2)$  in Eq. (2.18) are used. For  $v = 1$  a circular cavity is obtained. With a Taylor expansion of the radius around  $v = 1$  one can verify that the term  $(1 - v)$  is a proper deformation parameter corresponding to  $\lambda$ . The obtained error scaling for the ellipse is shown in Fig. 5.3 for both the even and the odd parity modes. Here, a dependence of the error scaling with the mode number  $m$  is observed. In particular for the mode  $m = 3$  [Fig. 5.3(a-b)] the third-order corrections give a significant improvement. However, for  $m = 5$  [Fig. 5.3(c-d)] there is almost no improvement from the evaluation of the third-order corrections. And even worse, the third-order predictions can become more faulty than the second-order predictions, see also Fig. 5.3(e-f) for  $m = 8$ . Note that again due to the numerical calculation of the reference value of  $x$  deviations from the scaling, i.e. a saturation, can be seen for small errors/small deformations.

An interesting observation in the predictions from the perturbation theory is that the complex frequency splitting  $\Delta x = x_+ - x_-$  is predicted in all the shown cases much better by the third order than by the second order even if the error scaling for the individual mode  $x_+$  or  $x_-$  is may worsen. This is illustrated in Fig. 5.4 where the results for the splitting  $\Delta x$  in the flatten quadrupole (a-b), the notched circle (c) and the ellipse (d-f) are shown. Especially, in Figs. 5.4(e-f) the third-order predictions for the splitting are surprisingly closer to the BEM results than the second-order predictions. However, in these both cases [and also for the flatten quadrupole mode  $m = 5$  shown in Fig. 5.4(b)] neither the second- nor the third-order perturbation theory gives very accurate results. Nevertheless, the shown data suggest that evaluating even higher orders in the perturbation theory might give even more accurate predictions for the splitting  $\Delta x$ . For such future evaluations of higher orders in the perturbation theory the presented formalism, i.e. the formulation of the relevant derivatives [see Eq. 5.27] with the function  $D_m^l(x)$  is advantageous.

Note that for all the studied systems in the limit of small deformations a power-law scaling of the splitting  $\Delta x$  with the deformation parameter is observed and predicted by the perturbation theory. This is in good agreement with the literature [Hackenbroich et al., 1998] where such a power-law was found for elliptical and quadrupole billiard. Furthermore, a power-law behavior is explained semiclassically with a tunneling coupling [Wilkinson, 1986].

It is mentioned here that the BEM is able to predict the splitting  $\Delta x$  much more precise than the actual values of  $x$  because dominant errors in  $x_+$  and  $x_-$  can cancel out if their difference is taken [see Appendix A.6 for a simple illustration example].

## 5.5 Chapter summary

In the first part of this chapter the perturbation theory for TM polarized modes in slightly deformed symmetric cavities developed by Dubertrand *et al.* was reviewed. In the second part of the chapter this perturbation theory was extended to the third order. The third-order correc-

tions in general promise an improved accuracy in the predictions of the complex wave numbers. In the applications it rather turns out that these improvements are quite controversial: In some cases indeed a significant improvement in the predictions is observed. However, for specific boundary deformations these improvements can be quite marginal. Especially in the ellipse it is furthermore observed that the third-order prediction can worsen the predictions. So far it is not clear which mechanism is responsible for this limitation.

However, an interesting feature of the third-order predictions is that the complex frequency splitting, i.e. the difference in the wave numbers of even and odd parity modes, is predicted more accurately by the third-order than by the second-order perturbation theory.

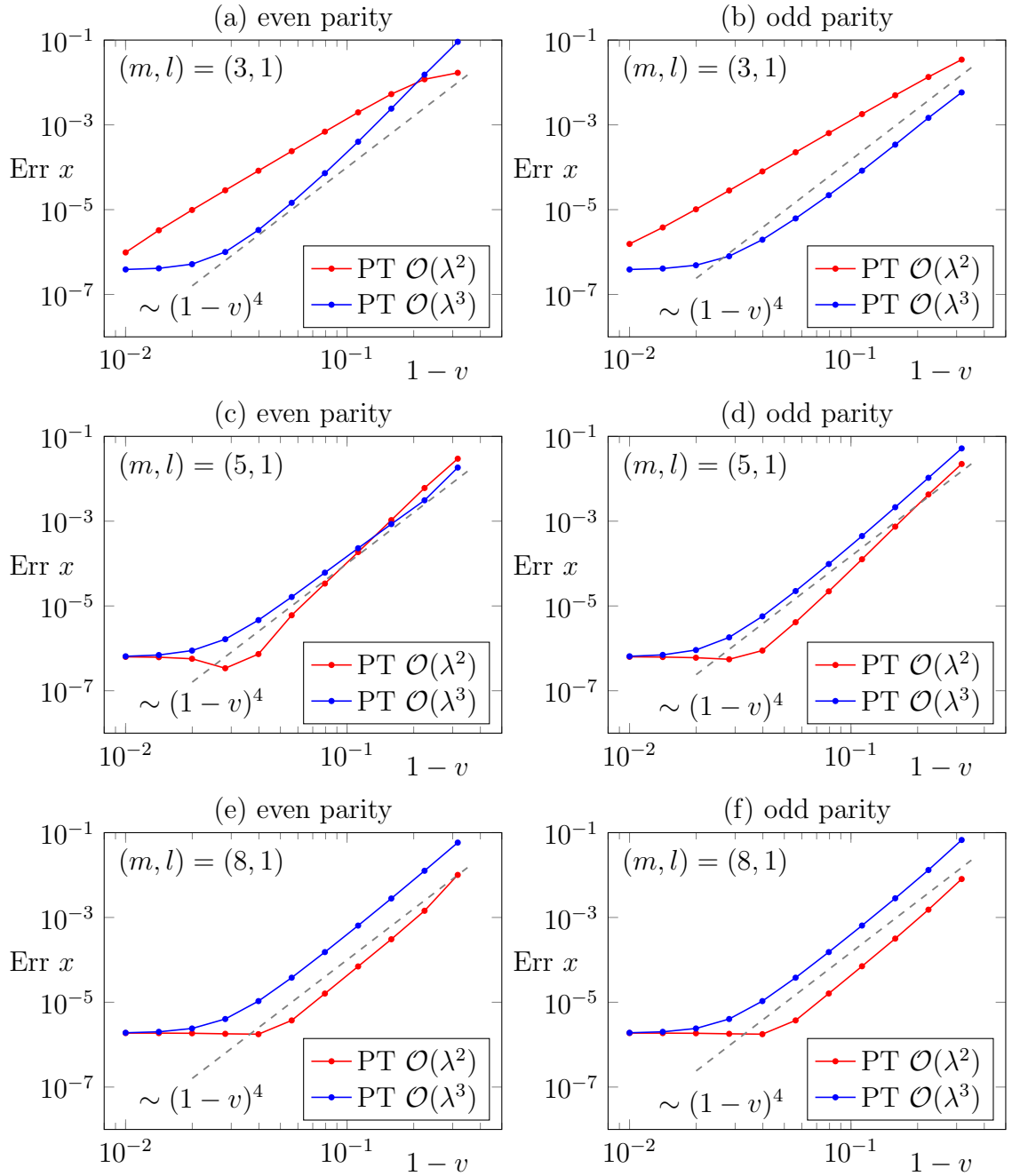


**Figure 5.3:** The figures show the error scaling of the (red) second- and (blue) third-order perturbation theory predictions of the complex wave number  $x$  in the ellipse with refractive index  $n = 2$  and varying axis ratio  $v$ . The results for the even parity are shown in the left panels and for the odd parity in right panels. The mode number  $m$  is (a-b)  $m = 3$ , (c-d)  $m = 5$ , and (e-f)  $m = 8$ ;  $l$  is fixed to one. Dashed lines are a guide to the eye and indicate a power law scaling with  $(1 - v)^4$ .

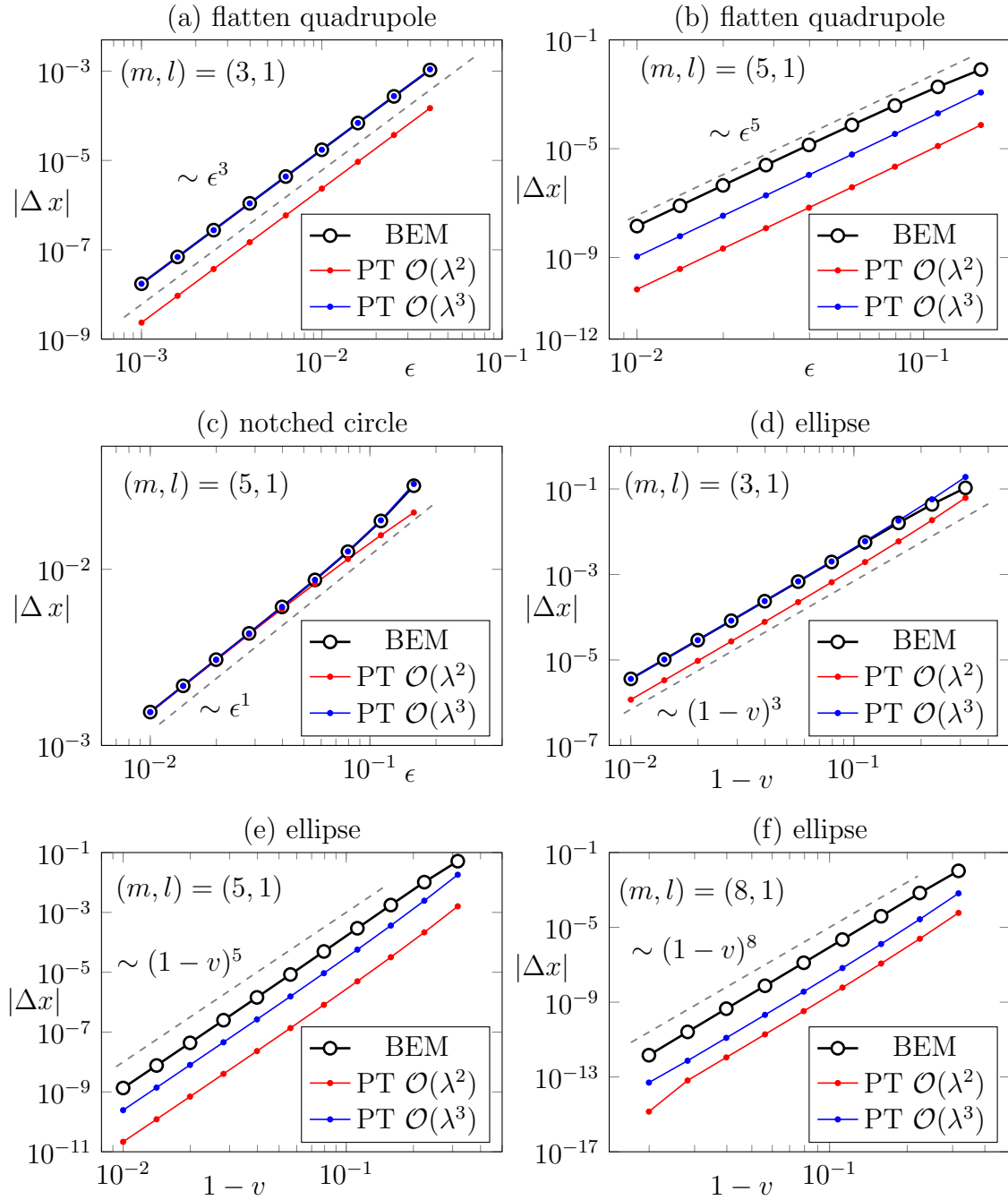


**Figure 5.4:** The figure shows the modulo of the complex frequency spitting  $\Delta x = x_+ - x_-$  between even and odd party modes in (a-b) the flatten quadrupole, (c) the notched circle with  $\sigma = 0.2$ , and (d-f) the ellipse. The refractive index is in each case set to  $n = 2$ . The predictions from the (red curve) second- and (blue curve) third-order perturbation theory are compared to the (black curve) BEM results. Black dashed lines are a guide to the eye and indicate a power-law scaling.



# 6 Perturbation theory for slightly deformed asymmetric microdisk cavities

The perturbation theory developed so far in literature [Dubertrand et al., 2008] can only treat symmetrically deformed microdisk cavities where modes can be classified by even and odd parity. Because of this distinction which can already be used for the degenerate modes in the unperturbed (circular) cavity the perturbation theory for symmetric deformations is a non-degenerate perturbation theory. However, in the generic case a cavity is asymmetrically deformed either via a desired asymmetric boundary curve or via small fabrication tolerances. Consequently, the separation of the modes into even and odd parity is no longer valid (see Sec. 3.3.2). Therefore, the perturbation theory for asymmetric deformations needs to determine the correct linear combination of degenerate modes in the unperturbed (circular) cavity first. Hence, it is a degenerate perturbation theory.

In this chapter, as one main result of this thesis, the perturbation theory for asymmetric deformed cavities is derived and discussed. First, in Sec. 6.1 the framework for this perturbation theory is explained and compared to the symmetric case. In the following sections the formulas for the wave number  $x = kR$  and the mode corrections are derived in first- (Sec. 6.2) and second order (Sec. 6.3). Finally, applications are discussed in Sec. 6.4 and a chapter summary is provided in Sec. 6.5.

## 6.1 General setup

In this section the general framework of the perturbation theory for asymmetric deformations (asymmetric-PT) is introduced. Especially it is discussed which modification to the perturbation theory for symmetric deformations (symmetric-PT) in Sec. 5 need to be established to properly account for the asymmetric cavity shape. For the asymmetric-PT it is still assumed that the cavity shape is given in polar coordinates by a function

$$r(\phi) = R + \lambda f(\phi) \tag{6.1}$$

with a formally small perturbation parameter  $\lambda$ . However, in contrast to Eq. (5.1) in the previous section, here,  $f(\phi) \neq f(-\phi)$  is in general asymmetric. The expansion of the boundary conditions into a Taylor series in  $\lambda$  [see Eq. (5.2)] is still valid. But in order to properly account for the mixture of degenerate modes in the circular cavity the ansatz for the wave function (5.3) needs to be modified: In contrast to simple superpositions of  $e^{im\phi}$  and  $e^{-im\phi}$  leading to even and odd parity in the symmetric-PT, here, a priori an arbitrary linear combination is allowed. Therefore, the ansatz of the wave function with dominant mode numbers  $(m, l)$  is given by

$$\psi_{\pm, \text{in}}(r, \phi) = \frac{J_m(nkr)}{J_m(nx)} [e^{iz} e^{im\phi} + e^{-iz} e^{-im\phi}] + \sum_{p \neq \pm m} a_p \frac{J_p(nkr)}{J_p(nx)} e^{ip\phi} \quad (6.2a)$$

$$\begin{aligned} \psi_{\pm, \text{out}}(r, \phi) &= \frac{H_m(kr)}{H_m(x)} [(1 + b_m) e^{iz} e^{im\phi} + (1 + b_{-m}) e^{-iz} e^{-im\phi}] \\ &+ \sum_{p \neq \pm m} (a_p + b_p) \frac{H_p(kr)}{H_p(x)} e^{ip\phi} \end{aligned} \quad (6.2b)$$

where the parameter  $z \in \mathbb{C}$  fixes the contributions of the unperturbed modes with  $\pm m$ . Note that the ansatz is written in the symmetrized form such that  $m \rightarrow -m$  results in  $z \rightarrow -z$ . And further note that the sums over  $p$  now range from  $-\infty$  to  $\infty$ . Since the correct linear combination of  $e^{im\phi}$  and  $e^{-im\phi}$  depends on the perturbation also  $z$  needs to be expanded in the perturbation parameter  $\lambda$  as

$$z = z_0 + \lambda z_1 + \mathcal{O}(\lambda^2). \quad (6.3)$$

Hence, the coefficient  $e^{\pm iz}$  is expanded as

$$e^{\pm iz} = e^{\pm iz_0} (1 \pm \lambda i z_1) + \mathcal{O}(\lambda^2). \quad (6.4)$$

It will be shown that the asymmetric-PT in first order fixes  $z_0 \in \mathbb{R}$  (see Sec. 6.2) and in second order  $z_1 \in \mathbb{C}$  is obtained (see Sec. 6.3) which could lead to a strong chirality. The other unknown quantities in the ansatz are  $x = kR$ ,  $a_p$ , and  $b_p$  which are expanded in the perturbation parameter  $\lambda$  as in the symmetric-PT, see scheme (5.4).

Consequently, the chirality of the optical mode

$$\alpha_{\text{ch}} = \frac{\sum_{p>0} |a_p|^2 - \sum_{p<0} |a_p|^2}{\sum_{p>0} |a_p|^2 + \sum_{p<0} |a_p|^2} \quad (6.5)$$

can be computed from the coefficients  $a_p$  with  $a_{\pm m} = e^{\pm iz}$  within the asymmetric-PT. Furthermore the expression of the far-field pattern [see Eq. (5.11)] needs to be modified according

to the ansatz for the wave function as

$$\begin{aligned}
F(\phi) = & (1 + b_m)e^{iz} \frac{e^{-i\pi m/2}}{H_m(x)} e^{im\phi} + (1 + b_{-m})e^{-iz} \frac{e^{-i\pi m/2}}{H_m(x)} e^{-im\phi} \\
& + \sum_{p \neq \pm m} (a_p + b_p) \frac{e^{-i\pi p/2}}{H_p(x)} e^{ip\phi}.
\end{aligned} \tag{6.6}$$

## 6.2 First-order perturbation theory

The derivation of the first-order asymmetric-PT starts similar to the symmetric case: The boundary conditions are evaluated in order  $\lambda^1$  which leads to Eqs. (5.12a)-(5.12b) which are repeated here for convenience

$$[\psi_{\pm, \text{in}} - \psi_{\pm, \text{out}}]^{(1)}(R, \phi) = -f(\phi) \partial_r [\psi_{\pm, \text{in}} - \psi_{\pm, \text{out}}]^{(0)}(R, \phi) \tag{6.7a}$$

$$\partial_r [\psi_{\pm, \text{in}} - \psi_{\pm, \text{out}}]^{(1)}(R, \phi) = -f(\phi) \partial_r^2 [\psi_{\pm, \text{in}} - \psi_{\pm, \text{out}}]^{(0)}(R, \phi). \tag{6.7b}$$

In order to solve this set of equations one needs to compute the terms  $\partial_r^u [\psi_{\pm, \text{in}} - \psi_{\pm, \text{out}}](R, \phi)$  with  $u = 0, 1, 2, 3$  for the ansatz (6.2). This computation is done in Appendix A.4. Hence, evaluating Eq. (6.7b) results in the conditional equation

$$\begin{aligned}
-(n^2 - 1)x_1 [e^{iz_0} e^{im\phi} + e^{-iz_0} e^{-im\phi}] + \sum_{p \neq \pm m} a_p^{(1)} S_p(x_0) e^{ip\phi} \\
= \frac{f(\phi)}{R} x_0 (n^2 - 1) [e^{iz_0} e^{im\phi} + e^{-iz_0} e^{-im\phi}]
\end{aligned} \tag{6.8}$$

for the quantities  $x_1$ ,  $z_0$ , and  $a_p^{(1)}$ . Note that Eq. (6.7a) is automatically fulfilled with the ansatz (6.2) of the wave function. To extract the unknown quantities from Eq. (6.8), first, the orthogonality of  $e^{\pm im\phi}$  is exploited. Thus, with the (dimensionless) Fourier harmonics of the asymmetric boundary deformation

$$A_q = \frac{1}{2\pi R} \int_0^{2\pi} f(\phi) e^{iq\phi} d\phi \tag{6.9}$$

one obtains the system of equations

$$-x_1 e^{iz_0} = x_0 [e^{iz_0} A_0 + e^{-iz_0} A_{-2m}] \tag{6.10a}$$

$$-x_1 e^{-iz_0} = x_0 [e^{iz_0} A_{2m} + e^{-iz_0} A_0] \tag{6.10b}$$

for  $x_1$  and  $z_0$ . The solutions of this system are the first-order corrections

$$z_0 = -\frac{1}{4} \text{Arg} \left( \frac{A_{2m}}{A_{-2m}} \right) + \mu \frac{\pi}{2} = \frac{1}{2} \text{Arg}(A_{-2m}) + \mu \frac{\pi}{2}; \tag{6.11}$$

$$x_1 = -x_0 [A_0 + e^{-2iz_0} A_{-2m}] \tag{6.12}$$

where  $A_{-2m} = A_{2m}^*$  and  $\mu \in \mathbb{Z}$  is a parameter selecting the particular mode of the mode pair. Therefore it is sufficient to restrict  $\mu \in \{0, 1\}$ . Other values of  $\mu$  will predict the same two modes. In Eq. (6.11) one sees that  $z_0$  is real. It fixes the phase of the involved unperturbed modes proportional to  $\exp(\pm im\phi)$  and does not lead to a finite chirality in Eq. (6.5). Note that Eq. (6.12) can be rewritten as

$$x_1 = -x_0 (A_0 \pm |A_{2m}|). \quad (6.13)$$

Hence, the first-order corrections in general lift the degeneracy in  $x_0$  of the mode pair in the unperturbed (circular) cavity. But since the correction is linear in  $x_0$  (with a real factor) it yields  $Q(x_0 + \lambda x_1) = Q(x_0)$  [see Eq. (5.17)], i.e. also in the asymmetric-PT the first-order corrections do not explain the spoiling of the  $Q$ -factor.

Next, the orthogonality of  $e^{ip\phi}$  with  $p \neq \pm m$  in Eq. (6.8) is exploited which leads to

$$a_p^{(1)} = \frac{(n^2 - 1)x_0}{S_p} [e^{iz_0} A_{m-p} + e^{-iz_0} A_{-m-p}] \quad (6.14)$$

which completes the derivation of the first-order corrections in the asymmetric-PT.

Note that especially for the solution of the system (6.10) it is assumed that  $A_{-2m} = A_{2m}^* \neq 0$ . For non-generic boundary shapes with vanishing Fourier harmonic  $A_{-2m}$  one cannot fix  $z_0$  in first-order perturbation theory and only a single value  $x_1 = -x_0 A_0$  is predicted for the mode pair.

## 6.3 Second-order perturbation theory

In this section the second order of the asymmetric-PT is derived. This requires to evaluate the boundary conditions (5.2) in order  $\lambda^2$  which leads like in the symmetric-PT to Eqs. (5.18) which are repeated here for convenience

$$\begin{aligned} [\psi_{\pm, \text{in}} - \psi_{\pm, \text{out}}]^{(2)}(R, \phi) &= -f(\phi) \partial_r [\psi_{\pm, \text{in}} - \psi_{\pm, \text{out}}]^{(1)}(R, \phi) \\ &\quad - \frac{f^2(\phi)}{2} \partial_r^2 [\psi_{\pm, \text{in}} - \psi_{\pm, \text{out}}]^{(0)}(R, \phi) \end{aligned} \quad (6.15a)$$

$$\begin{aligned} \partial_r [\psi_{\pm, \text{in}} - \psi_{\pm, \text{out}}]^{(2)}(R, \phi) &= -f(\phi) \partial_r^2 [\psi_{\pm, \text{in}} - \psi_{\pm, \text{out}}]^{(1)}(R, \phi) \\ &\quad - \frac{f^2(\phi)}{2} \partial_r^3 [\psi_{\pm, \text{in}} - \psi_{\pm, \text{out}}]^{(0)}(R, \phi). \end{aligned} \quad (6.15b)$$

With the ansatz (6.2) for the wave function and the terms calculated in Appendix A.4 one obtains from Eq. (6.15a)

$$b_m^{(2)} e^{iz_0} e^{im\phi} + b_{-m}^{(2)} e^{-iz_0} e^{-im\phi} + \sum_{p \neq \pm m} b_p^{(2)} e^{ip\phi} = \frac{1}{2} \frac{f^2(\phi)}{R^2} x_0^2 (n^2 - 1) [e^{iz_0} e^{im\phi} + e^{-iz_0} e^{-im\phi}] \quad (6.16)$$

and from Eq. (6.15b) one gets

$$\begin{aligned}
& \left[ -x_2 + \frac{x_1^2}{2x_0} \left( 1 + 2x_0 \frac{H'_m}{H_m} \right) \right] [e^{iz_0} e^{im\phi} + e^{-iz_0} e^{-im\phi}] - \frac{b_m^{(2)}}{n^2 - 1} \frac{H'_m}{H_m} e^{iz_0} e^{im\phi} \\
& - \frac{b_{-m}^{(2)}}{n^2 - 1} \frac{H'_m}{H_m} e^{-iz_0} e^{-im\phi} - x_1 i z_1 [e^{iz_0} e^{im\phi} - e^{-iz_0} e^{-im\phi}] \\
& + \frac{1}{n^2 - 1} \sum_{p \neq \pm m} \left[ a_p^{(1)} x_1 \frac{\partial S_p}{\partial x} + a_p^{(2)} S_p - b_p^{(2)} \frac{H'_p}{H_p} \right] e^{ip\phi} \\
& = \frac{f(\phi)}{R} \left( x_0 i z_1 [e^{iz_0} e^{im\phi} - e^{-iz_0} e^{-im\phi}] + x_1 [e^{iz_0} e^{im\phi} + e^{-iz_0} e^{-im\phi}] + x_0 \sum_{p \neq \pm m} a_p^{(1)} e^{ip\phi} \right) \\
& + \frac{1}{2} \frac{f^2(\phi)}{R^2} x_0 \left( 1 + x_0 \frac{H'_m}{H_m} \right) [e^{iz_0} e^{im\phi} + e^{-iz_0} e^{-im\phi}].
\end{aligned} \tag{6.17}$$

Note that the dependency on  $x_0$  is not explicitly written at the Hankel-functions and at  $S_p$ .

First, the orthogonality of  $e^{ip\phi}$  is used in Eq. (6.17). With the second (dimensionless) Fourier harmonics of the boundary

$$B_q = \frac{1}{2\pi R^2} \int_0^{2\pi} f^2(\phi) e^{iq\phi} d\phi \tag{6.18}$$

one obtains

$$b_p^{(2)} = \frac{1}{2} x_0^2 (n^2 - 1) [e^{iz_0} B_{m-p} + e^{-iz_0} B_{-m-p}] \tag{6.19a}$$

$$b_m^{(2)} = \frac{1}{2} x_0^2 (n^2 - 1) [B_0 + e^{-2iz_0} B_{-2m}] \tag{6.19b}$$

$$b_{-m}^{(2)} = \frac{1}{2} x_0^2 (n^2 - 1) [B_0 + e^{2iz_0} B_{2m}]. \tag{6.19c}$$

In the next step the quantities  $x_2$ ,  $z_1$ , and  $a_p^{(2)}$  are calculated from Eq. (6.16). Therefore, first, the orthogonality of  $e^{\pm im\phi}$  is used to get the system of equations

$$\begin{aligned}
\left[ -x_2 + \frac{x_1^2}{2x_0} \left( 1 + 2x_0 \frac{H'_m}{H_m} \right) - \frac{b_m^{(2)}}{n^2 - 1} \frac{H'_m}{H_m} \right] e^{iz_0} &= i x_1 z_1 e^{iz_0} + i x_0 z_1 [e^{iz_0} A_0 - e^{-iz_0} A_{-2m}] \\
&+ x_1 [e^{iz_0} A_0 + e^{-iz_0} A_{-2m}] + x_0 \sum_{p \neq \pm m} a_p^{(1)} A_{p-m} \\
&+ \frac{1}{2} x_0 \left( 1 + x_0 \frac{H'_m}{H_m} \right) [e^{iz_0} B_0 + e^{-iz_0} B_{-2m}]
\end{aligned} \tag{6.20a}$$

$$\begin{aligned}
\left[ -x_2 + \frac{x_1^2}{2x_0} \left( 1 + 2x_0 \frac{H'_m}{H_m} \right) - \frac{b_{-m}^2}{n^2 - 1} \frac{H'_m}{H_m} \right] e^{-iz_0} &= -ix_1 z_1 e^{-iz_0} + ix_0 z_1 [e^{iz_0} A_{2m} - e^{-iz_0} A_0] \\
&+ x_1 [e^{iz_0} A_{2m} + e^{-iz_0} A_0] + x_0 \sum_{p \neq \pm m} a_p^{(1)} A_{p+m} \\
&+ \frac{1}{2} x_0 \left( 1 + x_0 \frac{H'_m}{H_m} \right) [e^{iz_0} B_{2m} + e^{-iz_0} B_0]
\end{aligned} \tag{6.20b}$$

which is solved by

$$\begin{aligned}
z_1 = -\frac{ie^{2iz_0}}{4A_{-2m}} \left\{ \sum_{p \neq \pm m} a_p^{(1)} [e^{-iz_0} A_{p-m} - e^{iz_0} A_{p+m}] \right. \\
\left. - \frac{1}{2} \left( 1 + 2x_0 \frac{H'_m}{H_m} \right) [e^{2iz_0} B_{2m} - e^{-2iz_0} B_{-2m}] \right\}
\end{aligned} \tag{6.21}$$

$$\begin{aligned}
x_2 = x_0 \left\{ \frac{1}{2} \left( 3 [A_0 + e^{-2iz_0} A_{-2m}]^2 - [B_0 + e^{-2iz_0} B_{-2m}] \right) \right. \\
+ x_0 \frac{H'_m}{H_m} \left( [A_0 + e^{-2iz_0} A_{-2m}]^2 - [B_0 + e^{-2iz_0} B_{-2m}] \right) \\
\left. - e^{-iz_0} \sum_{p \neq \pm m} a_p^{(1)} A_{p-m} + 2iz_1 e^{-2iz_0} A_{-2m} \right\}.
\end{aligned} \tag{6.22}$$

Second, the orthogonality of  $e^{ip\phi}$  is used to solve Eq. (6.17) for  $a_p^{(2)}$  as

$$\begin{aligned}
a_p^{(2)} = \frac{(n^2 - 1)x_0}{S_p} \left\{ [A_0 + e^{-2iz_0} A_{-2m}] [e^{iz_0} A_{m-p} + e^{-iz_0} A_{-m-p}] \left( \frac{x_0}{S_p} \frac{\partial S_p}{\partial x} - 1 \right) \right. \\
+ \frac{1}{2} \left( 1 + x_0 \left[ \frac{H'_m}{H_m} + \frac{H'_p}{H_p} \right] \right) [e^{iz_0} B_{m-p} + e^{-iz_0} B_{-m-p}] \\
\left. + \sum_{k \neq \pm m} a_k^{(1)} A_{k-p} + iz_1 [e^{iz_0} A_{m-p} - e^{-iz_0} A_{-m-p}] \right\}.
\end{aligned} \tag{6.23}$$

Hence, all coefficients up to order  $\lambda^2$  in the expansion scheme (5.4) and  $z = z_0 + \lambda z_1$  have been calculated for asymmetric deformations.

In the following some remarks about the final second-order results are listed: (i) Since  $z_1$  is complex [see Eq. (6.21)] it affects the chirality in Eq. (6.5). (ii) For practical evaluations of the formulas it is useful to replace the infinite sums with finite sums ranging from  $p = -M$  to  $p = M$  with e.g.  $M = 150$ . (iii) In the formulas it is still assumed  $A_{-2m} = A_{2m}^* \neq 0$  to allow for a proper evaluation. (iv) Although the boundary conditions are evaluated in second order the parameter  $z$  is just fixed up to the order proportional to  $\lambda$ . Higher orders in  $z$  would

require to evaluate the boundary conditions in higher orders too.

## 6.4 Applications

In this section the previously derived formulas for the asymmetric-PT are applied to some example systems. The target is to predict the complex wave number, the mode pattern in the near- and the far-field, and the chirality of the optical modes and compare them to the numerically obtained values from the boundary element method (BEM) [Wiersig, 2003].

### The spiral

The first example is the spiral cavity defined by Eq. (2.19). The spiral has been shown to exhibit modes with strong chirality even for small notch size  $\epsilon$ , see Ref. [Wiersig et al., 2008]. Therefore it is an ideal example to illustrate the asymmetric-PT. Furthermore, the spiral has the advantage that  $A_q \neq 0$  for  $q \in \mathbb{Z}$  such that the derived formulas are formally applicable for all  $(m, l)$ . For the parameters  $(\epsilon, n) = (0.04, 2.0)$  studied e.g. in Refs. [Wiersig et al., 2008, Wiersig, 2008, Kullig and Wiersig, 2016b] the complex wave numbers for modes with  $l < 4$  and  $\text{Re } x < 20$  are shown in Fig. 6.1. Here, an overall good agreement of the asymmetric-PT with the numerical BEM is observed. Larger deviations occur only for larger values of  $\text{Re } x$  if two  $l$ -levels show an avoided crossing and therefore also exhibit a quasi-degeneracy in  $\text{Re } x$ . Note that such deviation occur in the symmetric-PT too. Further note that each of the points in Fig. 6.1 are actually two points according to the pair with  $\mu \in \{0, 1\}$ . They are too close to be distinguishable in the plot. But it can be seen in the magnification around  $\text{Re } x = 5.5$ . In this regime of low  $\text{Re } x$  the asymmetric-PT is able to predict the complex wave number for each mode of the pair accurately. (Note the different scales of  $\text{Im } x$  and  $\text{Re } x$  in the magnification.)

In order to show that the asymmetric-PT predicts also the chirality [see Eq. (6.5)] well despite that  $z$  is only linear in the perturbation parameter, the spiral with a slightly larger  $\epsilon = 0.05$  is analyzed in Fig. 6.2 (compare to Fig. 3.4 in Sec. 3.3.2). Similar to the good agreement in the complex wave number also the chirality matches overall well. Typically the predictions from the asymmetric-PT are slightly more accurate if the chirality is small which is consistent with a small  $\text{Im } z$ . Here, higher orders in the asymmetric-PT are expected to give improved accuracy since they allow to determine the second-order in the correction to  $z$ .

Note that for the spiral in both cases  $\epsilon = 0.04$  [Fig. 6.1] and  $\epsilon = 0.05$  [Fig. 6.2] the formal limit of the perturbation theory given by the criterion (5.9) is already reached at  $\text{Re } x \approx 11.4$  and  $\text{Re } x \approx 10.2$ , respectively. Nevertheless, even beyond this formal limit the asymmetric-PT gives reliable results.

Next, the predictions of the mode pattern is investigated in more detail: See Fig. 6.3 for a collection of several modes whose predictions from the asymmetric-PT are compared to the

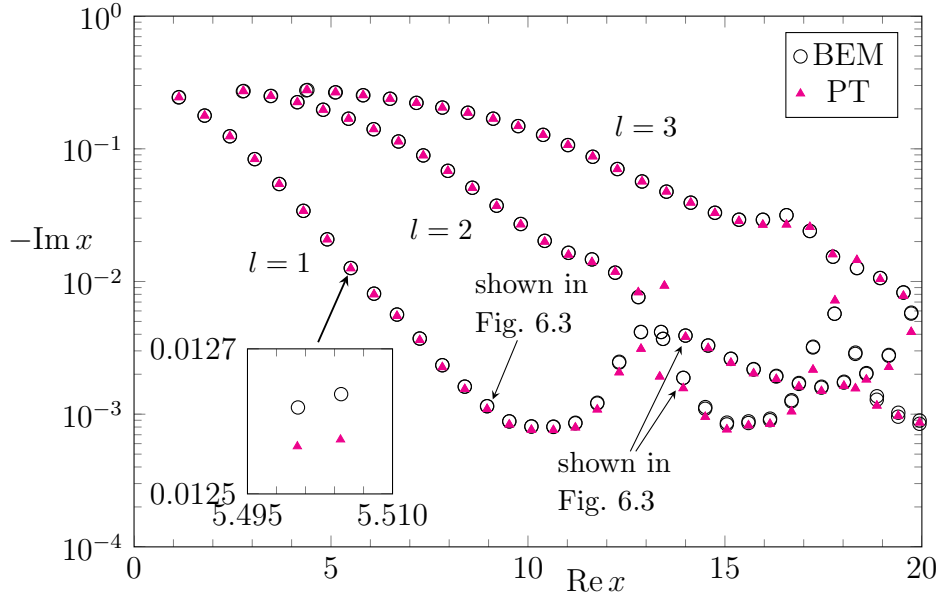


**Figure 6.1:** The complex wave numbers  $x = kR$  for the spiral cavity with  $(\epsilon, n) = (0.04, 2.0)$  are shown in complex plane. The asymmetric-PT predictions are illustrated by magenta triangles and the BEM results are drawn as open circles. The magnification illustrates the occurrence of the near-degenerate pairs.

numerical BEM results. In general the agreement is very well both in the near- and in the far-field pattern. In a closer look one sees that also the phases, i.e. the positions of the intensity extrema along the cavity's boundary nicely match. However, especially if the mode localizes on periodic quasiscar-like structures slight deviations between asymmetric-PT and BEM can be observed in the near-field pattern. In the far-field pattern the asymmetric-PT seems to slightly overestimate the fluctuations. However, the asymmetric-PT accurately predicts the dominant emission direction(s). Especially for the whispering-gallery modes in the spiral one observes a pronounced peak in the far-field pattern (for  $n = 2$ ) which indicates strong directional light emission opposite to the notch. This is in good agreement to the mechanism for directional emission in the notched ellipse [Wang et al., 2010] where a local boundary perturbation scatters the intensity to the opposite direction where it is focused to directional emission due to a lensing effect of the round cavity boundary.

In the following the mode number  $(m, l) = (14, 1)$  is fixed and the notch size  $\epsilon$  of the spiral is varied. This allows to investigate the predictions of the asymmetric-PT with increasing perturbation strength. Note that in the spiral cavity  $\epsilon$  is equal to the formal perturbation parameter  $\lambda$ . In Fig. 6.4 the results are summarized. The real part of  $x$  is dominated by the linear/first order which is directly related to the changing average radius of the cavity. Since the imaginary part of  $x_0$  in the circular cavity is quite small, the linear order in  $\text{Im } x$  almost does not contribute such that here the second-order dominates. The chirality  $\alpha_{\text{ch}}$  seems to be linear in  $\epsilon$  for very small deformations.



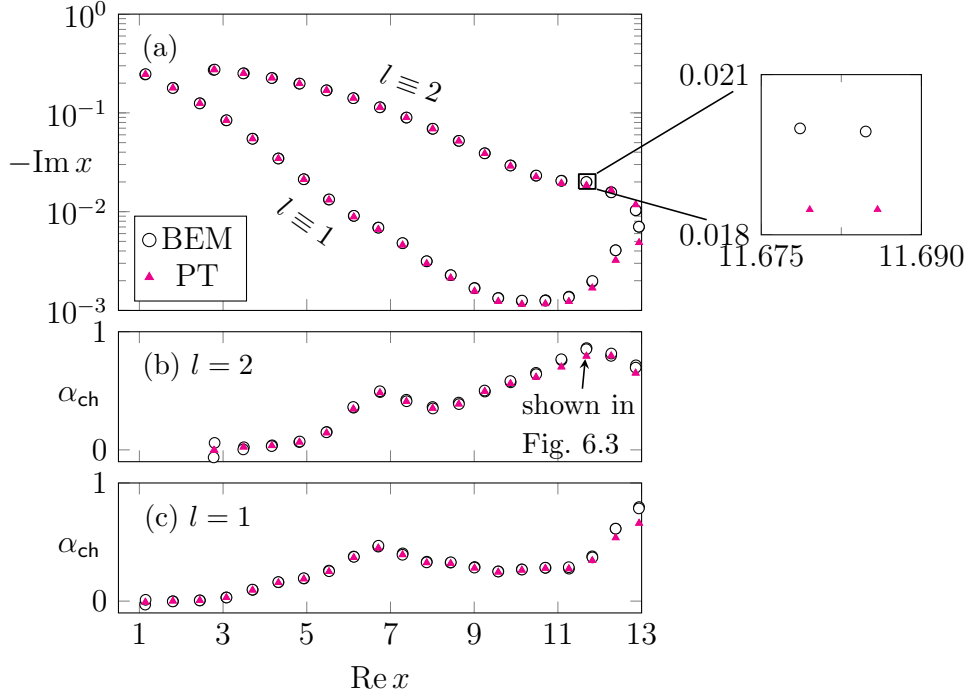


**Figure 6.2:** (a) The complex wave numbers of the spiral cavity with  $(\epsilon, n) = (0.05, 2.0)$  are shown in complex plane with a magnification around  $\text{Re } x = 11.68$ . (b) and (c) show the chirality of the  $l = 1$  and  $l = 2$  modes respectively. In all plots magenta triangles are asymmetric-PT predictions and open circles are BEM results.

In addition also the (complex) error of the asymmetric-PT is analyzed in Fig. 6.4(d-f) for the mode  $(m, l) = (14, 1)$ . Therefore, the difference

$$\text{Err}_c x = x_{\text{APT}} - x_{\text{BEM}} \quad (6.24)$$

between the perturbatively predicted  $x_{\text{APT}}$  and the BEM results  $x_{\text{BEM}}$  for the complex wave number is plotted. Since the asymmetric-PT is of second order in  $\lambda$  ( $\epsilon$  respectively) one expects the error to roughly follow  $\epsilon^3$ .

Since the spiral is an asymmetric cavity one cannot distinguish even and odd parity. However, because of the existence of mode pairs described by  $\mu = 0$  and  $\mu = 1$  the complex frequency splitting  $\Delta x = x_{\mu=0} - x_{\mu=1}$  can be calculated. The asymmetric-PT predictions for this splitting in the spiral are compared to the numerical BEM results in Fig. 6.5. The almost linear trend in the real part of the splitting is nicely captured by the asymmetric-PT. However the imaginary part of the splitting is beyond the second-order asymmetric-PT. At this point an extension to third order might give improved predictions for the splitting as in the symmetric-PT. But note that the imaginary part of the splitting only marginally contribute to the absolute value of  $\Delta x$  since it is more than one magnitude smaller than the real part.

## Notched circle

The next example investigated here is the asymmetrically notched circular cavity or notched circle for short. The boundary is described in polar coordinates by

$$\frac{r(\phi)}{R} = 1 + \sum_{\nu=0}^{N_\nu} \sum_{\xi=-\infty}^{\infty} \epsilon_\nu \exp\left(-\frac{(\phi - \phi_\nu - 2\pi\xi)^2}{2\sigma_\nu^2}\right) \quad (6.25)$$

where the parameters  $\epsilon_\nu$ ,  $\sigma_\nu > 0$ , and  $\phi_\nu$  determine the depth, width and position of the  $\nu$ -th notch, respectively. The notched circle has the advantage that the parameters of the notches, especially  $\phi_\nu$ , can be varied without changing the overall strength of the perturbation, i.e. the area where the deformed cavity varies from the circle can be kept almost constant. Furthermore, systems with two (and more) notches have already been discussed in literature: In Ref. [Schlehahn et al., 2013] it has been shown that the notched circle can be used to select the lasing mode in a cavity by spoiling the  $Q$ -factor of undesired modes. And in Ref. [Kim et al., 2014] the modes in the notched circle have been shown experimentally to exhibit a finite chirality near exceptional points. Moreover, the notched circle allows to study the limiting case where the asymmetric-PT converges to the symmetric-PT by placing notches of equal width symmetrically along the boundary.

In the following the double notched circle is discussed. First, in Fig. 6.6(a-c) the parameters  $(\epsilon_1, \sigma_1) = (-0.08, 0.07)$ ,  $(\epsilon_2, \sigma_2) = (-0.09, 0.03)$ , and  $\phi_1 = 0$  are fixed and  $\phi_2$  is varied. The non-trivial dependency of the complex wave number on  $\phi_2$  is quite well captured by the asymmetric-PT for both the real and the imaginary part of  $x$ . Note that the upper branch in Fig. 6.6(a) with higher  $\text{Re } kR$  has the lower  $Q$ -factor since the intensity maxima of the mode along the cavity's interface tend to be close to the notches. Therefore the mode is perturbed strongly by the notch. The oscillation in the real part of  $x$  has roughly a period of  $\pi/m$ . Shifting the notch position by this angle it interacts with the next intensity maximum along the cavity's interface.

Next, the parameters of the notches were changed to  $(\epsilon_1, \sigma_1) = (-0.056, 0.06)$  and  $(\epsilon_2, \sigma_2) = (-0.06, 0.035)$  such that the mode pair  $(m, l) = (10, 1)$  is close to an exceptional point (EP). By the variation of the second notch's position  $\phi_2$  the vicinity of the EPs is investigated in Fig. 6.6(d-f). The asymmetric-PT captures some main aspects like the almost degenerate wave numbers and the strong chirality. However in the detailed structure differences to the numerical BEM results are obtained: (i) In  $\text{Re } x$  the perturbation theory predicts two crossings close together while BEM results do not show these crossings; i.e. the system is not exactly on the EP but close to it, see magnification in Fig. 6.6(d). (ii) In the asymmetric-PT the predicted crossings in  $\text{Im } kR$  are not exactly at the same angles as the crossings in  $\text{Re } x$ . Furthermore, the curve shape between the predicted EPs differs from the BEM results, see magnification in Fig. 6.6(e). (iii) The asymmetric-PT predictions for the chirality converge to  $\pm 1$ . However

the change from 1 to  $-1$  is a sudden drop while BEM results show a smooth transition, see magnifications in Fig. 6.6(f).

Consequently, EPs seem to limit the predictions of the asymmetric-PT. Note that it is intuitive that the perturbation theory breaks down close to an EP because there two modes coalesce which is the strongest deviation from the unperturbed symmetric case where both modes are orthogonal. Maybe an improved ansatz of the wave function the vicinity of the EP could be considered to improve the accuracy around the EP. Nevertheless, for parameter  $\phi_2$  where the system is sufficiently away from the EP the mode properties are predicted well in Fig. 6.6(d-f). In order to compare the asymmetric-PT with the previously derived symmetric-PT a system with two notches of equal width  $\sigma_1 = \sigma_2 = 0.035$  which are placed at  $(\phi_1, \phi_2) = (0, 1.375)$  is studied. Since  $\epsilon_1 = -0.06$  is fixed a variation of  $\epsilon_2$  allows to cover the two symmetric cases  $\epsilon_2 = 0$  and  $\epsilon_2 = -0.06$  where the symmetric-PT is applicable. As shown in Fig. 6.7 in these cases of a symmetric cavity the asymmetric- and symmetric-PT predictions are the same. The asymmetric-PT additionally shows a good agreement for other values of  $\epsilon_2$  where no mirror-reflection symmetry is present.

### Constant width billiard

The next example is the billiard of constant width [see Eq. (4.21) and Fig. 4.16 in Sec. 4.2.3]. Note that this is a harder task since in the billiard of constant width the deformation to the circle is larger than in the examples discussed above. In Fig. 6.8(a) the asymmetric-PT predictions of the complex wave number are compared to the BEM results for  $l = 1$ . The agreement is very well until the real part of  $x$  becomes large such that the formal criterion for the perturbation theory (5.9) is violated. Since  $n = 2$  and the perturbation area  $\delta a/R^2 \approx 0.264$  Eq. (5.9) requires  $\text{Re } x \ll 7.8$  [see gray shaded region in Fig. 6.8].

The predictions for the complex wave number are accurate up to  $\text{Re } x = 7.8$ . However, the predictions for the chirality show errors already for  $\text{Re } x > 6$  [see Fig. 6.8(b)]. It is mentioned that close to  $\text{Re } x = 6$  the level  $l = 2$  [gray triangles in Fig. 6.8(a)] comes close to the level  $l = 1$  which can cause additional errors in the perturbation theory due to quasi-degeneracies in  $\text{Re } x$  between the levels [Dubertrand et al., 2008]. In the case of the constant width cavity these interactions seem to neutralize a strong chirality. However, for smaller values of  $\text{Re } x$  also the predictions for the chirality agree well with the numerically computed results.

Finally, in Fig. 6.9 the predictions for the near- and the far-field pattern for modes in the constant width cavity are shown. Consistently, with the predictions of the chirality the predictions are very well for small  $\text{Re } x$  (upper panels) and become erroneous for larger  $\text{Re } x$  (lower panel). In the BEM result of the faulty predicted mode pattern it can be seen that the mode is not identifiable rigorously as  $l = 1$  or  $l = 2$  what strengthens the argumentation that the  $l = 2$  level leads to the faulty predictions in this case.

However, the example of the billiard of constant width illustrates that the asymmetric-PT is not

based on the ray dynamic properties of the system. Especially a finite chirality is also predicted if the underlying classical phase space does not show (asymmetric) backscattering. Furthermore, ray chaos is not relevant for the asymmetric-PT since only the boundary deformation in real space is considered. However, if this deformation is strong such that the deformation area is large the asymmetric-PT (like the symmetric-PT) becomes incorrect. In Appendix A.5 it is demonstrated how a rescaled boundary can be used to minimize the perturbation area and therefore give improved accuracy of the perturbation theory.

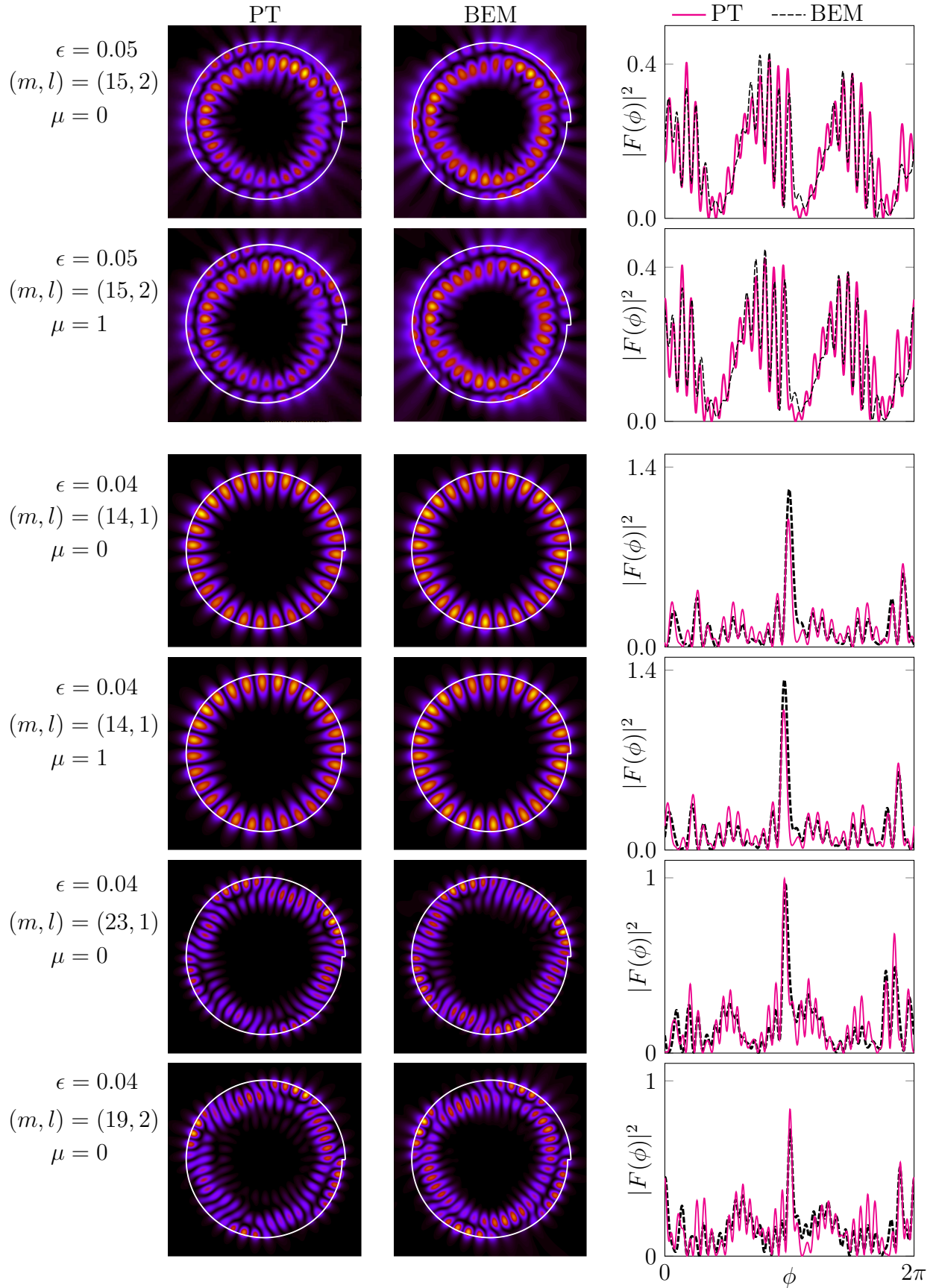


**Figure 6.3:** Modes in the spiral cavity: A comparison of the near-field pattern predicted by asymmetric-PT (left panels) and numerically determined with the BEM (middle panels). The far-field pattern are shown in the right panels (normalized to the area below the curves).

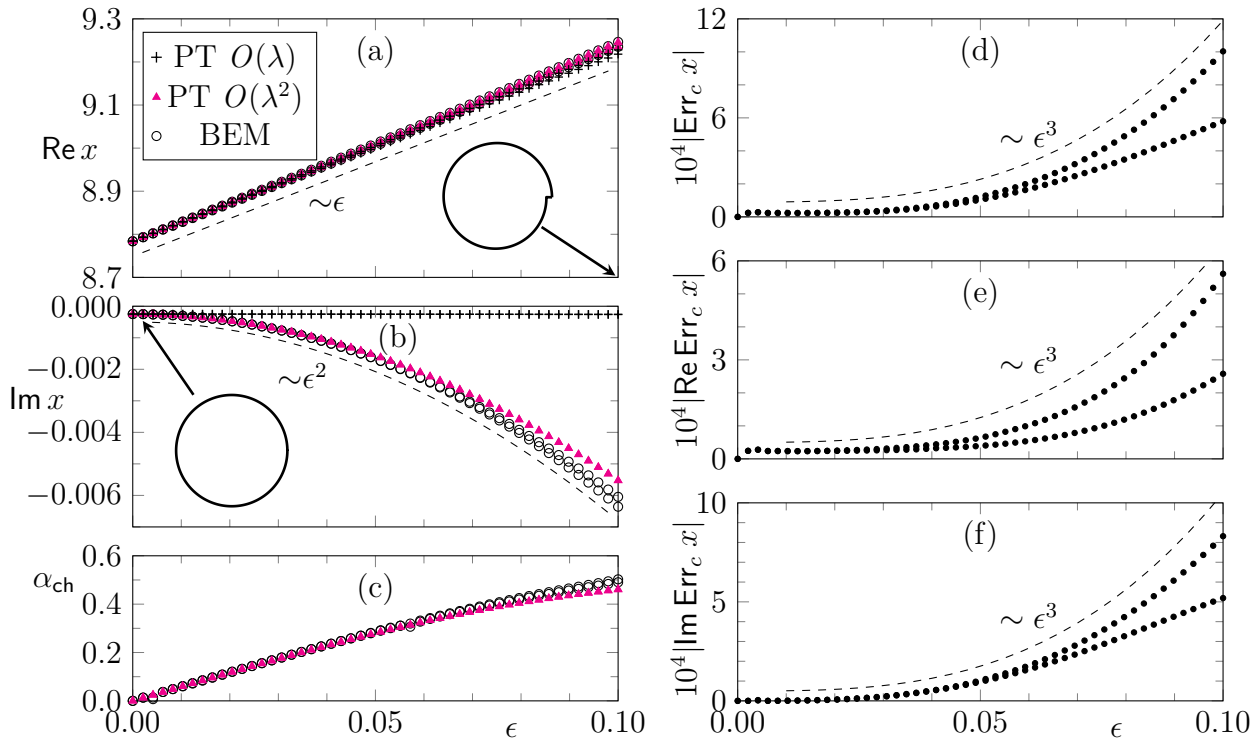


**Figure 6.4:** For the spiral cavity with  $(\epsilon, n) = (0.04, 2.0)$  and the optical mode pair  $(m, l) = (14, 1)$  the (a) real and (b) imaginary part of the complex wave number are shown. Magenta triangles (black crosses) are the second- (first-) order asymmetric-PT predictions and open circles are the BEM results. In (c) the chirality  $\alpha_{\text{ch}}$  [see Eq. (6.5)] is shown. In the right panel (d-f) the complex error  $\text{Err}_c x$  of the asymmetric-PT predictions is shown versus increasing deformation strength (notch size)  $\epsilon$ . Dashed curves in the plots illustrate the proportionality with powers of  $\epsilon$ .

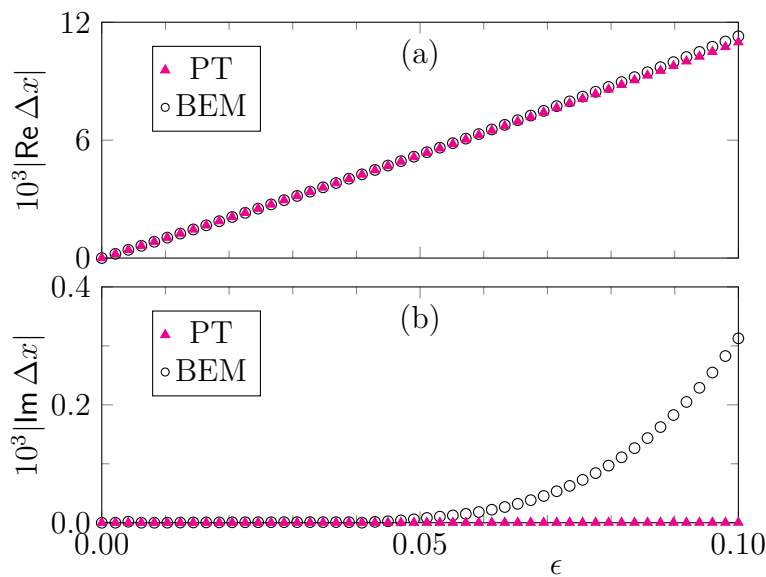


**Figure 6.5:** The (a) real and (b) imaginary part of the complex frequency splitting  $\Delta x$  of the mode pair  $(m, l) = (14, 1)$  in the spiral cavity with  $n = 2.0$  is shown. Magenta triangles are the predictions from the asymmetric-PT and black open circles are the BEM results.

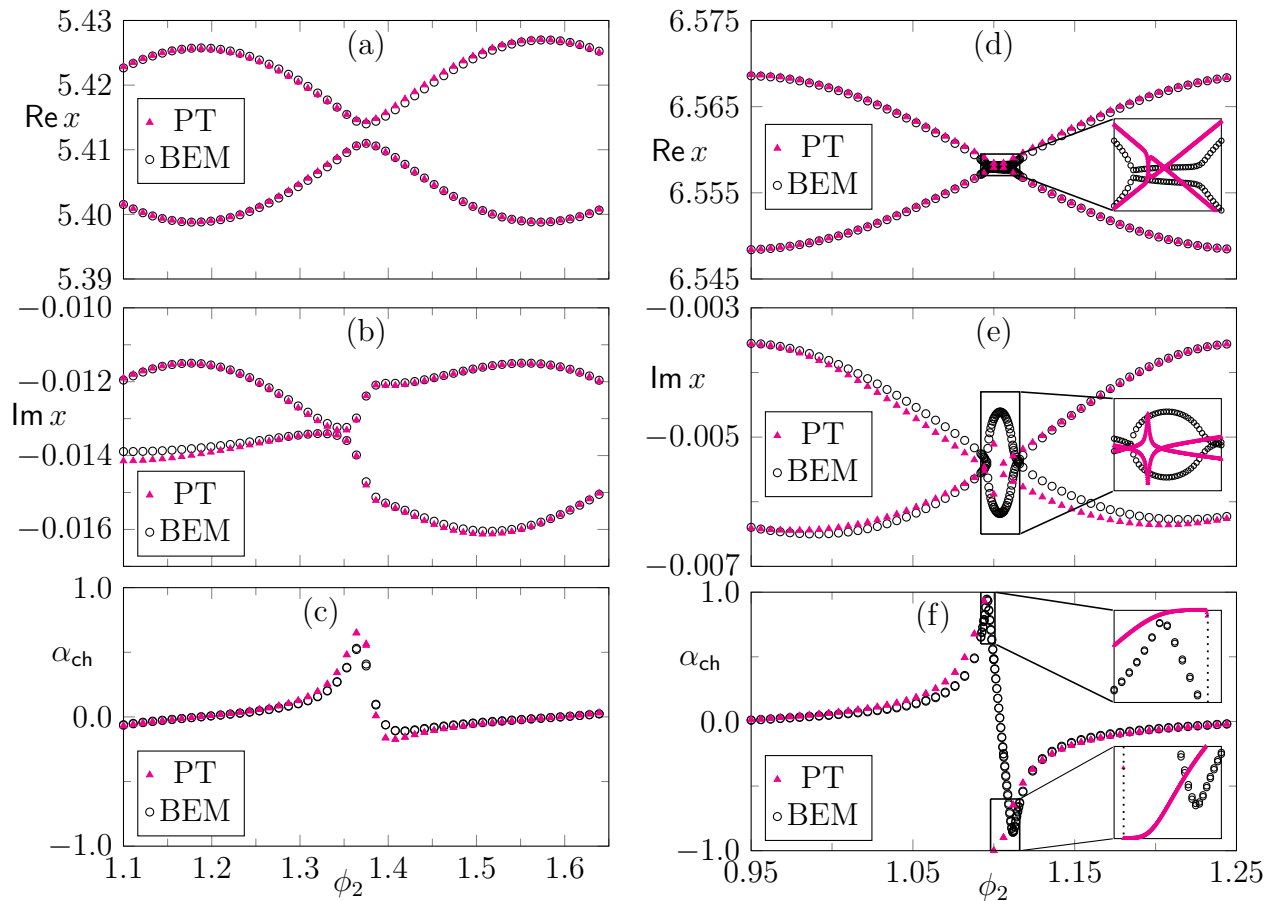


**Figure 6.6:** The figure shows (a/d) real and (b/e) imaginary part of the complex wave number  $x$  and (c/f) the chirality in a double notched cavity. In (a-c) the parameters are  $(\epsilon_1, \sigma_1, \epsilon_2, \sigma_2, n) = (-0.08, 0.07, -0.09, 0.03, 2.0)$  and in (d-f) the parameters  $(\epsilon_1, \sigma_1, \epsilon_2, \sigma_2, n) = (-0.056, 0.06, -0.06, 0.035, 2.0)$  have been fixed. The data for the mode (a-c)  $(m, l) = (8, 1)$  and (e-f)  $(m, l) = (10, 1)$  is shown. In all plots magenta triangles are asymmetric-PT predictions and black open circles are BEM results. In the magnifications in (f) a dashed line at  $\phi_2 = 1.0996$  is a guide to the eye.

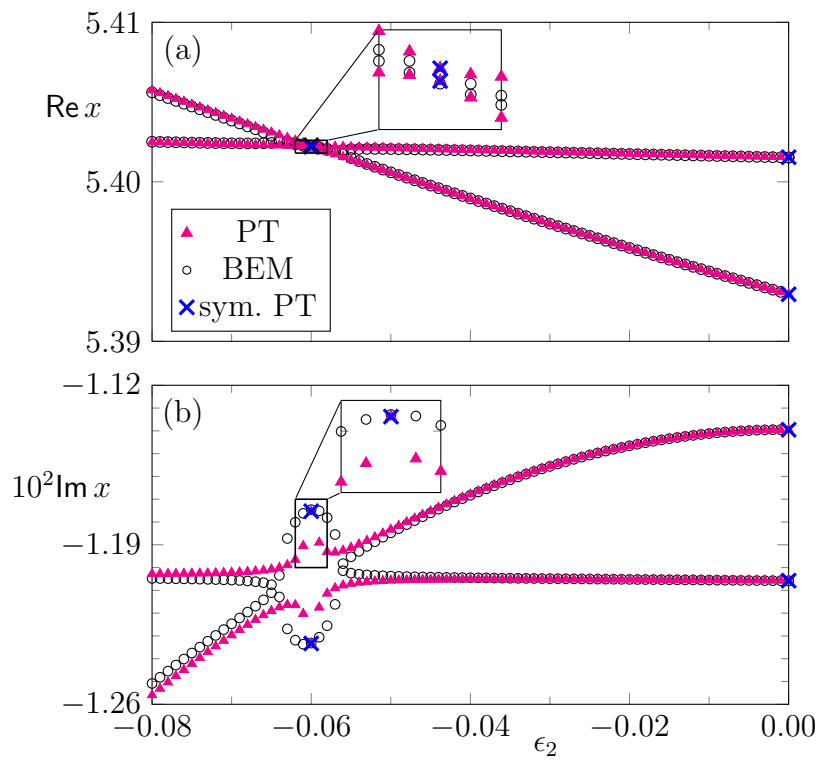


**Figure 6.7:** The (a) real and (b) imaginary part of the complex wave number of the mode  $(m, l) = (10, 1)$  in the notched cavity with  $\sigma_1 = \sigma_2 = 0.035$ ,  $(\phi_1, \phi_2) = (0, 1.375)$ ,  $\epsilon_1 = -0.06$ , and  $n = 2.0$ . is shown. Magenta triangles (blue crosses) are predictions from asymmetric-(symmetric-) PT and black open circles are BEM results.



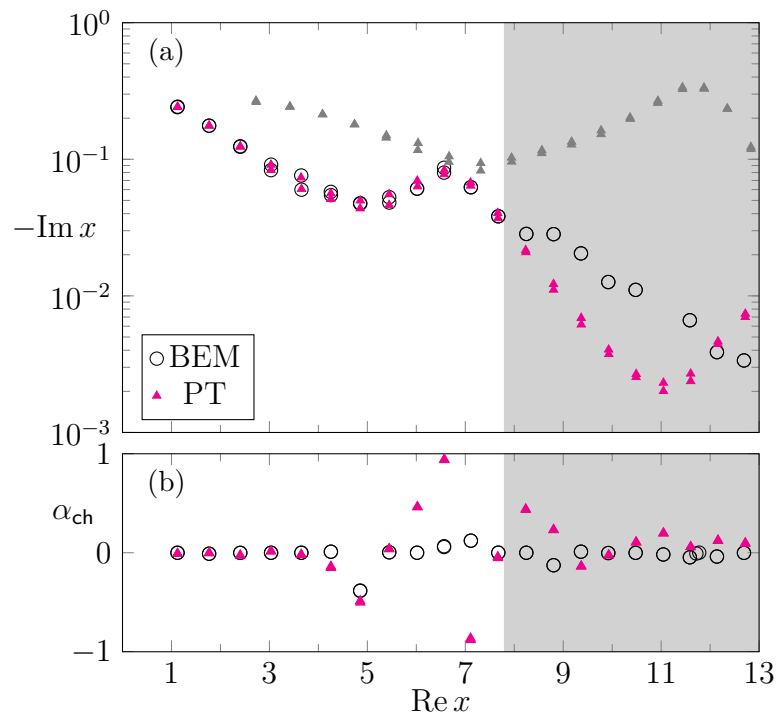


**Figure 6.8:** (a) The complex wave numbers for the billiard of constant width [see Fig. 4.16(a)] with  $n = 2.0$  are shown in complex plane for modes  $l = 1$ . (b) The chirality [see Eq. (6.5)] of the modes with  $l = 1$  is shown. Magenta triangles are predictions from the asymmetric-PT and open circles are BEM results. The gray triangles are predictions for the mode  $l = 2$ . In the gray shaded region the formal criterion (5.9) for the perturbation theory is violated.

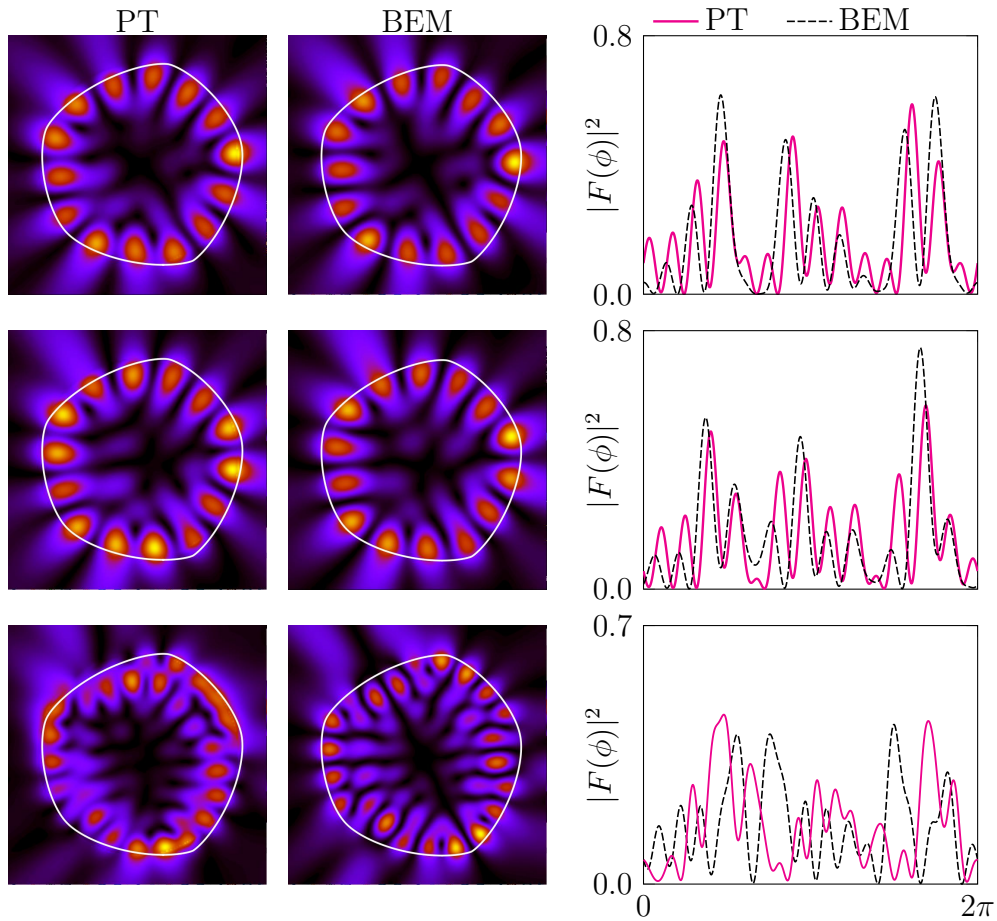


**Figure 6.9:** The intensity pattern of optical modes in the billiard of constant width with  $n = 2$  are shown in the left panel (asymmetric-PT) and middle panel (BEM). The right panel show the far-field intensity pattern which are normalized to the area below the curves. The mode numbers are  $(m, l, \mu) = (7, 1, 0)$ ,  $(m, l, \mu) = (7, 1, 1)$ , and  $(m, l, \mu) = (11, 1, 1)$  (from top to bottom).

---

## 6.5 Chapter summary

In this chapter the perturbation theory for symmetric deformed cavities [Dubertrand et al., 2008] has been extended to the case of asymmetric deformations. The derived formulas are analytical and reflect the key aspects of asymmetric cavities: The modes come in nearly-degenerate pairs where both modes have the same preferred sense of rotation. Therefore, in contrast to the symmetric-PT, the asymmetric-PT is a degenerate perturbation theory which first fixes the correct linear combination of the involved unperturbed modes in the circular cavity.

In the presented applications it has been shown that the asymmetric-PT not only predicts the complex wave number  $x$  and the chirality  $\alpha_{\text{ch}}$  but also the near-field and the far-field mode pattern very well. These results have been verified with the numerical BEM. The asymmetric-PT gives reliable results if the deformation area is small. But even if the formal criterion obtained by Dubertrand *et al.* [Dubertrand et al., 2008] for the symmetric-PT is not strictly fulfilled the predictions in many cases are reasonable.

The asymmetric-PT also captures signatures of exceptional points (EPs). However, for a detailed investigation of EPs more elaborate descriptions are necessary which are may given within higher orders in the perturbation theory.

Since the obtained formulas are analytical they allow for a further analysis regarding special situations. One example mentioned here are microdisk cavities with surface roughness where simple, analytical formulas for e.g. the average  $Q$ -spoiling can be derived [Wiersig and Kullig, 2017].

The main results of this chapter were published in Ref. [Kullig and Wiersig, 2016b].



# 7 Resonance-assisted tunneling for slightly deformed microdisk cavities

If an integrable system is perturbed resonance chains with an alternating sequence of stable and unstable periodic orbits develop naturally in phase space due to the Poincaré-Birkhoff theorem. In Sec. 2.2.1 this scenario was described for a deformed microdisk cavity. In quantum and wave mechanics such a resonance chain can drastically enhance the dynamical tunneling between classically disjoint regions in phase space which is hence called resonance-assisted tunneling (RAT). In this chapter the perturbation theory of RAT which was originally developed for kicked Hamiltonian systems (maps) [Keshavamurthy and Schlagheck, 2011, Brodier et al., 2002, Löck, 2009] is adapted to the case of microdisk cavities. Therefore, it is possible to predict the  $Q$ -factor of modes, the near-field and the far-field mode pattern. At the beginning of this chapter, in Sec. 7.1, the basic ideas of RAT in microdisk cavities and an outline for the RAT predictions is provided. Afterwards, in Sec. 7.2, an integrable approximation of the resonance chain in phase space is constructed and in Sec. 7.3 the mode and the  $Q$ -spoiling predictions based on this integrable approximation are derived. Finally, at the end of this chapter (Sec. 7.4) an outlook of a recently developed theory is given which allows to determine the splitting of the complex wave number between the even and the odd parity mode from the bouncing ball resonance chain in phase space. The chapter is summarized in Sec. 7.5.

## 7.1 Outline and basic ideas for the RAT predictions in microdisk cavities

In a recent experiment Kwak *et al.* [Kwak et al., 2015] showed that RAT plays an important role for microdisk cavities. In their experiments they verified that RAT couples optical modes and leads to avoided crossings in  $\text{Re } kR$ . Furthermore, they have shown that the coupling strength of the involved modes is proportional to the square of the resonance chain's area  $A$  in phase space.

The main purpose of the first part of this chapter is to demonstrate that not only  $\text{Re } kR$  is determined by RAT but also the  $Q$ -factor, the near-field, and the far-field pattern of the optical mode.

Already in Ref. [Bäcker et al., 2009] it was demonstrated that the  $Q$ -factor of an optical mode

is related to the dynamical tunneling process from regions of total internal reflection into the leaky region in phase space. Moreover, in Refs. [Nöckel and Stone, 1997, Hackenbroich and Nöckel, 1997, Shinohara et al., 2010, Shinohara et al., 2011, Lee and Chung, 2011, Creagh and White, 2012] it has been shown that dynamical tunneling in general can be used to explain the radiation of a mode from the microcavity. Hence, it is a natural guess that also RAT is able to predict the interesting properties of the mode.

In quantum mechanics RAT is usually studied in this context of kicked Hamiltonian systems (maps) with a mixed phase space. The target in these systems is to determine the tunneling rate of a metastable state in the regular region (regular island) into the chaotic part of the phase space. For this purpose a rich theory of RAT has been developed to predict e.g. the regular-to-chaotic tunneling rate (see Refs. [Keshavamurthy and Schlagheck, 2011, Brodier et al., 2002, Löck, 2009] and references therein for an introduction). Beside some recently developed semiclassical [Fritzsche et al., 2017], or perturbation-free [Mertig et al., 2016] approaches RAT is often treated within a perturbation theory for the phase space dynamics [Keshavamurthy and Schlagheck, 2011, Brodier et al., 2002, Löck et al., 2010, Eltschka and Schlagheck, 2005, Mouchet et al., 2006]. This perturbation theory for RAT in principle works as follows. In a first step one determines a fictitious integrable Hamiltonian  $H_0$  that mimics the regular dynamics near the resonance chain but smoothly interpolates through the resonance chain; i.e. the Hamiltonian  $H_0$  has no resonance chain but mimics the non-resonant tori of the regular region. From this Hamiltonian the so-called direct tunneling is derived [Bäcker et al., 2008, Mertig et al., 2013, Bäcker et al., 2010] which is e.g. quantified by a (direct) tunneling rate  $\gamma_m^d$  for the eigenstate  $\Psi_m$ . This direct tunneling dominates the dynamical (regular-to-chaotic) tunneling if the effects from the resonance chain are negligible.

In the second step, one models the resonance chain with an effective perturbative term  $\mathcal{V}_{r:s}$  to the integrable Hamiltonian  $H_0$ . This perturbative term results in a coupling of  $\Psi_n$  to  $\Psi_{n+jr}$  ( $j \in \mathbb{Z}$ ) where  $r:s$  is the order of the resonance chain, see Sec. 2.2.1. These restriction of the coupling related to  $r:s$  is called “selection rule” [Brodier et al., 2002]. Consequently, to predict the RAT-enhanced dynamical tunneling rate  $\gamma_m$  one superimpose the direct tunneling rates  $\gamma_{m+jr}^d$  with perturbatively determined coefficients from  $\mathcal{V}_{r:s}$  [Löck et al., 2010].

This procedure for kicked Hamiltonian systems is adapted to the case of slightly deformed optical microdisk cavities as follows. The fictitious integrable system  $H_0$  that smoothly interpolates through the resonance chain is actually not fictitious; it is the unperturbed circular cavity. Consequently, the eigenstates of  $H_0$  are identified with the optical modes in the circular cavity [Bäcker et al., 2009]. Hence, the direct tunneling rate  $\gamma_n^d$  is related to  $\text{Im } kR$  of a mode in the circle. Note that  $\text{Im } kR$  determines the decay rate of the mode which is governed by the tunneling rate from regions of total internal reflection into the leaky region in phase space. Since the microdisk is weakly deformed the main contribution to the  $Q$ -spoiling arises from the spoiling of  $\text{Im } kR$  whereas the change in  $\text{Re } kR$  is negligible. Therefore, the prediction of

$\text{Im } kR$  is equivalent to the prediction of  $1/Q = -2\text{Im } kR/(\text{Re } kR)$ .

Hence, in case of microdisk cavities the simplified procedure for the RAT predictions can be outlined [see Fig. 7.1]: (Step I) The resonance chain in the phase space of the deformed cavity is effectively modeled with a generalized pendulum Hamiltonian  $\mathcal{H}_{r:s}(q, p)$ . (Step II) One diagonalizes the Hamiltonian  $\mathcal{H}_{r:s}(q, p)$  perturbatively. With the derived coupling coefficients one can superimpose the modes of the circular cavity in order to predict the mode of the deformed cavity (near-field and far-field). And similarly one can superimpose  $\text{Im } kR$  of the circular cavity modes to predict  $\text{Im } kR$  of the mode in the deformed cavity.

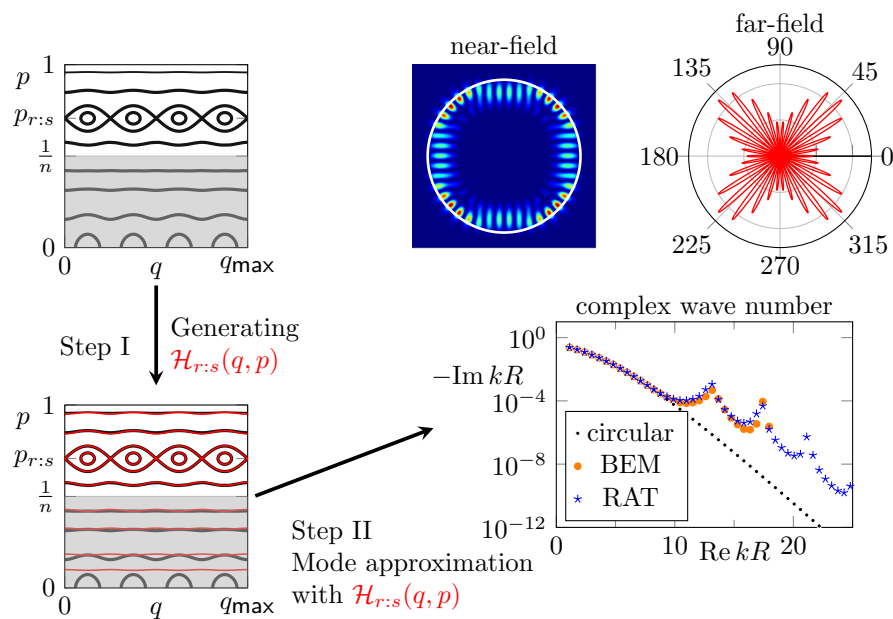


**Figure 7.1:** Overview of the procedure to determine RAT predictions in slightly deformed microdisk cavities.

In this outline there are two facts to mention: (i) The RAT-perturbation theory was originally developed for 1D kicked Hamiltonian systems. But in case of microdisk cavities one has in principle a 2D system. With the pendulum Hamiltonian  $\mathcal{H}_{r:s}(q, p)$  of the resonance chain one models this 2D system effectively by a Hamiltonian of a 1D system. Therefore one needs to keep in mind that the selection rules need to be adapted to respect both mode numbers; i.e. the mode  $(m, l)$  can couple to modes  $(m - jr, l + js)$  with  $j \in \mathbb{Z}$  [Kwak et al., 2015, Mertig, 2015]. (ii) Since microdisk cavities are open systems (with dielectric boundary conditions at the cavity's interface) the perturbative theory for the pendulum Hamiltonian  $\mathcal{H}_{r:s}(q, p)$  needs to be adapted in order to account for additional wave corrections. In particular the Goos-Hänchen shift is crucial.

## 7.2 The pendulum Hamiltonian – Phase-space approximation of a resonance chain

In this section the first step in the derivation of the RAT predictions, i.e. the phase-space approximation of a dominant resonance chain, is discussed for the case of microdisk cavities. Therefore, imagine a slightly deformed microdisk where a single resonance chain of order  $r:s$  is present in phase space at momentum  $p_{r:s} = \cos(\pi s/r)$  (compare to Sec. 2.2.1). On a basic level such a resonance-chain is modeled by a generalized pendulum approximation [Keshavamurthy and Schlagheck, 2011, Brodier et al., 2002, Kullig et al., 2014]

$$\mathcal{H}_{r:s}(q, p) = H_0(p) + 2\mathcal{V}_{r:s} \cos\left(2\pi r \frac{q}{q_{\max}} + q_0\right) \quad (7.1)$$

which creates  $r$  islands in phase space along the momentum where  $H_0(p)$  has a extremum. In the generalized pendulum Hamiltonian the function  $H_0(p)$  describes the dynamics of the unperturbed system without a resonance chain in a corotating frame. In case of microdisk cavities therefore  $H_0(p)$  can be obtained analytically from the dynamics in the circular cavity: In Sec. 2.2.1 the (dimensionless) frequency of the phase space dynamics in the circular cavity was obtained as [Eq. (2.11) divided by  $R$ ]

$$\omega(p) = 2 \arccos(p). \quad (7.2)$$

Furthermore, it is remarked that the (dimensionless) frequency of the  $r:s$  periodic orbit is  $\omega_{r:s} = 2\pi s/r$  [see Eq. (2.13)]. Therefore, the corotating frequency in Hamiltonian's equations of motion  $\omega(p) - \omega_{r:s} = \partial H_0(p)/\partial p$  can be integrated to define

$$H_0(p) = \int_{p_{r:s}}^p [\omega(\tilde{p}) - \omega_{r:s}] d\tilde{p}. \quad (7.3)$$

Consequently, for the  $r:s$  resonance chain in a microdisk cavity one obtains explicitly the dimensionless ( $k$  and  $R$  independent) Hamiltonian

$$H_0(p) = 2 \left( p \arccos(p) - \sqrt{1-p^2} + \sqrt{1-p_{r:s}^2} \right) - 2\pi p s/r. \quad (7.4)$$

From an expansion at  $p = p_{r:s}$  one can obtain the quadratic (pendulum) approximation

$$H_0(p) = \frac{(p - p_{r:s})^2}{2m_{r:s}} + \mathcal{O}[(p - p_{r:s})^3] \quad (7.5)$$

with  $m_{r:s} = -\sqrt{1-p_{r:s}^2}/2$ . Note that  $H_0$  is specified by the order  $r:s$  of the resonance chain only and does not depend on the deformation strength; i.e. the size of the resonance chain. An example for  $H_0(p)$  is shown for  $r:s = 4:1$  in Fig. 7.2(a) and for  $r:s = 9:2$  in Fig. 7.2(b). Note



that  $H_0(p)$  is concave due to the sign of the frequency  $\omega(p)$ . In the upper half of the phase space the frequency  $\omega(p)$  is positive.

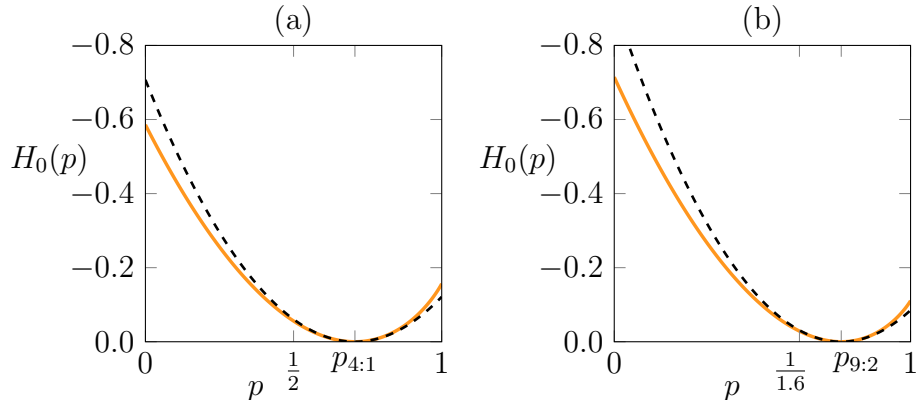


**Figure 7.2:** The figure shows the function  $H_0(p)$  given by Eq. (7.4) as orange solid curve and its quadratic approximation [Eq. (7.5)] as black dashed curve. In (a)  $r:s$  is set to 4:1 and in (b) to 9:2. Both examples are used later in this section.

The remaining system specific parameters in  $\mathcal{H}_{r:s}$  are  $\mathcal{V}_{r:s}$ ,  $q_0$  and  $q_{\max}$ . Here,  $q_{\max}$  and  $q_0$  are determined by the boundary's arc length and the position of the (un)stable periodic orbit of the resonance chain. Therefore, the remaining parameter quantifying the size of the resonances chain is  $\mathcal{V}_{r:s} > 0^1$ . In principle  $\mathcal{V}_{r:s}$  can be obtained via fitting. However, in the following strategies are discussed to obtain suitable values for  $\mathcal{V}_{r:s}$  from the billiard dynamics: First, one can use the area  $A$  of the resonance chain in the phase space of the deformed cavity and determine  $\mathcal{V}_{r:s}$  such that the pendulum approximation's resonance chain encloses the same area: With the quadratic approximation of  $H_0$  one derives as function for the separatrix

$$p(q) = p_{r:s} \pm \sqrt{2\mathcal{V}_{r:s} \sqrt{1 - p_{r:s}^2} [1 + \cos(2\pi r q / q_{\max} + q_0)]}. \quad (7.6)$$

By integrating this function the enclosed area of the separatrix in the pendulum Hamiltonian can be computed as function of  $\mathcal{V}_{r:s}$ . Finally, the value of  $\mathcal{V}_{r:s}$  matching the area  $A$  is

$$\mathcal{V}_{r:s} = \left( \frac{2\pi R}{q_{\max}} \right)^2 \frac{A^2}{256 \sqrt{1 - p_{r:s}^2}} \approx \frac{A^2}{256 \sqrt{1 - p_{r:s}^2}}. \quad (7.7)$$

Alternatively, an estimation for a suitable parameter  $\mathcal{V}_{r:s}$  can be obtained from the linearized dynamics around the stable fixed point [Eltchka and Schlagheck, 2005, Löck, 2009]: With the

<sup>1</sup>Note that here  $\mathcal{V}_{r:s}$  is defined positive. A negative sign in  $\mathcal{V}_{r:s}$  can be absorbed in  $q_0$ .

substitution  $\tilde{p} = p - p_{r:s}$  and  $\tilde{q} = q + q_{\max}q_0/(2\pi r)$  one writes

$$\dot{\tilde{q}} = \frac{\partial \mathcal{H}_{r:s}}{\partial p} = \frac{-2\tilde{p}}{\sqrt{1 - p_{r:s}^2}} \quad (7.8a)$$

$$\dot{\tilde{p}} = -\frac{\partial \mathcal{H}_{r:s}}{\partial q} = 2\mathcal{V}_{r:s} \frac{2\pi r}{q_{\max}} \sin\left(2\pi r \frac{\tilde{q}}{q_{\max}}\right) \approx 2\mathcal{V}_{r:s} \left(\frac{2\pi r}{q_{\max}}\right)^2 \tilde{q} \quad (7.8b)$$

with  $p_{r:s} = \cos(\pi s/r)$  [see Eq. (2.14)]. Note that in the approximation in Eq. (7.8b) the sine has been linearized to obtain a linear system whose solution can be written as

$$\begin{pmatrix} \tilde{q}(t) \\ \tilde{p}(t) \end{pmatrix} = \begin{pmatrix} \cos(\omega t) & C_1 \sin(\omega t) \\ C_2 \sin(\omega t) & \cos(\omega t) \end{pmatrix} \begin{pmatrix} \tilde{q}(0) \\ \tilde{p}(0) \end{pmatrix} \quad (7.9)$$

with constants  $C_{1/2}$  and

$$\omega^2 = \frac{4r^2 \mathcal{V}_{r:s}}{\sqrt{1 - p_{r:s}^2}} \left(\frac{2\pi}{q_{\max}}\right)^2. \quad (7.10)$$

Equation (7.9) can now be compared for  $t = r \cdot R$  with the linearized billiard map [Eq. (2.16)] given by the monodromy matrix  $J^r$  which yields

$$\text{Tr } J^r = 2 \cos(\omega r) \quad (7.11)$$

Consequently, with Eq. (7.10) one derives

$$\mathcal{V}_{r:s} = \left(\frac{q_{\max}}{2\pi R}\right)^2 \frac{\sqrt{1 - p_{r:s}^2}}{4r^4} \left(\arccos \left[\frac{\text{Tr } J^r}{2}\right]\right)^2. \quad (7.12)$$

Since the pendulum Hamiltonian has a  $r$ -fold rotational symmetry and also the systems which will be discussed in the following have this symmetry, it is practical to slightly simplify the derived result further to

$$\mathcal{V}_{r:s} = \left(\frac{q_{\max}}{2\pi R}\right)^2 \frac{\sqrt{1 - p_{r:s}^2}}{4r^2} \left(\arccos \left[\frac{\text{Tr } J^1}{2}\right]\right)^2. \quad (7.13)$$

Here, not the monodromy matrix of the  $r$ -fold iterated map  $J^r$  but the one obtained for a single iteration  $J^1$  is used.

The cavity which is considered in the following as illustration example is the multipole cavity (also called microflower) [Creagh and White, 2012, Boriskina et al., 2006, Qiu et al., 2007]. It is defined in polar coordinates by

$$\frac{r(\phi)}{R} = 1 + \epsilon \cos(N\phi) \quad (7.14)$$

with  $N \in \mathbb{N}$ . The cavity has a  $N$ -fold rotational symmetry which implies that the lowest order resonance chain has  $r = N$  because every  $r < N$  would violate the rotational symmetry. Therefore such a deformation allows to vary the desired dominant resonance chain in phase space. Especially, the three systems labeled with  $\mathcal{A}$ ,  $\mathcal{B}$ , and  $\mathcal{C}$  are used in the following. They are specified by the combinations of  $(\epsilon, N)$  and the refractive index  $n$  as listed in Tab. 7.1. The phase space dynamics of these three systems is shown in Fig. 7.3. Note that the refractive index is chosen such that most of the larger undesired resonance chains are inside the leaky region and therefore are negligible for the  $Q$ -spoiling.

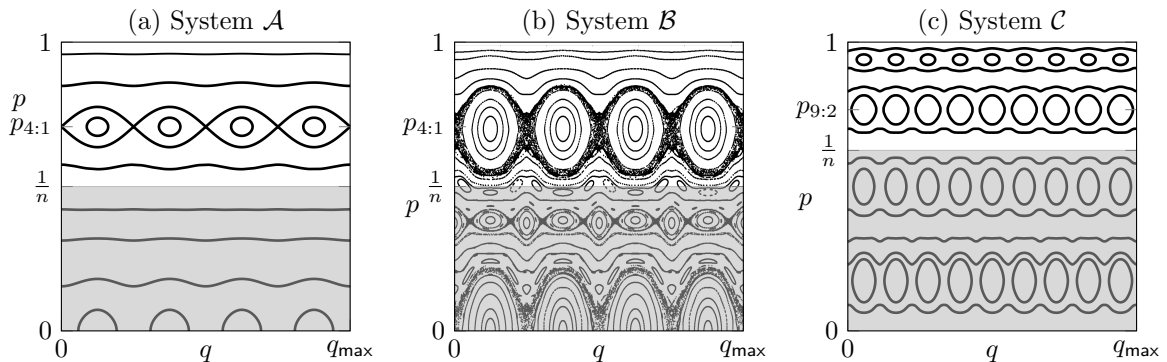


**Figure 7.3:** The phase space dynamics in the multipole cavities [Eq. (7.14)] specified by the parameters in Tab. 7.1 are shown as black curves/dots. The bright gray shaded region is the leaky region.

For these systems  $\mathcal{A}$ ,  $\mathcal{B}$ , and  $\mathcal{C}$  the generalized pendulum approximation [Eq. (7.1)] of the dominant resonance chain is computed with a nice agreement to the billiard dynamics as shown in Fig. 7.4. In Systems  $\mathcal{A}$  and  $\mathcal{C}$  the perturbation by the boundary deformation is small. Therefore also the resonance chain is not too large and surrounded only by a small chaotic layer. In these cases the value of  $\mathcal{V}_{r:s}$  from the stable fixed point [Eq. (7.13)] is accurate since the system is near-integrable. On the other hand in system  $\mathcal{B}$  the perturbation from the boundary deformation is quite strong resulting in a large resonance chain with large chaotic layer. Here, it is not sufficient to estimate  $\mathcal{V}_{r:s}$  from the stable fixed point. In such a case it is rather practical to derive the approximated area  $A$  of the resonance chain from the billiard dynamics numerically and use Eq. (7.7) for a proper value of  $\mathcal{V}_{r:s}$ .

System	$\epsilon$	$N$	$n$	$r:s$
System $\mathcal{A}$	0.0025	4	2.0	4:1
System $\mathcal{B}$	0.013	4	2.0	4:1
System $\mathcal{C}$	0.002	9	1.6	9:2

**Table 7.1:** The tabular shows the boundary parameters [see Eq. (7.14)] of the three systems which are discussed here. Furthermore, the refractive index  $n$  and the order of the dominant resonance chain above the critical line  $p = 1/n$  is shown.

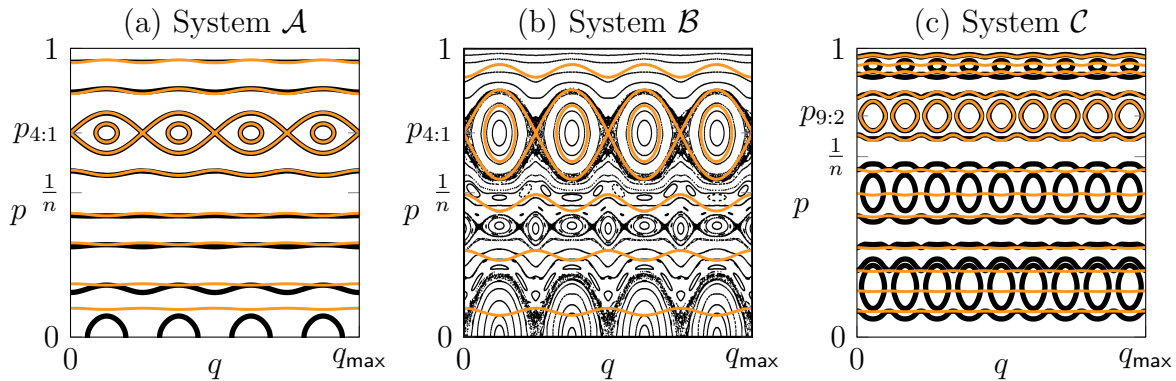


**Figure 7.4:** The contour curves of the generalized pendulum approximation [Eq. (7.1)] for the example systems are shown as orange curves. The underlying billiard dynamics is shown as black curves/dots.

In all of the shown cases the generalized pendulum approximation nicely mimics the phase space structure of the dominant resonance chain. In a more challenging case where e.g. the resonance chain is not along a line of constant momentum  $p$  additional canonical transformations can be applied to the generalized pendulum to match the billiard dynamics. In case of kicked Hamiltonian systems this procedure has been used in Ref. [Kullig et al., 2014] (based on the iterative canonical transformation method [Löbner et al., 2013]). Furthermore, for very complicated structures of the resonance chain a more general ansatz

$$\mathcal{H}_{r:s}(q, p) = H_0(p) + \sum_z 2V_{r:s,z}(p) \cos\left(2\pi r z \frac{q}{q_{\max}} + q_{0,z}\right) \quad (7.15)$$

would be promising. Such a normal form ansatz [Leboeuf and Mouchet, 1999] is also used in the case of kicked Hamiltonian systems for the predictions of RAT from a regular island into the chaotic region of the phase space [Keshavamurthy and Schlagheck, 2011, Brodier et al., 2002, Löck, 2009, Mertig et al., 2016, Fritzsche et al., 2017]. However, for the microdisk cavities studied here it turns out that the simple ansatz (7.1) is sufficient to model the dominant resonance chain, see Fig. 7.4.

### 7.3 $Q$ -spoiling and mode prediction from the phase-space approximation

In this section the second step in the derivation of the RAT predictions is derived. In particular the generalized pendulum  $\mathcal{H}_{r:s}$  is treated perturbatively in order to obtain the modes of the deformed cavity. In the following it is distinguished between the mode of the circular cavity  $\Psi_{m,l}$  with  $x_{m,l} = kR$  and the mode in the deformed cavity  $\tilde{\Psi}_{m,l}$  with  $\tilde{x}_{m,l} = \tilde{k}R$ .

With the selection rules for RAT, i.e. that modes  $(m - jr, l + js)$  with  $j \in \mathbb{Z}$  are coupled via

the resonance chain, the central assumption in this section is that one can express the mode of the deformed cavity as

$$\tilde{\Psi}_{m,l}(\vec{r}, \tilde{x}) = \mathcal{N}^{-1} \sum_{j \geq 0} a_j \Psi_{m-jr, l+j_s}(\vec{r}, \tilde{x}). \quad (7.16)$$

Here, the coefficients  $a_j \in \mathbb{C}$  are normalized by  $\mathcal{N}^2 = \sum_{j \geq 0} |a_j|^2$ . To be consistent with the limit of vanishing deformation  $a_0$  is set to one. In leading order  $\|\tilde{\Psi}\|^2$  defined by

$$\|\tilde{\Psi}(t)\|^2 = \int_{\text{cavity}} |\tilde{\Psi}|^2 dx dy = e^{-\Gamma t}. \quad (7.17)$$

is proportional to the loss rate  $\Gamma = -2c \text{Im} \tilde{x}/R$ . Therefore, the second central assumption for the  $Q$ -spoiling is

$$\text{Im} \tilde{x}_{m,l} = \mathcal{N}^{-2} \sum_{j \geq 0} |a_j|^2 \text{Im} \tilde{x}_{m-jr, l+j_s}. \quad (7.18)$$

Remaining, the coefficient  $a_j$  need to be determined from the Hamiltonian  $\mathcal{H}_{r:s}$ . To do so, the term  $2\mathcal{V}_{r:s} \cos(\dots)$  is treated as perturbation to  $H_0$  in Eq. (7.1). The result of the perturbation theory is known from literature [Brodier et al., 2002, Eltschka and Schlagheck, 2005, Löck et al., 2010]. With the selection rules regarding both  $m$  and  $l$  it yields

$$a_j = \prod_{u \leq j} \frac{\mathcal{V}_{r:s} e^{i\phi_0}}{H_0(p_{m,l}^{\text{mod}}) - H_0(p_{m-ur, l+us}^{\text{mod}})}. \quad (7.19)$$

About this result there are two remarks to mention: First, the applied perturbation theory is in the following sense not a standard perturbation theory. The mode with mode numbers  $(m, l)$  can directly couple to the mode  $(m-r, l+s)$ . However the coupling to the mode  $(m-2r, l+2s)$  is indirect via the mode  $(m-r, l+s)$ ; and so on for the higher coupling terms. That is the reason for the product in Eq. (7.19). The second remark is that in Eq. (7.19) the modified momenta  $p_{m,l}^{\text{mod}}$  have been introduced in order to respect the dielectric boundary conditions of the microdisk cavity. In the following the meaning of the modified momenta is explained and an explicit formula for  $p_{m,l}^{\text{mod}}$  is derived.

The Hamiltonian  $\mathcal{H}_{r:s}$  is modeled such that it mimics the closed system (billiard) dynamics of the cavity. However, in the open system the Goos-Hänchen shift and the Fresnel filtering lead to wavelength depended corrections that are usually incorporated in the so-called extended ray dynamics. Consequently, the resonance chain appears slightly different in the phase space of the extended ray dynamics. However, incorporating the openness into the ray dynamics and adapt  $\mathcal{H}_{r:s}$  is disadvantageous here because it would require to set up a new  $\mathcal{H}_{r:s}$  for each individual mode. Furthermore,  $H_0(p)$  would not be known analytically. Therefore, here a slightly different strategy is followed. Instead of adapting the ray dynamics to the wave

mechanics, here, the momentum  $p_{m,l}$  of the mode is modified to fit to the corresponding closed system billiard dynamics. It is known that the mode  $(m, l)$  localizes at the momentum  $p_{m,l} = m/(n\text{Re } x_{m,l})$  [see Eq. (3.39); Ref. [Nöckel, 1997]]. Therefore, the modified momentum is defined as  $p_{m,l}^{\text{mod}} = m/(n\text{Re } x_{m,l}) - \Delta p_{\text{open}}$  where  $\Delta p_{\text{open}}$  represents the corrections from the extended ray dynamics.

Next, an explicit expression for  $\Delta p_{\text{open}}$  is derived using various approximations. (i) Since the Fresnel filtering is typically small for large  $\text{Re } x$  it is neglected here completely. Nevertheless, the remaining Goos-Hänchen shift  $\Delta q(p)$  leads to a shift of the periodic orbits of the  $r:s$  resonance chain in  $p$ . An explicit formula for this periodic-orbit shift (POS) was derived in Ref. [Unterhinninghofen and Wiersig, 2010]

$$\Delta p_{\text{POS}} = \frac{\Delta q(p_{r:s})}{2r_c} \sqrt{1 - p_{r:s}^2} \quad (7.20)$$

where  $r_c$  is the radius of curvature. (ii) The slight differences of  $r_c$  of the stable and unstable periodic orbit are ignored; i.e. the average radius of curvature  $r_c \approx R$  is used. (iii) The Goos-Hänchen shift  $\Delta q(p)$  is approximated with the Artmann result [Artmann, 1948]

$$\Delta q(p) = \frac{2p}{\sqrt{n^2 p^2 - 1} \sqrt{1 - p^2 \text{Re } k}}. \quad (7.21)$$

This approximation seems to be outdated since more accurate estimations are known [Stockschläder et al., 2014, Unterhinninghofen and Wiersig, 2010]. However, the Artmann approximation is on the one hand suitable for a resonance chain being located in between but not close to  $p = 1/n$  and  $p = 1$ . And on the other hand the Artmann approximation is analytical and allows to compactly express the POS as shift in the mode number  $m$  as

$$\Delta m_{\text{POS}} = \frac{p_{r:s}}{\sqrt{p_{r:s}^2 - n^{-2}}}. \quad (7.22)$$

Therefore, also the modified momentum can be written in the compact form

$$p_{m,l}^{\text{mod}} = \frac{1}{n\text{Re } x_{m,l}} (m - \Delta m_{\text{POS}}). \quad (7.23)$$

Using this modified momentum the  $a_j$  are determined via Eq. (7.19). Consequently, the mode [Eq. (7.16)] with  $\text{Im } \tilde{x}_{m,l}$  from Eq. (7.18) can be computed. For the real part of the complex wave number it is  $\text{Re } \tilde{x}_{m,l} = \text{Re } x_{m,l}$  assumed here. Since in Ref. [Kwak et al., 2015] RAT was measured in the real part of the complex wave number an extended theory would need to account for the corrections in  $\text{Re } \tilde{x}_{m,l}$  too. However, for the  $Q$ -spoiling which is the main target of this section the relatively small changes in  $\text{Re } \tilde{x}_{m,l}$  are negligible since  $\text{Im } \tilde{x}_{m,l}$  changes by several orders of magnitude.

It is worth to mention that the coupling of the modes  $(m, l)$  and  $(m - r, l + s)$  given by  $a_1$

in Eq. (7.19) is proportional to  $A^2$  where  $A$  is the area of the resonance chain in phase space. This proportionality was measured experimentally in Ref. [Kwak et al., 2015].

Additionally to the prediction of  $\tilde{\Psi}_{m,l}$  and  $\text{Im } \tilde{x}_{m,l}$  the coefficients  $a_j$  allow to predict the far-field pattern  $F(\phi)$  of the mode in a similar manner as Eq. (7.16) namely as superposition of the far-field pattern of the circular modes

$$F(\phi) \approx \sum_{j \geq 0} a_j \frac{e^{-i\pi(m-jr)/2}}{H_{m-jr}(\tilde{x}_{m,l})} \chi_{\pm, m-jr}(\phi) \quad (7.24)$$

Here,  $\chi_{\pm, m-jr}(\phi)$  is either the  $(-)$  sine or the  $(+)$  cosine with period  $2\pi/(m-jr)$ .

### Application to example systems

Next, the derived predictions are applied to the example systems introduced in the previous section, see Tab. 7.1. The values for the coupling strength  $\mathcal{V}_{r:s}$  and the mode number shift  $\Delta m_{\text{POS}}$  due to the POS are shown in Tab. 7.2.

System	$\mathcal{V}_{r:s}$	$\Delta m_{\text{POS}}$
System $\mathcal{A}$	0.0017965	1.41421
System $\mathcal{B}$	0.0085653	1.41421
System $\mathcal{C}$	0.00116968	1.72944

**Table 7.2:** The tabular shows the parameters  $\mathcal{V}_{r:s}$  for the coupling strength, i.e. the size of the resonance chain, and the mode number shift [Eq. (7.22)] due to the POS for the three systems studied here.

With these parameter Eq. (7.18) can be evaluated which lead to the predictions of  $\text{Im } \tilde{x}_{m,l}$  shown in Fig. 7.5 for the three systems  $\mathcal{A}$ ,  $\mathcal{B}$ , and  $\mathcal{C}$ .<sup>2</sup> The periodic peaks in  $\text{Im } x$  are characteristic for RAT; compare e.g. to the peaks in the eigenphase splitting in Ref. [Brodier et al., 2002] or to the peaks in the tunneling rate in Ref. [Löck et al., 2010]. The agreement of the RAT predictions to the numerical BEM is very well keeping in mind that a variety of approximations has been used. A further comparison to the BEM results for larger  $\text{Re } x$  is hindered by the small  $|\text{Im } \tilde{x}| \lesssim 10^{-6}$  which cannot be resolved accurately by the BEM. This restrictions does not hold for the RAT predictions since the evaluation of the derived formulas is quite simple from a numerical point of view. However for very large  $\text{Re } x$  it is expected that Eq. (7.18) becomes inaccurate because resonance chains of higher order will become important. These effects from the so-called multi-resonance-assisted tunneling are so far not implemented. However it is remarkable that even in system  $\mathcal{B}$  reasonable predictions are obtained in the shown

<sup>2</sup>It is mentioned that for the System  $\mathcal{C}$  the quadratic approximation of  $H_0$  is used which gives a slightly better result than the full  $H_0$  from Eq. (7.4). The suspected reason are the additional effects from the resonance chain  $r:s=9:1$  closer to  $p = 1$ , see Fig. 7.3(c) which result in an additional perturbation to  $H_0$ .

range of  $\text{Re } x$  although the resonance chain has a considerable large chaotic layer; i.e. the system cannot be treated as near-integrable.

In Fig. 7.6 the predictions of the near-field mode pattern are shown for the modes of system  $\mathcal{A}$  around the first peak in  $\text{Im } \tilde{x}$ . They are compared to the ones obtained by BEM. Additionally, in order to illustrate the origin of the peaks in  $\text{Im } \tilde{x}$  the curve  $H_0(p)$  with the marked modified momenta is shown. In (a), before the peak, the mode is quite similar to a mode in the circular cavity. Here, the difference in the energy denominator  $H_0(p_{m,l}^{\text{mod}}) - H_0(p_{m-r,l+s}^{\text{mod}})$  in Eq. (7.19) is large such that the coupling of the modes  $(m, l)$  and  $(m - r, l + s)$  is weak. In particular  $a_1$  is small. By increasing the mode number  $m$  the momentum  $p_{m,l}$  and therefore also  $p_{m,l}^{\text{mod}}$  becomes larger. Consequently,  $H_0(p_{m,l}^{\text{mod}})$  becomes of the order of  $H_0(p_{m-r,l+s}^{\text{mod}})$  as shown in Fig. 7.6(b) which results in a strong coupling of the modes  $(m, l)$  and  $(m - r, l + s)$ . Here the mode of the deformed cavity localizes at the unstable periodic orbit which is correctly predicted by the RAT perturbation theory. If one increases the mode number  $m$  further to  $m = 22$  as shown in Fig. 7.6(c) one reaches the case where  $H_0(p_{m,l}^{\text{mod}})$  is almost degenerate with  $H_0(p_{m-r,l+s}^{\text{mod}})$ . Here, the predictions of the mode pattern collapse due to the small denominator in Eq. (7.19). Note that in this case  $\text{Im } \tilde{x}_{m,l}$  do not diverge due to the normalization factor  $\mathcal{N}^{-2}$ . It is rather determined by roughly the value of  $\text{Im } x_{m-r,l+s}$  because of the large coupling to this mode. Further note that the predicted near-field pattern is therefore also quite similar to the one of the mode  $\tilde{\Psi}_{m-r,l+s}$  (not shown). After further increasing the mode number to  $m = 23$  [see Fig. 7.6(d)] the modes  $(m, l)$  and  $(m - r, l + s)$  become off-resonant again such that  $|\text{Im } \tilde{x}_{m,l}|$  drops. But the energy denominator has now changed the sign which results in the localization of the mode at the unstable periodic orbit. This prediction is again in a nice agreement with the numerical BEM result.

Similarly, the second peak in  $\text{Im } \tilde{x}_{m,l}$  has its origin in a strong coupling between the modes  $(m, l)$  and  $(m - 2r, l + 2s)$  due to a small denominator in  $a_2$ . Therefore the  $j$ -th peak in  $\text{Im } \tilde{x}_{m,l}$  is identified with a strong coupling to the mode  $(m - jr, l + js)$ .

In principle, for modes with  $(m, l > 1)$  also the coupling to the mode  $(m + jr, l - js)$  needs to be considered. In an interesting case such a mode  $(m, l)$  (with a low  $Q$ -factor) is below the resonance chain and couples to a mode (with a high  $Q$ -factor) above the resonance chain resulting in a slightly higher  $Q$ -factor in the deformed cavity than in the circular cavity for the mode  $(m, l > 1)$ . Such a scenario was shown in Sec. 3.4.2 [see Fig. 3.8]. However, this  $Q$ -enhancement for modes  $(m, l > 1)$  is only marginal for the systems studied here and in the relevant regime of  $kR$ . Nevertheless, it could be implemented in an extended version of the RAT perturbation theory.

### Far-field predictions from RAT

Using Eq. (7.24) the far-field pattern of an optical mode can be predicted. In Fig. 7.7 this is done for the modes in system  $\mathcal{A}$  whose near-field pattern are shown in Fig. 7.6. The overall



agreement to the numerical BEM is quite well. At first glance this nice agreement especially for the mode  $(m, l) = (22, 1)$  at the resonance peak is surprising since the near-field prediction is erroneous. However one needs to keep in mind that this error comes from the wrongly predicted coupling strength  $a_1$  to the mode  $(m - r, l + s) = (18, 2)$  whose near-field pattern can be clearly distinguished from the one of the mode  $(m, l) = (22, 1)$ . However the far-field pattern of the mode  $(m - r, l + s) = (18, 2)$  [green dotted curve in Fig 7.7(c)] looks quite similar to the one of the mode  $(m, l) = (22, 1)$  [Creagh and White, 2012]. Therefore the wrongly predicted coupling coefficient  $a_1$  does not result in a significant error in the far-field prediction.

### The effect of the POS shift

Next, it is clarified that the POS and therefore the Goos-Hänchen shift is indeed very substantial for the mode predictions via RAT. Since it shifts the momentum  $p_{m,l}$  to the modified momentum  $p_{m,l}^{\text{mod}}$  it consequently also shifts the position of the RAT-peak where the energy denominator vanishes. Even if the shift  $\Delta m_{\text{POS}}$  from the POS in the mode number is only around  $\Delta m_{\text{POS}} \approx 1.5$  it can result in a quite large shift of the RAT-peak. This is illustrated in Fig. 7.8(a) where for system  $\mathcal{C}$  the RAT predictions without the POS are shown in comparison to the predictions including the POS. If one ignores the POS the RAT-peak is predicted quite too early; i.e. for the mode  $(m, l) = (33, 1)$  instead of  $(m, l) = (44, 1)$ . In Fig. 7.8(b-c) it is shown that the small shift in  $p$  due to the POS can tune the modes into resonance (c) or out of resonance (b).

### Connection to the boundary perturbation theory

Next, the RAT theory is compared to the perturbation theory based on the cavity's boundary deformation which was the topic of the last two chapters. Since the cavities studied in this chapter have a mirror-reflection symmetry one can apply the symmetric-PT [Dubertrand et al., 2008], see Sec. 5, in order to obtain predictions for  $\tilde{x}_{m,l}$ . First, one should mention that both theories, RAT and symmetric-PT, are applicable to slightly deformed cavities. For the symmetric-PT the criterion of its validity is that the area where the refractive index is changed via the deformation needs to be small [see Eq. (5.9)]. In contrast the RAT theory it requires that one can identify a dominant resonance chain in phase space. Therefore, the deformation needs to be small as well such that no large resonance chains of higher order or large chaotic regions are generated outside of the leaky region.

A further similarity is that both theories use a perturbative approach. The theory from Dubertrand *et al.* treat the deformation in real space perturbatively but the RAT theory solves an effective Hamiltonian for the phase space dynamics perturbatively.

A remarkable difference is that the symmetric-PT is valid for small  $\text{Re } x$ . But since the RAT

theory is based on the ray dynamics it is in this sense a semiclassical theory<sup>3</sup> and therefore expected to be valid also for larger  $\text{Re } x$ .

A direct comparison of the predictions based on the symmetric-PT and the RAT-predictions can be seen in Fig. 7.9 for system  $\mathcal{C}$ . Since the first-order perturbation theory [Eq. (5.14)] gives corrections only linear in  $x_0$  it is not able to predict the RAT-peak in  $\text{Im } x$ . The second-order perturbation theory [Eq. (5.22)] contains terms being nonlinear in  $x_0$  and it nicely describes the first RAT-peak in  $\text{Im } x$ . For these small values of  $\text{Re } x$  the second-order perturbation theory predictions are more accurate than the RAT predictions which can be seen e.g. at the saddle of the RAT-peak around  $\text{Re } x \approx 20 \dots 30$ .

However, for larger  $\text{Re } x$  the second-order perturbation theory is not able to predict the second RAT-peak in  $\text{Im } x$  although the criterion (5.9) is fulfilled till  $\text{Re } x \approx 68$ . In case of a simple deformation  $f = \cos(N\phi)$  where  $N \equiv r$  correspond to the order of the dominant resonance chain this can be explained from the coupling matrices  $A_{pm}$ ,  $B_{pm}$  [Eqs. (5.16), (5.20)]. These matrices reduce to

$$A_{pm} = \frac{2 - \delta_{0,p}}{4} (\delta_{m-p,\pm r} + \delta_{m+p,r}) \quad (7.25a)$$

$$B_{pm} = \frac{2 - \delta_{0,p}}{8} (\delta_{m-p,\pm 2r} + \delta_{m+p,2r} + 2\delta_{m,p}). \quad (7.25b)$$

In Eq. (5.22) for the second-order corrections  $x_2$  terms  $A_{pm}$  and only  $B_{mm}$  enter. Therefore,  $A_{pm}$  correctly describes the coupling between the modes  $(m, l)$  and  $(m - r, l + s)$ . But the coupling to the mode  $(m - 2r, l + 2s)$  which would be encoded in  $B_{pm}$  with  $p = m - 2r$  does not enter in  $x_2$ . It is mentioned that the third-order corrections  $x_3$  [Eq. (5.34)] for this special type of deformation vanish for the relevant modes at the peak because of the simple cosine deformation.

However, for the perturbation theory such a simple boundary deformation is very non-generic since higher coupling terms in  $A_{pm}$  and  $B_{pm}$  vanish. In order to illustrate this fact one can perform the perturbation theory not for the simple deformation  $f(\phi) = \cos(N\phi)$  but for the flatten version of the deformation

$$\frac{r(\phi)}{R} = \sqrt{1 + 2\epsilon \cos(N\phi)}. \quad (7.26)$$

Since  $\epsilon$  is small the boundary shape of the flatten and the simple cosine perturbation is almost equal but the flatten version exhibits higher order terms in  $A_{pm}$  (and  $B_{pm}$ ) being proportional to  $\delta_{m-p,\pm lr}$ ,  $l \in \mathbb{N}$ . In Fig. 7.10 the results of the perturbation theory applied to the flatten cavity shape are compared to the previously obtained results (BEM and RAT) for the simple version of the deformation. For small  $\text{Re } kR$  the perturbation theory applied to

<sup>3</sup>In the literature about RAT the term ‘‘semiclassical’’ is often used slightly different; e.g. if the Hamiltonian  $\mathcal{H}_{r,s}$  is solved with WKB-quantization schemes. Therefore, a semiclassical RAT theory is related to complex paths in phase space [Fritzsche et al., 2017, Mertig, 2013].

the flatten boundary is almost equal to the perturbation theory applied to the simple version. However around the second RAT-peak the third-order perturbation theory can at least capture signatures of the peak. Note that these signatures can be seen also (but barely) in the second order perturbation theory as well. Nevertheless, the RAT theory is still much more accurate for the second RAT-peak than the boundary perturbation theory. However, this example illustrates that too simple boundary shapes, e.g. with a single cosine, are quite non-generic for the boundary perturbation theory since important aspects cannot be captured due to the vanishing coupling matrix elements.

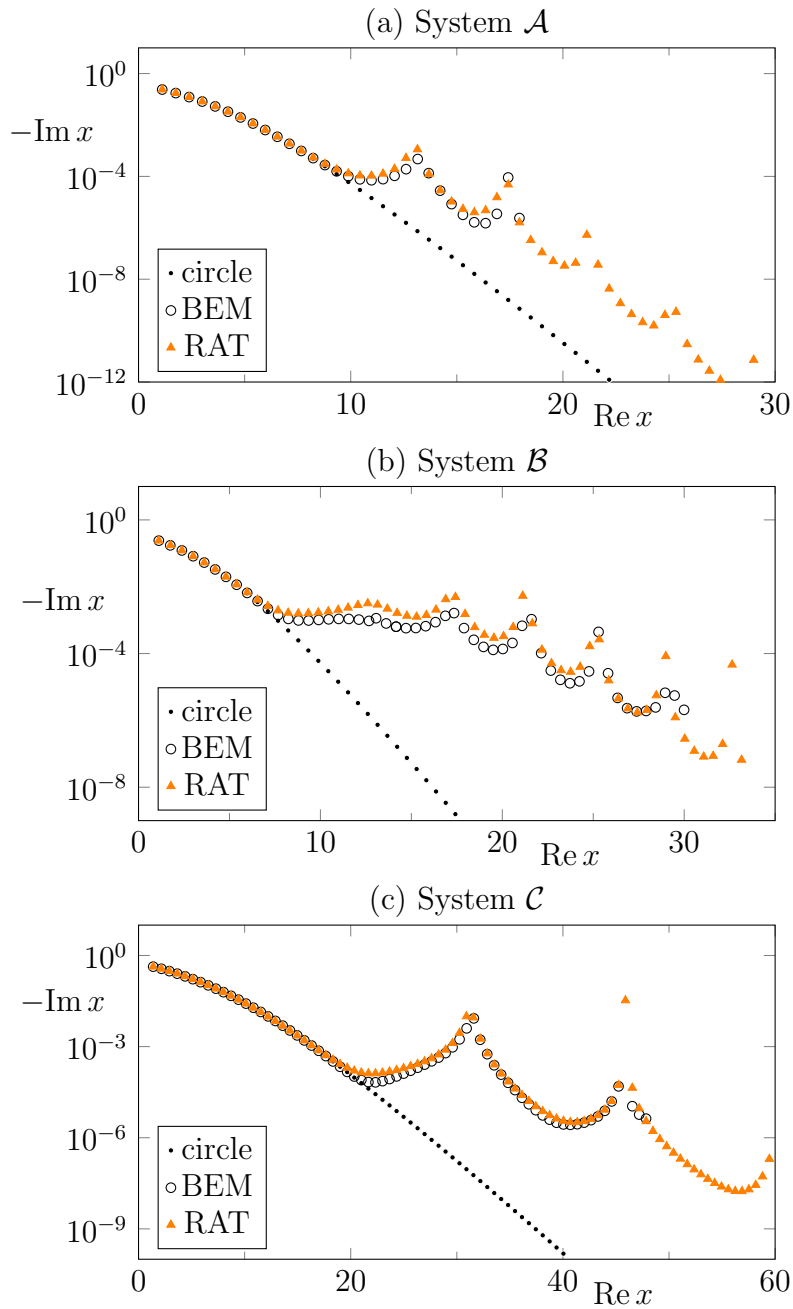


**Figure 7.5:** For the three systems  $\mathcal{A}$ ,  $\mathcal{B}$ , and  $\mathcal{C}$  the (orange triangles) RAT predictions [Eq. (7.18)] for the imaginary part of the complex wave number  $x = kR$  are compared to BEM results (open black circles). The results for the circular disk are shown as black dots. The shown data correspond to modes with radial mode number  $l = 1$ .

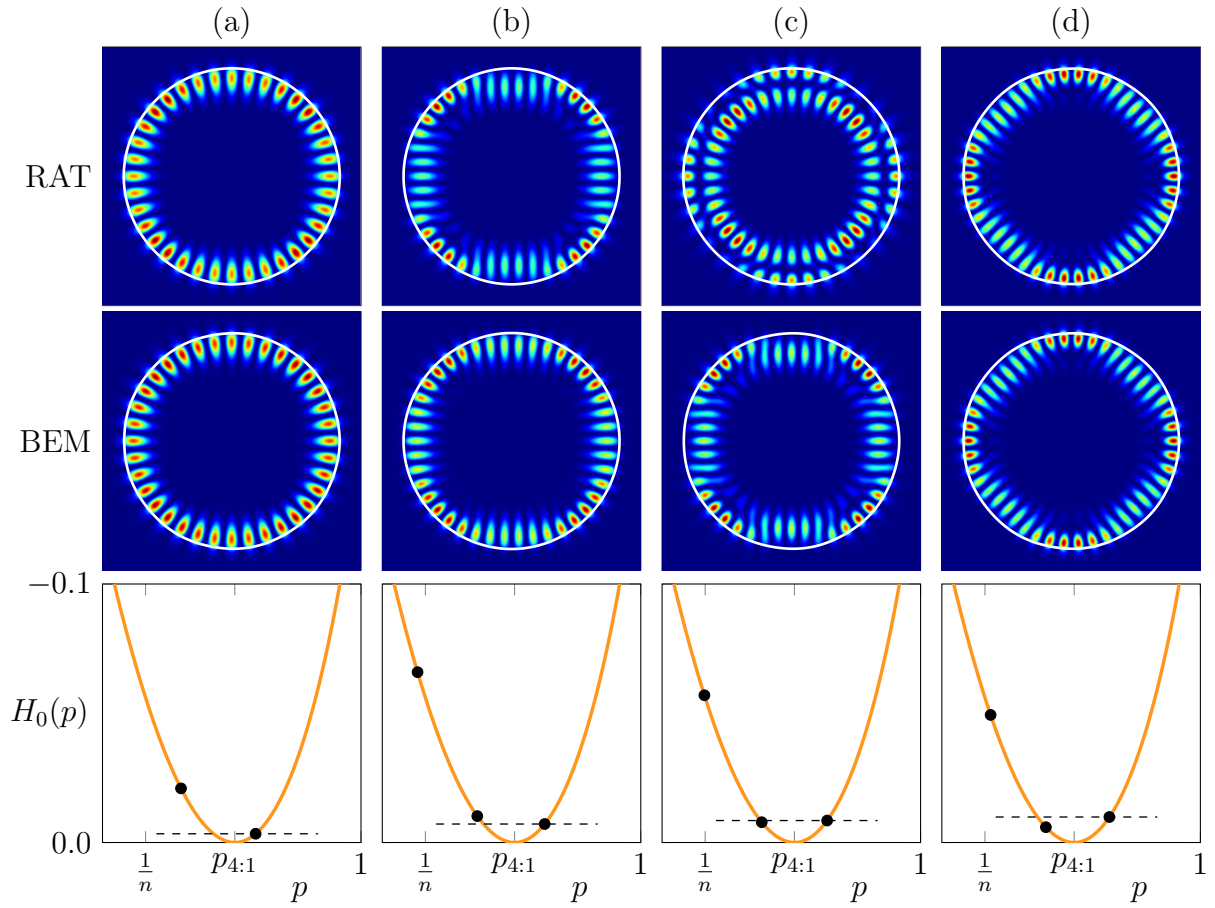


**Figure 7.6:** For the modes (a)  $(m, l) = (18, 1)$ , (b)  $(m, l) = (21, 1)$ , (c)  $(m, l) = (22, 1)$ , and (d)  $(m, l) = (23, 1)$  in system  $\mathcal{A}$  the near-field intensity mode patterns computed by (upper panel) RAT [Eq. (7.16)] and (middle panel) BEM are shown. In the lower panel the function  $H_0(p)$  is shown as orange curve where black dots mark the modified momenta  $p_{m-jr, l+js}^{\text{mod}}$ . A dashed line at  $H_0(p_{m, l}^{\text{mod}})$  serves as guide to the eye.

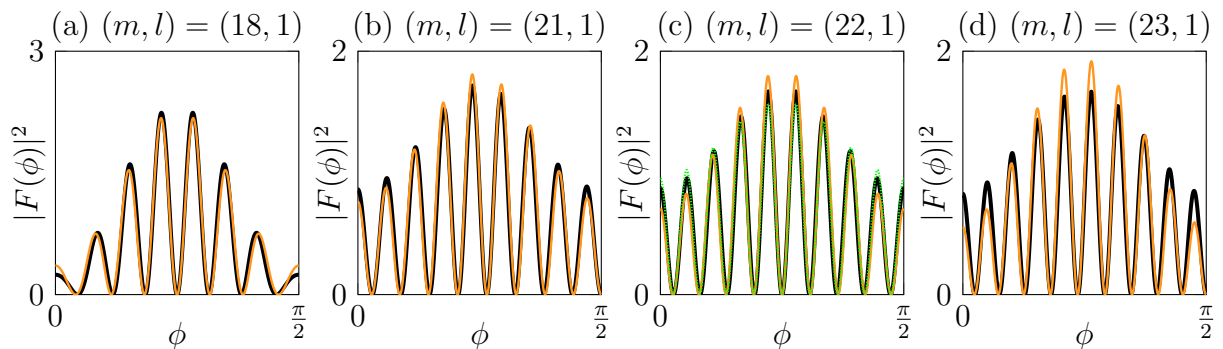


**Figure 7.7:** For the modes (a)  $(m, l) = (18, 1)$ , (b)  $(m, l) = (21, 1)$ , (c)  $(m, l) = (22, 1)$ , and (d)  $(m, l) = (23, 1)$  in system  $\mathcal{A}$  the far-field intensity pattern predicted by (orange curves) RAT is compared to the (black curves) BEM results. In (c) the far-field calculated with the BEM for the mode  $(m, l) = (18, 2)$  is shown additionally as green dotted curve. Due to the 4-fold rotational symmetry the angle  $\phi$  is restricted to the interval  $[0, \pi/2]$ . All curves are normalized to have the same area below the curves.

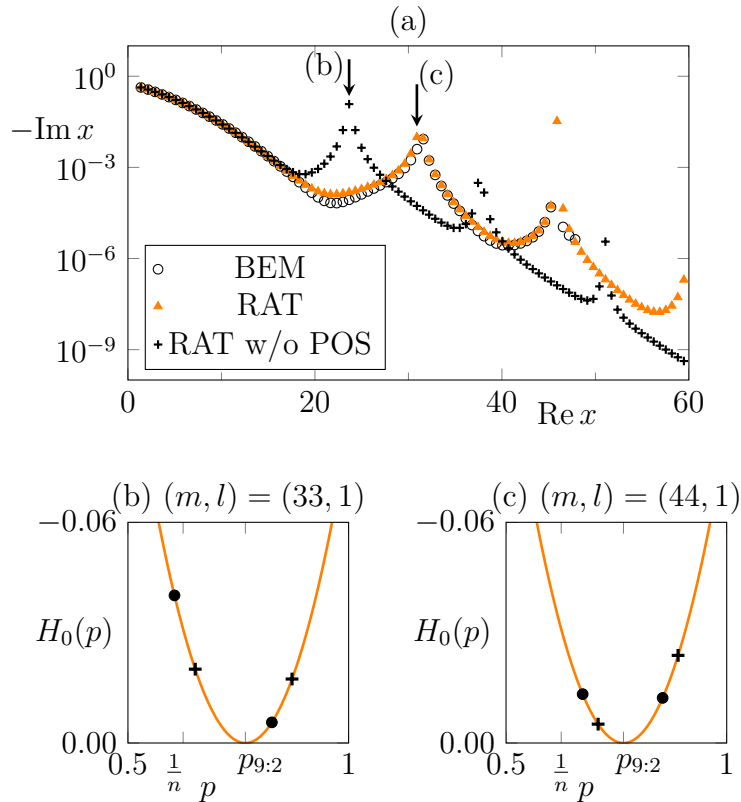


**Figure 7.8:** (a) The (orange triangles) RAT predictions for  $\text{Im } x$  based on Eq. (7.18) including the POS are compared to (empty circles) the BEM results for modes with  $l = 1$  in system  $\mathcal{C}$ . Additionally the RAT predictions without the POS are shown as black crosses. For the mode numbers (b)  $(m, l) = (33, 1)$  and (c)  $(m, l) = (44, 1)$  the parabola  $H_0(p)$  is shown as orange curve. The modified momenta  $p_{m,l}^{\text{mod}}$  and  $p_{m-r,l+s}^{\text{mod}}$  are illustrated by black dots. The conventional momenta  $p_{m,l}$  and  $p_{m-r,l+s}$  (without the POS correction) are marked as black crosses.

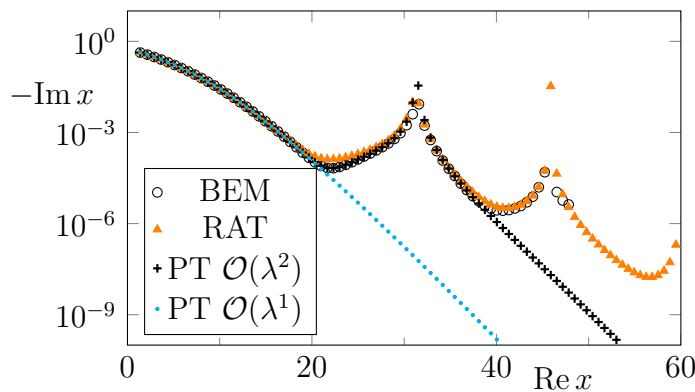


**Figure 7.9:** The complex wave numbers are shown for modes with radial mode number  $l = 1$  in system  $\mathcal{C}$ . Results from the BEM are shown as open black circles. The RAT predictions [Eq. (7.18)] are shown as orange triangles. Furthermore, the results of the boundary perturbation theory in (light blue dots) first- and (black crosses) second order are shown.

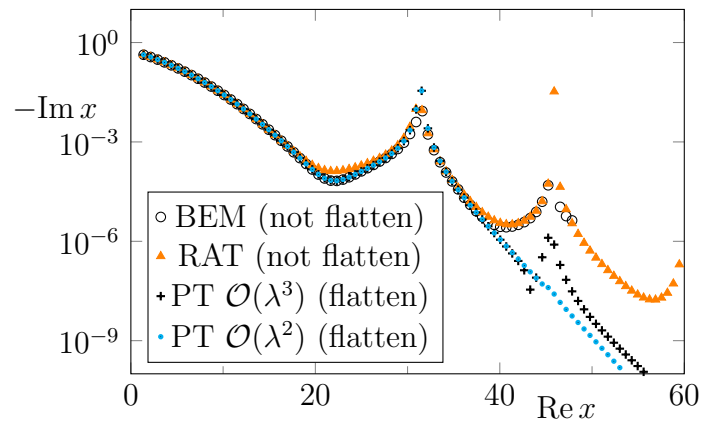


**Figure 7.10:** The complex wave numbers are shown for modes with radial mode number  $l = 1$  in system  $\mathcal{C}$ . Results from the BEM are shown as open black circles. The RAT predictions [Eq. (7.18)] are shown as orange triangles. The results of the third-order perturbation theory applied to the flatten version of the boundary deformation [Eq. (7.26)] are shown as black crosses and the corresponding second-order results are the light blue dots.

## 7.4 Outlook: $kR$ splitting of even and odd parity modes due to resonance-assisted tunneling

In the previous section it was shown that a single  $r:s$  resonance chain outside the leaky region couples the modes  $(m, l)$  and  $(m - jr, l + js)$  with  $j \in \mathbb{Z}$ . However, in this section now the focus is on the resonance chain inside the leaky region; to be precise on the bouncing ball resonance chain (BBC) which is along  $p = 0$ . In the circular cavity the line  $p = 0$  is obviously centered between the traveling waves  $(m, l)$  and  $(-m, l)$ . However, in a slightly deformed cavity with a mirror-reflection symmetry these traveling waves need to be superimposed to standing waves with even and odd parity to form a mode. In other words the deformation of the cavity give rise to a coupling between the traveling waves  $\pm m$ . The proposal here is to explain this coupling with a RAT process across the BBC. Consequently, predictions for the real part of the splitting  $\text{Re } \Delta \tilde{x}_{m,l} = \text{Re } \tilde{x}_{m,l}^+ - \text{Re } \tilde{x}_{m,l}^-$  of the even (+) and odd (-) parity modes in the deformed cavity are obtained.

Following, the outline for that RAT predictions from the previous section, first, the phase space structure of the BBC is modeled with the effective generalized pendulum Hamiltonian [Eq. (7.1)]. Since the BBC is located at the momentum  $0 = p_{r:s} = \cos(\pi s/r)$  it yields

$$\frac{s}{r} = \frac{1}{2} \pmod{1}. \quad (7.27)$$

Hence,  $H_0(p)$  simplifies to

$$H_0(p) = 2 \left( p \arccos(p) - \sqrt{1 - p^2} + 1 \right) - \pi p = -p^2 + \mathcal{O}(p^4). \quad (7.28)$$

Remaining, the coupling strength  $V_{1:2}$  of the BBC needs to be determined. Here, Eq. (7.7) is promising since the area  $A$  of (a typically large) BBC can be computed numerically from the billiard dynamics or approximated by an integration of the adiabatic curve [see Eq. (3.40)].

In the second step the splitting  $\Delta \tilde{x}_{m,l}$  between the even and the odd parity modes is determined within a perturbative approach from the Hamiltonian matching the BBC. Since the traveling waves  $(m, l)$  and  $(-m, l)$  are degenerate in the circular (unperturbed) cavity the perturbation theory for the splitting  $\Delta \tilde{x}_{m,l}$  is a degenerate perturbation theory. In Refs. [Keshavamurthy, 2005, Keshavamurthy, 2007] it was shown that the eigenvalue splitting  $\Delta E_m$  between the energies regarding even and odd eigenfunctions of the (quantum) pendulum Hamiltonian

$$H(q, p) = \frac{p^2}{2M} + 2V \cos(2\phi) \quad (7.29)$$



can be obtained perturbatively as

$$\Delta E_m = 2V \prod_{\substack{u=-(m-2) \\ \Delta u=2}}^{(m-2)} \frac{V}{E_m - E_u} \quad (7.30)$$

where  $E_m$  and  $E_u$  are the energies of the free particle Hamiltonian  $p^2/(2M)$ . In Eq. (7.30)  $u$  takes the values  $u = -(m-2), -(m-4), \dots, (m-4), (m-2)$  because of the particular form of the perturbation proportional to  $\cos(2\theta)$ . In order to adapt this result to a microdisk cavity whose BBC is described by an Hamiltonian (7.1) the connection between  $\Delta E_m$  and  $\text{Re} \Delta \tilde{x}_{m,l}$  needs to be figured out as follows. The energies of the circular (unperturbed) cavity are identified by inserting  $p_{m,l} = m/(n\text{Re} x_{m,l})$  into Eq. (7.5) which yields

$$E_m \equiv H_0(p_{m,l}) = \frac{1}{[n\text{Re} x_{m,l}]^2} \frac{(m - m_{r:s})^2}{\sqrt{1 - p_{r:s}^2}} \sim \frac{1}{[n\text{Re} x_{m,l}]^2} \quad (7.31)$$

with  $m_{r:s} = p_{r:s} n\text{Re} x_{m,l} \in \mathbb{R}$ . Thus, from the total differential one obtains

$$\frac{\Delta E_m}{E_m} = 2 \frac{\text{Re} \Delta \tilde{x}_{m,l}}{\text{Re} x_{m,l}} \quad (7.32)$$

where  $\Delta E_m$  and  $\text{Re} \Delta \tilde{x}_{m,l}$  are defined positive. By inserting this relation into Eq. (7.30) with  $V = V_{r:s}$  one obtains

$$\text{Re} \Delta \tilde{x}_{m,l} = \text{Re} x_{m,l} \frac{V_{r:s}}{E_m} \prod_{\substack{u=-(m-2) \\ \Delta u=2}}^{(m-2)} \frac{V_{r:s} e^{i\phi_0}}{E_m - E_u} \quad (7.33a)$$

$$= \text{Re} x_{m,l} \frac{V_{r:s}/\hbar^2}{E_m/\hbar^2} \prod_{\substack{u=-(m-2) \\ \Delta u=2}}^{(m-2)} \frac{V_{r:s}/\hbar^2 e^{i\phi_0}}{E_m/\hbar^2 - E_u/\hbar^2}. \quad (7.33b)$$

In the second equation all terms are expanded with  $\hbar^2$ . In contrast to Eq. (7.30) this expansion is necessary for microdisk cavities because each energy  $E_m \sim \hbar^2$  scales with a different  $\hbar = 1/(n\text{Re} x_{m,l})$  [see Eq. (7.31)]. Hence, one needs to rescale each of the terms with the corresponding  $\hbar^2$  in order to make them comparable in the ( $kR$  independent) Hamiltonian. Note that this rescaling is crucial for the terms occurring in the product but not for the prefactor where  $\hbar$  in the numerator and the denominator are the same. Furthermore, the prefactor can be simplified further by exploiting the assumption that mode  $m$  is a well-confined whispering-gallery mode ( $l = 1$ ); i.e.  $\text{Re} x_{m,l} \gg 1$  and  $|\text{Im} x_{m,l}| \ll \text{Re} x_{m,l}$ . In this case the asymptotic relation  $m = n\text{Re} x_{m,l}$  [Dubertand et al., 2008] can be used to remove the term  $E_m$ . Hence,

one obtains the final prediction for the frequency splitting from the BBC as

$$\text{Re } \Delta \tilde{x}_{m,l} = \text{Re } x_{m,l} V_{r:s} \prod_{\substack{u=-(m-2) \\ \Delta u=2}}^{(m-2)} \frac{V_{r:s} [\text{Re } x_{u,l}]^2 e^{i\phi_0}}{H_0(p_{m,l}) [\text{Re } x_{m,l}]^2 - H_0(p_{u,l}) [\text{Re } x_{u,l}]^2}. \quad (7.34)$$

Note that in the similar Eq. (7.19) the wavelength scaling of the individual terms does not occur. The reason is that  $\text{Re } x_{m,l}$  is almost equal to  $\text{Re } x_{m-r,l+s}$  at the RAT-peak of the  $Q$ -spoiling. Therefore, it was neglected in that case. However, in the case of Eq. (7.34)  $\text{Re } x_{m,l}$  and  $\text{Re } x_{u,l}$  are quite different since both correspond to modes with the same radial mode number  $l = 1$  but different azimuthal mode numbers  $m$  and  $u$ ; i.e.  $\text{Re } x_{u,l} < \text{Re } x_{m,l}$  for  $u < m$ . Thus, the wavelength scaling cannot be neglected in Eq. (7.34). Further note that in Eq. (7.34) the conventional momenta  $p_{u,l} = u/(n \text{Re } x_{u,l})$  enter because the GHS corrections vanish for the resonance chain of the bouncing ball orbit at  $p_{r:s} = 0$  [see Eqs. (7.22)-(7.23)].

In the following the results of this approach for the splitting  $\text{Re } \Delta \tilde{x}_{m,l}$  are discussed: The formula (7.34) allows to interpret the RAT process which couples  $(m, l)$  and  $(-m, l)$  as a stepwise process. In case of an ordinary  $r:s=2:1$  BBC this means that the mode  $(-m, l)$  couples to the mode  $(-m+2, l)$ , then to  $(-m+4, l)$ , and so on until it reaches  $(m, l)$ . Therefore, every mode  $(m, l)$  can couple to its counterpart  $(-m, l)$  which results in a finite frequency splitting of each mode in the deformed cavity.

However, the interesting consequence of this mechanism occur for BBC of higher order. Since Eq. (7.27) contains the modulus one can imagine e.g. a  $r:s=4:2$  BBC which can occur in systems with a 4-fold rotational symmetry. In this case the mode  $(-m, l)$  couples first to  $(-m+4, l)$  and next to  $(-m+8, l)$  and so on, for an illustration see Fig. 7.11. However, for each odd mode number  $m$  it is therefore impossible to couple to its counterpart  $-m$ . Consequently, one expects a vanishing splitting in the deformed cavity for the modes with odd  $m$  and a finite splitting for the modes with even  $m$ .

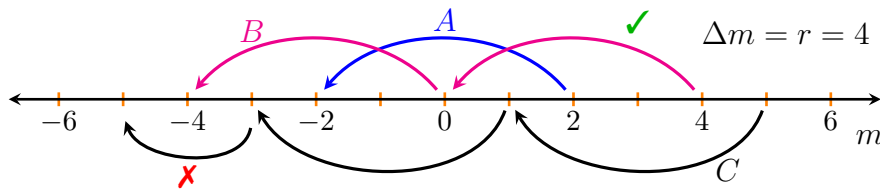


**Figure 7.11:** Illustration of the coupling mechanism between the traveling waves  $m$  and  $-m$  in a cavity with a  $r:s=4:2$  BBC. The (A) blue and (B) magenta paths lead to a finite splitting between even and odd parity modes in the deformed cavity for  $m = 2$  and  $m = 4$ , respectively. The (C) black path illustrates an impossible coupling path for the mode  $m = 5$  resulting in a vanishing splitting.

In Fig. 7.12 the splitting results for such higher-order BBCs are shown. The cavity studied here is the multipole [Eq. (7.14)] with refractive index  $n = 1.5$ . For each even  $N$  the corresponding

BBC is of the order  $r:s=N:N/2$ . Therefore, Eq. (7.34) can be applied to the modes  $(m, l) = (N/2, 1), (N, 1), (3N/2, 1), \dots$  and for all other modes the splitting  $\Delta\tilde{x}$  should vanish. As shown in Fig. 7.12 these predictions quite nicely correspond to the BEM results. The numerically determined splitting for the modes which are not covered by Eq. (7.34) is of the order  $10^{-13}$  and therefore within the error range of the numerics.

However, for larger mode numbers  $m$  Eq. (7.34) systematically underestimates the splitting. The reason therefore is that Eq. (7.34) only accounts for the effects of the BBC. But with higher mode number  $m$  more and more phase space structures, especially resonance chains of higher order at finite momentum  $p_{r:s} \neq 0$ , give contributions to the splitting. The contributions from such higher order resonance chains are discussed in the next paragraph.

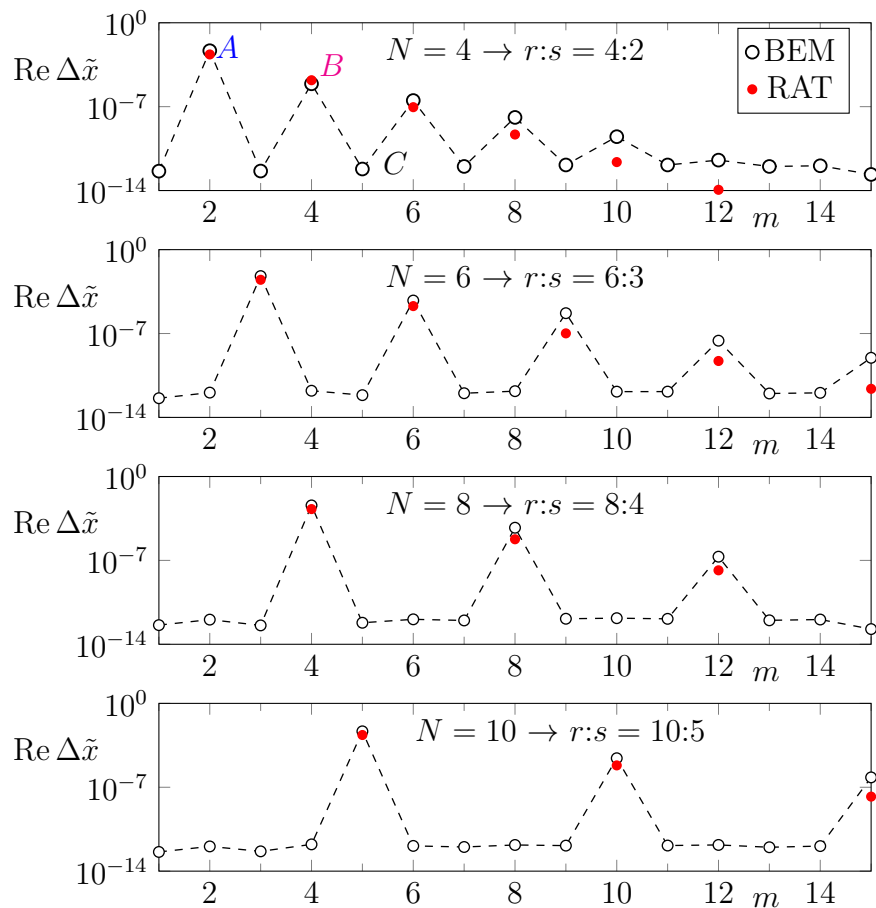


**Figure 7.12:** Splitting between even and odd parity modes in the multipole cavity [Eq. (7.14)] with refractive index  $n = 1.5$ . The BEM results are shown as open black circles connected by dashed lines and the RAT-predictions from Eq. (7.34) are shown as red dots. The parameter  $\epsilon$  is set to (a-b)  $\epsilon = 0.002$  and (c-d)  $\epsilon = 0.001$ . The paths corresponding to Fig. 7.11 are labeled.

### Splitting enhancement via multi-resonance-assisted tunneling

So far the predictions for the splitting are based on the BBC only. However, in the previous section it was already shown that resonance chains of higher order which are located at a finite momentum  $p_{r:s} \neq 0$  can result in a coupling of modes with different mode number  $l$  which manifests e.g. in  $Q$ -spoiling. Therefore, the purpose in the following is to combine the splitting predictions from Eq. (7.34) for the BBC with the RAT-coupling mechanism for a higher order resonance chain, see Sec. 7.3. In order to treat these effects, first, the notation needs to be fixed: The BBC is still labeled with  $r:s$ . However, the additional resonance chain at finite momentum  $p_{\tilde{r}:\tilde{s}}$  has the order  $\tilde{r}:\tilde{s}$ . Then the splitting obtained so far as tunneling over the BBC only is illustrated in Fig. 7.13(a). The additional tunneling path which includes the  $\tilde{r}:\tilde{s}$  resonance chain is shown in Fig. 7.13(b). In such a case the mode  $(m, l)$  gets contributions from the mode  $(m - \tilde{r}, l + \tilde{s})$  which then uses the BBC to couple to its counter-propagating counterpart. This second tunneling path is supposed to become important for larger  $m$  when the mode  $(m, l)$  is located above  $p_{\tilde{r}:\tilde{s}}$ .

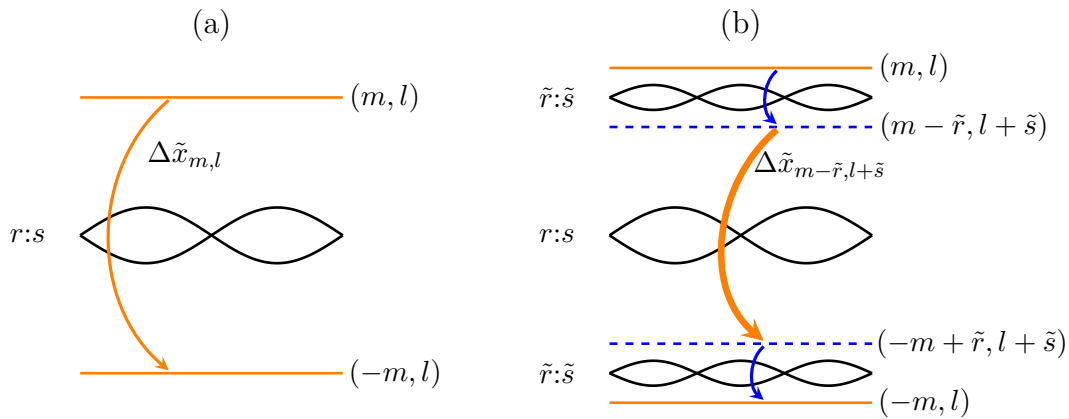


**Figure 7.13:** Illustration of the tunneling paths for the complex frequency splitting  $\Delta \tilde{x}$ . In (a) the BBC couples the traveling wave  $(m, l)$  with its counter-propagating counterpart which results in the splitting predicted by Eq. (7.34). In (b) the additional tunneling path is shown which first uses a RAT-coupling via the  $\tilde{r}:\tilde{s}$  resonance chain [see Eqs. (7.16) and (7.19)].

In order to predict this RAT-enhanced splitting  $\Delta \tilde{x}^{\text{enh}}$  which now accounts for the additional RAT step an ansatz in the spirit of Eq. (7.18) is used

$$\text{Re } \Delta \tilde{x}^{\text{enh}} = \sum_{j \geq 0} |a_j|^2 \text{Re } \Delta \tilde{x}_{m-j\tilde{r}, l+j\tilde{s}} \quad (7.35)$$

where the coefficients  $a_j$  are given by Eq. (7.19) (for the  $\tilde{r}:\tilde{s}$  resonance chain); and  $a_0 = 1$ . As an example system in the following the quadrupole cavity is studied for  $\epsilon = 0.035$  and a refractive index  $n = 3.0$ . In Fig. 7.14 the results for the splitting are shown versus the mode

number  $m$  for modes with  $l = 1$ . In the regime of small  $m < 8$  the splitting is governed by the BBC only (orange curve). However, for  $9 < m < 19$  the numerically obtained values (BEM) start to deviate from the prediction of Eq. (7.34) and show a peak-like structure. This deviation can be traced back to the  $\tilde{r}:\tilde{s} = 6:2$  resonance chain in phase space. Therefore, Eq. (7.35) can be applied which nicely predicts the enhanced splitting up to  $m \approx 19$  (blue curve). However, for even larger  $m$  also this prediction fails because not only the  $\tilde{r}:\tilde{s} = 6:2$  resonance chain but also other resonance chains contribute. For example Eq. (7.35) applied to the  $\tilde{r}:\tilde{s} = 4:1$  resonance chain indicates the slightly enhanced splitting for  $m = 21$  (red curve). Therefore, it is suggested that in an extended version of the splitting prediction for such modes with large  $m$  all or at least many important resonance chains are taken into account. Note that the identification of these important resonance chains is not trivial since a simple criterion concerning the area in phase space fails. For example in the quadrupole the 6:2 resonance chain is smaller than the 4:1 resonance chain but it becomes already important for smaller mode numbers  $m \approx 9$ . Hence, also the momentum  $p_{\tilde{r}:\tilde{s}}$  of the resonance chain is crucial. Resonance chains with lower  $p_{\tilde{r}:\tilde{s}}$  are crossed already at a small  $m$  and therefore influence the splitting of these modes.

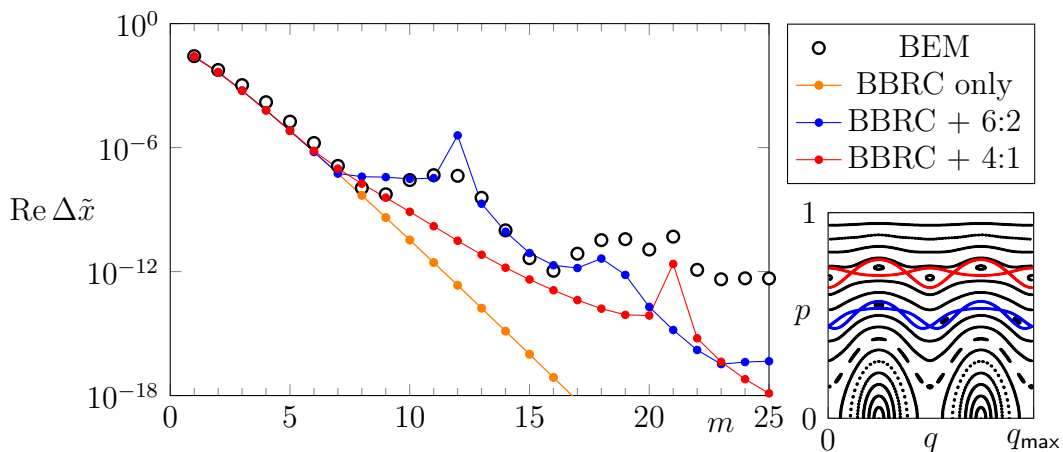


**Figure 7.14:** The figure shows the real part of the complex frequency splitting of even and odd parity modes with  $l = 1$  in the quadrupole cavity with  $\epsilon = 0.035$  and refractive index  $n = 3.0$ . The BEM results are shown as open black circles. The predictions based on Eq. (7.12) are shown as orange connected dots, and the predictions based on Eq. (7.35) for  $\tilde{r}:\tilde{s} = 6:2$  [ $\tilde{r}:\tilde{s} = 4:1$ ] are shown as blue [red] connected dots, respectively. The right inset shows a phase space portrait of the billiard dynamics with the highlighted resonance chains.

However, the presented results highlight the importance of RAT for the splitting in the real part of the complex frequency  $\Delta\tilde{x}$  between even and odd parity modes in slightly deformed, i.e. near-integrable, microdisk cavities.

## 7.5 Chapter summary

In this chapter the influences of nonlinear resonance chains in the phase space to the optical modes have been discussed. Such resonance chains develop naturally from slight boundary deformations.

In the first part of the chapter a dominant resonance chain above the critical line  $p = 1/n$  is considered. Such a resonance chain of order  $r:s$  can couple the mode  $(m, l)$  with the modes  $(m - jr, l + js)$ ,  $j \in \mathbb{Z}$ , which results for whispering-gallery modes ( $l = 1$ ) in a spoiling of the  $Q$ -factor. This  $Q$ -spoiling can be predicted within a generalized pendulum approximation of the dominant resonance chain. Furthermore, the phase space approximation allows to predict the near- and far-field mode pattern. A crucial point in these predictions are the corrections of the billiard dynamics due to the dielectric boundary conditions at the cavity's interface. Especially, the corrections from the Goos-Hänchen shift are important for the predictions of the characteristic peaks in  $\text{Im } kR$ .

In the second part of the chapter an outlook has been provided how the resonance chain of the bouncing ball orbit can be used to describe the splitting of the complex frequency between modes with even and odd parity in cavities with a mirror-reflection symmetry. It turns out that for larger mode numbers  $m$ , i.e. large  $\text{Re } x$ , also resonance chains at finite momentum contribute to this splitting which can be modeled in a first draft. However, the generalization of this ansatz to the semiclassical regime of very large  $m$  is of future interest.

Another future challenge is the description of the  $Q$ -spoiling and the mode splitting in slightly deformed asymmetric cavities using resonance-assisted tunneling. This might also provide a tunneling approach to asymmetric backscattering.

# 8 Summary and conclusion

In this thesis aspects of the non-Hermitian physics in deformed optical microdisk cavities are studied in the ray and the wave dynamics. In fully asymmetric cavities, i.e. in cavities whose boundary has no mirror-reflection symmetry generically asymmetric backscattering occurs in the wave mechanics as a signature of the non-Hermitian dynamics. In the first main part of this thesis (in Sec. 4) the asymmetric backscattering has been studied within the ray dynamics. To this end a finite approximation of the Frobenius-Perron operator (FPO) for the time evolution of classical phase-space intensities has been constructed. The eigenstates of the FPO show an interesting correspondence to the optical modes. In particular there exists a pair of non-orthogonal and copropagating eigenstates with a large lifetime; i.e. an large eigenvalue modulus. Similar to the wave dynamics an effective  $2 \times 2$  Hamiltonian for this eigenstate pair can be constructed. Furthermore, both eigenstates show a very good agreement to an average of long-lived optical modes in terms of an averaged Husimi function. For the construction of the FPO it was assumed that the dynamics in the cavity is chaotic and that the ray dynamics mixes the regions of clockwise and counter-clockwise propagation in the phase space. For such cavities a proper ray dynamical description of asymmetric backscattering has been invented.

The issue of the second main part of this thesis was the generalization of the perturbation theory for slightly deformed cavities. Here, a degenerate perturbation theory based on the analytical solutions of the circular cavity allows to treat also fully asymmetric cavities without mirror-reflection symmetry. Consequently, analytical formulas for the complex wave number  $kR$  and the mode pattern have been derived. These formulas lead to accurate results for slight deformations and small values of  $kR$  which has been confirmed at several generic examples. The generalized perturbation theory captures the interesting non-Hermitian phenomena in fully asymmetric deformed cavities like a finite chirality of modes and signatures of exceptional points. Furthermore, the generalized perturbation theory provides a foundation for further analytical investigations of deformed microdisk cavities.

The third main topic discussed in this thesis was the effect of nonlinear resonance chains in the phase space of symmetrically deformed microdisk cavities. It was shown that such resonance chains not only affect the wavelength of optical modes, i.e. the real part of the complex wave number  $kR$  which was experimentally verified before, but also the imaginary part of the complex wave number  $kR$  via resonance-assisted tunneling. Therefore such resonance chains lead to a spoiling of the  $Q$ -factor. By modeling one dominant resonance chain in the

phase space with an effective generalized pendulum Hamiltonian one can derive predictions for the  $Q$ -spoiling, the mode pattern, and the far-field pattern of a single mode. Here, an incorporation of the Goos-Hänchen shift in the model is crucial for the accurate prediction of the characteristic resonance-assisted tunneling peaks in the imaginary part of  $kR$ .

Moreover, it was shown that the resonance chains in the phase space also affect the even and odd parity mode pair: Via resonance-assisted tunneling over the resonance chain of the bouncing ball orbit the small splitting between these modes with even and odd parity can be explained. Therefore resonance-assisted tunneling provides a new approach to explain the formation of optical modes in slightly deformed cavities. For future investigations it would be valuable to extend the RAT-framework to cavities without mirror-reflection symmetry.



# A Appendix

## A.1 Calculation of billiard dynamics

In this appendix the numerical procedure to determine the billiard dynamics of rays in a microdisk cavity is described. It is assumed that the cavity's boundary is given in polar coordinates by a dimensionless and may implicit defined function

$$\rho(\phi) = \frac{r(\phi)}{R}. \quad (\text{A.1})$$

Therefore, the dimensionless arc length is defined as

$$q(\phi) = \int_0^\phi \sqrt{\rho(x)^2 + \rho'(x)^2} dx. \quad (\text{A.2})$$

Here, the integration in general needs to be done numerically. Only in a few non-generic cases as e.g. for the ellipse one can solve the integral analytically. In order to iterate an initial condition  $(q_1, p_1)$  in phase space, first, the real space position on the boundary  $(x_1, y_1)$  and the direction vector  $\vec{v} = (v_x, v_y)$  of the ray is computed. Therefore, Eq. (A.2) needs to be inverted numerically via a root search for  $\phi$  as

$$\phi(q_{\text{target}}) : \quad q(\phi) - q_{\text{target}} = 0 \quad (\text{A.3})$$

to obtain  $\phi_1 = \phi(q_1)$ . Hence, the starting position of the ray is given by

$$\begin{pmatrix} x_1 \\ y_1 \end{pmatrix} = \begin{pmatrix} \rho(\phi_1) \cos \phi_1 \\ \rho(\phi_1) \sin \phi_1 \end{pmatrix}. \quad (\text{A.4})$$

To determine the vector  $\vec{v}$  which indicates the traveling direction of the ray, first, the local tangent vector

$$\vec{t} = \frac{1}{\sqrt{\rho'(\phi_1)^2 + \rho(\phi_1)^2}} \begin{pmatrix} \rho'(\phi_1) \cos \phi_1 - \rho(\phi_1) \sin \phi_1 \\ \rho'(\phi_1) \sin \phi_1 + \rho(\phi_1) \cos \phi_1 \end{pmatrix} \quad (\text{A.5})$$

and inward pointing normal vector

$$\vec{n} = \begin{pmatrix} -t_y \\ t_x \end{pmatrix} = \frac{1}{\sqrt{\rho'(\phi_1)^2 + \rho(\phi_1)^2}} \begin{pmatrix} -\rho'(\phi_1) \sin \phi_1 - \rho(\phi_1) \cos \phi_1 \\ \rho'(\phi_1) \cos \phi_1 - \rho(\phi_1) \sin \phi_1 \end{pmatrix} \quad (\text{A.6})$$

is computed. Thus, the vector  $\vec{v}$  of the ray is given by

$$\vec{v} = p_1 \vec{t} + \sqrt{1 - p_1^2} \vec{n}. \quad (\text{A.7})$$

The ray reaches the new reflection point at the boundary after a (dimensionless) flight time  $t_c > 0$ . Hence, the function

$$f(t) = x^2(t) + y^2(t) - \rho^2(\phi(t)) \quad (\text{A.8})$$

with  $[x(t), y(t)] = [x_1, y_1] + t[v_x, v_y]$  and  $\phi(t) = \arctan[y(t)/x(t)]$  has a root at  $t_c$ ; i.e.  $f(t_c) = 0$ . The root search needs to be done numerically with e.g. a Newton method. Note that not only  $t_c$  but also  $t = 0$  is a root of  $f$  and if the cavity is non-convex there might exist even more roots with finite  $t$ . To obtain the correct value of  $t_c$  it is therefore necessary to have a proper initial guess for the Newton method. This can be done by using a polygon approximation of the boundary. Hence, one can compute all the intersections of the ray with the segments of the polygon first which can be done for each segment analytically. Then a proper initial guess is the smallest approximated flight time larger than zero. Once the new intersection point is found from Eq. (A.8) as  $[x_2, y_2] = [x(t_c), y(t_c)]$  the new phase space position  $q_2$  can be determined from Eq. (A.2). The new momentum  $p_2$  can be calculated from the local tangent vector at  $q_2$  as  $p_2 = \vec{t} \cdot \vec{v}$  and therefore the mapping  $(q_1, p_1) \mapsto (q_2, p_2)$  is determined.

In the following it is discussed how the procedure described above can be accelerated to shorten the computational time for the determination of a single iteration. One of the most time consuming steps in the procedure is the evaluation of the integral in Eq. (A.2) since the function  $q(\phi)$  is needed several times; e.g. for the Newton method to determine the inverse  $\phi(q)$ , see Eq. (A.3). To optimize the evaluation of  $q(\phi)$  the integrand is expressed in a Fourier series as

$$\sqrt{\rho(x)^2 + \rho'(x)^2} \approx \frac{\tilde{a}_0}{2} + \sum_{n=1}^N \tilde{a}_n \cos(nx) + \tilde{b}_n \sin(nx) \quad (\text{A.9})$$

where the coefficients are given by

$$\tilde{a}_n = \frac{1}{\pi} \int_0^{2\pi} \sqrt{\rho(x)^2 + \rho'(x)^2} \cos(nx) dx \quad (\text{A.10})$$

$$\tilde{b}_n = \frac{1}{\pi} \int_0^{2\pi} \sqrt{\rho(x)^2 + \rho'(x)^2} \sin(nx) dx. \quad (\text{A.11})$$

The numerical truncation parameter  $N$  needs to be chosen sufficiently large. For most cases studied in this thesis  $N \sim 40 \dots 100$  gives already accurate results. The Fourier expansion allows for an analytical integration in Eq. (A.2) which yields

$$q(\phi) \approx \frac{\tilde{a}_0}{2}\phi + \sum_{n=1}^N \tilde{a}_n \int_0^\phi \cos(nx) dx + \tilde{b}_n \int_0^\phi \sin(nx) dx \quad (\text{A.12})$$

$$= \frac{\tilde{a}_0}{2}\phi + \sum_{n=1}^N \frac{\tilde{a}_n}{n} \sin(n\phi) - \frac{\tilde{b}_n}{n} \cos(n\phi). \quad (\text{A.13})$$

The advantage is that the coefficients could be precomputed and recalled in every function call of  $q(\phi)$ . Note that if the system exhibits a mirror-reflection symmetry  $\tilde{b}_n = 0$  for all  $n$ .

Similar, also the inverse  $\phi(q)$  can be expressed in a Fourier series with precomputed coefficients. For a typical deformed cavity this optimization for  $q(\phi)$  and  $\phi(q)$  results in a speed up by a factor 5...30. Hence, it is helpful for e.g. the calculation of the Frobenius-Perron operator.

## A.2 Asymmetric backscattering in the angular momentum

### A.2.1 The Fourier-truncated spiral: An example system for asymmetric backscattering

In this section the generalized Fourier-truncated spiral is introduced. This cavity is a nice system for asymmetric backscattering since it has a smooth boundary curve that violates mirror-reflection symmetry. The cavity is defined in polar coordinates via

$$\frac{r(\phi)}{R} = 1 + \epsilon \sum_{j=1}^{N_p} \frac{(-1)^{j+1}}{j} \cos\left(j\phi + \delta\frac{\pi}{2}\right). \quad (\text{A.14})$$

Here,  $\delta \in [0, 1]$  is an asymmetry parameter which leads to a symmetric cavity if  $\delta = 0$ . An asymmetric cavity is obtained for  $\delta > 0$ . The number of Fourier terms  $N_p$  should not be chosen too large to avoid the Gibbs phenomenon in the boundary. The overall perturbation strength is fixed with  $\epsilon$ . In the limit ( $\delta = 1, N_p \rightarrow \infty$ ) a spiral cavity with notch size  $\pi\epsilon R$  is obtained. For an illustration of the shape for different parameter combinations see Fig. A.1.

In this thesis mainly  $\epsilon = 0.07$ ,  $\delta = 1$ , and  $N_p = 4$  is chosen. For these parameters the phase space is dominantly chaotic with very small (almost not visible) bouncing ball islands at  $p = 0$  inside the leaky region.

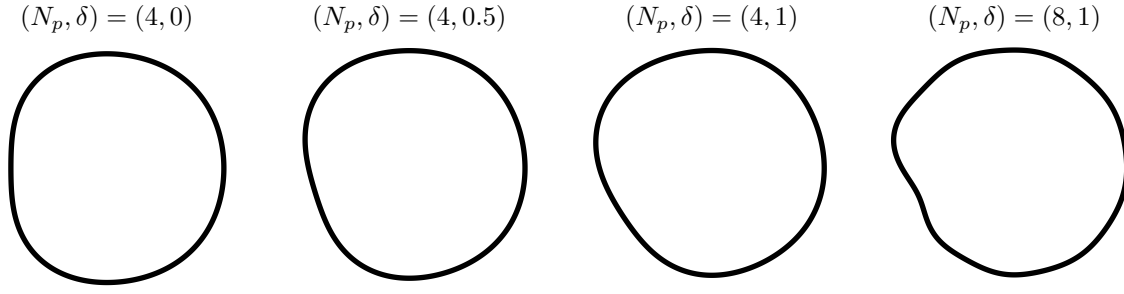


**Figure A.1:** Illustration of the Fourier-truncated spiral (A.14) for different parameters  $(N_p, \delta)$ . The parameter  $\epsilon = 0.07$  is fixed.

### A.2.2 The curve $L_z(q, p) = 0$ in phase space

In this section an analytical expression for the curve of vanishing angular momentum in phase space is obtained. To do so cavities defined via a continuous function  $r(\phi)$  are assumed.

For any point in the 2D real space the angular momentum of a ray is defined via

$$L_z = (\vec{r} \times \vec{p})_z = xp_y - yp_x. \quad (\text{A.15})$$

The angular momentum  $L_z$  of a ray changes only at the reflections. Therefore, in the following Eq. (A.15) is evaluated right after the reflection at the boundary: Using  $r = r(\phi)$  and

$$x = r \cos \phi \quad (\text{A.16a})$$

$$y = r \sin \phi \quad (\text{A.16b})$$

$$p_x = t_x p + n_x \sqrt{1 - p^2} \quad (\text{A.16c})$$

$$p_y = t_y p + n_y \sqrt{1 - p^2} \quad (\text{A.16d})$$

with tangent  $\vec{t} = (t_x, t_y)$  [see Eq. (A.5)] and normal vector  $\vec{n} = (n_x, n_y) = (-t_y, t_x)$  [see Eq. (A.6)] the curve of vanishing angular momentum can be calculated as follows

$$0 = L_z = \frac{r \cos \phi}{\sqrt{r'^2 + r^2}} \left( p [r' \sin \phi + r \cos \phi] + \sqrt{1 - p^2} [r' \cos \phi - r \sin \phi] \right) - \frac{r \sin \phi}{\sqrt{r'^2 + r^2}} \left( p [r' \cos \phi - r \sin \phi] - \sqrt{1 - p^2} [r' \sin \phi + r \cos \phi] \right) \quad (\text{A.17a})$$

$$= \frac{r \left( r' \sqrt{1 - p^2} + pr \right)}{\sqrt{r'^2 + r^2}}. \quad (\text{A.17b})$$

Here,  $r'$  is the derivative of the radius with respect to the angle. Because  $r \neq 0$  it follows that the term in the parentheses needs to vanish. Hence,

$$\mathbf{p} \equiv p(\phi) = \frac{-r'}{\sqrt{r'^2 + r^2}} \quad (\text{A.18})$$

is obtained. Since  $\phi = \phi(q)$  Eq. (A.18) defines a curve  $p(q)$  in phase space where the angular momentum is zero.

Interestingly, the image (one billiard map iteration) of this curve is given by its mirror-reflection at  $p = 0$ ; i.e. by  $r'/\sqrt{r'^2 + r^2}$ . This can be proven via a time-reversal symmetry argument as follows: If one takes an arbitrary point on the curve  $L_z(q_0, p_0) = 0$  the ray crosses the origin and is mapped to  $(q_1, p_1)$  whose angular momentum is in general not zero. However, the backward traveling ray  $(q_1, -p_1)$  at  $(q_1, p_1)$  crosses again the origin and is therefore on the curve  $L_z = 0$ . Hence, after one mapping of the whole curve  $L_z = 0$  one needs to flip it at  $p = 0$  to obtain the original curve  $L_z = 0$  again. Therefore, the image of the curve  $L_z = 0$  is its mirror-reflection at  $p = 0$ .

### A.2.3 Backscattering concerning $L_z(q, p) = 0$

In this section the backscattering concerning the curve of vanishing angular momentum (A.18) [which is in the following denoted by  $\mathbf{p}$ ] is investigated. The main target is to show that in the  $2 \times 2$  model of clockwise (CW) and counter-clockwise (CCW) propagating motion

$$\begin{pmatrix} \Omega_1 & A \\ B & \Omega_2 \end{pmatrix} \quad (\text{A.19})$$

the diagonal terms  $\Omega_1$  and  $\Omega_2$  are equal if the propagation is defined relative to  $\mathbf{p}$ . To simplify the following calculations the curves

$$\mathbf{p}_- = \frac{-|r'|}{\sqrt{r'^2 + r^2}} \quad (\text{A.20a})$$

$$\mathbf{p}_+ = \frac{|r'|}{\sqrt{r'^2 + r^2}} \quad (\text{A.20b})$$

are defined. These are the parts of  $\mathbf{p}$  and its image which lie only in the lower or the upper half of the phase space. Similar to the turn style mechanism for partial barriers the matrix elements in (A.19) are given by integrals over phase areas. Since microcavities can be treated as open billiards the areas need to be weighted with the reflectivity  $R(p)$ , see (2.23a), to get the intensity which is exchanged during one iteration. The matrix elements are therefore given

by

$$\Omega_1 = \int_0^{q_{\max}} \int_{\mathbf{p}_+}^1 R(p) \frac{dp dq}{q_{\max}} \quad (\text{A.21a})$$

$$\Omega_2 = \int_0^{q_{\max}} \int_{-1}^{\mathbf{p}_-} R(p) \frac{dp dq}{q_{\max}} \quad (\text{A.21b})$$

$$A = \int_0^{q_{\max}} \int_{\mathbf{p}_-}^{-\mathbf{p}} R(p) \frac{dp dq}{q_{\max}} \quad (\text{A.21c})$$

$$B = \int_0^{q_{\max}} \int_{\mathbf{p}_-}^{\mathbf{p}} R(p) \frac{dp dq}{q_{\max}} \quad (\text{A.21d})$$

with  $\mathbf{p}$ ,  $\mathbf{p}_-$ ,  $\mathbf{p}_+$  according to Eqs. (A.18), (A.20a), (A.20b). Next, it is assumed that CW and CCW regions are weakly coupled such that the curves defined by Eqs. (A.20a) and (A.20b) are completely inside the leaky region. Which is also true if the refractive index  $n$  is not too large; e.g. for  $n \lesssim 4$  in the Fourier-truncated spiral with  $(\epsilon, \delta, N_p) = (0.07, 1, 4)$ . In the leaky region the reflectivity is symmetric  $R(p) = R(-p)$  and analytical such that it has a power series

$$R(p) = \sum_{n=0}^{\infty} a_{2n} p^{2n}. \quad (\text{A.22})$$

Inserting Eqs. (A.20a), (A.20b) and (A.22) into the integrals one gets

$$A = \frac{1}{q_{\max}} \int_0^{q_{\max}} \int_{\mathbf{p}_-}^{-\mathbf{p}} \sum_{n=0}^{\infty} a_{2n} p^{2n} dp dq \quad (\text{A.23a})$$

$$= \frac{1}{q_{\max}} \int_0^{q_{\max}} \sum_{n=0}^{\infty} \frac{a_{2n}}{2n+1} (-\mathbf{p}^{2n+1} - \mathbf{p}_-^{2n+1}) dq \quad (\text{A.23b})$$

$$= \frac{1}{q_{\max}} \sum_{n=0}^{\infty} \frac{a_{2n}}{2n+1} \int_0^{2\pi} [-\mathbf{p}^{2n+1} - \mathbf{p}_-^{2n+1}] \sqrt{r^2 + r'^2} d\phi \quad (\text{A.23c})$$

$$= \frac{1}{q_{\max}} \sum_{n=0}^{\infty} \frac{a_{2n}}{2n+1} \left[ \int_0^{2\pi} |r'| \left( \frac{r'^2}{r^2 + r'^2} \right)^n d\phi + \int_0^{2\pi} r' \left( \frac{r'^2}{r^2 + r'^2} \right)^n d\phi \right] \quad (\text{A.23d})$$

$$= \frac{1}{q_{\max}} \sum_{n=0}^{\infty} \frac{a_{2n}}{2n+1} [I_n + \delta I_n] \quad (\text{A.23e})$$

$$B = \frac{1}{q_{\max}} \int_0^{q_{\max}} \int_{\mathbf{p}_-}^{\mathbf{p}} \sum_{n=0}^{\infty} a_{2n} p^{2n} dp dq \quad (\text{A.23f})$$

$$= \frac{1}{q_{\max}} \int_0^{q_{\max}} \sum_{n=0}^{\infty} \frac{a_{2n}}{2n+1} (\mathbf{p}^{2n+1} - \mathbf{p}_-^{2n+1}) dq \quad (\text{A.23g})$$

$$= \frac{1}{q_{\max}} \sum_{n=0}^{\infty} \frac{a_{2n}}{2n+1} \int_0^{2\pi} [\mathbf{p}^{2n+1} - \mathbf{p}_-^{2n+1}] \sqrt{r^2 + r'^2} d\phi \quad (\text{A.23h})$$

$$= \frac{1}{q_{\max}} \sum_{n=0}^{\infty} \frac{a_{2n}}{2n+1} \left[ \int_0^{2\pi} |r'| \left( \frac{r'^2}{r^2 + r'^2} \right)^n d\phi - \int_0^{2\pi} r' \left( \frac{r'^2}{r^2 + r'^2} \right)^n d\phi \right] \quad (\text{A.23i})$$

$$= \frac{1}{q_{\max}} \sum_{n=0}^{\infty} \frac{a_{2n}}{2n+1} [I_n - \delta I_n] \quad (\text{A.23j})$$

$$\Omega_1 = \frac{1}{q_{\max}} \int_0^{q_{\max}} \int_{\mathbf{p}_+}^1 R(p) dp dq \quad (\text{A.23k})$$

$$= \frac{1}{q_{\max}} \int_0^{q_{\max}} \left( \int_{\mathbf{p}_+}^0 R(p) dp + \int_0^{1/n} R(p) dp + \int_{1/n}^1 R(p) dp \right) dq \quad (\text{A.23l})$$

$$= \frac{1}{q_{\max}} \int_0^{q_{\max}} \left( -\sum_{n=0}^{\infty} \frac{a_{2n}}{2n+1} \mathbf{p}_+^{2n+1} + \frac{1}{2} \int_{-1/n}^{1/n} R(p) dp + 1 - \frac{1}{n} \right) dq \quad (\text{A.23m})$$

$$= 1 - \frac{1}{n} + \mu - \frac{1}{q_{\max}} \sum_{n=0}^{\infty} \frac{a_{2n}}{2n+1} I_n \quad (\text{A.23n})$$

$$\Omega_2 = \frac{1}{q_{\max}} \int_0^{q_{\max}} \int_{-1}^{\mathbf{p}_-} R(p) dp dq \quad (\text{A.23o})$$

$$= \frac{1}{q_{\max}} \int_0^{q_{\max}} \left( \int_{-1}^{-1/n} R(p) dp + \int_{-1/n}^0 R(p) dp + \int_0^{\mathbf{p}_-} R(p) dp \right) dq \quad (\text{A.23p})$$

$$= \frac{1}{q_{\max}} \int_0^{q_{\max}} \left( -\frac{1}{n} + 1 + \frac{1}{2} \int_{-1/n}^{1/n} R(p) dp + \sum \frac{a_n}{2n+1} \mathbf{p}_-^{2n+1} \right) dq \quad (\text{A.23q})$$

$$= 1 - \frac{1}{n} + \mu - \frac{1}{q_{\max}} \sum_{n=0}^{\infty} \frac{a_{2n}}{2n+1} I_n. \quad (\text{A.23r})$$

Here, the integrals

$$\mu = \int_{-1/n}^{1/n} R(p) \frac{dp}{2} \quad (\text{A.24a})$$

$$I_n = \int_0^{2\pi} |r'| \left( \frac{r'^2}{r^2 + r'^2} \right)^n d\phi \quad (\text{A.24b})$$

$$\delta I_n = \int_0^{2\pi} r' \left( \frac{r'^2}{r^2 + r'^2} \right)^n d\phi \quad (\text{A.24c})$$

have been used. Although Eqs. (A.23e), (A.23j), (A.23n), and (A.23r) contain infinite sums it allows some conclusions: (i) Eqs. (A.23n) and (A.23r) are the same such that  $\Omega_1 = \Omega_2$ . (ii) The asymmetry in the matrix elements  $A$  and  $B$  has its origin in  $\delta I_n$  such that maximizing  $\delta I_n$  allows to search for “more asymmetric” cavities. This is illustrated at the Fourier-truncated spiral by varying the asymmetry parameter  $\delta$ , see Eq. (A.14). The numerically determined chirality  $S$  (see Tab. 4.2) coincides quite well with  $\delta I_1$  as shown in Fig. A.2. This can be seen by subtracting Eq. (A.23j) [ $B$ ] from Eq. (A.23e) [ $A$ ] which provides a series in the  $\delta I_n$ . The higher order terms  $\delta I_2, \delta I_3, \dots$  give minor contributions with the same trend in  $\delta$ .<sup>1</sup> (iii) The

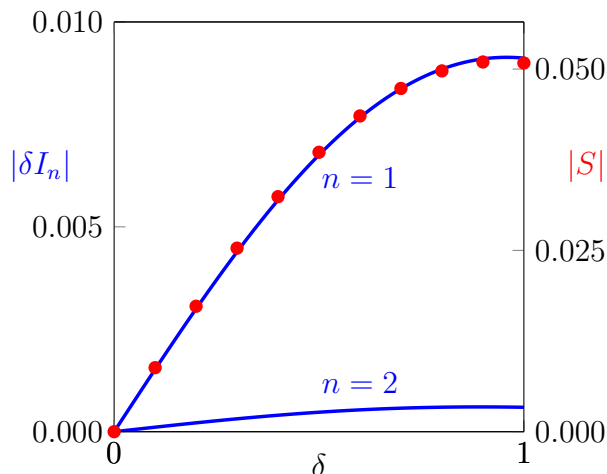


**Figure A.2:** For the Fourier-truncated spiral with  $\epsilon = 0.07$ , asymmetry parameter  $\delta$ , and refractive index  $n = 3$  the chirality  $S$  (red dots) and the integrals  $\delta I_1, \delta I_2$  (blue curves) are shown. Note that  $y$ -axis is scaled for  $S$  according to the right labels and for  $\delta I_n$  according to the left labels.

non-linear terms in the reflectivity are crucial to get asymmetric backscattering in the ray dynamics. If e.g. a model system with constant reflectivity is assumed it yields

$$A - B \sim \delta I_0 = \int_0^{2\pi} r' d\phi = 0 \quad (\text{A.25})$$

and therefore no asymmetry in the backscattering is observed.

A further interesting issue is the backscattering in constant width billiards [Gutkin, 2007]. Here, the line  $p = 0$  is an invariant curve which cannot be crossed by trajectories starting in lower or upper half of the phase space, see e.g. Fig. 4.16 in Sec. 4.2.3 for an example. Therefore, a ray dynamical origin of asymmetric backscattering has been ruled out in Ref. [Wiersig et al., 2011] for such cavities which is definitely true if the backscattering regarding the line  $p = 0$  is considered. However, the backscattering regarding the curve  $L_z(q, p) = 0$  can have a ray dynamical origin since this curve is not invariant. Therefore the numerically obtained matrix

<sup>1</sup>Interestingly the maximum of  $|\delta I_1|$  is not at  $\delta = 1$  but at  $\delta \approx 0.95$ . This is confirmed numerically by  $|S(\delta = 0.95)| = 0.05106$  which is slightly larger than  $|S(\delta = 1)| = 0.05084$ .



elements of the  $2 \times 2$  Hamiltonian (A.19) are  $\Omega_1 = \Omega_2 \approx 0.75603$ ,  $A \approx 0.02824$ , and  $B \approx 0.02837$ . They reflect a slight asymmetry in the backscattering with  $S = (A - B)/(A + B) \approx -0.00236$  (values obtained for  $n = 3.0$  and the cavity from Fig. 4.16). Note that both  $A \neq 0$  and  $B \neq 0$  indicate that the intensity is scattered from CW to CCW and vice versa.

## A.2.4 Shifting the angular momentum center

In this section it is discussed how a shift of the origin changes the backscattering concerning the curve  $L_z = 0$ . It is assumed that the new origin at  $(x_c, y_c)$  is still inside the cavity such that the angular momentum with respect to the new origin is

$$L_z = (x - x_c)p_y - (y - y_c)p_x. \quad (\text{A.26})$$

A similar calculation as in (A.17) results in the curve  $\mathbf{p}$  of vanishing angular momentum

$$p = \frac{-g}{\sqrt{g^2 + h^2}} \quad (\text{A.27})$$

where  $g$  and  $h$  are functions of the angle  $\phi$ . They are given by

$$g = rr' - r'(x_c \cos \phi + y_c \sin \phi) + r(x_c \sin \phi - y_c \cos \phi) \quad (\text{A.28a})$$

$$h = r^2 + r'(y_c \cos \phi - x_c \sin \phi) - r(x_c \cos \phi + y_c \sin \phi). \quad (\text{A.28b})$$

For an illustration of several curves  $\mathbf{p}$  with different  $(x_c, y_c)$  see Fig. A.3. Note that  $r = r(\phi)$  and  $r' = r'(\phi)$  are defined with respect to the original (non-shifted) origin. Since Eq. (A.27) is formally the same in the shifted and non-shifted case the calculation (A.23) of the matrix elements can be done in a same manner but with the redefined integrals

$$I_n = \int_0^{2\pi} |g| \left( \frac{g^2}{g^2 + h^2} \right)^n \sqrt{\frac{r'^2 + r^2}{g^2 + h^2}} d\phi \quad (\text{A.29a})$$

$$\delta I_n = \int_0^{2\pi} g \left( \frac{g^2}{g^2 + h^2} \right)^n \sqrt{\frac{r'^2 + r^2}{g^2 + h^2}} d\phi. \quad (\text{A.29b})$$

Note that for  $(x_c, y_c) \rightarrow (0, 0)$  the original definitions of  $\mathbf{p}$ ,  $I_n$ , and  $\delta I_n$  as in Eqs. (A.18), (A.24b), and (A.24c) are restored.

In Fig. A.4 the backscattering in the Fourier-truncated spiral with a varying angular momentum center is illustrated. As shown in Fig. A.4(b) even in the symmetric case  $\delta = 0$  a asymmetry in the backscattering ( $S \neq 0$ ) can be observed. Only if the angular momentum center is chosen at the mirror-reflection line  $y = 0$  the backscattering is symmetric. This is intuitive since every  $y \neq 0$  is not a mirror-reflection symmetry line of the cavity.

Interestingly, also for the asymmetric deformation  $\delta = 1$  as shown in Fig. A.4(a) there exists

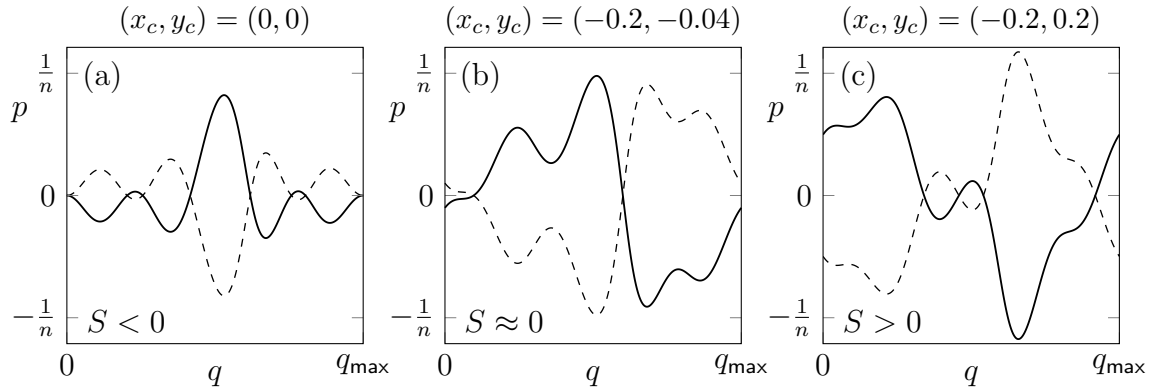


**Figure A.3:** The black solid curves  $\mathbf{p}$  ( $L_z(q, p) = 0$ ) are shown for different angular momentum centers in (a) to (c). Black dashed curves represent the one times iterated solid curves. In (a) CW propagation and in (c) CCW propagation is preferred while in (b) no rotation is preferred. Compare this preferred sense of rotation, i.e.  $S$ , with Fig. A.4 (a).

curves of vanishing asymmetry in the backscattering (shown as white curves). These curves cannot be related to a mirror-reflection symmetry of the boundary. It is rather only the phase space mapping of the curve  $\mathbf{p}$  (and their image) which determines them. This is illustrated in Fig. A.3: Roughly speaking, if the curve  $L_z = 0$  has a large extension in the upper but a small extension in the lower half of the phase space then its image has a small extension in the upper but a large extension in the lower half of the phase space. Consequently, the matrix element  $B$  is larger than  $A$  (because the reflectivity is symmetric to  $p = 0$  and increases for larger  $|p|$ ). This situation leads to  $S < 0$  which is illustrated in Fig. A.3(a). The opposite situation resulting in  $S > 0$  can be seen in Fig. A.3(c). In case of almost vanishing asymmetry in the backscattering  $S \approx 0$  the curve  $\mathbf{p}$  and its image have almost the same extension in the upper and lower half of the phase space as shown in Fig. A.3(b) which results in matrix elements  $A \approx B$ .

The main aspects of the backscattering with a varying angular momentum center can be already captured by the analytical expression  $\delta I_1$  from Eq. (A.29b), see Fig. A.4(c)-(d). The curves of vanishing  $S$  are predicted nicely with  $\delta I_1$ . However, for larger shifts  $(x_c, y_c)$  the predictions based on  $\delta I_1$  become less accurate. Note that for larger shifts  $(x_c, y_c)$  Eq. (A.29b) is strictly speaking not valid since the curve  $\mathbf{p}$  exceeds  $1/n$  what was excluded in the derivation of the matrix elements.

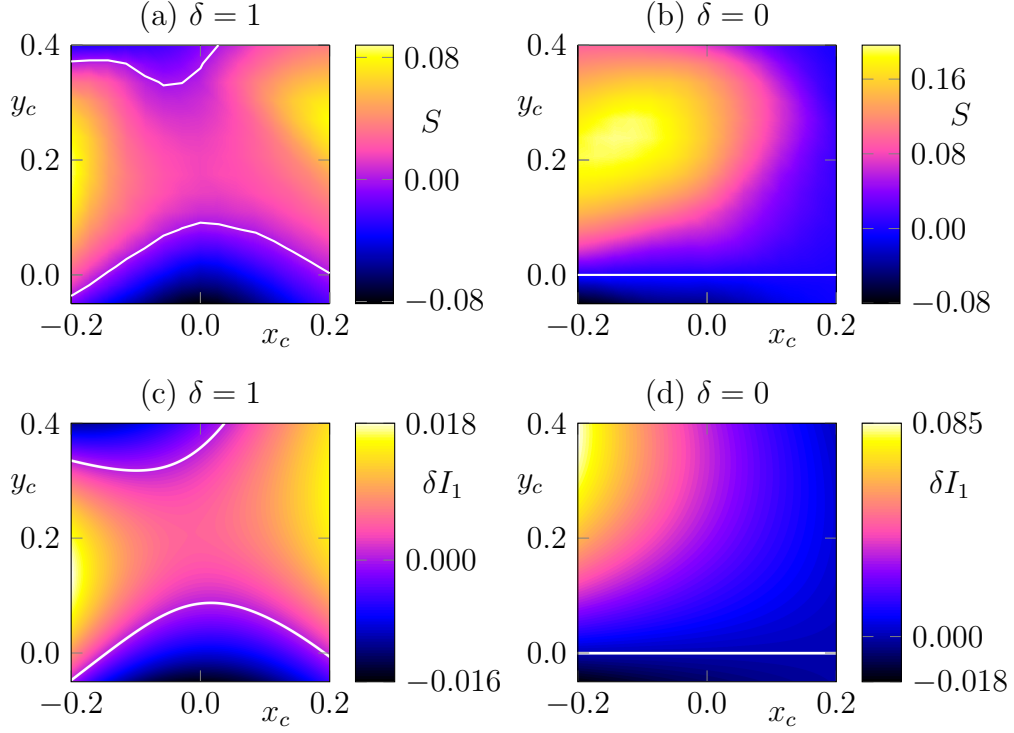


**Figure A.4:** (a) and (b) show the numerically determined overlap  $S = (A - B)/(A + B)$  in the Fourier-truncated spiral with  $(\epsilon, N_p, n) = (0.07, 4, 3.0)$  and corresponding  $\delta$  with varying angular momentum center  $(x_c, y_c)$ . In (c) and (d) the analytical solutions  $\delta I_1$  [see Eq. (A.29b)] are shown. A white curve illustrates  $S = 0$  in (a)-(b) and  $\delta I_1 = 0$  in (c)-(d).

### A.3 Derivatives of the function $\tilde{D}_m^l(x)$

In section 5.3 the third-order corrections to the complex wave number  $x = kR$  are derived as [see Eq. (5.34)]

$$\begin{aligned}
x_3 \partial_x \tilde{D}_m^1 &= -x_1 x_2 \partial_x^2 \tilde{D}_m^1 - \frac{1}{6} x_1^3 \partial_x^3 \tilde{D}_m^1 + b_m^{(3)} x_0 \frac{H'_m}{H_m} + b_m^{(2)} x_1 \left[ x_0 \left( \frac{H''_m}{H_m} - \frac{H_m'^2}{H_m^2} \right) + \frac{H'_m}{H_m} \right] \\
&\quad - \left( x_2 \partial_x \tilde{D}_m^2 + \frac{1}{2} x_1^2 \partial_x^2 \tilde{D}_m^2 \right) A_{mm} \\
&\quad - \frac{1}{2} x_1 \partial_x \tilde{D}_m^3 B_{mm} - \frac{1}{6} \tilde{D}_m^4 C_{mm} + b_m^{(2)} x_0^2 \frac{H''_m}{H_m} A_{mm} \\
&\quad - \sum_{p \neq m} \left[ A_{mp} \left( a_p^{(2)} \tilde{D}_p^2 + a_p^{(1)} x_1 \partial_x \tilde{D}_p^2 \right) + \frac{1}{2} B_{mp} a_p^{(1)} \tilde{D}_p^3 - A_{mp} b_p^{(2)} x_0^2 \frac{H''_p}{H_p} \right] \quad (\text{A.30})
\end{aligned}$$

where the function

$$\tilde{D}_m^l(x) = x^l n^l \frac{J_m^{[l]}(nx)}{J_m} - x^l \frac{H_m^{[l]}(x)}{H_m} \quad (\text{A.31})$$

and its derivatives with respect to  $x$  enter ( $^{[l]}$  denotes the  $l$ -th derivative). In this appendix these derivatives  $\partial_x^u \tilde{D}_m^l$  are listed explicitly to allow for a direct implementation. The derivatives are calculated and exported to L<sup>A</sup>T<sub>E</sub>X using the computer algebra system Maple as

$$\tilde{D}_m^1 = -\frac{J_{m+1}(nx)nx}{J_m(nx)} + \frac{xH_{m+1}^{(1)}(x)}{H_m^{(1)}(x)} \quad (\text{A.32})$$

$$\begin{aligned} \partial_x \tilde{D}_m^1 &= -xn^2 - \frac{xn^2(J_{m+1}(nx))^2}{(J_m(nx))^2} + 2\frac{mnJ_{m+1}(nx)}{J_m(nx)} + x + \frac{x(H_{m+1}^{(1)}(x))^2}{(H_m^{(1)}(x))^2} \\ &\quad - 2\frac{mH_{m+1}^{(1)}(x)}{H_m^{(1)}(x)} \end{aligned} \quad (\text{A.33})$$

$$\begin{aligned} \partial_x^2 \tilde{D}_m^1 &= 1 + 2\frac{xH_{m+1}^{(1)}(x)}{H_m^{(1)}(x)} + 2\frac{mH_{m+1}^{(1)}(x)}{H_m^{(1)}(x)x} + 4\frac{H_{m+1}^{(1)}(x)m^2}{H_m^{(1)}(x)x} \\ &\quad - 6\frac{(H_{m+1}^{(1)}(x))^2 m}{(H_m^{(1)}(x))^2} - n^2 + 6\frac{n^2(J_{m+1}(nx))^2 m}{(J_m(nx))^2} - 4\frac{nJ_{m+1}(nx)m^2}{xJ_m(nx)} \\ &\quad - 2\frac{mnJ_{m+1}(nx)}{xJ_m(nx)} + 2\frac{x(H_{m+1}^{(1)}(x))^3}{(H_m^{(1)}(x))^3} - \frac{(H_{m+1}^{(1)}(x))^2}{(H_m^{(1)}(x))^2} - 2m \\ &\quad - 2\frac{xn^3 J_{m+1}(nx)}{J_m(nx)} + 2n^2 m + \frac{n^2(J_{m+1}(nx))^2}{(J_m(nx))^2} - 2\frac{xn^3(J_{m+1}(nx))^3}{(J_m(nx))^3} \end{aligned} \quad (\text{A.34})$$

$$\begin{aligned}
\partial_x^3 \tilde{D}_m^1 = & -2 \frac{n^2 m}{x} - 4 \frac{n^2 m^2}{x} + 2 \frac{n^3 J_{m+1}(nx)}{J_m(nx)} - 4 \frac{m H_{m+1}^{(1)}(x)}{x^2 H_m^{(1)}(x)} + 28 \frac{\left(H_{m+1}^{(1)}(x)\right)^2 m^2}{x \left(H_m^{(1)}(x)\right)^2} \\
& - 8 \frac{H_{m+1}^{(1)}(x) m^3}{x^2 H_m^{(1)}(x)} - 12 \frac{H_{m+1}^{(1)}(x) m^2}{x^2 H_m^{(1)}(x)} - 24 \frac{\left(H_{m+1}^{(1)}(x)\right)^3 m}{\left(H_m^{(1)}(x)\right)^3} - 8 \frac{x n^4 \left(J_{m+1}(nx)\right)^2}{\left(J_m(nx)\right)^2} \\
& - 2 \frac{n^2 \left(J_{m+1}(nx)\right)^2}{x \left(J_m(nx)\right)^2} - 6 \frac{x n^4 \left(J_{m+1}(nx)\right)^4}{\left(J_m(nx)\right)^4} + 18 \frac{\left(H_{m+1}^{(1)}(x)\right)^2 m}{x \left(H_m^{(1)}(x)\right)^2} - 16 \frac{m H_{m+1}^{(1)}(x)}{H_m^{(1)}(x)} \\
& + 12 \frac{n J_{m+1}(nx) m^2}{x^2 J_m(nx)} + 8 \frac{x \left(H_{m+1}^{(1)}(x)\right)^2}{\left(H_m^{(1)}(x)\right)^2} + 2x + 16 \frac{n^3 J_{m+1}(nx) m}{J_m(nx)} + 4 \frac{m n J_{m+1}(nx)}{x^2 J_m(nx)} \\
& - 28 \frac{n^2 \left(J_{m+1}(nx)\right)^2 m^2}{x \left(J_m(nx)\right)^2} + 8 \frac{n J_{m+1}(nx) m^3}{x^2 J_m(nx)} + 24 \frac{n^3 \left(J_{m+1}(nx)\right)^3 m}{\left(J_m(nx)\right)^3} \\
& - 18 \frac{n^2 \left(J_{m+1}(nx)\right)^2 m}{x \left(J_m(nx)\right)^2} + 2 \frac{m}{x} - 2 x n^4 + 4 \frac{m^2}{x} + 2 \frac{\left(H_{m+1}^{(1)}(x)\right)^2}{x \left(H_m^{(1)}(x)\right)^2} - 2 \frac{H_{m+1}^{(1)}(x)}{H_m^{(1)}(x)} \\
& + 6 \frac{x \left(H_{m+1}^{(1)}(x)\right)^4}{\left(H_m^{(1)}(x)\right)^4} + 6 \frac{n^3 \left(J_{m+1}(nx)\right)^3}{\left(J_m(nx)\right)^3} - 6 \frac{\left(H_{m+1}^{(1)}(x)\right)^3}{\left(H_m^{(1)}(x)\right)^3} \tag{A.35}
\end{aligned}$$

$$\tilde{D}_m^2 = -n^2 x^2 + \frac{J_{m+1}(nx) n x}{J_m(nx)} + x^2 - \frac{x H_{m+1}^{(1)}(x)}{H_m^{(1)}(x)} \tag{A.36}$$

$$\begin{aligned}
\partial_x \tilde{D}_m^2 = & -2 \frac{m n J_{m+1}(nx)}{J_m(nx)} - n^2 x + 2 \frac{m H_{m+1}^{(1)}(x)}{H_m^{(1)}(x)} - \frac{x \left(H_{m+1}^{(1)}(x)\right)^2}{\left(H_m^{(1)}(x)\right)^2} + x \\
& + \frac{n^2 \left(J_{m+1}(nx)\right)^2 x}{\left(J_m(nx)\right)^2} \tag{A.37}
\end{aligned}$$

$$\begin{aligned}
\partial_x^2 \tilde{D}_m^2 &= 1 - 2 \frac{x H_{m+1}^{(1)}(x)}{H_m^{(1)}(x)} - 2 \frac{m H_{m+1}^{(1)}(x)}{H_m^{(1)}(x)x} - 4 \frac{H_{m+1}^{(1)}(x)m^2}{H_m^{(1)}(x)x} + 6 \frac{\left(H_{m+1}^{(1)}(x)\right)^2 m}{\left(H_m^{(1)}(x)\right)^2} - n^2 \\
&\quad - 2 \frac{x \left(H_{m+1}^{(1)}(x)\right)^3}{\left(H_m^{(1)}(x)\right)^3} + \frac{\left(H_{m+1}^{(1)}(x)\right)^2}{\left(H_m^{(1)}(x)\right)^2} + 2m + 4 \frac{n J_{m+1}(nx)m^2}{x J_m(nx)} + 2 \frac{mn J_{m+1}(nx)}{x J_m(nx)} \\
&\quad - 6 \frac{n^2 \left(J_{m+1}(nx)\right)^2 m}{\left(J_m(nx)\right)^2} + 2 \frac{xn^3 J_{m+1}(nx)}{J_m(nx)} - 2n^2 m - \frac{n^2 \left(J_{m+1}(nx)\right)^2}{\left(J_m(nx)\right)^2} \\
&\quad + 2 \frac{xn^3 \left(J_{m+1}(nx)\right)^3}{\left(J_m(nx)\right)^3} \tag{A.38}
\end{aligned}$$

$$\begin{aligned}
\tilde{D}_m^3 &= \frac{J_{m+1}(nx)n^3 x^3}{J_m(nx)} - x^2 n^2 m - 2 \frac{J_{m+1}(nx)nx}{J_m(nx)} - \frac{J_{m+1}(nx)m^2 nx}{J_m(nx)} + n^2 x^2 \\
&\quad - \frac{x^3 H_{m+1}^{(1)}(x)}{H_m^{(1)}(x)} + x^2 m + 2 \frac{x H_{m+1}^{(1)}(x)}{H_m^{(1)}(x)} + \frac{x H_{m+1}^{(1)}(x)m^2}{H_m^{(1)}(x)} - x^2 \tag{A.39}
\end{aligned}$$

$$\begin{aligned}
\partial_x \tilde{D}_m^3 &= \frac{x^3 n^4 \left(J_{m+1}(nx)\right)^2}{\left(J_m(nx)\right)^2} - 2 \frac{xn^2 \left(J_{m+1}(nx)\right)^2}{\left(J_m(nx)\right)^2} + 2 \frac{x^2 H_{m+1}^{(1)}(x)m}{H_m^{(1)}(x)} + \frac{x \left(H_{m+1}^{(1)}(x)\right)^2 m^2}{\left(H_m^{(1)}(x)\right)^2} \\
&\quad - 2 \frac{H_{m+1}^{(1)}(x)m^3}{H_m^{(1)}(x)} - xn^2 m^2 - 4 \frac{m H_{m+1}^{(1)}(x)}{H_m^{(1)}(x)} + 2 \frac{x^2 n^3 J_{m+1}(nx)}{J_m(nx)} - 2xn^2 m - x^3 \\
&\quad + 2 \frac{x \left(H_{m+1}^{(1)}(x)\right)^2}{\left(H_m^{(1)}(x)\right)^2} - 2 \frac{x^2 n^3 J_{m+1}(nx)m}{J_m(nx)} + 4 \frac{mn J_{m+1}(nx)}{J_m(nx)} - \frac{xn^2 \left(J_{m+1}(nx)\right)^2 m^2}{\left(J_m(nx)\right)^2} \\
&\quad + 2 \frac{n J_{m+1}(nx)m^3}{J_m(nx)} - 2 \frac{x^2 H_{m+1}^{(1)}(x)}{H_m^{(1)}(x)} - \frac{x^3 \left(H_{m+1}^{(1)}(x)\right)^2}{\left(H_m^{(1)}(x)\right)^2} \\
&\quad + xm^2 + x^3 n^4 + 2xm \tag{A.40}
\end{aligned}$$

## A.4 Derivatives for the asymmetric perturbation theory

In this appendix the terms  $\partial_r^u [\psi_{\pm, \text{in}} - \psi_{\pm, \text{out}}](R, \phi)$  with  $u = 0, 1, 2, 3$  which are needed for the derivation of the asymmetric-PT are calculated. The wave function is given by the ansatz

(6.2) which is repeated here for convenience

$$\psi_{\pm,\text{in}}(r, \phi) = \frac{J_m(nkr)}{J_m(nx)} [e^{iz} e^{im\phi} + e^{-iz} e^{-im\phi}] + \sum_{p \neq \pm m} a_p \frac{J_p(nkr)}{J_p(nx)} e^{ip\phi} \quad (\text{A.41})$$

$$\begin{aligned} \psi_{\pm,\text{out}}(r, \phi) &= \frac{H_m(kr)}{H_m(x)} [(1 + b_m) e^{iz} e^{im\phi} + (1 + b_{-m}) e^{-iz} e^{-im\phi}] \\ &+ \sum_{p \neq \pm m} (a_p + b_p) \frac{H_p(kr)}{H_p(x)} e^{ip\phi}. \end{aligned} \quad (\text{A.42})$$

Evaluating the ansatz for  $r = R$  straightforwardly leads to

$$[\psi_{\pm,\text{in}} - \psi_{\pm,\text{out}}] = -b_m e^{iz} e^{im\phi} - b_{-m} e^{-iz} e^{-im\phi} - \sum_{p \neq \pm m} b_p e^{ip\phi}. \quad (\text{A.43})$$

Note that here (and in the following) the dependency  $(R, \phi)$  at the left-hand-side is not explicitly written.

Next, the first derivative ( $u = 1$ ) is computed as follows

$$\begin{aligned} \partial_r [\psi_{\pm,\text{in}} - \psi_{\pm,\text{out}}] &= \underbrace{\left[ nk \frac{J'_m}{J_m}(nx) - k \frac{H'_m}{H_m}(x) \right]}_{kS_m(x)} [e^{iz} e^{im\phi} + e^{-iz} e^{-im\phi}] \\ &- k \frac{H'_m}{H_m}(x) [b_m e^{iz} e^{im\phi} + b_{-m} e^{-iz} e^{-im\phi}] \\ &+ \sum_{p \neq \pm m} a_p \underbrace{\left[ nk \frac{J'_p}{J_p}(nx) - k \frac{H'_p}{H_p}(x) \right]}_{kS_p(x)} e^{ip\phi} - \sum_{p \neq \pm m} kb_p \frac{H'_p}{H_p}(x) e^{ip\phi} \end{aligned} \quad (\text{A.44a})$$

$$\begin{aligned} &= k \left\{ S_m(x) [e^{iz} e^{im\phi} + e^{-iz} e^{-im\phi}] - \frac{H'_m}{H_m}(x) [b_m e^{iz} e^{im\phi} + b_{-m} e^{-iz} e^{-im\phi}] \right. \\ &\quad \left. + \sum_{p \neq \pm m} \left( a_p S_p(x) - b_p \frac{H'_p}{H_p}(x) \right) e^{ip\phi} \right\} \end{aligned} \quad (\text{A.44b})$$

As the next step the second derivative ( $u = 2$ ) is computed. Therefore, one first writes

$$\begin{aligned} \partial_r^2 [\psi_{\pm,\text{in}} - \psi_{\pm,\text{out}}] &= \left[ n^2 k^2 \frac{J''_m}{J_m}(nx) - k^2 \frac{H''_m}{H_m}(x) \right] [e^{iz} e^{im\phi} + e^{-iz} e^{-im\phi}] \\ &- k^2 \frac{H''_m}{H_m}(x) [b_m e^{iz} e^{im\phi} + b_{-m} e^{-iz} e^{-im\phi}] \\ &+ \sum_{p \neq \pm m} a_p \left[ n^2 k^2 \frac{J''_p}{J_p}(nx) - k^2 \frac{H''_p}{H_p}(x) \right] e^{ip\phi} - \sum_{p \neq \pm m} b_p k^2 \frac{H''_p}{H_p}(x) e^{ip\phi}. \end{aligned} \quad (\text{A.45})$$

At this point the relation

$$\frac{J_p''}{J_p}(z) = -\frac{1}{z} \frac{J_p'}{J_p}(z) - \left(1 - \frac{p^2}{z^2}\right). \quad (\text{A.46})$$

from the Bessel-equation is used which is also valid for the Hankel-functions. Hence, one can simplify

$$n^2 k^2 \frac{J_p''}{J_p}(nx) - k^2 \frac{H_p''}{H_p}(x) = k^2 \left[ -\frac{n}{x} \frac{J_p'}{J_p}(nx) + \frac{1}{x} \frac{H_p'}{H_p}(x) - n^2 \left(1 - \frac{m^2}{(nx)^2}\right) + 1 - \frac{m^2}{x^2} \right] \quad (\text{A.47a})$$

$$= k^2 \left[ -\frac{1}{x} S_p(x) - (n^2 - 1) \right] \quad (\text{A.47b})$$

$$= -\frac{k}{R} [S_p(x) + x(n^2 - 1)]. \quad (\text{A.47c})$$

This simplification can be inserted in Eq. (A.45) which yields

$$\begin{aligned} \partial_r^2 [\psi_{\pm, \text{in}} - \psi_{\pm, \text{out}}] = & -\frac{k}{R} \left\{ [S_m(x) + x(n^2 - 1)] [e^{iz} e^{im\phi} + e^{-iz} e^{-im\phi}] \right. \\ & + x \frac{H_m''}{H_m}(x) [b_m e^{iz} e^{im\phi} + b_{-m} e^{-iz} e^{-im\phi}] \\ & \left. + \sum_{p \neq \pm m} a_p [S_p(x) + x(n^2 - 1)] e^{ip\phi} + x \sum_{p \neq \pm m} b_p \frac{H_p''}{H_p}(x) e^{ip\phi} \right\}. \end{aligned} \quad (\text{A.48})$$

Finally, the third derivative ( $u = 3$ ) is computed as

$$\begin{aligned} \partial_r^3 [\psi_{\pm, \text{in}} - \psi_{\pm, \text{out}}] = & \left[ n^3 k^3 \frac{J_m'''}{J_m}(nx) - k^3 \frac{H_m'''}{H_m}(x) \right] [e^{iz} e^{im\phi} + e^{-iz} e^{-im\phi}] \\ & - k^3 \frac{H_m'''}{H_m}(x) [b_m e^{iz} e^{im\phi} + b_{-m} e^{-iz} e^{-im\phi}] \\ & + \sum_{p \neq \pm m} a_p \left[ n^3 k^3 \frac{J_p'''}{J_p}(nx) - k^3 \frac{H_p'''}{H_p}(x) \right] e^{ip\phi} - \sum_{p \neq \pm m} b_p k^3 \frac{H_p'''}{H_p}(x) e^{ip\phi}. \end{aligned} \quad (\text{A.49})$$

At this point one can use the relation

$$\frac{J_p'''}{J_p}(z) = \left( \frac{p^2 + 2}{z^2} - 1 \right) \frac{J_p'}{J_p}(z) + \frac{1}{z} - 3 \frac{p^2}{z^3} \quad (\text{A.50})$$

obtained from the Bessel-equation which is again also valid for the Hankel functions. Hence,



it can be simplified

$$n^3 k^3 \frac{J_p'''}{J_p}(nx) - k^3 \frac{H_p'''}{H_p}(x) = k^3 \left\{ \frac{p^2 + 2}{x^2} \left[ n \frac{J_p'}{J_p}(nx) - \frac{H_p'}{H_p}(x) \right] + \underbrace{\left[ -n^3 \frac{J_p'}{J_p}(nx) + \frac{H_p'}{H_p}(x) \right]}_{- \left[ n^2 \left( n \frac{J_p'}{J_p}(nx) - \frac{H_p'}{H_p}(x) \right) + (n^2 - 1) \frac{H_p'}{H_p}(x) \right]} \right. \\ \left. + \frac{n^2}{x} - 3 \frac{p^2}{x^3} - \frac{1}{x} + 3 \frac{p^2}{x^3} \right\} \quad (\text{A.51a})$$

$$= k^3 \left\{ \frac{p^2 + 2}{x^2} S_p(x) - n^2 S_p(x) - (n^2 - 1) \frac{H_p'}{H_p}(x) + \frac{1}{x} (n^2 - 1) \right\} \quad (\text{A.51b})$$

$$= S_m(x) k \left( \frac{p^2 + 2}{R^2} - k^2 n^2 \right) - k^3 (n^2 - 1) \frac{H_p'}{H_p}(x) + k^2 \frac{n^2 - 1}{R} \quad (\text{A.51c})$$

$$= \frac{x_0^2}{R^3} (n^2 - 1) \left( 1 - x_0 \frac{H_p'}{H_p}(x_0) \right) + \mathcal{O}(\lambda). \quad (\text{A.51d})$$

Inserting the result into Eq. (A.49) yields

$$\partial_r^3 [\psi_{\pm, \text{in}} - \psi_{\pm, \text{out}}] = \frac{x_0^2}{R^3} (n^2 - 1) \left( 1 - x_0 \frac{H_m'}{H_m}(x_0) \right) [e^{iz_0} e^{im\phi} + e^{-iz_0} e^{-im\phi}] + \mathcal{O}(\lambda). \quad (\text{A.52})$$

Hence, the terms  $\partial_r^u [\psi_{\pm, \text{in}} - \psi_{\pm, \text{out}}](R, \phi)$  have been calculated up to their required order in  $\lambda$ .

## A.5 Improving the perturbation theory using scaling

In this section it is explained how a rescaling of the cavity size can be used to get an improved prediction of  $x = kR$  from the perturbation theory. This improvement is valuable in cases where the boundary perturbation function  $f(\phi)$  enlarges (or reduces) the overall cavity size. A typical example is the spiral where  $f(\phi) < 0$  for all  $\phi > 0$ .

The key idea of the scaling improvement is not to use  $r(\phi)$  directly but to introduce a rescaled radius  $r_\eta(\phi)$

$$r_\eta(\phi) = \eta r(\phi) \quad (\text{A.53})$$

of the cavity. Consequently, the rescaled boundary deformation function is

$$f_\eta(\phi) = r_\eta(\phi) - R. \quad (\text{A.54})$$

The scaling factor  $\eta$  is then chosen such that it minimizes the area where  $f_\eta(\phi)$  changes the refractive index of the circular cavity of radius  $R$ , see Fig. A.5(a-b) for the rescaling of a spiral with  $\epsilon = 0.2$ .

Using the rescaled deformation function for the Fourier harmonics  $A_q$  and  $B_q$  [see Eqs. (6.9) and (6.18)] for the asymmetric-PT or in the  $A_{pm}$ ,  $B_{pm}$ ,  $C_{pm}$  [see Eqs. (5.16), (5.20), and (5.30)] for the symmetric-PT results in a prediction  $x_\eta$  of the rescaled cavity. Thereby, the complex wave number  $x$  of the original non-rescaled cavity is obtained via

$$x = \eta x_\eta. \quad (\text{A.55})$$

In the following the rescaling improvements are illustrated at the spiral cavity [see Eq. (2.19)]. First, the optimal scaling  $\eta$  needs to be deduced for a given notch size  $\epsilon$ . Therefore, Fig. A.5(c) shows the perturbation area as function of the scaling factor  $\eta$  and notch size  $\epsilon$ . The optimal scaling factor is well described by

$$\eta = 1 + \frac{\epsilon}{2} \quad (\text{A.56})$$

which is shown as white line in Fig. A.5. Using this scaling factor for the perturbation theory results in improved predictions of the wave number  $x$  as shown in Fig. A.6 for the modes  $(m, l) = (18, 1)$  in the spiral with  $n = 2.0$ .

Note that additionally to the scaling improvement also a shifting of the cavity in  $x$ - $y$  plane can be used to minimize the area of perturbation. This procedure has already been demonstrated in Ref. [Kraft and Wiersig, 2014] to be valuable for the Limaçon.

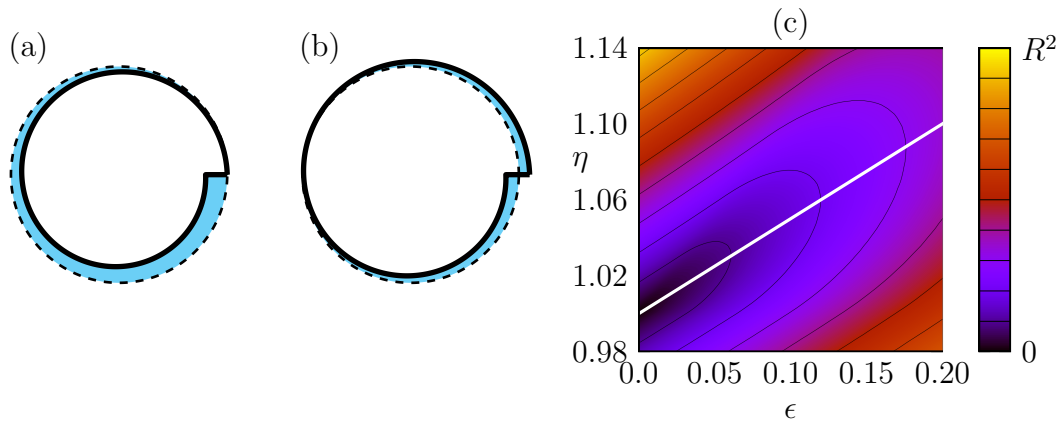


**Figure A.5:** (a) The spiral and (b) the rescaled spiral cavity is shown as black solid curve. The cyan colored region is the area of perturbation  $\delta a$  regarding the circle of radius  $R$  (dashed black curve). (c) The area of the perturbation  $\delta a$  depending on notch size  $\epsilon$  of the spiral and scaling factor  $\eta$  is color encoded from dark (small perturbation area) to bright (large perturbation area). Black solid curves are contour lines. The white line is the optimal scaling to minimize the perturbation area [see Eq. (A.56)].

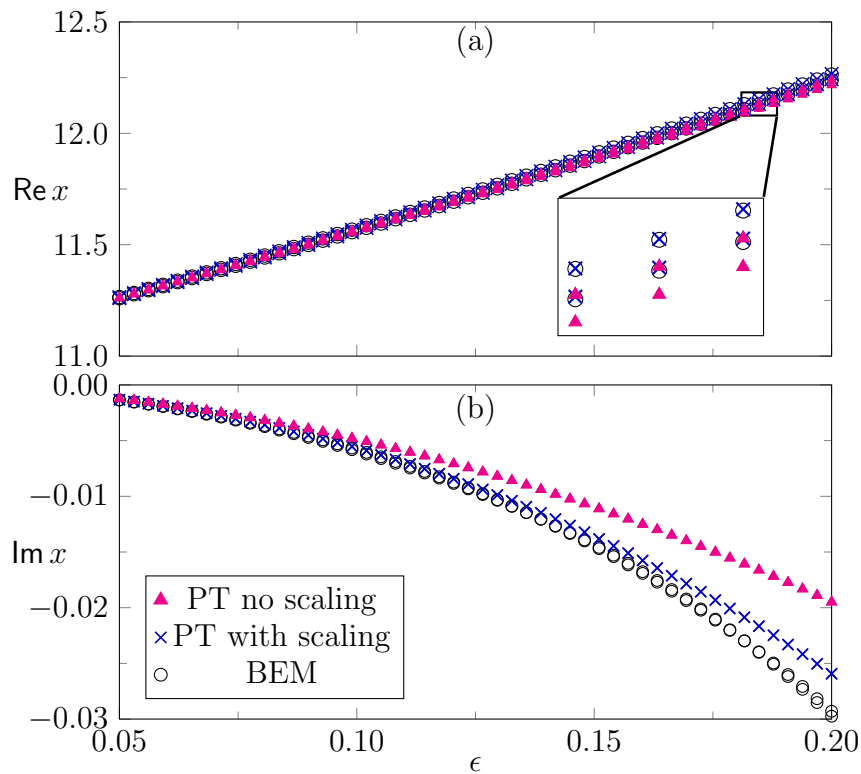


**Figure A.6:** (a) The real and (b) the imaginary part of the complex wave number  $x$  of the optical mode pair  $(m, l) = (18, 1)$  in a spiral cavity with  $n = 2.0$  is shown as function of notch size  $\epsilon$ . Dark blue crosses and magenta triangles represent perturbation theory with  $[\eta$  as in Eq. (A.56)] and without  $[\eta = 1]$  scaling. The BEM results are shown as black open circles.

## A.6 Illustration of the BEM error for the splitting $\Delta x$

In this short appendix it is illustrated why the boundary element method (BEM) for microdisk cavities [Wiersig, 2003] is able to predict the complex frequency splitting  $\Delta x = x_+ - x_-$  more precise than the actual values of  $x_+$  and  $x_-$  itself.

A main part in the BEM algorithm is the integration of a kernel over boundary elements (see e.g. the computation of the matrix elements  $B_{il}$  and  $C_{il}$  in Ref. [Wiersig, 2003]). This motivates to choose a simple numerical integration as an illustration example here: Assume that the two integrals  $\lambda_1$  and  $\lambda_2$  should be computed numerically, e.g. via a Riemann sum or a Gauss quadrature. Further assume that each integral depends on a (small) parameter  $\epsilon$ . For the illustration it is specified

$$\lambda_1(\epsilon) = \int_0^{2\pi} \left[ 1 + \sin(x - \sqrt{3}) + 3\epsilon^2 x^2 \right] dx = 2\pi + (2\pi)^3 \epsilon^2 \quad (\text{A.57a})$$

$$\lambda_2(\epsilon) = \int_0^{2\pi} \left[ 1 + \sin(x - \sqrt{3}) + 2\epsilon^2 x \right] dx = 2\pi + (2\pi)^2 \epsilon^2. \quad (\text{A.57b})$$

Then, each numerically determined integral  $\lambda_1$  and  $\lambda_2$  can have an individually significant error. Especially, the determination of  $\lambda_{1/2}(0)$  also contains errors from the numerical integration. However, by choosing the same numerical parameters for the integration discretization  $\int \rightarrow \sum_i^N \Delta x_i$ . The error of difference  $\Delta\lambda = \lambda_1 - \lambda_2$  can be quite small. Roughly speaking, the errors of the sine integration completely vanishes if the same discretization scheme is used. On the other hand if different discretization schemes for  $\lambda_1$  and  $\lambda_2$  are chosen the error of the sine integration does not cancel out and  $\Delta\lambda$  scales similar to  $\lambda_{1/2}$ . For an illustration of this situation see Fig. A.7.

The relation to the case of a microdisk cavity is as follows:  $\lambda_{1/2}$  represent the complex wave numbers of the even and odd parity modes which depend on a deformation parameter  $\epsilon$ . For the case of the circular cavity ( $\epsilon = 0$ ) the accurate computation of the wave number with BEM is quite elaborated since one often cannot resolve the very small imaginary part of  $x$ . However, if the complex frequency splitting  $\Delta x$  is computed this error from the circular cavity cancels out.

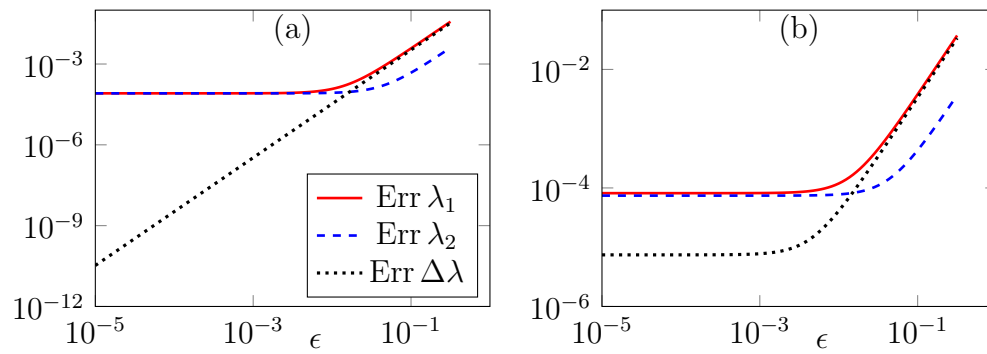


**Figure A.7:** (a) The error of (red solid curve)  $\lambda_1$ , (blue dashed curve)  $\lambda_2$  [see Eqs. (A.57)], and (black dotted curve)  $\Delta\lambda = \lambda_1 - \lambda_2$  for the numerical integration (Riemann sum) with same discretization  $N_1 = N_2 = 1000$  is shown. In (b) the errors for a slightly different discretization  $N_2 = 1100$  for  $\lambda_2$  integration is shown.



# Bibliography

- [Albert et al., 2010] Albert, F., Braun, T., Heindel, T., Schneider, C., Reitzenstein, S., Höfling, S., Worschech, L., and Forchel, A. (2010). Whispering gallery mode lasing in electrically driven quantum dot micropillars. *Appl. Phys. Lett.*, 97(10):101108.
- [Altmann, 2009] Altmann, E. (2009). Emission from dielectric cavities in terms of invariant sets of the chaotic ray dynamics. *Phys. Rev. A*, 79:013830.
- [Altmann et al., 2008] Altmann, E., Del Magno, G., and Hentschel, M. (2008). Non-hamiltonian dynamics in optical microcavities resulting from wave-inspired corrections to geometric optics. *EPL (Europhysics Letters)*, 84(1):10008.
- [Altmann et al., 2013] Altmann, E., Portela, J., and Tél, T. (2013). Leaking chaotic systems. *Rev. Mod. Phys.*, 85:869–918.
- [Armani et al., 2007] Armani, A., Kulkarni, R., Fraser, S., Flagan, R., and Vahala, K. (2007). Label-free, single-molecule detection with optical microcavities. *Science*, 317(5839):783–787.
- [Armani et al., 2003] Armani, D., Kippenberg, T., Spillane, S., and Vahala, K. (2003). Ultra-high-q toroid microcavity on a chip. *Nature*, 421:925–928.
- [Arnol'd, 1963] Arnol'd, V. (1963). Proof of a theorem of an kolmogorov on the invariance of quasi-periodic motions under small perturbations of the hamiltonian. *Russian Mathematical Surveys*, 18(5):9–36.
- [Artmann, 1948] Artmann, K. (1948). Berechnung der seitenversetzung des totalreflektierten strahles. *Ann. Phys.*, 437(1-2):87–102.
- [Bäcker et al., 2010] Bäcker, A., Ketzmerick, R., and Löck, S. (2010). Direct regular-to-chaotic tunneling rates using the fictitious-integrable-system approach. *Phys. Rev. E*, 82:056208.
- [Bäcker et al., 2008] Bäcker, A., Ketzmerick, R., Löck, S., and Schilling, L. (2008). Regular-to-chaotic tunneling rates using a fictitious integrable system. *Phys. Rev. Lett.*, 100:104101.
- [Bäcker et al., 2009] Bäcker, A., Ketzmerick, R., Löck, S., Wiersig, J., and Hentschel, M. (2009). Quality factors and dynamical tunneling in annular microcavities. *Phys. Rev. A*, 79:063804.

- [Beck and Schögl, 1993] Beck, C. and Schögl, F. (1993). *Thermodynamics of Chaotic Systems*. Cambridge University Press.
- [Bender and Boettcher, 1998] Bender, C. and Boettcher, S. (1998). Real spectra in non-hermitian hamiltonians having  $\mathcal{PT}$  symmetry. *Phys. Rev. Lett.*, 80:5243–5246.
- [Berry, 2004] Berry, M. (2004). Physics of nonhermitian degeneracies. *Czechoslovak Journal of Physics*, 54(10):1039–1047.
- [Birkhoff, 1913] Birkhoff, G. (1913). Proof of poincaré’s geometric theorem. *Trans. Amer. Math. Soc.*, 14.
- [Böckler et al., 2008] Böckler, C., Reitzenstein, S., Kistner, C., Debusmann, R., Löffler, A., Kida, T., Höfling, S., Forchel, A., Grenouillet, L., Claudon, J., and Gérard, J. (2008). Electrically driven high-q quantum dot-micropillar cavities. *Appl. Phys. Lett.*, 92(9):091107.
- [Boriskina et al., 2006] Boriskina, S., Benson, T., Sewell, P., and Nosich, A. (2006). Directional emission, increased free spectral range, and mode q-factors in 2-d wavelength-scale optical microcavity structures. *IEEE Journal of Selected Topics in Quantum Electronics*, 12(6):1175–1182.
- [Boriskina et al., 2004] Boriskina, S., Sewell, P., Benson, T., and Nosich, A. (2004). Accurate simulation of two-dimensional optical microcavities with uniquely solvable boundary integral equations and trigonometric galerkin discretization. *J. Opt. Soc. Am. A*, 21(3):393–402.
- [Brandstetter et al., 2014] Brandstetter, M., Liertzer, M., Deutsch, C., Klang, P., Schoöberl, J., Türeci, H. E., Strasser, G., Unterrainer, K., and Rotter, S. (2014). Reversing the pump dependence of a laser at an exceptional points. *Nat. Commun.*, 5:4034.
- [Brodier et al., 2002] Brodier, O., Schlagheck, P., and Ullmo, D. (2002). Resonance-assisted tunneling. *Ann. Phys.*, 300(1):88 – 136.
- [Bunimovich, 1979] Bunimovich, L. A. (1979). On the ergodic properties of nowhere dispersing billiards. *Comm. Math. Phys.*, 65(3):295–312.
- [Cao and Wiersig, 2015] Cao, H. and Wiersig, J. (2015). Dielectric microcavities: Model systems for wave chaos and non-hermitian physics. *Rev. Mod. Phys.*, 87:61–111.
- [Carlo et al., 2015] Carlo, G., Rivas, A., and Spina, M. (2015). Classical to quantum correspondence in dissipative directed transport. *Phys. Rev. E*, 92:052907.
- [Carmon et al., 2008] Carmon, T., Schwefel, H., Yang, L., Oxborrow, M., Stone, A., and Vahala, K. (2008). Static envelope patterns in composite resonances generated by level crossing in optical toroidal microcavities. *Phys. Rev. Lett.*, 100:103905.



- [Chern et al., 2003] Chern, G., Tureci, H., Stone, A., Chang, R., Kneissl, M., and Johnson, N. (2003). Unidirectional lasing from ingan multiple-quantum-well spiral-shaped micropillars. *Appl. Phys. Lett.*, 83(9):1710–1712.
- [Chirikov, 1960] Chirikov, B. (1960). Resonance processes in magnetic traps. *Journal of Nuclear Energy. Part C, Plasma Physics, Accelerators, Thermonuclear Research*, 1(4):253.
- [Collot et al., 1993] Collot, L., Lefèvre-Seguin, V., Brune, M., Raimond, J., and Haroche, S. (1993). Very high- $q$  whispering-gallery mode resonances observed on fused silica microspheres. *EPL (Europhys. Lett.)*, 23(5):327.
- [Creagh and White, 2012] Creagh, S. and White, M. (2012). Differences between emission patterns and internal modes of optical resonators. *Phys. Rev. E*, 85:015201.
- [Crespi et al., 1993] Crespi, B., Perez, G., and Chang, S.-J. (1993). Quantum poincaré sections for two-dimensional billiards. *Phys. Rev. E*, 47:986–991.
- [Daraei et al., 2006] Daraei, A., Tahraoui, A., Sanvitto, D., Timpson, J. A., Fry, P., Hopkinson, M., Guimaraes, P. S. S., Vinck, H., Whittaker, D., Skolnick, M. S., and Fox, A. M. (2006). Control of polarized single quantum dot emission in high-quality-factor microcavity pillars. *Appl. Phys. Lett.*, 88:051113.
- [Davis and Heller, 1981] Davis, M. and Heller, E. (1981). Quantum dynamical tunneling in bound states. *The Journal of Chemical Physics*, 75(1):246–254.
- [Dembowski et al., 2004] Dembowski, C., Dietz, B., Gräf, H.-D., Harney, H. L., Heine, A., Heiss, W. D., and Richter, A. (2004). Encircling an exceptional point. *Phys. Rev. E*, 69:056216.
- [Dembowski et al., 2001] Dembowski, C., Gräf, H.-D., Harney, H. L., Heine, A., Heiss, W. D., Rehfeld, H., and Richter, A. (2001). Experimental observation of the topological structure of exceptional points. *Phys. Rev. Lett.*, 86:787–790.
- [Dubertrand et al., 2008] Dubertrand, R., Bogomolny, E., Djellali, N., Leberant, M., and Schmit, C. (2008). Circular dielectric cavity and its deformations. *Phys. Rev. A*, 77:013804.
- [El-Ganainy et al., 2007a] El-Ganainy, R., Makris, K., Christodoulides, D., and Musslimani, Z. (2007a). Theory of coupled optical  $pt$ -symmetric structures. *Opt. Lett.*, 32(17):2632–2634.
- [El-Ganainy et al., 2007b] El-Ganainy, R., Makris, K., Christodoulides, D., and Musslimani, Z. (2007b). Theory of coupled optical  $pt$ -symmetric structures. *Opt. Lett.*, 32(17):2632–2634.
- [Eltschka and Schlagheck, 2005] Eltschka, C. and Schlagheck, P. (2005). Resonance- and chaos-assisted tunneling in mixed regular-chaotic systems. *Phys. Rev. Lett.*, 94:014101.

- [Ermann and Shepelyansky, 2010] Ermann, L. and Shepelyansky, D. (2010). Ulam method and fractal weyl law for perron-frobenius operators. *Eur. Phys. J. B*, 75(3):299–304.
- [Frahm and Shepelyansky, 2010] Frahm, K. and Shepelyansky, D. (2010). Ulam method for the chirikov standard map. *Eur. Phys. J. B*, 76(1):57–68.
- [Frahm and Shepelyansky, 2013] Frahm, K. and Shepelyansky, D. (2013). Poincaré recurrences and ulam method for the chirikov standard map. *Eur. Phys. J. B*, 86(7).
- [Fritzsche et al., 2017] Fritzsche, F., Bäcker, A., Ketzmerick, R., and Mertig, N. (2017). Complex-path prediction of resonance-assisted tunneling in mixed systems. *Phys. Rev. E*, 95:020202.
- [Frobenius, 1912] Frobenius, G. (1912). *Über Matrizen aus nicht negativen Elementen*. Reimer.
- [Garrett et al., 1961] Garrett, C., Kaiser, W., and Bond, W. (1961). Stimulated emission into optical whispering modes of spheres. *Phys. Rev.*, 124:1807–1809.
- [Ge et al., 2013] Ge, L., Song, Q., Redding, B., and Cao, H. (2013). Extreme output sensitivity to subwavelength boundary deformation in microcavities. *Phys. Rev. A*, 87:023833.
- [Gehler et al., 2015] Gehler, S., Löck, S., Shinohara, S., Bäcker, A., Ketzmerick, R., Kuhl, U., and Stöckmann, H.-J. (2015). Experimental observation of resonance-assisted tunneling. *Phys. Rev. Lett.*, 115:104101.
- [Gmachl et al., 1998] Gmachl, C., Capasso, F., Narimanov, E., Nöckel, J., Stone, A., Faist, J., Sivco, D., and Cho, A. (1998). High-power directional emission from microlasers with chaotic resonators. *Science*, 280(5369):1556–1564.
- [Gmachl et al., 2002] Gmachl, C., Narimanov, E., Capasso, F., Baillargeon, J., and Cho, A. (2002). Kolmogorov–arnold–moser transition and laser action on scar modes in semiconductor diode lasers with deformed resonators. *Opt. Lett.*, 27(10):824–826.
- [Goos and Hänchen, 1947] Goos, F. and Hänchen, H. (1947). Ein neuer und fundamentaler versuch zur totalreflexion. *Ann. Phys.*, 436(7-8):333–346.
- [Götzinger et al., 2006] Götzinger, S., de S. Menezes, L., Mazzei, A., Kühn, S., Sandoghdar, V., and Benson, O. (2006). Controlled photon transfer between two individual nanoemitters via shared high-q modes of a microsphere resonator. *Nano Letters*, 6(6):1151–1154. PMID: 16771571.
- [Guo et al., 2009a] Guo, A., Salamo, G. J., Duchesne, D., Morandotti, R., Volatier-Ravat, M., Aimez, V., Siviloglou, G., and Christodoulides, D. (2009a). Observation of  $\mathcal{PT}$ -symmetry breaking in complex optical potentials. *Phys. Rev. Lett.*, 103:093902.

- [Guo et al., 2009b] Guo, A., Salamo, G. J., Duchesne, D., Morandotti, R., Volatier-Ravat, M., Aimez, V., Siviloglou, G. A., and Christodoulides, D. N. (2009b). Observation of  $\mathcal{PT}$ -symmetry breaking in complex optical potentials. *Phys. Rev. Lett.*, 103:093902.
- [Gutkin, 2007] Gutkin, B. (2007). Dynamical 'breaking' of time reversal symmetry. *Journal of Physics A: Mathematical and Theoretical*, 40(31):F761.
- [Gutzwiller, 1991] Gutzwiller, M. (1991). *Chaos in Classical and Quantum Mechanics*. Interdisciplinary Applied Mathematics. Springer New York.
- [Götte et al., 2013] Götte, J., Shinohara, S., and Hentschel, M. (2013). Are fresnel filtering and the angular goos-hänchen shift the same? *Journal of Optics*, 15(1):014009.
- [Haake, 2010] Haake, F. (2010). *Quantum signatures of chaos (3rd edition)*. Springer.
- [Hackenbroich et al., 1998] Hackenbroich, G., Narimanov, E., and Stone, A. D. (1998). Quantum perturbation theory for the level splitting in billiards. *Phys. Rev. E*, 57:R5–R8.
- [Hackenbroich and Nöckel, 1997] Hackenbroich, G. and Nöckel, J. (1997). Dynamical tunneling in optical cavities. *EPL (Europhys. Lett.)*, 39(4):371.
- [Harayama and Shinohara, 2011] Harayama, T. and Shinohara, S. (2011). Two-dimensional microcavity lasers. *Laser & Photonics Reviews*, 5(2):247–271.
- [Heiss, 2000] Heiss, W. (2000). Repulsion of resonance states and exceptional points. *Phys. Rev. E*, 61:929–932.
- [Heiss, 2012] Heiss, W. (2012). The physics of exceptional points. *Journal of Physics A: Mathematical and Theoretical*, 45(44):444016.
- [Heiss and Harney, 2001] Heiss, W. and Harney, H. (2001). The chirality of exceptional points. *The European Physical Journal D - Atomic, Molecular, Optical and Plasma Physics*, 17(2):149–151.
- [Heller, 1984] Heller, E. (1984). Bound-state eigenfunctions of classically chaotic hamiltonian systems: Scars of periodic orbits. *Phys. Rev. Lett.*, 53:1515–1518.
- [Hentschel and Kwon, 2009] Hentschel, M. and Kwon, T.-Y. (2009). Designing and understanding directional emission from spiral microlasers. *Opt. Lett.*, 34(2):163–165.
- [Hentschel and Richter, 2002] Hentschel, M. and Richter, K. (2002). Quantum chaos in optical systems: The annular billiard. *Phys. Rev. E*, 66:056207.
- [Hentschel and Schomerus, 2002] Hentschel, M. and Schomerus, H. (2002). Fresnel laws at curved dielectric interfaces of microresonators. *Phys. Rev. E*, 65:045603.

- [Hentschel et al., 2003] Hentschel, M., Schomerus, H., and Schubert, R. (2003). Husimi functions at dielectric interfaces: Inside-outside duality for optical systems and beyond. *EPL (Europhys. Lett.)*, 62(5):636.
- [Hodaei et al., 2014] Hodaei, H., Miri, M.-A., Heinrich, M., Christodoulides, D., and Khajavikhan, M. (2014). Parity-time-symmetric microring lasers. *Science*, 346(6212):975–978.
- [Hokr et al., 2016] Hokr, B., Schmidt, M., Bixler, J., Dyer, P., Noojin, G., Redding, B., Thomas, R., Rockwell, B., Cao, H., Yakovlev, V., and Scully, M. (2016). A narrow-band speckle-free light source via random raman lasing. *Journal of Modern Optics*, 63(1):46–49.
- [Husimi, 1940] Husimi, K. (1940). Some formal properties of the density matrix. *Proceedings of the Physico-Mathematical Society of Japan. 3rd Series*, 22(4):264–314.
- [Ilchenko et al., 2001] Ilchenko, V., Gorodetsky, M., Yao, X., and Maleki, L. (2001). Microtorus: a high-finesse microcavity with whispering-gallery modes. *Opt. Lett.*, 26(5):256–258.
- [Ilchenko and Matsko, 2006] Ilchenko, V. and Matsko, A. (2006). Optical resonators with whispering-gallery modes-part ii: applications. *IEEE Journal of Selected Topics in Quantum Electronics*, 12(1):15–32.
- [Inan and Marshall, 2011] Inan, U. and Marshall, R. (2011). *Numerical Electromagnetics: The FDTD Method*. Cambridge University Press, Cambridge.
- [Jackson, 1998] Jackson, J. (1998). *Classical Electrodynamics*. Wiley.
- [Kato, 1966] Kato, T. (1966). *Perturbation Theory for Linear Operators*. Springer, New York.
- [Keshavamurthy, 2005] Keshavamurthy, S. (2005). On dynamical tunneling and classical resonances. *The Journal of Chemical Physics*, 122(11):114109.
- [Keshavamurthy, 2007] Keshavamurthy, S. (2007). Dynamical tunnelling in molecules: quantum routes to energy flow. *International Reviews in Physical Chemistry*, 26(4):521–584.
- [Keshavamurthy and Schlagheck, 2011] Keshavamurthy, S. and Schlagheck, P. (2011). *Dynamical Tunneling: Theory and Experiment*. Taylor & Francis.
- [Kim et al., 2009] Kim, C., Lee, S., Oh, K., and Kim, J. (2009). Experimental verification of quasiscattered resonance mode. *Applied Physics Letters*, 94(23):231120.
- [Kim et al., 2014] Kim, M., Kwon, K., Shim, J., Jung, Y., and Yu, K. (2014). Partially directional microdisk laser with two rayleigh scatterers. *Opt. Lett.*, 39(8):2423–2426.
- [Kim et al., 2015] Kim, S. K., Kim, S. H., Kim, G. H., and Lee, Y. H. (2015). Experimental confirmation of whispering gallery modes with different parities in elliptical microdisks. *J. Korean Phys. Soc.*, 47:3.

- [Kippenberg et al., 2011] Kippenberg, T., Holzwarth, R., and Diddams, S. (2011). Microresonator-based optical frequency combs. *Science*, 332(6029):555–559.
- [Kolmogorov, 1954] Kolmogorov, A. (1954). On the conservation of conditionally periodic motions under small perturbation of the hamiltonian. *Dokl. Akad. Nauk SSSR*, 98:527–530.
- [Körber et al., 2015] Körber, M., Bäcker, A., and Ketzmerick, R. (2015). Localization of chaotic resonance states due to a partial transport barrier. *Phys. Rev. Lett.*, 115:254101.
- [Kraft and Wiersig, 2014] Kraft, M. and Wiersig, J. (2014). Perturbative analysis of whispering-gallery modes in limaçon-shaped microcavities. *Phys. Rev. A*, 89:023819.
- [Kraft and Wiersig, 2016] Kraft, M. and Wiersig, J. (2016). Inverse problem for light emission from weakly deformed microdisk cavities. *Phys. Rev. A*, 94:013851.
- [Kreismann et al., 2017] Kreismann, J., Sinzinger, S., and Hentschel, M. (2017). Three-dimensional limaçon: Properties and applications. *Phys. Rev. A*, 95:011801.
- [Kullig et al., 2014] Kullig, J., Löbner, C., Mertig, N., Bäcker, A., and Ketzmerick, R. (2014). Integrable approximation of regular regions with a nonlinear resonance chain. *Phys. Rev. E*, 90:052906.
- [Kullig and Wiersig, 2016a] Kullig, J. and Wiersig, J. (2016a). Frobenius–perron eigenstates in deformed microdisk cavities: non-hermitian physics and asymmetric backscattering in ray dynamics. *New Journal of Physics*, 18(1):015005.
- [Kullig and Wiersig, 2016b] Kullig, J. and Wiersig, J. (2016b). Perturbation theory for asymmetric deformed microdisk cavities. *Phys. Rev. A*, 94:043850.
- [Kwak et al., 2015] Kwak, H., Shin, Y., Moon, S., Lee, S.-B., Yang, J., and An, K. (2015). Nonlinear resonance-assisted tunneling induced by microcavity deformation. *Sci. Rep.*, 5:9010.
- [Lai et al., 1986] Lai, H., Cheng, F., and Tang, W. (1986). Goos–hänchen effect around and off the critical angle. *J. Opt. Soc. Am. A*, 3(4):550–557.
- [Lazutkin, 1973] Lazutkin, V. (1973). The existence of caustics for a billiard problem in a convex domain. *Mathematics of the USSR-Izvestiya*, 7(1):185.
- [Lebœuf and Mouchet, 1999] Lebœuf, P. and Mouchet, A. (1999). Normal forms and complex periodic orbits in semiclassical expansions of hamiltonian systems. *Annals of Physics*, 275(1):54 – 112.

- [Lee et al., 1998] Lee, K., Leung, P., and Pang, K. (1998). Iterative perturbation scheme for morphology-dependent resonances in dielectric spheres. *J. Opt. Soc. Am. A*, 15(5):1383–1393.
- [Lee et al., 2002] Lee, S.-B., Lee, J.-H., Chang, J.-S., Moon, H.-J., Kim, S., and An, K. (2002). Observation of scarred modes in asymmetrically deformed microcylinder lasers. *Phys. Rev. Lett.*, 88:033903.
- [Lee et al., 2009] Lee, S.-B., Yang, J., Moon, S., Lee, S.-Y., Shim, J.-B., Kim, S., Lee, J.-H., and An, K. (2009). Observation of an exceptional point in a chaotic optical microcavity. *Phys. Rev. Lett.*, 103:134101.
- [Lee and Chung, 2011] Lee, S.-Y. and Chung, Y. (2011). Complex stationary-phase points in dynamical-tunneling emissions. *Phys. Rev. A*, 84:045805.
- [Lee et al., 2004] Lee, S.-Y., Rim, S., Ryu, J.-W., Kwon, T.-Y., Choi, M., and Kim, C.-M. (2004). Quasiscarred resonances in a spiral-shaped microcavity. *Phys. Rev. Lett.*, 93:164102.
- [Lee et al., 2008a] Lee, S.-Y., Rim, S., Ryu, J.-W., Kwon, T.-Y., M., C., and Kim, C.-M. (2008a). Ray and wave dynamical properties of a spiral-shaped dielectric microcavity. *Journal of Physics A: Mathematical and Theoretical*, 41(27):275102.
- [Lee et al., 2008b] Lee, S.-Y., Ryu, J.-W., Shim, J.-B., Lee, S.-B., Kim, S. W., and An, K. (2008b). Divergent petermann factor of interacting resonances in a stadium-shaped microcavity. *Phys. Rev. A*, 78:015805.
- [Levi et al., 1993] Levi, A., Slusher, R., McCall, S., Glass, J., S. Pearton, J., and Logan, R. (1993). Directional light coupling from microdisk lasers. *Appl. Phys. Lett.*, 62(6):561–563.
- [Leymann et al., 2013] Leymann, H. A. M., Hopfmann, C., Albert, F., Foerster, A., Khanbekyan, M., Schneider, C., Höfling, S., Forchel, A., Kamp, M., Wiersig, J., and Reitzenstein, S. (2013). Intensity fluctuations in bimodal micropillar lasers enhanced by quantum-dot gain competition. *Phys. Rev. A*, 87:053819.
- [Lichtenberg and Lieberman, 1992] Lichtenberg, A. and Lieberman, M. (1992). *Regular and Chaotic Dynamics*. Applied mathematical sciences. Springer.
- [Liu et al., 2016] Liu, Z.-P., Zhang, J., Özdemir, S., Peng, B., Jing, H., Lü, X.-Y., Li, C.-W., Yang, L., Nori, F., and Liu, Y. (2016). Metrology with  $\mathcal{PT}$ -symmetric cavities: Enhanced sensitivity near the  $\mathcal{PT}$ -phase transition. *Phys. Rev. Lett.*, 117:110802.
- [Löbner et al., 2013] Löbner, C., Löck, S., Bäcker, A., and Ketzmerick, R. (2013). Integrable approximation of regular islands: The iterative canonical transformation method. *Phys. Rev. E*, 88:062901.

- [Löck, 2009] Löck, S. (2009). *Dynamical Tunneling in Systems with a Mixed Phase Space*. PhD thesis, Technische Universität Dresden.
- [Löck et al., 2010] Löck, S., Bäcker, A., Ketzmerick, R., and Schlagheck, P. (2010). Regular-to-chaotic tunneling rates: From the quantum to the semiclassical regime. *Phys. Rev. Lett.*, 104:114101.
- [Lohmeyer, 2002] Lohmeyer, M. (2002). Mode expansion modeling of rectangular integrated optical microresonators. *Optical and Quantum Electronics*, 34(5):541–557.
- [Luo and Poon, 2007] Luo, X. and Poon, A. (2007). Coupled spiral-shaped microdisk resonators with non-evanescent asymmetric inter-cavity coupling. *Opt. Express*, 15(25):17313–17322.
- [Mackay et al., 1984] Mackay, R., Meiss, J., and Percival, I. (1984). Transport in hamiltonian systems. *Physica D: Nonlinear Phenomena*, 13(1):55 – 81.
- [MacKay et al., 1984] MacKay, R. S., Meiss, J. D., and Percival, I. C. (1984). Stochasticity and transport in hamiltonian systems. *Phys. Rev. Lett.*, 52:697–700.
- [Markarian, 1993] Markarian, R. (1993). New ergodic billiards: exact results. *Nonlinearity*, 6(5):819.
- [Mather, 1982] Mather, J. (1982). Glancing billiards. *Ergodic Theory and Dynamical Systems*, 2(3-4):397–403.
- [Mazzei et al., 2007] Mazzei, A., Götzinger, S., Menezes, S., Zumofen, G., Benson, O., and Sandoghdar, V. (2007). Controlled coupling of counterpropagating whispering-gallery modes by a single rayleigh scatterer: A classical problem in a quantum optical light. *Phys. Rev. Lett.*, 99:173603.
- [McCall et al., 1992] McCall, S., Levi, A., Slusher, R., Pearton, S., and Logan, R. (1992). Whispering-gallery mode microdisk lasers. *Appl. Phys. Lett.*, 60(3):289–291.
- [Meiss, 1992] Meiss, J. D. (1992). Symplectic maps, variational principles, and transport. *Rev. Mod. Phys.*, 64:795–848.
- [Merano et al., 2009] Merano, M., Aiello, A., van Exter, M., and Woerdman, J. P. (2009). Observing angular deviations in the specular reflection of a light beam. *Nat. Photon.*, 3(6):337–340.
- [Mertig, 2013] Mertig, N. (2013). *Complex Paths for Regular-to-Chaotic Tunneling Rates*. PhD thesis, Technische Universität Dresden.
- [Mertig, 2015] Mertig, N. (2015). unpublished.

- [Mertig et al., 2016] Mertig, N., Kullig, J., Löbner, C., Bäcker, A., and Ketzmerick, R. (2016). Perturbation-free prediction of resonance-assisted tunneling in mixed regular-chaotic systems. *Phys. Rev. E*, 94:062220.
- [Mertig et al., 2013] Mertig, N., Löck, S., Bäcker, A., Ketzmerick, R., and Shudo, A. (2013). Complex paths for regular-to-chaotic tunnelling rates. *EPL (Europhys Lett.)*, 102(1):10005.
- [Michler et al., 2012] Michler, M., Bäcker, A., Ketzmerick, R., Stöckmann, H.-J., and Tomsovic, S. (2012). Universal quantum localizing transition of a partial barrier in a chaotic sea. *Phys. Rev. Lett.*, 109:234101.
- [Michler et al., 2000] Michler, P., Imamoglu, A., Mason, M. D., Carson, P. J., Strouse, G. F., and Buratto, S. K. (2000). Quantum correlation among photons from a single quantum dot at room temperature. *Nature*, 406:968–970.
- [Moser, 1962] Moser, J. (1962). On invariant curves of area-preserving mappings of an annulus. *Nachr. Akad. Wiss. Göttingen Math.-Phys. Kl.*, II:1–20.
- [Mouchet et al., 2006] Mouchet, A., Eltschka, C., and Schlagheck, P. (2006). Influence of classical resonances on chaotic tunneling. *Phys. Rev. E*, 74:026211.
- [Nöckel, 1997] Nöckel, J. (1997). *Resonances in Nonintegrable Open Systems*. PhD thesis, Yale University.
- [Nöckel and Stone, 1996] Nöckel, J. and Stone, A. (1996). Chaotic light: a theory of asymmetric cavity resonators. In Chang, R. K. and Campillo, A. J., editors, *Optical Processes in Microcavities*. World Scientific, Singapore.
- [Nöckel and Stone, 1997] Nöckel, J. and Stone, A. (1997). Ray and wave chaos in asymmetric resonant optical cavities. *Nature*, 385(6611):45–47.
- [Nöckel et al., 1994] Nöckel, J., Stone, A., and Chang, R. (1994). Q spoiling and directionality in deformed ringcavities. *Opt. Lett.*, 19(21):1693–1695.
- [Nöckel et al., 1996] Nöckel, J., Stone, A., Chen, G., Grossman, H., and Chang, R. (1996). Directional emission from asymmetric resonant cavities. *Opt. Lett.*, 21(19):1609.
- [Oskooi et al., 2010] Oskooi, A., Roundy, D., Ibanescu, M., Bermel, P., Joannopoulos, J., and Johnson, S. (2010). Meep: A flexible free-software package for electromagnetic simulations by the {FDTD} method. *Computer Physics Communications*, 181(3):687 – 702.
- [Ott, 1993] Ott, E. (1993). *Chaos in Dynamical Systems*. Cambridge University Press, Cambridge.



- [Park et al., 2004] Park, H.-G., Kim, S.-H., Kwon, S.-H., Ju, Y.-G., Yang, J.-K., Baek, J.-H., Kim, S.-B., and Lee, Y.-H. (2004). Electrically driven single-cell photonic crystal laser. *Science*, 305(5689):1444–1447.
- [Pelton et al., 2002] Pelton, M., Santori, C., Vucković, J., Zhang, B., Solomon, G., Plant, J., and Yamamoto, Y. (2002). Efficient source of single photons: A single quantum dot in a micropost microcavity. *Phys. Rev. Lett.*, 89:233602.
- [Peng et al., 2014a] Peng, B., Ozdemir, S., Lei, F., Monifi, F., Gianfreda, M., Long, G., Fan, S., Nori, F., Bender, C., and Yang, L. (2014a). Parity-time-symmetric whispering-gallery microcavities. *Nature Physics*, 10(5):394–398.
- [Peng et al., 2016] Peng, B., Özdemir, S., Liertzer, M., Chen, W., Kramer, J., Yilmaz, H., Wiersig, J., Rotter, S., and Yang, L. (2016). Chiral modes and directional lasing at exceptional points. *Proceedings of the National Academy of Sciences*, 113(25):6845–6850.
- [Peng et al., 2014b] Peng, B., Özdemir, Ş. K., Rotter, S., Yilmaz, H., Liertzer, M., Monfi, F., Bender, C. M., Nori, F., and Yang, L. (2014b). Loss-induced suppression and revival of lasing. *Science*, 17:328–332.
- [Perron, 1907] Perron, O. (1907). Zur theorie der matrices. *Mathematische Annalen*, 64(2):248–263.
- [Poincaré, 1912] Poincaré, H. (1912). Sur un théorème de géométrie. *Rendiconti del Circolo Matematico di Palermo (1884-1940)*, 33(1):375–407.
- [Post, 1967] Post, E. (1967). Sagnac effect. *Rev. Mod. Phys.*, 39:475–493.
- [Qiu et al., 2007] Qiu, S., Cai, J., Li, Y., and Han, Z. (2007). Mode frequency shifts and q-factor changes in 2d microflower cavity and its deformed cavity. *Optics Communications*, 277(2):406 – 410.
- [Redding et al., 2012] Redding, B., Ge, L., Song, Q., Wiersig, J., Solomon, G., and Cao, H. (2012). Local chirality of optical resonances in ultrasmall resonators. *Phys. Rev. Lett.*, 108:253902.
- [Rex et al., 2002] Rex, N., Tureci, H., Schwefel, H. L., Chang, R., and Stone, A. (2002). Fresnel filtering in lasing emission from scarred modes of wave-chaotic optical resonators. *Phys. Rev. Lett.*, 88:094102.
- [Robnik and Berry, 1985] Robnik, M. and Berry, M. (1985). Classical billiards in magnetic fields. *Journal of Physics A: Mathematical and General*, 18(9):1361.

- [Ruter et al., 2010] Ruter, C., Makris, K., El-Ganainy, R., Christodoulides, D., Segev, M., and Kip, D. (2010). Observation of parity-time symmetry in optics. *Nature Physics*, 6:192.
- [Rüter et al., 2010] Rüter, C. E., Makris, K. G., El-Ganainy, R., Christodoulides, D. N., Segev, M., and Kip, D. (2010). Observation of parity-time symmetry in optics. *Nature Physics*, 6:192–195.
- [Ryu et al., 2017] Ryu, J., Lee, J.-W., Yi, C.-H., Kim, J.-H., Lee, I.-G., Kim, H.-S., Kim, S.-B., Oh, K., and Kim, C.-M. (2017). Chirality of a resonance in the absence of backscatterings. *Opt. Express*, 25(4):3381–3386.
- [Sarma et al., 2015] Sarma, R., Ge, L., Wiersig, J., and Cao, H. (2015). Rotating optical microcavities with broken chiral symmetry. *Phys. Rev. Lett.*, 114:053903.
- [Schermer et al., 2015] Schermer, M., Bittner, S., Singh, G., Ulysse, C., Lebental, M., and Wiersig, J. (2015). Unidirectional light emission from low-index polymer microlasers. *App. Phys. Lett.*, 106(10):101107.
- [Schlehahn et al., 2013] Schlehahn, A., Albert, F., Schneider, C., Höfling, S., Reitzenstein, S., Wiersig, J., and Kamp, M. (2013). Mode selection in electrically driven quantum dot microring cavities. *Opt. Express*, 21(13):15951–15958.
- [Schomerus and Hentschel, 2006] Schomerus, H. and Hentschel, M. (2006). Correcting ray optics at curved dielectric microresonator interfaces: Phase-space unification of fresnel filtering and the goos-hänchen shift. *Phys. Rev. Lett.*, 96:243903.
- [Schomerus and Wiersig, 2014] Schomerus, H. and Wiersig, J. (2014). Non-hermitian-transport effects in coupled-resonator optical waveguides. *Phys. Rev. A*, 90:053819.
- [Shim et al., 2011] Shim, J.-B., Wiersig, J., and Cao, H. (2011). Whispering gallery modes formed by partial barriers in ultrasmall deformed microdisks. *Phys. Rev. E*, 84:035202.
- [Shinohara et al., 2010] Shinohara, S., Harayama, T., Fukushima, T., Hentschel, M., Sasaki, T., and Narimanov, E. (2010). Chaos-assisted directional light emission from microcavity lasers. *Phys. Rev. Lett.*, 104:163902.
- [Shinohara et al., 2011] Shinohara, S., Harayama, T., Fukushima, T., Hentschel, M., Sunada, S., and Narimanov, E. (2011). Chaos-assisted emission from asymmetric resonant cavity microlasers. *Phys. Rev. A*, 83:053837.
- [Shinohara et al., 2009] Shinohara, S., Hentschel, M., Wiersig, J., Sasaki, T., and Harayama, T. (2009). Ray-wave correspondence in limaçon-shaped semiconductor microcavities. *Phys. Rev. A*, 80:031801.

- [Smotrova et al., 2005] Smotrova, E., Nosich, A., Benson, T., and Sewell, P. (2005). Cold-cavity thresholds of microdisks with uniform and nonuniform gain: quasi-3-d modeling with accurate 2-d analysis. *IEEE Journal of Selected Topics in Quantum Electronics*, 11(5):1135–1142.
- [Song et al., 2009] Song, Q., Fang, W., Liu, B., Ho, S.-T., Solomon, G., and Cao, H. (2009). Chaotic microcavity laser with high quality factor and unidirectional output. *Phys. Rev. A*, 80:041807.
- [Stewart, 2001] Stewart, G. (2001). *Matrix Algorithms Volume 2: Eigensystems*. SIAM.
- [Stöckmann, 2000] Stöckmann, H.-J. (2000). *Quantum chaos: an introduction*. Cambridge University Press.
- [Stockschlädler et al., 2014] Stockschlädler, P., Kreismann, J., and Hentschel, M. (2014). Curvature dependence of semiclassical corrections to ray optics: How goos-hänchen shift and fresnel filtering deviate from the planar case result. *EPL (Europhys. Lett.)*, 107(6):64001.
- [Stone, 2001] Stone, A. (2001). Wave-chaotic optical resonators and lasers. *Physica Scripta*, 2001(T90):248.
- [Sunada and Harayama, 2006] Sunada, S. and Harayama, T. (2006). Sagnac effect in resonant microcavities. *Phys. Rev. A*, 74:021801.
- [Sunada and Harayama, 2007] Sunada, S. and Harayama, T. (2007). Design of resonant microcavities: application to optical gyroscopes. *Opt. Express*, 15(24):16245–16254.
- [Türeci et al., 2002] Türeci, H., Schwefel, H., Stone, A., and Narimanov, E. (2002). Gaussian-optical approach to stable periodic orbit resonances of partially chaotic dielectric microcavities. *Opt. Express*, 10(16):752–776.
- [Türeci et al., 2005] Türeci, H., Schwefel, H., Jacquod, P., and Stone, A. (2005). Chapter 2 - modes of wave-chaotic dielectric resonators. volume 47 of *Progress in Optics*, pages 75 – 137. Elsevier.
- [Ulam, 1960] Ulam, S. (1960). *A collection of mathematical problems*. Interscience tracts in pure and applied mathematics. Interscience Publishers.
- [Unterhinninghofen, 2011] Unterhinninghofen, J. (2011). *Ray-wave correspondence and extended ray dynamics in optical microcavities*. PhD thesis, Otto-von-Guericke-Universität Magdeburg.
- [Unterhinninghofen and Wiersig, 2010] Unterhinninghofen, J. and Wiersig, J. (2010). Interplay of goos-hänchen shift and boundary curvature in deformed microdisks. *Phys. Rev. E*, 82:026202.

- [Unterhinninghofen et al., 2008] Unterhinninghofen, J., Wiersig, J., and Hentschel, M. (2008). Goos-hänchen shift and localization of optical modes in deformed microcavities. *Phys. Rev. E*, 78:016201.
- [Vahala, 2003] Vahala, K. (2003). Optical microcavities. *Nature (London)*, 424:839.
- [van den Berg and Fokkema, 1979] van den Berg, P. and Fokkema, J. (1979). The rayleigh hypothesis in the theory of diffraction by a cylindrical obstacle. *IEEE Transactions on Antennas and Propagation*, 27(5):577–583.
- [Vollmer and Arnold, 2008] Vollmer, F. and Arnold, S. (2008). Whispering-gallery-mode biosensing: label-free detection down to single molecules. *Nature Methods*, 5:591.
- [Vollmer et al., 2008] Vollmer, F., Arnold, S., and Keng, D. (2008). Single virus detection from the reactive shift of a whispering-gallery mode. *PNAS*, 105(52):20701–20704.
- [Wang et al., 2010] Wang, Q., Yan, C., Yu, N., Unterhinninghofen, J., Wiersig, J., Pflügl, C., Diehl, L., Edamura, T., Yamanishi, M., Kan, H., and Capasso, F. (2010). Whispering-gallery mode resonators for highly unidirectional laser action. *PNAS*, 107(52):22407–22412.
- [Watanabe et al., 2004] Watanabe, T., Choyal, Y., Minami, K., and Granatstein, V. L. (2004). Range of validity of the rayleigh hypothesis. *Phys. Rev. E*, 69:056606.
- [Wauer and Rother, 2009] Wauer, J. and Rother, T. (2009). Considerations to rayleigh’s hypothesis. *Optics Communications*, 282(3):339 – 350.
- [Weber et al., 2001] Weber, J., Haake, F., Braun, P., Manderfeld, C., and Seba, P. (2001). Resonances of the frobenius-perron operator for a hamiltonian map with a mixed phase space. *Journal of Physics A: Mathematical and General*, 34(36):7195.
- [Weber et al., 2000] Weber, J., Haake, F., and Šeba, P. (2000). Frobenius-perron resonances for maps with a mixed phase space. *Phys. Rev. Lett.*, 85:3620–3623.
- [Wiersig, 2003] Wiersig, J. (2003). Boundary element method for resonances in dielectric microcavities. *Journal of Optics A: Pure and Applied Optics*, 5(1):53.
- [Wiersig, 2006] Wiersig, J. (2006). Formation of long-lived, scarlike modes near avoided resonance crossings in optical microcavities. *Phys. Rev. Lett.*, 97:253901.
- [Wiersig, 2008] Wiersig, J. (2008). Reciprocal transmissions and asymmetric modal distributions in waveguide-coupled spiral-shaped microdisk resonators: Comment. *Opt. Express*, 16(8):5874–5875.
- [Wiersig, 2011] Wiersig, J. (2011). Structure of whispering-gallery modes in optical microdisks perturbed by nanoparticles. *Phys. Rev. A*, 84:063828.

- [Wiersig, 2012] Wiersig, J. (2012). Perturbative approach to optical microdisks with a local boundary deformation. *Phys. Rev. A*, 85:063838.
- [Wiersig, 2014a] Wiersig, J. (2014a). Chiral and nonorthogonal eigenstate pairs in open quantum systems with weak backscattering between counterpropagating traveling waves. *Phys. Rev. A*, 89:012119.
- [Wiersig, 2014b] Wiersig, J. (2014b). Enhancing the sensitivity of frequency and energy splitting detection by using exceptional points: Application to microcavity sensors for single-particle detection. *Phys. Rev. Lett.*, 112:203901.
- [Wiersig, 2016] Wiersig, J. (2016). Sensors operating at exceptional points: General theory. *Phys. Rev. A*, 93:033809.
- [Wiersig et al., 2011] Wiersig, J., Eberspächer, A., Shim, J.-B., Ryu, J.-W., Shinohara, S., Hentschel, M., and Schomerus, H. (2011). Nonorthogonal pairs of copropagating optical modes in deformed microdisk cavities. *Phys. Rev. A*, 84:023845.
- [Wiersig et al., 2009] Wiersig, J., Gies, C., Jahnke, F., Aszmann, M., Berstermann, T., Bayer, M., Kistner, C., Reitzenstein, S., Schneider, C., Hofling, S., Forchel, A., Kruse, C., Kalden, J., and Hommel, D. (2009). Direct observation of correlations between individual photon emission events of a microcavity laser. *Nature*, 460:245–249.
- [Wiersig and Hentschel, 2006] Wiersig, J. and Hentschel, M. (2006). Unidirectional light emission from high- $q$  modes in optical microcavities. *Phys. Rev. A*, 73:031802.
- [Wiersig and Hentschel, 2008] Wiersig, J. and Hentschel, M. (2008). Combining directional light output and ultralow loss in deformed microdisks. *Phys. Rev. Lett.*, 100:033901.
- [Wiersig et al., 2008] Wiersig, J., Kim, S., and Hentschel, M. (2008). Asymmetric scattering and nonorthogonal mode patterns in optical microspirals. *Phys. Rev. A*, 78:053809.
- [Wiersig and Kullig, 2017] Wiersig, J. and Kullig, J. (2017). Optical microdisk cavities with rough sidewalls: A perturbative approach based on weak boundary deformations. *Phys. Rev. A*, 95:053815.
- [Wilkinson, 1986] Wilkinson, M. (1986). Tunnelling between tori in phase space. *Physica D: Nonlinear Phenomena*, 21(2):341 – 354.
- [Yan et al., 2009] Yan, C., Wang, Q., Diehl, L., Hentschel, M., Wiersig, J., Yu, N., Pflügl, C., Capasso, F., Belkin, M., Edamura, T., Yamanishi, M., and Kan, H. (2009). Directional emission and universal far-field behavior from semiconductor lasers with limaçon-shaped microcavity. *Appl. Phys. Lett.*, 94(25):251101.

- [Yang et al., 2006] Yang, J., Moon, S., Lee, S.-B., Lee, J.-H., An, K., Shim, J.-B., Lee, H.-W., and Kim, S.-W. (2006). Development of a deformation-tunable quadrupolar microcavity. *Review of Scientific Instruments*, 77(8):083103.
- [Yeo and Selvaraju, 1993] Yeo, S. P. and Selvaraju, S. (1993). Computational tests on use of rayleigh hypothesis in elliptical-waveguide analysis. *IEEE Transactions on Magnetics*, 29(2):1620–1623.
- [Yi et al., 2009] Yi, C.-H., Kim, M.-W., and Kim, C.-M. (2009). Lasing characteristics of a limaçon-shaped microcavity laser. *Appl. Phys. Lett.*, 95(14):141107.
- [Yi et al., 2011] Yi, C.-H., Lee, S., Kim, M.-W., Cho, J., Lee, J., Lee, S.-Y., Wiersig, J., and Kim, C.-M. (2011). Light emission of a scarlike mode with assistance of quasiperiodicity. *Phys. Rev. A*, 84:041803.
- [Yu et al., 2015] Yu, H.-H., Yi, C.-H., and Kim, C.-M. (2015). Mechanism of q-spoiling in deformed optical microcavities. *Opt. Express*, 23(9):11054–11062.
- [Zhang et al., 1995] Zhang, J., Chu, D., Wu, S., Ho, S., Bi, W., Tu, C., and Tiberio, R. (1995). Photonic-wire laser. *Phys. Rev. Lett.*, 75:2678–2681.
- [Zhu et al., 2010] Zhu, J., Özdemir, S., He, L., and Yang, L. (2010). Controlled manipulation of mode splitting in an optical microcavity by two rayleigh scatterers. *Opt. Express*, 18(23):23535–23543.

## Acknowledgments

First of all I thank Prof. J. Wiersig for giving me the opportunity to work in his group on such an interesting topic and his supervision during my PhD time. In particular I want to emphasize his guidance with valuable advises and comments in lots of discussions.

Furthermore, the support from the DFG within the project “Nicht-Hermitesche Effekte durch asymmetrische Rückstreuung in optischen Mikroresonatoren” is acknowledged.

I am very grateful for many fruitful discussions about my work with Dr. N. Mertig, Dr. M. Körber, F. Fritsche, Dr. A. Bäcker, Prof. R. Ketzmerick, Dr. P. Stockschläder, J. Kreismann, Prof. M. Hentschel, and Prof. L. Ge.

All the members of the working group in Magdeburg, Dr. G. Kasner, Dr. M. Khanbekyan, Dr. C.H. Yi, Dr. A. Leymann, A. Foerster, B. Melcher, S. Neumeier, M. Badel, M. Kraft, J. Kramer, have contributed to a very nice and pleasant working climate such that it was always a pleasure to discuss and talk with them.

Dr. G. Kasner deserves an additional thanks for fixing every kind of problem I had with the computer. And S. Simon deserves the acknowledgment for the help with every administrative issue occurring during my PhD time.

I thank the two referees for spending their time to read and evaluate my thesis.

Furthermore, I want to thank my former fellow students Tim, Maik, Marco, and Stefan. Whenever I meet them again it was always nice to talk about the latest progress.

Last but not least I want to thank my parents for their continuous support during all the years.





## List of Publications

- **Kullig, J.**, Löbner, C., Mertig, N., Bäcker, A., and Ketzmerick, R., *Integrable approximation of regular regions with a nonlinear resonance chain*, Phys. Rev. E 90, 052906 (2014)
- **Kullig, J.** and Wiersig, J., *Frobenius–Perron eigenstates in deformed microdisk cavities: non-Hermitian physics and asymmetric backscattering in ray dynamics*, New J. Phys. 18, 015005 (2016)
- **Kullig, J.** and Wiersig, J., *Q spoiling in deformed optical microdisks due to resonance-assisted tunneling*, Phys. Rev. E 94, 022202 (2016)
- **Kullig, J.** and Wiersig, J., *Perturbation theory for asymmetric deformed microdisk cavities*, Phys. Rev. A 043850 (2016)
- Mertig, N., **Kullig, J.**, Löbner, C., Bäcker, A., and Ketzmerick, R., *Perturbation-Free Prediction of Resonance-Assisted Tunneling in Mixed Regular–Chaotic Systems*, Phys. Rev. E 94, 062220 (2016)
- Yi, C.-H., **Kullig, J.**, Lee, J.-W., Kim, J.-H., Yu, H.-H., Wiersig, J., and Kim, C.-M., *Separatrix modes in weakly deformed microdisk cavities*, Opt. Express 7, 8048 (2017)
- Wiersig, J. and **Kullig, J.**, *Optical microdisk cavities with rough sidewalls: A perturbative approach based on weak boundary deformations*, Phys. Rev. A 95, 053815 (2017)



## Erklärung

Hiermit erkläre ich, dass ich die von mir eingereichte Dissertation zum Thema

Non-Hermitian physics in deformed optical microdisk  
cavities: Asymmetric backscattering and  $Q$ -spoiling

selbständig verfasst, nicht schon als Dissertation verwendet habe und die benutzten Hilfsmittel und Quellen vollständig angegeben wurden.

Weiterhin erkläre ich, dass ich weder diese noch eine andere Arbeit zur Erlangung des akademischen Grades doctor rerum naturalium (Dr. rer. nat.) an anderen Einrichtungen eingereicht habe.

Dipl.-Phys. Julius Kullig

Magdeburg, den 21.06.2017